

EFFECTS OF FRACTURE GEOMETRY ON FLUID FLOW
THROUGH THE MONTEREY FORMATION, CALIFORNIA –
AN APPLICATION OF A 3D DISCRETE
FRACTURE SIMULATOR

CENTRE FOR NEWFOUNDLAND STUDIES

**TOTAL OF 10 PAGES ONLY
MAY BE XEROXED**

(Without Author's Permission)

RICHARD ALAN SCHAEFER

CENTRE FOR WFLD. STUDIES
JAN 12 1995
MEMORIAL UNIVERSITY
OF NEWFOUNDLAND



National Library
of Canada

Acquisitions and
Bibliographic Services Branch

395 Wellington Street
Ottawa, Ontario
K1A 0N4

Bibliothèque nationale
du Canada

Direction des acquisitions et
des services bibliographiques

395, rue Wellington
Ottawa (Ontario)
K1A 0N4

Author: [illegible]

Date: [illegible]

NOTICE

The quality of this microform is heavily dependent upon the quality of the original thesis submitted for microfilming. Every effort has been made to ensure the highest quality of reproduction possible.

If pages are missing, contact the university which granted the degree.

Some pages may have indistinct print especially if the original pages were typed with a poor typewriter ribbon or if the university sent us an inferior photocopy.

Reproduction in full or in part of this microform is governed by the Canadian Copyright Act, R.S.C. 1970, c. C-30, and subsequent amendments.

AVIS

La qualité de cette microforme dépend grandement de la qualité de la thèse soumise au microfilmage. Nous avons tout fait pour assurer une qualité supérieure de reproduction.

S'il manque des pages, veuillez communiquer avec l'université qui a conféré le grade.

La qualité d'impression de certaines pages peut laisser à désirer, surtout si les pages originales ont été dactylographiées à l'aide d'un ruban usé ou si l'université nous a fait parvenir une photocopie de qualité inférieure.

La reproduction, même partielle, de cette microforme est soumise à la Loi canadienne sur le droit d'auteur, SRC 1970, c. C-30, et ses amendements subséquents.

Canada

**EFFECTS OF FRACTURE GEOMETRY ON FLUID FLOW
THROUGH THE MONTEREY FORMATION, CALIFORNIA - AN
APPLICATION OF A 3D DISCRETE FRACTURE SIMULATOR.**

BY

© RICHARD ALAN SCHAEFER

A thesis submitted to the School of Graduate
Studies in partial fulfillment of the
requirements for the degree of
Master of Science

Department of Earth Science
Memorial University of Newfoundland

May, 1994

St. John's, Newfoundland



National Library
of Canada

Acquisitions and
Bibliographic Services Branch

395 Wellington Street
Ottawa, Ontario
K1A 0N4

Bibliothèque nationale
du Canada

Direction des acquisitions et
des services bibliographiques

395, rue Wellington
Ottawa (Ontario)
K1A 0N4

Number / Numéro de référence

Classification / Numéro de classement

The author has granted an irrevocable non-exclusive licence allowing the National Library of Canada to reproduce, loan, distribute or sell copies of his/her thesis by any means and in any form or format, making this thesis available to interested persons.

L'auteur a accordé une licence irrévocable et non exclusive permettant à la Bibliothèque nationale du Canada de reproduire, prêter, distribuer ou vendre des copies de sa thèse de quelque manière et sous quelque forme que ce soit pour mettre des exemplaires de cette thèse à la disposition des personnes intéressées.

The author retains ownership of the copyright in his/her thesis. Neither the thesis nor substantial extracts from it may be printed or otherwise reproduced without his/her permission.

L'auteur conserve la propriété du droit d'auteur qui protège sa thèse. Ni la thèse ni des extraits substantiels de celle-ci ne doivent être imprimés ou autrement reproduits sans son autorisation.

ISBN 0-315-91617-6

Canada

ABSTRACT

Outcrops of the fractured and folded sedimentary Monterey Formation located along or near the coast of central California were sampled to characterize the geometry of the fracture system and determine the impact of the fracture geometry on rock mass permeability. A scanline mapping technique was used to obtain: orientation, trace length, spacing, mineral infill, termination, censoring, and shape data for over 1700 individual discontinuities. Analyzing the general fracture characteristics, using cluster analysis of the poles to fracture planes, and taking into account the different structural settings, it was determined that there were two to three fracture sets at each of six different locations. Four of these locations, were part of a "small-scale" fracture survey where short scanlines (≤ 30 m) sampled fractures 0.25 m or greater in trace length from individual outcrops. The other two locations, were a composite of sites sampled for "large-scale" fractures (extensive breccias and faults) with trace lengths greater than 3 m, using long (100 m to 1400 m) scanlines. The strike of the dominant fracture set at most small-scale sites was sub-parallel to bedding dip direction. Generally the fractures in the subordinate set had shorter trace lengths that terminated against and were approximately perpendicular to the fractures making up the dominant set. The two large-scale sites had three sets, one sub-horizontal, one sub-parallel to bedding strike, and the other sub-parallel to bedding dip direction, all with similar mean lengths.

Statistical methods were used to correct for some of the biases, associated with scanline mapping, in the trace length, spacing and orientation data. Straight lines, drawn through the data points on probability plots show that the fracture trace length and spacing data can be approximated by a lognormal distribution. The statistics of trace length, density, and

orientation obtained from the field data, along with assumed aperture distributions were used in a 3-D discrete fracture flow simulator to evaluate the impact of the variability in fracture orientation, fracture interconnectivity, and aperture on rock mass permeability. Simulations of rock mass cubes with side length of 8 to 18 meters for the small-scale data and 100 to 150 meters for the large-scale data, found that the fracture geometry was well connected and imparted a strong anisotropy to flow in the horizontal section and less so in the vertical section, when the same aperture was assigned to each fracture. When the apertures for individual fractures were generated using a lognormal distribution the computed directional permeabilities became even more anisotropic to flow.

ACKNOWLEDGEMENTS

The advice and guidance from my advisor, Dr. John Gale, through all phases of this thesis, and his friendship, are gratefully acknowledged. I am especially appreciative for the opportunity to take on this thesis, the computer resources he made available and his concentrated attention during the editing of this thesis.

I would like to gratefully acknowledge the financial support from Chevron Petroleum Technology Company (CPTC) and for their permission to use the Monterey field fracture data, which made this thesis possible. I am especially indebted to Dr. A. B. Carpenter of CPTC, who as a member of my thesis committee gave technical guidance and input to many phases of this thesis, and was generous in financial and moral support.

A portion of the work for this thesis was part of an overall research project, headed by Dr. Gale, examining the impact of fractures on enhanced hydrocarbon recovery from fractured oil reservoirs and was funded by Supply and Services Canada Center for Mineral and Energy Technology, Shell Canada Research, Hibernia Management Development Corporation, Fracflow Consultants Inc. and Imperial Oil Limited with additional funding provided by an NSERC operating grant to Dr. Gale. Thanks are extended to these organizations.

This thesis has greatly benefited from the advice and insight of several other scientists that I would like to thank; Dr. A. Herbert of AEA Harwell Laboratory, England, for guidance and help with the NAPSAC computer program, Dr. G. Viele of the University of Missouri, at Columbia, who's expertise on the structural geology of the study areas was of great help, Dr.

A. Rouleau of the Université du Québec à Chicoutimi, for his help in using the NETWRK/NETFLO computer programs. I would also like to thank all the Chevron employees who helped in collecting the fracture data.

Most importantly, I would like to express my appreciation to my mother and my siblings, and my wife's parents and her family for their love and support during this long thesis process. And to Carmen, my wife, who produced many of the figures, and endured it all with me, a lifetime is not long enough to say thank-you!

TABLE OF CONTENTS

	Page
ABSTRACT	ii
ACKNOWLEDGEMENTS	iv
LIST OF TABLES	viii
LIST OF FIGURES	x
CHAPTER 1. INTRODUCTION	1
1.1 BACKGROUND	1
1.2 OBJECTIVES and SCOPE	3
1.3 PREVIOUS WORK	6
1.3.1 Characterization of the Monterey fracture system	6
1.3.2 Folding and Fracturing of Sedimentary Rocks	11
1.3.3 Fracture Network and Fracture Flow Modeling	18
CHAPTER 2. GEOLOGIC SETTING	21
2.1 REGIONAL GEOLOGY	21
2.2 LOCAL GEOLOGY	29
2.2.1 Government Point	29
2.2.2 Jalama Beach	31
2.2.3 Point Arguello	34
2.2.4 Lompoc Landing/Purisima Point	35
2.2.5 Lions Head	37
CHAPTER 3. FRACTURE DATA COLLECTION AND ANALYSIS	39
3.1 DATA COLLECTION AND MAPPING PROCEDURE	39
3.2 GENERAL FRACTURE CHARACTERISTICS	46
3.2.1 Small-scale fracture system	46
3.2.2 Large-scale fracture system	60
3.2.3 Relationship to Structure	64
3.3 FRACTURE ORIENTATION	69
3.3.1 Small-Scale Data	69
3.3.2 Large-Scale Data	81
3.4 FRACTURE TRACE LENGTH	84
3.4.1 Small-Scale Data	86
3.4.2 Large-Scale Data	93
3.5 FRACTURE SPACING	98
3.5.1 Small-Scale Data	100
3.5.2 Large-Scale Data	104

	Page
CHAPTER 4. NUMERICAL SIMULATION	108
4.1 INTRODUCTION	108
4.2 TWO DIMENSIONAL SIMULATION	109
4.2.1 Model Description	109
4.2.2 Input and Results	111
4.3 THREE DIMENSIONAL SIMULATION	121
4.3.1 Model Description	121
4.3.2 Input and Results	122
 CHAPTER 5. DISCUSSION, SUMMARY AND CONCLUSIONS	 148
5.1 FRACTURE MAPPING AND STATISTICS	149
5.2 NUMERICAL MODELING	155
5.3 CONCLUSIONS AND RECOMMENDATIONS	159
 REFERENCES	 161
 APPENDIX A. FRACTURE MAPPING DATA FILES	 169
 APPENDIX B. EXAMPLES OF SCANLINE MAPS FOR BOTH SURVEYS	 202
 APPENDIX C. DETERMINING FRACTURE SETS AND ORIENTATION BIAS .	 209

TABLES

		Page
Table 3.1.	Scanline summary for each site in the small-scale survey.	46
Table 3.2.	Summary of fracture types and types of mineral infill for each site in the small-scale survey.	49
Table 3.3.	Raw trace length statistics by mineral infill for small-scale survey sites.	51
Table 3.4.	Scanline summary for each site in the large-scale survey.	61
Table 3.5.	Summary of fracture types and infill for sites in the large-scale survey.	61
Table 3.6.	Basic statistics of trace length for breccia zones and faults measured in the two mapped "large-scale" areas.	61
Table 3.7.	Mean fracture orientation and bedding orientation per site/station in the small-scale survey.	70
Table 3.8.	Mean orientations of sets for large-scale fractures that have been rotated so that all bedding have a common strike.	82
Table 3.9.	General statistics of raw trace length for each set in the small-scale survey.	89
Table 3.10.	Means and standard deviations, in meters, for fracture sets in small-scale survey.	92
Table 3.11.	General statistics of raw trace length for each set in the large-scale survey.	94
Table 3.12.	Trace length and fracture length, large-scale survey. Means and standard deviations, in meters, for each fracture set.	97
Table 3.13.	General statistics of corrected spacings for each set in the small-scale survey.	101
Table 3.14.	General statistics of corrected spacings for each set in the large-scale survey.	104
Table 4.1.	Trace length and spacing statistics for each fracture set, used in 2-D simulations.	112
Table 4.2.	Probabilities of a generated fracture exceeding a certain length for a given mean and standard deviation (Std.Dev.) from a lognormal distributions.	127

	Page
Table 4.3.	Comparison of corrected trace length means and spacings, from realizations, with the input statistics for the GP A and B models. 127
Table 4.4.	Input statistics for the models chosen to evaluate directional permeability. See text for discussion. 129
Table 4.5.	Summary of output from realizations used in evaluating the effect of fracture orientation and aperture have on permeability. 131
Table 4.6.	Position and magnitude (in millidarcies) of principal permeability axes calculated using equations from Scheidegger (1954). 137
Table 4.7.	Statistical summary of realizations used to determine variability in the magnitude of permeability in the x and z directions for the Government Point and South Vandenberg B models. 138
Table 5.1.	Summary of mean orientation, trace length and spacing for each fracture set. 154
Table C.1.	Statistics of the orientation data presented on stereonets in Figures C.1 through C.3. 228

FIGURES

		Page
Figure 1.1.	General location map of the study sites.	4
Figure 1.2.	Flexural - slip process, beds slip against each other when bending, friction between layers produces drag folds in brittle layers (after Dunham and Blake, 1987).	7
Figure 1.3.	Conjugate folds, fold hinges commonly cross. Kink type has sharp hinge area, Box type has rounded hinges (after Ramsay and Huber, 1987).	9
Figure 1.4.	Potential dilation openings in kink bands of a conjugate fold (after Ramsay and Huber, 1987).	9
Figure 1.5.	Type and orientation of joints associated with folds (after Price, 1966).	12
Figure 1.6.	Joint set patterns on folds and associated stress fields (after Stearns, 1968).	13
Figure 2.1.	Generalized stratigraphic column showing position of each study area (after MacKinnon, 1989; Gale et al., 1991).	22
Figure 2.2.	Location of structural domains.	25
Figure 3.1.	Logging form for fracture mapping surveys.	41
Figure 3.2.	Schematic diagram illustrating some of the mapping conventions used in this study.	42
Figure 3.3.	Explanation of coding conventions for scanline fracture mapping.	43
Figure 3.4.	Cut effect, (after Ramsay and Huber, 1987). Fracture pattern seen depends on orientation of exposure.	45
Figure 3.5.	Lower hemisphere equal area plots of poles to fracture planes for GP - Government Point, JB - Jalama Beach, LL - Lompoc Landing, and LH - Lions Head.	48
Figure 3.6.	Bar charts of raw trace length per mineral infill, for small-scale sites.	52
Figure 3.7.	Box plot summary display of raw trace length distributions, for GP - Government Point sites 1, 2 & 3, JB - Jalama Beach sites 1-4, 5, & 6; LL - Lompoc Landing, and LH - Lions Head.	54
Figure 3.8.	Lower hemisphere equal area plots of poles to fracture planes coded by mineral infill.	55

	Page	
Figure 3.9.	Box plots of raw trace length for different trace shapes (large scale roughness) for small-scale survey sites.	56
Figure 3.10	Lower hemisphere equal area plots of poles to fracture planes for different trace shapes (large scale roughness).	57
Figure 3.11	Box plots of raw trace length for different fracture surface roughnesses, for small-scale survey sites.	58
Figure 3.12	Lower hemisphere equal area plots of poles to fracture planes for different fracture surface roughnesses.	59
Figure 3.13	Three dimensional distribution of faults and breccia zones measured during large-scale survey. NV - North Vandenberg, SV - South Vandenberg.	63
Figure 3.14	Strike rose diagrams for features at each area from both surveys, relevant folds and faults are shown. a.) Sites in the Santa Barbara Channel structural domain. b.) Sites in the Onshore Santa Maria structural domain.	65
Figure 3.15	Histograms of angular difference between bedding strike and strike of discontinuities, for each area in the small-scale survey.	67
Figure 3.16	Lower hemisphere equal area plots of poles to mean fracture planes with bedding plane as great circle for each Government Point station. Stations P4 and P5 are combined as GP3.	71
Figure 3.17	Lower hemisphere equal area plots of poles to mean fracture planes with bedding plane as great circle for each site at Jalama Beach.	72
Figure 3.18	Lower hemisphere equal area plots of poles to mean fracture planes with bedding plane as great circle for the Lompoc Landing (LL) and Lions Head sites.	73
Figure 3.19	a.) Lower hemisphere equal area plots of poles to fracture planes that have been rotated, for Government Point and Jalama Beach fracture sets. Bed strike rotated to "N-S" axis and to a horizontal position. b.) For fractures set at Lompoc Landing and Lions Head.	75
Figure 3.20	Lower hemisphere equal area plots of mean poles of fracture sets shown in Figure 3.19 a. and b., bedding rotated data.	77
Figure 3.21	Box plot summary display showing the spread and distributions, of the bedding rotated orientation data.	79

	Page	
Figure 3.22	Lower hemisphere equal area stereoplots of poles to fracture planes for the large-scale survey. NV - combined data from two sites in the Onshore Santa Maria domain, SV - combined data from all sites in the Santa Barbara Channel domain.	83
Figure 3.23	Bar charts of trace length by censoring for each fracture set. a.) GP - Government Point; JB - Jalama Beach sites 1-4. b.) JB - Jalama Beach sites 5&6. c.) LL - Lompoc Landing.	87 88 89
Figure 3.24	Probability plots using plotting position for censored data. Example shows comparison of trace length data for Government Point set 1h to the lognormal and exponential distributions.	91
Figure 3.25	Bar charts of trace length by censoring for each fracture set. NV - North Vandenberg; SV - South Vandenberg.	95
Figure 3.26	Probability plots using plotting position for censored data. Example shows comparison of trace length data for South Vandenberg set 1 to the lognormal and exponential distributions.	96
Figure 3.27	Scanline schematic illustrating correction for spacing.	99
Figure 3.28	Box plot summary display for each set, showing the spread and distributions of spacing. GP,1 and GP,2 - Government Point sets 1 and 2, JB14 - Jalama Beach sites 1 through 4 sets 1 and 2, JB56 - Jalama Beach sites 5 and 6 sets 1, 2 and 3, LL - Lompoc Landing sets 1 and 2. N = sample size.	102
Figure 3.29	Example of probability plots showing comparison of spacing data to theoretical lognormal and exponential distributions, for Government Point (GP) set 1.	103
Figure 3.30	Box plot summary display for each set, showing the spread and distributions of spacing. North Vandenberg sets 1, 2; South Vandenberg sets 1, 2 and 3.	106
Figure 3.31	Example of probability plots showing comparison of spacing data to theoretical lognormal and exponential distributions, for South Vandenberg set 1.	107
Figure 4.1.	Diagrams showing input parameters for modeling fluid flow through generated fracture network from Government Point data, (a) horizontal plane, (b) N-S vertical section, (c) E-W vertical section.	115

	Page
Figure 4.2. Diagrams showing input parameters for modeling fluid flow through generated fracture network from Jalama Beach data, (a) horizontal plane, (b) N-S vertical section, (c) E-W vertical section.	116
Figure 4.3. Diagrams of relative flux as a function of direction for uncorrected and corrected trace lengths from Government Point data, (a) horizontal plane, (b) N-S vertical section, (c) E-W vertical section.	117
Figure 4.4. Diagrams of relative flux as a function of direction for uncorrected trace lengths from Jalama Beach data, (a) horizontal plane, (b) N-S vertical section, (c) E-W vertical section.	118
Figure 4.5. Relative flux as a function of direction in the E-W vertical section at (a) Government Point for the corrected fracture trace length data and, (b) Jalama Beach for the raw fracture trace length data. Both networks include the bedding plane shears as a third fracture set with a mean trace length of 30m.	119
Figure 4.6. Relative flux as a function of direction in the horizontal plane at Government Point for the corrected fracture trace length data and variable aperture.	120
Figure 4.7. Graphs showing the relationship of permeability to block size. gp - Government Point; jb14 - Jalama Beach sites 1-4; jb56 - Jalama Beach sites 5&6; ll - Lompoc Landing; nv - North Vandenberg; sv - South Vandenberg. b is for "B" model input, a for "A" model input, x and z indicate direction of gradient.	124
Figure 4.8. Directional permeability and $1/k^h$ plots for Government Point B model. Horizontal and vertical scales in same units.	139
Figure 4.9. Directional permeability and $1/k^h$ plots for Government Point A model. Horizontal and vertical scales in same units.	140
Figure 4.10. Directional permeability and $1/k^h$ plots for Jalama Beach sites 1 - 4 B model. Horizontal and vertical scales in same units.	141
Figure 4.11. Directional permeability and $1/k^h$ plots for Jalama Beach sites 5&6 B model. Horizontal and vertical scales in same units.	142
Figure 4.12. Directional permeability and $1/k^h$ plots for Lompoc Landing B model. Horizontal and vertical scales in same units.	143
Figure 4.13. Directional permeability and $1/k^h$ plots for North Vandenberg B model. Horizontal and vertical scales in same units.	144

	Page
Figure 4.14	Directional permeability and $1/k^*$ plots for South Vandenberg B model. Horizontal and vertical scales in same units. 145
Figure 4.15	Directional permeability and $1/k^*$ plots for Government Point B model with variable aperture. Horizontal and vertical scales in same units. 146
Figure 4.16	Directional permeability and $1/k^*$ plots for South Vandenberg B model with variable aperture. Horizontal and vertical scales in same units. 147
Figure B.1.	Examples of small-scale fracture survey scanline maps. 203
Figure B.2.	Examples of large-scale fracture survey scanline maps. 206
Figure C.1.	Lower hemisphere equal area plots of poles to fracture planes at Government Point, stations C1, P1, and P2. 218
Figure C.2.	Lower hemisphere equal area plots of poles to fracture planes at Jalama Beach, sites 1, 2, and 3. 220
Figure C.3.	Lower hemisphere equal area plots of poles to fracture planes at Lompoc Landing and Lions Head. 222
Figure C.4.	Contoured lower hemisphere equal area plots of poles to fracture planes at Government Point, stations C1, P1, and P2. 223
Figure C.5.	Contoured lower hemisphere equal area plots of poles to fracture planes at Jalama Beach, sites 1, 2, and 3. 225
Figure C.6.	Contoured lower hemisphere equal area plots of poles to fracture planes at Lompoc Landing and Lions Head. 227
Figure C.7.	Examples of graphs and stereoplots used to visually evaluate the fit of the orientation data for each set to the theoretical Fisher probability distribution. See text for further discussion. 230
Figure C.8.	Lower hemisphere equal area plots of poles to fracture planes for the large-scale features mapped along the coast southeast of Rocky Point, SV474 and SV475 are the numbers of the photo map base, and for railroad cuts near Rocky Point (SV477) and Point Arquello (SV478). 232
Figure C.9.	Lower hemisphere equal area plots of poles to fracture planes for large-scale features mapped near Lompoc Landing (NV497) and Purisma Point (NV501). 233

	Page
Figure C.10. Contoured lower hemisphere equal area plots of poles to fracture planes for the large-scale features mapped along the coast southeast of Rocky Point, SV474 and SV475 are the numbers of the photo map base. Contours are percent of poles in one percent area.	234
Figure C.11. Contoured lower hemisphere equal area plots of poles to fracture planes for large-scale features mapped near Lompoc Landing (NV497) and Purisma Point (NV501).	236
Figure C.12. Lower hemisphere equal area stereoplots of poles to planes for all large-scale features mapped in the Santa Barbara Channel structural domain. Poles have been rotated so bedding strikes north-south and is horizontal.	237
Figure C.13. Lower hemisphere equal area stereoplots of poles to planes for all large-scale features mapped in the Onshore Santa Maria structural domain. Poles have been rotated so bedding strikes north-south and is horizontal.	238

CHAPTER 1. INTRODUCTION

1.1 BACKGROUND

Characterization of discontinuities plays an important role in understanding the mechanical and hydraulic behaviour of a rock mass or a fractured oil and gas reservoir. Fractured rock mass permeabilities depend on the number of fracture sets, their orientation, spacing, length, and character. In order to effectively model a fracture system and understand the effects of fractures on rock mass permeability, it is important to measure accurately the fracture parameters and appropriately determine the statistical nature of these parameters. In the last few decades oil companies have invested significantly in exploring fractured oil and gas reservoirs such as those found in the Monterey Formation (Crain et al., 1985; MacKinnon, 1989) off the California coast. Even though accurate fracture characterization and modeling is important to the economic development of these offshore reservoirs, there are few published data on the fractures in the Monterey Formation.

Although matrix porosity is present, much of the production from the structures in the Monterey Formation is related to permeability associated with tectonic features on a wide range of scales; open fold hinges, fault zones, shear zones, breccia zones and joints (Viele, 1984; Crain et al., 1985; MacKinnon, 1989). In the report by Viele(1984), it was shown that the tectonic fractures were related to widespread conjugate folding in the Monterey Formation. Measurements made of the lengths of the major fold axes and fault zones from geological maps (Dibblee, 1950) indicate that these features must form a small percentage of the total reservoir porosity, but reservoir performance suggests they form zones of very high

permeability (Gale et al., 1991). It appears that the Monterey reservoirs are a variation of the classical dual porosity, dual permeability reservoir (MacKinnon, 1989; Gale et al., 1991). The major features form the main conduits for fluid movement, and the small-scale features and matrix form both the feeder streets and the bulk of the storage or porosity in the reservoir. In order to adequately describe a fractured reservoir, such as in the Monterey Formation, there is a need to know as much as possible about the relationships between the small and large scale fracture systems, their spatial variability, their geometric and genetic relationships to parent structures, and the stress field(s) that created them, as well as their orientation with respect to the existing stress field.

Geophysical methods, such as 3D seismic surveys, can define large scale features in the subsurface but only near a bore hole can adequate data be obtained for the small-scale features. Outcrop fracture mapping studies have shown that it is possible to obtain good orientation, size and shape data on fractures, and from these data to describe statistically the fracture geometry of a rock mass (LaPointe and Hudson, 1985; Gale et al., 1991). One approach to studying and characterizing fractured reservoirs from outcrop fracture data has been proposed by Gale et al. (1991), which was the approach used in this study. This approach was based on systematic fracture mapping programs that provide detailed data bases on the geometry (orientation, trace length and spacing) of the small-scale (joints) and large-scale (fracture zones, breccias and shear zones) fracture systems. The collected data were used to provide a detailed statistical characterization of the fracture system.

The next step was to incorporate these fracture statistics into a fracture network simulator to determine the anisotropy to flow and fracture interconnectivity within the fractured reservoir. Simulation of fracture networks that include data on the fracture apertures will lead to quantitative estimates of flowrates.

1.2 OBJECTIVES and SCOPE

This research study was undertaken to provide a detailed statistical description of the fracture system in the Monterey Formation, based on outcrop mapping, and to evaluate the impact of the fracture geometry on flow and fluid velocity in the reservoir, using a 3D discrete fracture simulator.

The statistical description of the fracture system was based on the evaluation of the fracture data collected for Chevron Oil Field Research Company during the period 1985 through 1989. Fracture data were collected using the scanline mapping technique (LaPointe and Hudson, 1985), from surface outcrops of the Monterey formation at several different locations along the coast of California from Point Conception to Point Sal (Figure 1.1). A rigorous statistical analysis of the general fracture characteristics has been completed, for each of the mapped areas, to determine the general fracture patterns and the degree of correlation between main fracture attributes. Cluster analysis on the overall fracture orientation data sets was used to define the main fracture groupings. Statistical analysis of these groupings, with consideration of mapping biases (Terzaghi, 1965; Priest and Hudson, 1981; LaPointe and Hudson, 1985; Priest, 1985), produced a set of statistics for the main fracture clusters.

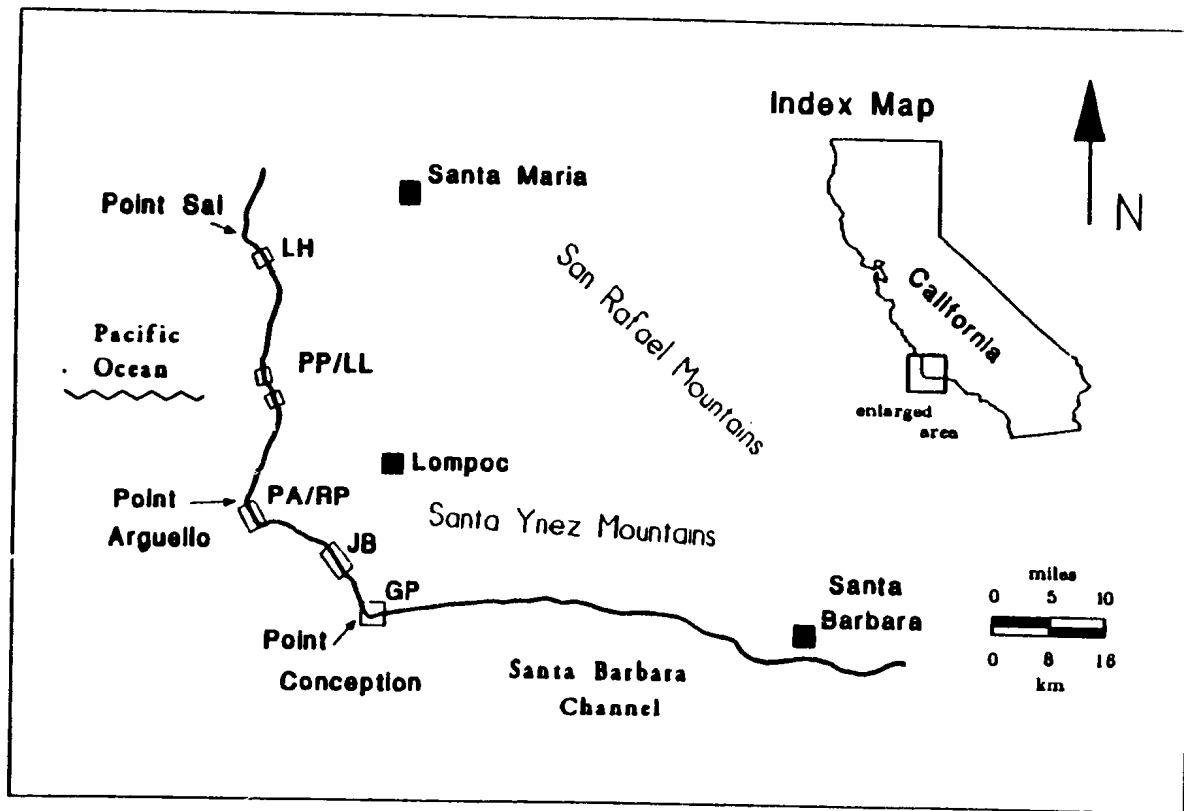


Figure 1.1. General location map of the study sites. GP - Government Point; JB - Jalama Beach; LH - Lions Head; PA/RP - Point Arguello/Rocky Point; PP/LL - Furisma Point/Lompoc Landing.

The fracture statistics computed from the field data were used in the 3D fracture network simulator, NAPSAC, to determine the effects of the fracture geometry on flow properties and to develop the appropriate flow and transport properties for equivalent porous media models. NAPSAC (Herbert et al., 1990) uses the statistical data for each fracture set as input parameters to generate a simulated fracture network, and then calculates steady-state fluid flow through the generated network. The flow is described in terms of piezometric head and is assumed to be restricted to the fractures with no contribution to flow from the rock matrix.

The fracture network is generated using the statistics for up to six distinct sets. Discrete fractures can also be included. Fracture orientation angles, lengths, and effective apertures for each set can be assigned from several statistical distributions. The network is generated within a cuboid region which is made larger than the desired solution region to avoid any edge effects. Fractures not intersecting the solution region are discarded. Constant head boundary conditions are assigned based on assumed gradients. Once the network is generated all intersections are determined and a number of network nodes are set along each intersection. NAPSAC then calculates the pressure field, obtained from the mass conservation equation, along the intersections of the fracture planes. The flux across a fracture plane is assumed to be linearly related to the pressure gradient and follows the "parallel plate" or fracture flow law. NAPSAC assumes the fracture is rectangular in shape and solves for each response function using a finite-element technique. The boundary conditions for this calculation are no flux around the edges of fracture planes that do not form intersections, and specified pressures along all the fracture intersections on the plane. Each rectangular

representation of a fracture is discretized into a regular mesh of linear triangle elements. The transmissivity for each element can be chosen independently, which allows for fracture aperture variation to be included, if data are available, and allows a portion of each fracture to be closed off if it is outside of the solution region.

1.3 PREVIOUS WORK

1.3.1 Characterization of the Monterey fracture system

Publications that discuss the tectonic development of the Santa Barbara coastal area include Ernst (1981) and Ingersoll and Ernst (1987). The stratigraphy, diagenesis and deformation of the Monterey Formation in this area, is discussed by Garrison et al. (1981), Isaacs et al. (1983), Dunham and Blake (1987), MacKinnon (1989) and others. These publications and a thesis by Grivetti (1982) give a good overview of the observations and interpretations of the fracturing in the Monterey Formation.

Grivetti (1982) gives a detailed description of the fracturing in the Monterey Formation, in the northern Santa Barbara county area. He describes the intense folding and fracturing that occurs in the chert beds of the Monterey. Based on his field work, Grivetti (1982) concluded that rock type controls fracture density, thus fracture porosity is highest in the cherts. Most fractures formed due to folding or faulting. Folds, especially in the cherts, are mainly due to a flexural-slip process (Figure 1.2) and are locally rotated. Two fracture sets approximately

orthogonal to each other were recognized by Grivetti, with one sub-perpendicular to bedding strike.

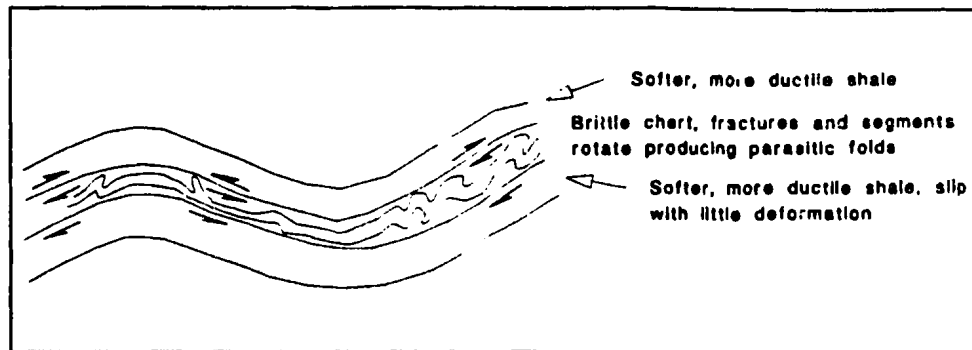


Figure 1.2. Flexural - slip process, beds slip against each other when bending, friction between layers produces parasitic folds in brittle layers (after Dunham and Blake, 1987).

Belfield et al. (1983) discuss the fracturing and brecciation of the Monterey, and present data from their observations of outcrops in the Santa Barbara coastal area. They concur with Grivetti, that fracture intensity is controlled by rock type, and is tectonic in origin, at least for fractures important in the movement of hydrocarbons. They also point out that other non-tectonic fractures, are common in some rocks and locations, such as syneresis cracks, which look similar to desiccation cracks but form by sub-aqueous shrinkage due to the loss of pore water. Belfield et al. (1983) present fracture data for one location in two stereograms and a histogram, showing that the fractures dip steeply and are sub-perpendicular to bedding. These extensional fractures strike northeast and are preferentially filled with tar. They cite evidence from earthquake p-axes data (Lee et al., 1979) to explain this preferred orientation for the tar filled fractures. These p-axes data imply that the average direction for the maximum compressive principal stress is $32^{\circ}(N32^{\circ}E)$. They conclude that fluids would tend to migrate up fractures that are normal to the minimum compressive stress, which is perpendicular to the

maximum stress direction. It is inferred that the intermediate and minimum principal stresses are of similar magnitude since strike-slip and reverse motion occur on faults in this area. This is assuming that the stress field was similar to the present day stress field when the fractures were filled with tar.

Snyder et al. (1983) and Snyder (1987) address the effects of rock material and diagenesis on the deformation of the Monterey. The diagenetic state of biogenic silica which progresses from opal-A through opal-CT to quartz with increasing temperature can have an influence on the style of deformation (Snyder et al., 1983). Beds of similar rock type, such as chert or porcelanite, may contain biogenic silica in different states of diagenesis which in turn cause a possible difference in fracture density. Snyder (1987) states that the folds in the Monterey Formation which were formed by flexural slip, tend to be upright with bedding remaining parallel in concentric and chevron folds. The observed parallelism of bedding in these folds leads to space problems, as evidenced by folds dying out vertically or being faulted. Snyder confirms the earlier observations that the dominant fractures are perpendicular to the bedding plane and strike parallel to the bedding dip.

Viele (1984) described the regional fracturing and folding of the Monterey in the Santa Maria basin area and proposed underlying mechanisms that produced this deformation. From his study, Viele concluded that: (1) conjugate folds are the predominate structures in the Monterey Formation (Figure 1.3), (2) zones of dilation are common in the hinge areas of conjugate folds which, in the absence of ductile deformation, form major permeability

fairways (Figure 1.4), and (3) major fractures are extension fractures formed normal to the fold axes.

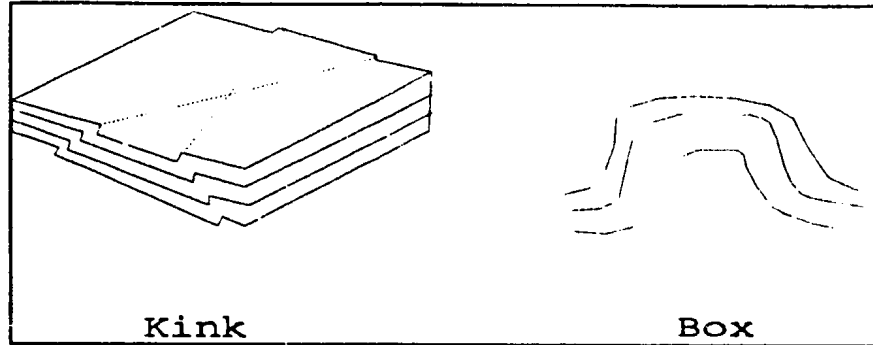


Figure 1.3. Conjugate folds, fold hinges commonly cross. Kink type has sharp hinge, box type rounded hinges. (after Ramsay and Huber, 1987)

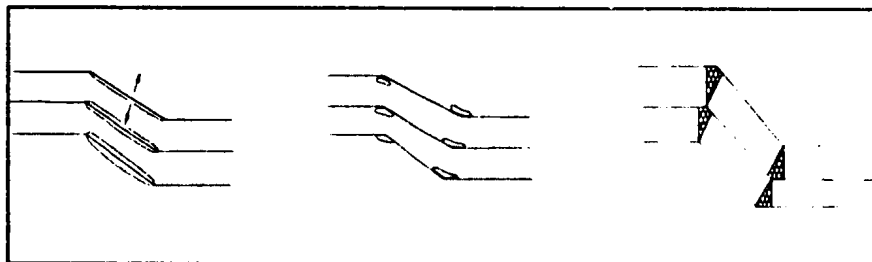


Figure 1.4. Potential dilation openings in kink bands of a conjugate fold (after Ramsay and Huber, 1987).

In a second study by Chevron (Gale et al., 1991) a preliminary description of the fracture systems was produced. This work consisted of detailed areal and scanline mapping, similar to LaPointe and Hudson (1985), of fractures intersecting coastal outcrops in four areas; Point Conception, Jalama Beach, Lions Head and Lompoc Landing. A number of fracture parameters were measured including fracture location, orientations, trace lengths, fracture

filling materials, and surface characteristics. Over 1500 joints and fractures were measured at the four locations with more than 90% coming from 13 outcrop locations at Point Conception and Jalama Beach. From this study, it was determined that there were two main vertical fracture sets, a dominant extension set and a less prevalent cross set. Gale et al. (1991), reported average orientations for the extensional set as N41°E, similar to what Belfield et al. (1983) reported, and a cross set approximately orthogonal to the extensional set. Statistical data were used in a 2-D stochastic fracture network model to generate and determine the effects of fracture geometry on reservoir permeability. This 2-D modeling, using a constant fracture aperture, showed a strong anisotropy to flow with the maximum flow rate direction oriented approximately parallel to the strike of the extensional set.

Narr (1991) discussed fracture densities in the Monterey Formation using data collected from outcrop and core studies. He defined fracture density according to his fracture-spacing index which is a dimensionless number equal to the "mechanical" bed thickness divided by the median spacing between fractures. A "mechanical" bed is defined as the jointed layer between boundaries that the joints do not cross. This bed may or may not consist of a single rock type. Of the 57 mechanical beds that Narr measured, the median thickness was 3.0 cm and ranged from 0.1 to 40 cm (Narr, p.1307, 1991). Narr states that the predominant fracture set is extensional but, unlike other workers, he concluded that fracture density depends more on mechanical bed thickness and structural position than on rock composition. Narr observed that jointing in most of the rock types was enhanced by weathering and unloading, and he found no appreciable difference in fracture density between rock types. However, Narr's lithologic analysis of rock hand-specimens was probably not adequate to

recognize the compositional changes, especially clay and organic matter, between some rock types (Carpenter, pers. comm., 1992).

1.3.2 Folding and Fracturing of Sedimentary Rocks

The number of fracture sets and their mean orientation in a strata that is folded, depends on the orientation of the stresses active during the folding, along with the size and shape of the fold, the strength of the rock, and the thickness of the bedding (Price, 1966, Stearns, 1968). In rock that is not complexly folded, Price proposed that four main sets of joints, two tension sets and two shear sets, would be created. As seen in Figure 1.5a, one tension set is parallel to the fold axes (b), a second tension set (ac) is perpendicular to the fold axes, and these tension fractures bisect the angles formed by the two conjugate shear fracture sets. In Figure 1.5b the relative orientation of the joints to the fold limbs is shown. The joints parallel with the ac plane are extensional and form parallel to the direction of the major principal stress. Joints parallel to the fold axis (b) are longitudinal and perpendicular to the major principal stress. The shear joints (S) form at an angle to the major principal stress.

Stearns (1968) wrote that there are four different configurations (Figure 1.6) for the three principal stresses in a fold, depending on which principal stresses are parallel and perpendicular to the bedding plane. These four different stress configurations can produce a total of ten different fracture orientations (eleven if a shear joint forms parallel to bedding). Stearns' (1968) field observations, of Wyoming anticlines, showed that four main joint patterns were associated with these folds (see Figure 1.6). The fracture sets, in the first

pattern (Figure 1.6a), are due to compression parallel to the dip direction, and in the second pattern (Figure 1.6b) are due to extension parallel to dip. The extension joints in pattern 2 and those in pattern 1, are similar to Price's bc fractures and ac fractures respectively.

Stearns points out that this classification of joints in relation to the fold axis is not valid for the extension fractures at the nose of a fold. The orientation of extension joints at the nose of a fold is dependent on bedding rotation and not the fold axis.

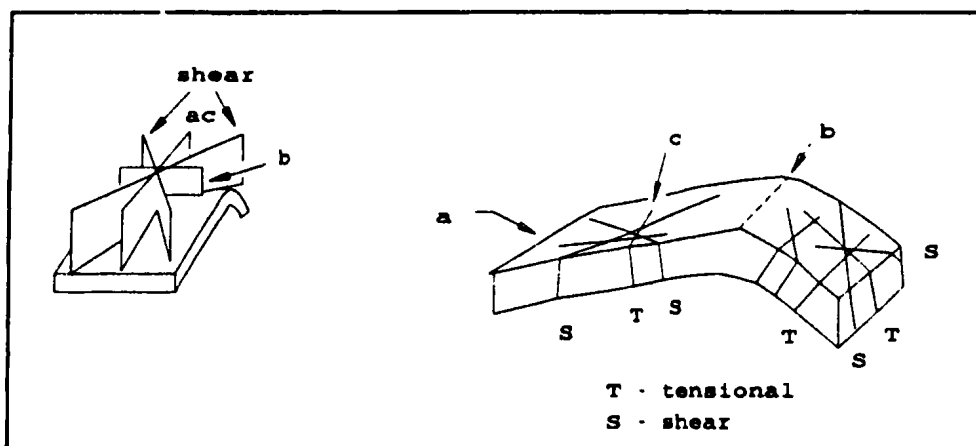


Figure 1.5. Type and orientation of joints associated with folds (after Price, 1966).

The fractures of pattern 3 (Figure 1.6c) form in a "normal fault position" relative to the bedding plane, and represent extension parallel to dip direction. The joints in pattern 4 (Figure 1.6d) formed due to compression parallel to dip direction, and have "thrust fault"-like orientation relative to bedding. Stearns (1968) observed that patterns 1 and 2 were widespread and strongly developed and that patterns 3 and 4 were shorter and locally developed. Stearns offered the conclusion that pattern 1 developed early in the folding

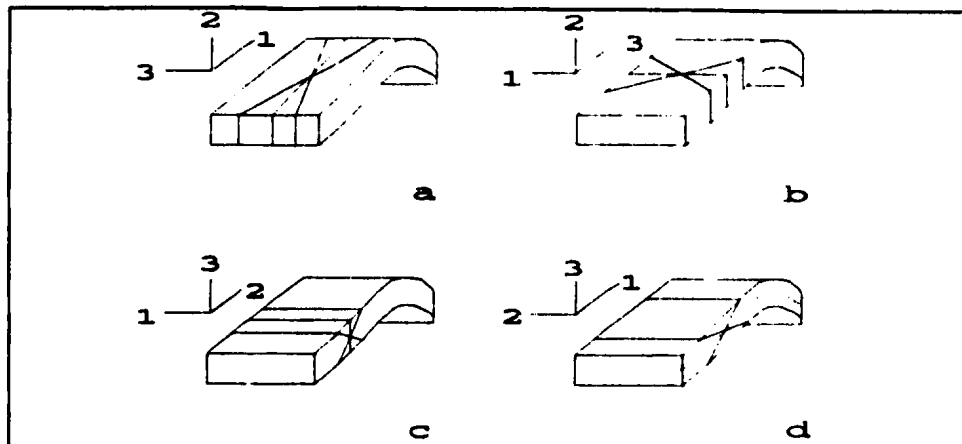


Figure 1.6. Joint set patterns on folds and associated stress fields (after Stearns, 1968).
Patterns: 1 = a; 2 = b; 3 = c; 4 = d.

process, with pattern 2 developing only when extensional forces become large, perpendicular to the fold, and patterns 3 and 4 resulting from local flexure or buckling of beds.

Jaroszewski (1984), states that even though the stress history of a folded rock may be complex, observations show that fractures have a relatively regular orientation within folds and that the joints are fairly uniformly developed throughout the folded area.

Hodgson (1961) and McQuillan (1973) among others, have concluded that no relationship exist between joints and folds. Stearns (1968), however, argues that the relationship may not be evident from mapped patterns if sampling does not cover all areas of the fold (ie. fold hinges, limbs). Also the joint set orientation, and density can be complicated by repeated folding and/or the change in the principal stress orientations, which may cause a different pattern to overlay an existing pattern. Along with other factors such as rock type, bed thickness, and competence of the rock, a definitive joint pattern may be hard to recognize. Since most rock masses are not homogeneous in regard to their physical and mechanical

properties, it would be unlikely that a folded rock mass would exactly exhibit the idealized fracture patterns mentioned above. However, from the many field and laboratory observations it is clear that the general patterns of joints associated with folds, as mentioned by Stearns, Price, Jaroszewski, and others (Hancock, 1985; Polishook and Flexer, 1985; Reches, 1976; and Winsor, 1979) should not be ignored.

The ability to move or extract oil in a fractured reservoir, in relation to the fracture network, depends on the concentration (density) of fracturing, interconnectivity of fractures, length of fractures, and openness (aperture) of the fractures. Gorham (1979) states that a one millimetre wide fracture that crosses a well can provide enough permeability to produce 7000 to 10,000 bbl/day, depending on pressure and fluid viscosity. As discussed earlier, there are several fracture patterns associated with folds, and of these patterns, Stearns and Friedman (1972) concluded that two patterns normally have sufficient density and extent to create potential reservoirs. These are pattern 1 and 2 as seen in Figure 1.6a & b.

From field studies, Stearns and Friedman made several observations and conclusions about each pattern. They found that pattern 1 was usually continuous vertically (10's of meters) and horizontally (up to 100's of meters) as single joints or zones across the entire fold structure. The joints had a wide range of trace lengths but distribution was skewed toward longer traces, with a narrow range of orientations. Because of the extent of this set, this pattern could effect fluid communication for long distances, but also, there are three possible directions of communication between the fractures and a borehole. Pattern 2 is observed as shorter, 2-3 meters at most, and usually it is the trend of all three fractures that is continuous along the

fold. This pattern exhibits more of a interconnection between the fractures of different sets than what was observed with pattern 1. Due to this "lacy" interconnection, and smaller joints, there is a stronger chance of block rotation and dilation in the fracture zones. This led Stearns and Friedman to conclude that pattern 2 may be a more effective passage way for fluid movement than pattern 1. The communication between pattern 2 and a wellbore would be favoured in the direction parallel to the fold trend.

As indicated above, fracture density in a rock mass is affected by rock type and bed thickness. It has been observed that thinner beds, under the same stress regime, will tend to fracture more than thicker beds. Price (1966), McQuillan (1973), and Narr (1991) have shown that bed thickness is the dominant factor in determining joint spacing in sedimentary rock at some localities. Pollard and Segall (1987) introduced a model for joint spacing based on the premise that the perturbation of the stress field, around a joint, effects the development of an adjacent joint, and the range of influence is based on the length of the joint. The length of the joint, based on observations, is assumed to be determined by the thickness of the jointed layer. Models by Price (1966) and Hobbs (1967) consider rock type important in determining joint frequency, due to varying rock properties. Both models determine joint frequency by using rock property terms that rely on how a rock responds to stress and strain. It stands to reason that joint spacing would, in part, be influenced by rock composition, since brittle failure of the rock depends on the rock's mechanical properties.

Position on a structure has also been found to be an important factor in fracture density (Murray, 1968; Stearns & Friedman, 1972; Gorham, 1979; Jaroszewski, 1984). Fracture

density seems to be greatest where the rate of the change in dip is greatest, in other words at the strongest curvature of the fold. Sharply angled folds, such as chevron or kink folds, will have a concentration of joints at the hinge area, and a fold that is more in a semi-circular shape will have a more regular distribution of joints (Jaroszewski, 1984). Stearns and Friedman (1972) found that pattern 2 is more affected by the rate of curvature, since the fracturing process that developed the pattern is a result of cataclasis flow. Fracturing can be so intense in this area of greatest change in curvature that the rock can be completely shattered by unordered fracturing (Stearns and Friedman, 1972). Murray (1968) from his work with a fractured reservoir in North Dakota, also concluded that fracture intensity was greatest in the area of strongest curvature. He developed mathematical formulas relating fracture porosity and fracture permeability to bed thickness and structural curvature. Fracture porosity equals the product of curvature and bed thickness and fracture permeability is equal to the third power of the above product. This exact mathematical relationship between fracture porosity and permeability may not hold true for other folds but the basic parameters may still be well correlated. Gorham (1979) found oil production was best from wells that cut through the hinge line of the monocline structure in the San Juan Basin of New Mexico. Field and core studies revealed three joint sets all perpendicular to bedding. From these field observations Gorham made four basic conclusions: (1) fractures are best developed in flexures with maximum curvature, (2) if the axial fold trace is inclined the hinge line migrates laterally with depth, (3) open fractures developed best parallel to the fold trend, and (4) fractures are perpendicular to bedding but have greater lateral extent than vertical continuity. Similar conclusions were drawn by Quillan and Stearns (1986) from a study of fractures in core. They noticed that subtle changes in the rate of change in dip did not result in an increase in

fracture intensity but a high rate of change did, the ratio of extension fractures to shear fractures locally increased with increase in curvature, and fracture intensity depended on rock type.

In the Monterey Formation, rock composition is probably a major factor controlling fracture density, even though folding occurred at low confining pressure (Viele, 1984), with bed thickness and position on structure being secondary. At all study sites, where the brittle chert layers were present, the cherts had the highest fracture density, followed by porcelanite and dolostone, and the more ductile shales had the lowest fracture density. From the published data, it appears that fracture frequency is higher in the cherts beds than in any other rocks with comparable bed thickness.

As seen in published studies, brittle deformation in the Monterey Formation is dominated by extensional fracturing. However, there is great variability in the orientation of the fractures. Belfield et al. (1983) reported that fractures along the coast of the Santa Barbara Channel show orientations sub-perpendicular to bedding strike and, although it was not explicitly stated, their figures show at least a 40° scatter in the fracture strike direction. Similarly, Stearn's (1968) states a 30° spread in strike is not uncommon. Snyder (1987) proposed that a general model for the fracturing of the Monterey could be pattern 1 in Figure 1.6a. Several problems exist, however, in trying to apply this model to the fold-related fracturing in the Monterey. All fracture sets shown in pattern 1 are not fully developed, and the orientation of the sets that are present do not match the predicted trends (Snyder, 1987).

1.3.3 Fracture Network and Fracture Flow Modeling

Numerical models of flow through fractured media can be grouped by the number of fluids being considered (oil, gas, water) and the type of fractured formation (discrete fracture, single block, multi-fracture or continuum) flow is occurring through (van Golf-Racht, 1982). To determine the equivalent permeability of a fractured rock mass, models are either based on the assumption fractures are continuous, or that the fractures are discrete and of finite size (Long et al., 1982). Van Golf-Racht (1982) and Litvak (1986) discussed several of these different types of models, and Wang (1991) offered a review of recently published fracture flow and transport models.

Models, by Snow (1969), Caldwell (1971), and Duguid and Lee (1977) integrated fracture geometry with hydrologic data, assuming that the fractures were continuous to some flow or pressure boundary. They used tensor mathematics to compute an equivalent porous media permeability. Although this approach is useful, it does not take into account the discontinuous nature of fracture systems. Discrete fracture flow models for non-porous media include the steady-state pipe-flow model by Wilson et al. (1970) and the steady-state three-dimensional planar model by Wittke (1970). Transient fluid flow through fractured porous media has been modeled by Huskey and Crawford (1967), Asfari and Witherspoon (1973) and others.

Discrete fracture flow models have been used by Gale (1975) and Noorishad et al. (1982) to investigate coupling between effective stress, fracture deformation, and fluid pressure. Initial efforts at modeling fluid flow through discontinuous networks of fractures have included the printed circuit boardwork of Hudson and LaPointe (1980) and the two-dimensional, finite

element, fracture network flow models of Long et al. (1982), Rouleau (1984), Samaniego and Priest (1984) and Andersson et al. (1984). Recent developments have included some preliminary attempts at three dimensional fracture network models (Dershowitz et al., 1985; Long et al. 1985, and Herbert et al., 1990).

The incorporation of statistical data is necessary in the generation of a discrete fracture network model and commonly a Monte Carlo method is used, although a few recent works have used a fractal geometry approach (Wang, 1991). Barton and Larsen (1985) and Turcotte (1986) described a fracture network using fractals and Chilès (1988) used fractal characterization to simulate a fracture network. The effectiveness of this approach in modeling fluid flow through a fractal fracture network has not been well established.

The Monte Carlo method has been well established and has been used by many workers for simulating fracture networks in two and three dimensions; a few notable works are by Long and Witherspoon (1985), LaPointe and Hudson (1985), Rouleau and Gale (1987), Long and Bilaux (1987), and Herbert et al. (1990). In this method, the number of fracture sets present within the generation region is specified and each set is independently generated. The fracture centers are generated according to the designated fracture density of each set. Fracture density is either the number of fractures per unit area or the sum of fracture lengths per unit area in 2D models or the sum of fracture area per unit volume in 3D models. A fixed number of points, governed by the fracture density and corresponding to the center of the fracture traces, are randomly generated inside the boundaries of the model. Orientations and trace lengths are randomly assigned to each center following the statistical distributions

stipulated for each set, and fractures crossing the boundaries of the generation region are truncated at the boundary.

All of these numerical models that analyze flow through networks of discontinuous fractures solve for Darcy type steady state flow. The boundary conditions for flow and the pressure gradient are designated for the exterior of the fracture system and a system of equations are solved to determine the fluid pressures or gradients throughout the fracture network. By summing the calculated flow rates in the individual fracture segments, the total flow rate across the system boundaries is estimated. The equivalent porous media bulk permeability can be calculated from the bulk fluid flow and the overall pressure gradient. To estimate the anisotropy in fracture permeability, the flow boundaries are rotated relative to the fracture network and the flow rate is evaluated as a function of azimuth. Parameter studies can be undertaken to determine the relative importance of fracture geometry, aperture distribution, and the role of large-scale fractures on the flux through, and the fluid pressure distribution in, the fracture system.

CHAPTER 2. GEOLOGIC SETTING

2.1 REGIONAL GEOLOGY

The discontinuity data analyzed in this thesis were obtained from outcrops of the Monterey Formation at five primary sites (see Figure 1.1) along the coast of south-central California between Government Point and Point Sal. The Monterey Formation is a sequence of siliceous sedimentary rocks originating from diatomaceous and calcareous material that was deposited in several deep marine basins approximately between 17 and 6 mya (Snyder, 1987, MacKinnon, 1989). Six rock types comprise the bulk of the formation, four (diatomaceous rock, siliceous shale(mudstone), porcelanite, and chert) are related to the diagenesis of biogenic silica, with the other two being phosphatic shale and dolostone. All occur as poorly to thinly laminated strata but locally beds can be massive and as much as a couple of meters thick, with dolostone usually forming the thickest beds. The diatomaceous rock is characteristically weathered brown, siliceous shale is dark brown to grayish-yellow, phosphatic shale is usually very dark in color, porcelanite and chert are highly variable from light to dark colors, and dolostone is commonly weathered to yellow or orangeish tan. Hardness of the rock types grade from the hardest being chert, followed by dolostone, porcelanite, the two shales, and the softest is the diatomaceous rock. Matrix porosity is also related to rock type: siliceous shales have the highest porosity, and chert and dolostone have the lowest (MacKinnon, 1989). Figure 2.1 shows a generalized stratigraphic section of the Monterey Formation and the position of the mapped locations within the section. The stratigraphy follows that of Isaacs(1981) and Pisciotto (1981).

Generalized Stratigraphic Column

Position of Mapped Areas

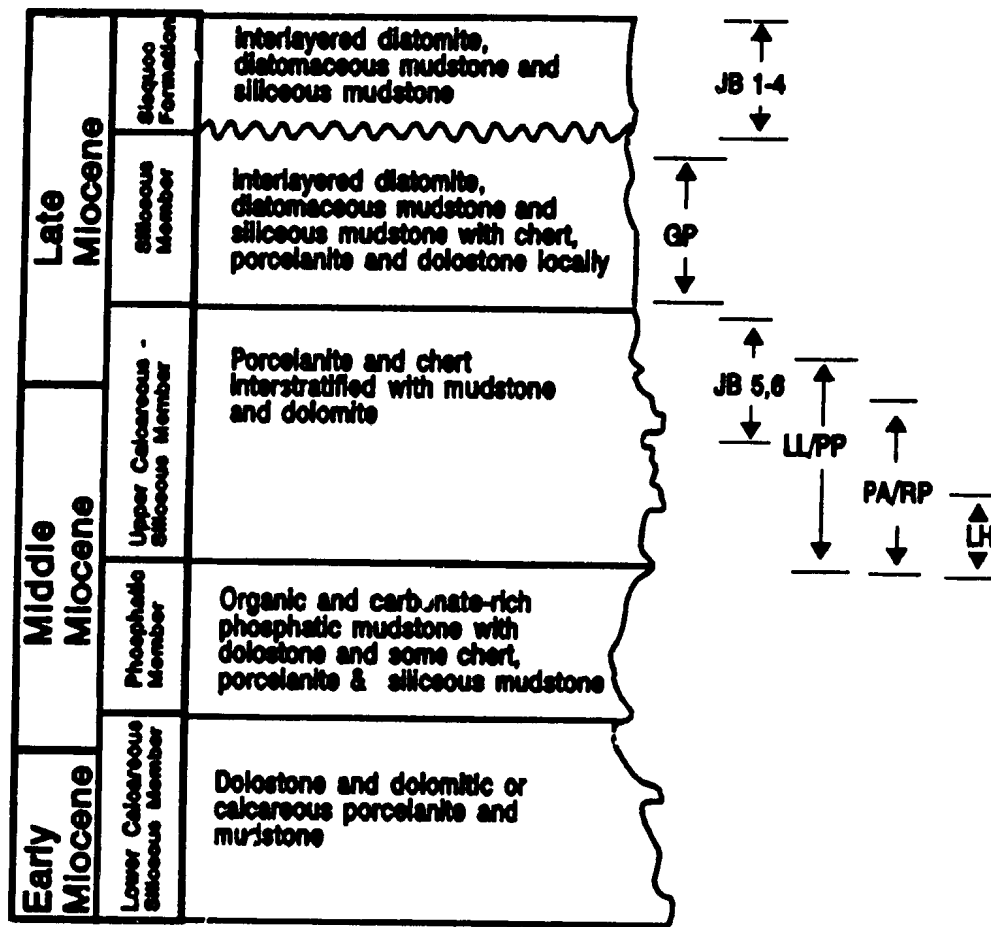


Figure 2.1. Generalized stratigraphic column showing position of study areas (after MacKinnon, 1989; Gale et al., 1991). GP - Government Point, JB - Jalama Beach, LH - Lions Head; PA/RP - Point Arguello/Rocky Point; PP/LL - Purisma Point/Lompoc Landing.

At the five sites the rock outcrops varied from sub-horizontal to near vertical cliff sections. Dimensions of the exposures also varied, from ten's of square meters to over a hundred, fairly continuous, meters in length with cliff heights of 5 to 10 meters. Structures shown in outcrop scale are not evenly distributed and are diverse in style. Fold geometries vary between rock types, and folding styles range from chevron to conjugate (box) folds. Small scale, low-angle, ramp faults associated with folding were observed in some locales and small normal faults are also present at most of the sites. A regional picture of the tectonic evolution that produced these complex structures in the Monterey Formation is still being developed for this area. Discussion of the development of the central coast tectonic basins can be found in articles by, Woodring and Bramlette (1950), Dibblee (1950), Blake et al. (1978), Hall (1981), Hornafuis et al. (1986), MacKinnon (1989), and Luyendyk (1991), but as noted by Snyder et al. (1983), no published studies provide a total structural composite of this area. It is beyond the scope of this thesis to try and detail the tectonic events that created the structures in the Miocene Monterey, but it is important to mention observations about the stratigraphy and structures with which the discontinuity data are associated. Much of the following discussion, on the structures in the Monterey Formation, relied heavily upon the work and observations of Viele (pers. comm., 1991).

Viele (1984) reported that fold hinges within the Monterey Formation, are generally nonparallel, but have an average wavelength of under one kilometer with a range from 0.5 to 1.5 kilometers, and amplitudes that are one-third to one-half the wavelength. Mapped trace length of folds showed that 78% of 162 folds shown, have a length of 5 km or less, and even though many of the folds are censored by alluvium, only 18 showed a length of more than 5

km. Fault trace lengths were reported as being generally(85%) less than 6 km, with the longest traces, over 12 km, being associated with the eastern portion of the Santa Ynez fault. Traces of faults in the subsurface of the Santa Maria Basin are at least as long as the fold hinges (Viele, 1984).

In an earlier report (Gale et al., 1991) on some of these fracture data it was mentioned that the study sites were probably in one of two structural domains: the Santa Barbara Channel domain or the Onshore Santa Maria basin domain (Figure 2.2). The most southerly field sites at Government Point and Jalama Beach and Point Arguello, are considered to be located in the Santa Barbara structural domain. Sites at Lompoc Landing/Purisima Point and Lions Head are in the Onshore Santa Maria domain.

The Santa Barbara structural domain located in the western portion of Transverse ranges is bounded by E-W-striking, left-lateral wrench faults, the Santa Ynez-Big Pine on the north and the Channel Island-Malibu on the south (Figure 2.2). This domain is inferred to extend westward to the Amberjack high, located offshore of Point Conception (Crain et al., 1985) and eastward to the San Andreas fault system. The stratigraphy of the Santa Barbara domain is a thick, up to 3000 m, sequence of marine and non-marine sandstones and shales ranging from Cretaceous to Oligocene in age, unconformably overlain by Miocene marine sediments (Vetter et al., 1969, USGS FES 74-20, 1974). The thickness of the Miocene Monterey Formation ranges from 700 to 1000 meters but is thinner where the formation onlaps the Amberjack high (Gale et al., 1991). On shore, this sequence is in the form of a homocline with the strata striking nearly parallel to the coastline with southerly dips of 25 to 70 degrees.

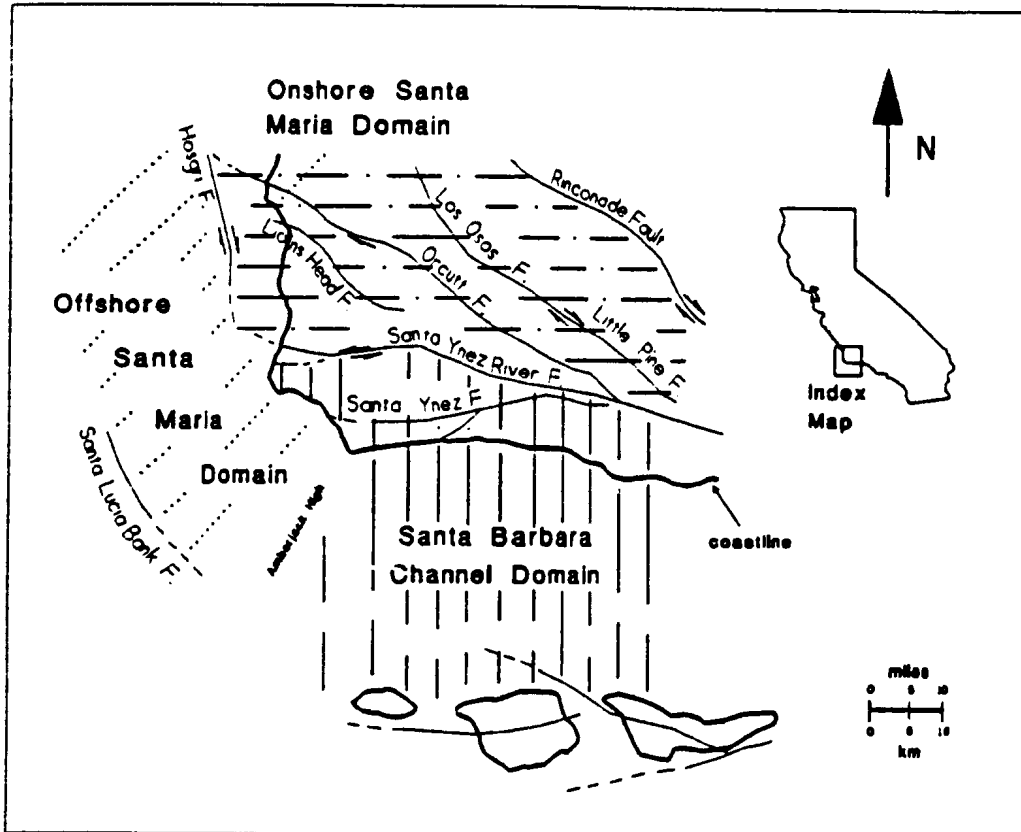


Figure 2.2. Location of structural domains. See text for discussion (after Gale et al, 1991; Snyder, 1987).

Near Point Conception the sediments curve with the coastline and northeasterly dips of 10-25° are observed in the coastal outcrops. Further up the coast toward Point Arguello, the strata are cut by the E-W left-lateral Jalama fault and then the E-W left-lateral Honda fault. The strata also show a series of anticlines and synclines whose fold axes are sub-perpendicular to the shoreline (Dibblee, 1950, Viele, 1984). From magnetic declination data it is interpreted that the Miocene rocks within the domain have experienced a clockwise rotation of 70-120° since the beginning of the Miocene, with about 30° rotation in the last 6 million years, due to the right lateral movement between the North American and the Pacific Plates (Hornafuis et al., 1986, Luyendyk, 1991). It is also interpreted that the major episode of folding, faulting, and associated fracturing, occurred in the Monterey Formation during Mid and Late Pleistocene (Snyder et al., 1983, MacKinnon, 1989).

The second structural domain of concern to this thesis is the Onshore Santa Maria structural domain just north of the Santa Barbara Channel domain. The triangular-shaped Onshore Santa Maria domain is bounded by three major strike-slip faults; the Santa Ynez-Big Pine on the south, the Rinconada on the east, and Hosgri fault on the west (Figure 2.2). The stratigraphy of this domain differs from the Santa Barbara Channel domain in that the thick succession of Cretaceous to Oligocene sediments is absent, so the Miocene Monterey or the immediately underlying units, the Miocene Rincon or Vaqueros Formations, rest on either the Jurassic Franciscan Formation, the Cretaceous Espada Formation, or the Miocene Tranquillon Volcanics (Dibblee, 1950; Hall, 1981). Along Honda Creek, the Monterey is in fault contact with the Honda Shale of Jurassic age. A complete stratigraphic section of the Monterey Formation is present in the western part of the domain and ranges in thickness from 600 m to

1500 m (1800 to 4500 ft). Hall (1981) believes the Santa Maria basin is a pull-apart structure that started to form approximately 14 mya along the "existing Santa Maria River - Foxen Canyon - Little Pine - Lompoc - Solvang fault system", and Hall offers this as the reason for the lack of early Tertiary sediments.

Broad conjugate folds are present throughout the structural domain, so the strata at many outcrops are nearly flat lying. Most of the fold axes shown on Dibblee's (1950) map in the western part of the domain lie in the Monterey Formation, with only the largest folds extending into the older formations (Gale et al., 1991). A probable explanation for this observation is that the Monterey deformed by folding above a decollement fault plane between the Monterey and the older formations, or that numerous detachment surfaces lie within the Monterey Formation (Viele, pers. comm. 1991). Based on a structure contour map of the top of the Monterey in the western Santa Maria structural domain, Viele (pers. comm. 1991) states that the overall geometry is that of conjugate folding possibly modified by recent faulting. The amplitude of the folds range from 1300 to 3000 meters (4000 to 10000 ft.) and the length of the fold hinges ranges from 11 to over 30 kilometers. Detailed measurements of fold geometry were not reported, but the report concluded that all evidence suggests the Monterey deformed as a relatively stiff unit through bulk rotations associated with shears without significant amounts of internal strain. Snyder et al. (1983) observed that the primary structures in the Monterey are: "large scale faults associated with the San Andreas, large scale folds with wavelengths up to 10 km and associated faults, small scale disharmonic kink, chevron and concentric folds with associated faults and decollements, and complexly fractured, faulted, and brecciated brittle layers. Penetrative thrusting and shearing are

conspicuously absent." Snyder et al. (1983) also state that the deformation observed in the Miocene formations show classic evidence for wrench fault tectonics and uplift that is related to the development of the San Andreas fault system. Fracture and fold data reported by Viele (1984) from Mussel Rock, Lions Head, Purisima Point, and Sweeny Road tend to mimic right-lateral wrench tectonics. The NW-striking faults in the Onshore Santa Maria domain are believed by most workers to possess varying amounts of late Tertiary dextral strike-slip displacement.

None of the mapped sites were located in the offshore Santa Maria structural domain, but it is briefly mentioned here for completeness and its' close association to the other two structural domains. The offshore Santa Maria structural domain is bounded by the Santa Lucia fault on the west, the Amberjack high on the south, the right-lateral oblique-slip Hosgri fault system on the east (Figure 2.2), and contains numerous folds that trend NNW-SSE (Viele, pers. comm. 1991). As in the case of the Onshore Santa Maria domain, the Cretaceous and Oligocene sands and shales are generally absent. The thickness of the Monterey Formation is variable, but at some locales it averages less than 650 meters(2000 feet) (Dibblee, 1950, p.37). According to Dunham and Blake (1987) the material characteristics of the Monterey rocks in this domain are similar to those in the Onshore Santa Maria basin, which in turn differ from the material characteristics of the Monterey in the Santa Barbara structural domain.

2.2 LOCAL GEOLOGY

The locations of the study sites relative to the regional structural domains are shown in Figure 2.2. The stratigraphy of the sites is shown in Figure 2.1. The areas are described in sequence starting at the south-eastern location and moving toward the northwest.

2.2.1 Government Point

At Government Point the Monterey Formation forms near vertical cliff faces varying in height from a few meters to over 10 meters. Quaternary alluvium overlays the outcrops. In this area, the Monterey also is exposed in wave-washed horizontal outcrops that cover between 50 m² to several hundred square meters. Mudstone and siliceous mudstone are the dominant rocks exposed between Government Point and Point Conception. Commonly they are black to oily brown, very thin bedded to finely laminated, and they weather out in platy to massive beds. The massive beds are mostly dolomitic and form ledges and dip slopes in many places. The underlying beds on the facing slopes tend to be more shaly, friable and rich in organic material. These beds contain many small flecks and nodules of phosphatic material; also present are disseminated dolomite and local lenses of dolomite as much as 1.20 m in length and 0.40 m in thickness; the lenses of dolomite weather to a light orange-tan color. X-ray diffraction analysis of samples from this location showed that the phase of biogenic silica in the samples is opal-CT (Carpenter, pers. comm. 1991). Dibblee's (1950) map shows that the rocks at Government Point are in the upper Monterey.

The rock outcrops at Government Point lie on the southern limb of a broad syncline recognized by Dibblee (1950) (Figure 2.2) which lies between Government Point and the south-facing dip slope of the Santa Ynez Range. Bedding strikes vary between 285° and 320° with dips of 9° to 20° toward the north-northeastward with the steeper dips in the northwest outcrops. The bedding strike variation seem to be related to poorly defined small synclines and anticlines that plunge toward the northeast. Toward Point Conception, the strike bends slightly toward the northwest and the dip of about 20° swings accordingly toward the northeast.

Fracturing of the Monterey at Government Point is dominated by fold-related extension type fractures, many tar filled, that are perpendicular to bedding and trend sub-parallel to bedding dip. Individual fractures generally have openings of less than 40 mm in width, but the openings pinch and swell along the fracture trace on the face of the cliff. Sub-perpendicular to the extension fractures are numerous cross joints, probably the result of unloading and weathering. Cross joints are generally tight but a small number were observed with some tar infillings. Average trace length of all discontinuities measured is approximately 1.75 meters and a little under 30% of all fractures have a trace greater than 2 meters. Zones of tar-filled breccias are also present that cut through the extent of the outcrop and range from 1 to 3 m in width. The tar-filled breccias have trends similar to the extension fractures but their boundaries are irregular across the face of the outcrop. Similar fracture types were observed by Belfield et al. (1983) in outcrops further east in the Santa Barbara basin. At South Elwood, transverse joints with or without tar-filled breccia are distributed normal to structural strike, dip steeply, and serve as important conduits for hydrocarbon transport (Belfield et al. ,

1983). Several zones of high angle faulting were also observed to the west of Government Point and to the west of Point Conception. The dips of the fault planes were variable, and zones of breccia fill some bends in the fault planes. The faults are extension faults parallel or sub parallel to the trend of the extension fractures.

The rocks at Government Point contain numerous bedding-plane shears as is typical of most Monterey outcrops. These shears tend to be the location of water seeps and a thin gouge zone containing ferric iron oxides and gypsum produced by the alteration of pyrite. The presence of seeps and mineral alteration indicates that the bedding-plane shears are zones of relatively high permeability at least near the surface. Tar-filled fractures associated with and parallel to the bedding-plane shears are present in some places.

2.2.2 Jalama Beach

Structural attitudes between Jalama Beach State Park and the southern boundary of Vandenberg AFB may be divided into three groups: a southern segment, a short middle segment, and a northern segment (Viele, pers. comm. 1991).

The southern segment extends from Jalama Creek northwesterly for about 350 m. Exposures are sub-vertical cliffs and steep dip slopes of mostly light gray, platy, opal-A diatomites and siliceous shales, locally interstratified with light yellowish-brown beds of dolomite as much as 1 m in thickness. These are probably outcrops of the Sisquoc Formation that have a gradational contact with the Upper Monterey exposed farther north up the beach. Toward the

northern end of this segment, beds of dolomite, seasonally covered by sand, contain numerous synsedimentary slump folds, defined by thinly laminated and "swirled" layers (Gale et al., 1991). The slump folds themselves are unrelated to the regional structure for they lie in beds bounded by bedding planes parallel to the regional dip. No beds of opal-CT or chert are present in this southern exposed segment.

Attitudes of bedding along this stretch of beach are consistent. Strikes range from 330° with dips around 30° SW in the southeast portion of this section to 05° with dips of 22° to 29° W in the northwest. The slight changes in strike from northwesterly to northerly define very broad, poorly defined anticlines and synclines plunging seaward at plunges of less than 5° . In general the region is part of the broad regional dip slope forming the southern flank of the Santa Ynez Mountains and the southern limb of the regional anticlinorium.

The discontinuities show considerable spread in trends but extensional fractures are well represented. In some beds that form the steep dip slopes, two closely spaced joint sets are present forming pencil thin slivers of rock. Of the measured discontinuities at this location, the average trace length is 1.35 meters, 30% have traces greater than 2 meters, with some iron staining. No tar and no breccias were observed in this southern segment. About 150 m from Jalama Creek a few small dip faults parallel the set of extension fractures and are themselves extension faults.

The middle segment of the outcrops at Jalama Beach is approximately 300 m in length of sub-vertical cliffs and contains the only zone of structural disruption. The rocks are thin beds of

grayish-tan siliceous shales and represent the top of the Monterey at this location (Viele, pers. comm. 1991). Beds dip between 5° and 15° SW and strikes vary between 295° and 335° . At the southern end of the middle segment, reversals of dip define a series of Chevron and conjugate folds of short wave length. A few small thrust faults break the forelimbs of the folds and translate the rocks short distances either northward or southward, with the northward translations being more common (Viele, pers. com. 1991). According to the maps and cross sections of Dibblee (1950) these folds are inclined toward the north and seem to be parasitic folds on the southern limb of the Santa Ynez Mountains anticlinorium (Viele, 1984). Locally, there are a few thrust faults of mostly east southeasterly strike and northerly dip cutting the rocks.

Since the cliffs show the dip face of the beds, very few longitudinal joints were observed. The extensional fractures are generally perpendicular to bedding but exhibit a large degree of scatter in strike direction. Most of the extensional fractures cut strongly across bedding planes but no tar and very little iron staining was observed.

The northernmost segment of the Jalama Beach traverse is separated from the other segments by several hundred meters of slumped Pleistocene terrace sediments and beach sand. Rocks at these outcrops are representative of the upper calcareous-siliceous member of the Monterey Formation (see Figure 2.1). Outcrops include thin beds of opal-CT chert, interstratified with opal-CT porcelanite, and scattered beds of dolomite. Bedding strikes are fairly well confined between 305° and 325° with dips between 30° and 36° to the southwest. Well defined conjugate folds buckle the chert beds, and extension fractures are numerous normal to the fold

hinges. Fractures filled with gypsum are more numerous than in the other two segments, and calcite filled veins are common here where as none were observed in the other areas.

Decollement surfaces floor the folded cherts, but the extension fractures extend vertically with a wider spacing across the decollements. Several of the conjugate folds lie in relatively steep dipping beds and were probably rotated to their present attitude from originally flat-lying beds (Viele, pers. comm. 1991).

2.2.3 Point Arguello

In this area the Monterey is exposed in two railroad cuts, each about 0.5 km in length, and in dramatic cliff sections that can be more than 40 meters high. Rock outcrops are almost continuous, but sometimes hazardous to access, for nearly 6 kilometers to the south and 3 kilometers to the north of Point Arguello. The exposed strata are representative of the upper calcareous-siliceous member (MacKinnon, 1989). Black chert is common in thin ribbon beds to thick massive beds, typically interbedded with porcelanite and siliceous shales, and as at other locations, dolomite forms thick beds locally. A few thin, black, phosphatic beds were observed at beach outcrops near Rocky Point. Generally bedding strikes northwest-southeast and dips to the southeast are mostly between 10° and 20° but locally can be as steep as 60°. Dibblee (1950) mapped two anticlines (or one with a E-W kink just north of Rocky Point) that trend NW-SE paralleling the coast line. Common in this area are thrust faults along bedding that eventual ramp through the bedding to an upper bedding plane following along the axial surfaces of kink folds (Viele, pers. comm. 1991). Viele (1984)

points out that this ramping and associated rotation of fold limbs form wedge-shaped dilation zones of potentially high permeability.

The dominant discontinuities are high angle extension fractures that strike toward the northeast, and locally are tar filled. Carbonate filled extension fractures, tar-filled breccia zones, and extensional faults with centimeter to meter displacements are also common through this section. An uncommon feature seen at a railroad cut near Point Arguello are two, 1 to 2 meter wide, sandstone dikes. The dikes cut the bedding at right angles and strike in the same general direction as the extension fractures. It is believed that the sand is derived from the Eocene-Oligocene formations which underlie the Monterey (Viele, pers. comm. 1991).

2.2.4 Lompoc Landing/Purisima Point

This specific area has also been discussed by Dunham and Blake (1987) in considerable detail and by MacKinnon (1989) in somewhat less detail. In the area of Lompoc Landing the Monterey Formation outcrops as nearly flat benches that extend several meters from short alluvial cliffs into the ocean. Moving north along the coast, approximately 5 km toward Purisima Point, the Monterey is covered by beach gravel, sand and water, and is only exposed in short cliff sections until within several hundred meters of Purisima Point when again the Monterey is exposed at beach level. Along this stretch of coast the strata exposed are from the upper calcareous-siliceous member of Isaac's classification. The dominant rocks are very thin-bedded cherts interstratified with siliceous shales and dolomite. The dolomitic

beds form resistant ledges as much as a meter thick. The biogenic silica phase is dominantly opal-CT with some silica altered to quartz near Purisima Point (Dunham and Blake, 1987).

Most of the bedding in this region dips less than 10° toward the north, except where locally disturbed by small faults and folds. In the thin-bedded cherts numerous conjugate fold hinges are present separating flat anticlinal crests from flat bottomed synclines. Gale et al.(1991) reported wavelengths ranging from 0.50 to 1.75 m, and amplitudes from less than 10 to 100 mm, on measurements of 17 folds. The sample was small but a reconnaissance of the area suggests it was representative. Plunges of the hinge lines were low, generally less than 8° , and clustered around two bearings, one at 095° and the other at 260° (Gale et al., 1991). Therefore, as seen in outcrop, anticlines pass directly into synclines as hinge lines cross one another. Most of the hinge areas are associated with small thrust faults that flatten downward into detachment surfaces at the base of the chert layers. The total amount of shortening in the folds is estimated to be less than 10% (Gale et al., 1991).

As pointed out by Dunham and Blake (1987), the chert beds are cut by numerous closely-spaced extension fractures that are perpendicular or nearly perpendicular to the fold hinges. Stronger extension fractures of similar orientation but at wider spacing cut the siliceous shales and dolomitic beds. The extension fractures are cut locally by larger shear zones many of which are filled by tar-cemented breccias. The shear zones postdate the extension fractures because the extension fractures are rotated with a right slip sense of movement by the shears (Viele, pers. comm., 1991). North of Lompoc Landing, along the southwesterly-facing shore of Purisima Point, thick, resistant ribs of breccia mark the location of shear zones which may

also be associated with the Hosgri fault. These breccia ridges, which are 1 to 2 meters wide, were at some time highly permeable zones but are now strongly cemented and resistant to the wave action. The system of conjugate folds and extension fractures seem to have undergone a later deformation associated with the right lateral faults of the California coast ranges (Gale et al., 1991).

2.2.5 Lions Head

The Lions Head area was covered extensively by Dunham and Blake (1987), including a measured, nearly complete, section of the "classic Western Santa Maria Basin Monterey" formation, and detailed discussions of the strata and structures at this location. In the area of Lions Head, portions of all lithologic members of the Monterey Formation are present (Dunham and Blake, 1987) in stratigraphic sections that average less than 650 meters (2000 ft) in thickness (Dibblee, 1950, p.37). At the coastal outcrops the Lions Head fault juxtaposes the Jurassic Point Sal Ophiolite against the basal phosphatic shale and dolomite. The stratigraphic sequence can be followed moving away from the fault south along the beach outcrops. First are the dark brown phosphatic shales interbedded with a few grayish-tan dolomites. The shales contain numerous nodules of dolomite and the interstratified beds of dolomite range in thickness from about 0.50 to 1.50 meters. The phosphatic shales are the dominant rock for a couple of hundred meters; then there are less than one hundred meters of interspersed dolostones, chert, porcelanite, and siliceous shale beds. The thin contorted cherty units and thin bedded siliceous shales dominate this section. The biogenic silica at Lions Head is all in the quartz phase indicating an advanced state of diagenesis.

There is some debate whether the Lions Head fault is a right-lateral or left-lateral strike slip fault (Viele, pers. comm. 1991; Sylvester and Darrow, 1979), but whatever the fault mechanism, north-south compressional stresses strongly folded the Monterey strata on the southern side of the fault in this area. Most of the beds at Lions Head strike approximately east-west and have dips greater than 60° either to the north or south. Numerous small conjugate folds, having hinge lines that plunge westward at 20° to 30° , occur in the steeply dipping limbs of the cherts. Numerous extension fractures, some filled with tar, transect the folds perpendicular to the hinge lines. The extension fractures and conjugate folds at Lions Head formed early in the deformation and were rotated to their present position on the steeply dipping limbs of larger folds by later deformation which may have been associated with movement along the Lions Head fault (Viele, 1984).

CHAPTER 3. FRACTURE DATA COLLECTION AND ANALYSIS

All of the fracture data referred to and analyzed for this thesis were collected for Chevron Oil Field Research Company and were included in unpublished internal company reports. One of these reports, Viele (1984), and other documents by Viele (pers. comm., 1989) are frequently referenced in this thesis.

3.1 DATA COLLECTION AND MAPPING PROCEDURES

Methods employed in collecting fracture data depend on rock exposure and the intended use of the data. There are two basic approaches to outcrop fracture mapping: subjectively selecting the discontinuities to measure, or systematically measuring all fractures, greater than a given size, that cross a traverse or scanline laid out on the outcrop or that occur within a given area (ISRM, 1978). With either approach it is important to conduct preliminary reconnaissance to evaluate the rock types, rock exposure and location of the outcrops within the local geologic structures (ISRM, 1978). Both methods, have been used effectively, and according to Reches (1976), at some locations result in similar conclusions on general fracture geometry. The approach in this study was based on scanline and areal mapping techniques similar to the procedure used by Gale and Strähle (1988) in mine drifts at Stripa, Sweden.

Two surveys, of outcrops along the coast of central California (see Figure 1.1), were conducted in order to measure the small and large-scale fractures in the Monterey Formation. The first, called the "small-scale" survey, sampled outcrops 25 to 100 m² in area and collected data on fractures with trace lengths of 0.25 meters or greater, using 2 to 30 meter

long scanlines. The second survey used 100 m to 1400 m long scanlines to collect data on "large-scale" breccia zones and faults that had trace lengths greater than 3 meters. Data on these large-scale fractures allow for a description of the fracture system in the Monterey Formation on a scale between the small-scale fractures and the regional scale fractures. Based on their appearance in outcrop, these large-scale fractures appear to be the main zones of permeability at the reservoir scale.

For the small-scale survey, photos were taken, as near as possible, perpendicular to the exposures. For the flat lying outcrops, photos were taken from a helicopter hovering approximately 30 meters above the outcrop. The photos were enlarged and, with mylar overlays, used as a mapping base to record the location of the scanline along with the trace and position for each fracture that crossed the scanline. The scanline consisted of a tape measure secured to the rock and stretch taut across the outcrop, and where possible several scanlines were used at oblique angles to each other. The rock type, bedding dip and dip direction were recorded for each scanline along with the direction and inclination of the scanline. Each fracture that crossed the scanline, was numbered sequentially, and the following characteristics were measured and recorded: distance where the fracture crosses the scanline, fracture type, dip, dip direction, trace length, censoring of fracture trace length due to natural cover, fracture infill mineralization, large scale roughness (shape), small scale (surface) roughness, and termination mode. To ensure accurate and consistent data, measurements were made by one member of the team while another recorded the data on systematic logging forms (Figure 3.1). Dip and dip direction of the fracture were taken with a strato-compass that has several levelling bubbles and a rigid plate that can be aligned with

LEFT SIDE OF FORM								
LOCATION:								
PHOTOS:								
FLAG	LOCATOR	SCAN #	SCAN TREND	SCAN PLUNGE	FRAC. #	SCAN DISTANCE	FRAC. TYPE	DIP
33	COMMENT LINE							
22		AB	115	+4				
11	PHOTO1				1	0.45	F	85
11					2	1.01	FZ	88
RIGHT SIDE OF FORM								
DATE:				WEATHER:				
WORKERS:								
DIP DIR.	TRACE LENGTH	CEN.	INFILL	ROUGH. LS, SS	ROCK TYPE	TERM.	COMMENTS	
053	1.28	0	T	P, S	SM	0		
260	3.40	1	T	P, R	SM	4		

Figure 3.1. Logging form used for fracture mapping surveys. Entries correspond to discontinuities in Figure 3.2, headings and abbreviations are explained in the text and in Figure 3.3.

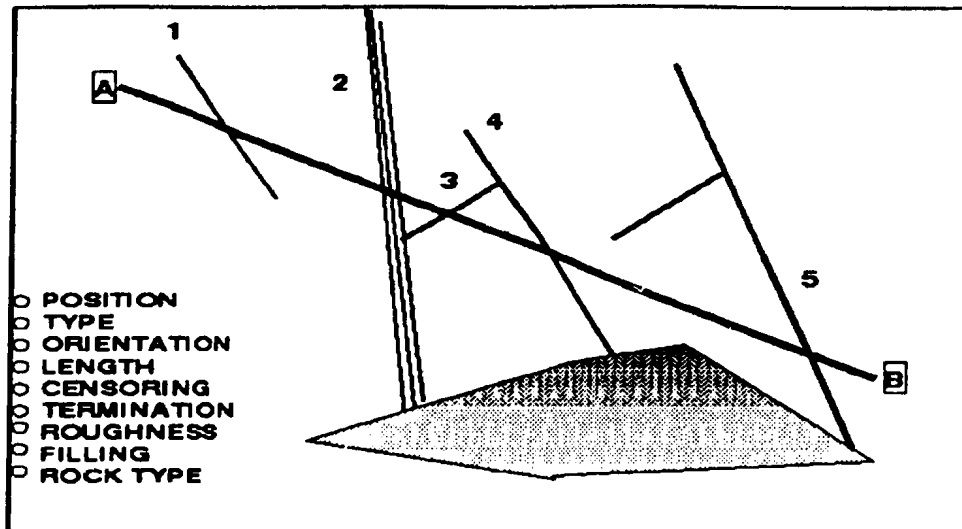


Figure 3.2. Schematic diagram illustrating some of the mapping conventions used in this study. Numbers correspond to fracture numbers on logging form; Figure 3.1.

the plane of the fracture, which allowed for fairly quick and consistent measurements. These fracture mapping conventions are illustrated schematically in Figure 3.2, with explanations for the terms in Figure 3.3.

Color air photos taken in 1988, for a coastal survey by the State of California, were enlarged and used as the photo base for the large-scale fracture survey. The scale on the photo mapping base was 25.4 mm equals 60 meters. The recorded characteristics for each major fracture included; spacing, dip azimuth, dip, horizontal and vertical trace length, censoring, and infill mineralization. For convenience, the large-scale data were organized according to the number of the air photo on which the feature was located.

Coding Conventions - Scanline Fracture Mapping	
Column 1	Flag; 11 = fracture data, 22 = scanline data, 33 = comment line
Column 2	Locator; photo or map number
When Flag = 11	
Column 6	Fracture number
Column 7	Distance on tape where fracture crosses scanline
Column 8	Fracture type; BD = bedding contact, BZ = breccia zone, FZ = fracture zone, JT = joint
Column 9	Dip direction (0-360°, azimuthal bearing)
Column 10	Dip Inclination (0-90°)
Column 11	Fracture trace length
Column 12	Censoring; 0 = both ends exposed, 1 = one end covered 2 = both ends covered
Column 13	Infilling material; Q = Quartz, CL = Clay, FE = Iron Oxide C = Carbonate, T = Tar, G = Gypsum
Column 14	Large scale roughness (trace shape); P = flat plane, C = curved plane, S = stepped, I = irregular, U = undulating
Column 14	Small scale roughness (surface roughness); S = smooth, R = rough
Column 15	Rock type; C = chert, D = dolostone, M = mudstone, P = porcelanite, prefix - A = argillaceous, D = dolomitic, S = siliceous
Column 16	Termination type; 0 = both ends free, 1 = one end terminates against another fracture 2 = both ends terminate against fractures 3 = end splays 4 = ends are censored
Column 17	Comments
When Flag = 22	
Column 3	Scanline number
Column 4	Scan trend (0-360°, azimuthal bearing)
Column 5	Scan inclination (+ is upward)

Figure 3.3. Explanation of coding conventions for scanline fracture mapping.

The main focus of a fracture survey is to determine the number of sets and their orientation and spacing, in order to draw conclusions on the structure and stress history of the area, or to determine the fracture permeability, or determine the effect of the fracture system on the mechanical properties of the rock mass. An assumption common to all fracture studies is that the areas sampled are representative of the total area that is being assessed. As pointed out by Terzaghi (1965), no survey will give complete information about the fracture system but a well conducted survey will furnish data that have a high probability of providing a representative sample of the actual fracture system in the rock mass. In order to achieve a good approximation of the actual distributions, of fracture orientation, trace length, and spacing, it is important to recognize the assumptions, biases, and errors that underlie the sampling process.

Errors occur when determining the orientation of a fracture due to the shape of the fracture trace or when the fracture is too "tight" to obtain a good dip reading. Usually the rock surface and the fracture trace are weathered so there is some separation of the fracture walls, so several measurements of dip and dip direction can be made along the trace and the measurements averaged. The parameters of fracture type, and large and small scale roughness are qualitative and subjective. This subjectivity can be minimized if all data are collected by one worker or if a definitive, systematic field technique is used, followed by a rigorous statistical analysis.

In any statistical analysis of fracture data, except for a geostatistical approach, it is assumed that the data are from a homogeneous fracture system. No rock fracture system is truly

homogeneous but for statistical analysis homogeneity may be assumed when sampling in large areas and the scanline is a number of times longer than the largest block size, as defined by the fracture system (LaPointe and Hudson, 1985).

LaPointe and Hudson (1985) also point out that there is a bias towards sampling longer trace lengths, since the longer the trace the higher the

probability of crossing the sampling line. There is also a bias toward sampling fractures that are at a high angle to the scanline, and a bias associated with the orientation of the outcrop, the "cut effect" (Figure 3.4), discussed by Ramsay and Huber (1987). To compensate for these biases, three mutually orthogonal scanlines should be used (if possible) when sampling, and/or statistical methods such as those presented by Terzaghi (1965) or Priest (1985) should be applied when analyzing the fracture orientation data. When it is too time consuming to sample every fracture that crosses a sampling line, a lower limit of fracture trace length may be stipulated. It should be noted that this truncation of trace length data adds a bias against shorter lengths. Usually the effect of truncation on the central tendency is small, unless truncation is greater than ten percent of the mean length (LaPointe and Hudson, 1985). The truncation bias and the bias created by censoring, are usually compensated for by using a statistical estimator such as the maximum likelihood method and assuming a known distribution for the data.

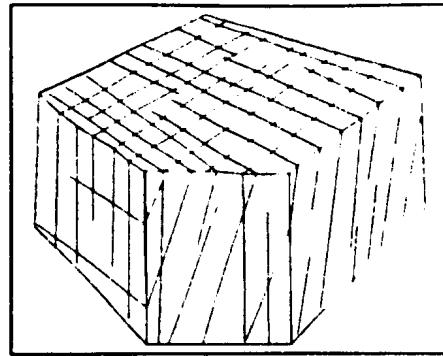


Figure 3.4. Cut effect, (after Ramsay and Huber, 1987). Fracture pattern seen depends on orientation of exposure.

3.2 GENERAL FRACTURE CHARACTERISTICS

3.2.1 Small-scale fracture system

Sites at four areas, Government Point (GP), Jalama Beach (JB), Lompoc Landing (LL), and Lions Head (LH) (Figure 1.1), were mapped for the small-scale fracture survey. The number of sites, stations at each site, total scanline length covered at each station and total number of fractures that were measured at each station, for the four different areas, are shown in Table 3.1. Examples of the detailed outcrop maps are given in Appendix B.

Table 3.1. Scanline summary for each site in the small-scale survey.

AREA	SITE	STATION	NUMBER OF LINES	TOTAL SCAN LENGTH(m)	TOTAL # OF FRACTURES	
GP	1	C1	12	71.8	180	
		P1	5	44.1	226	
		P2	3	36.8	204	
	2	C2	5	31.7	136	
		3	P4	1	24.5	43
			P5	3	46.2	74
JB	1	1	3	21.4	51	
	2	1	2	6.0	20	
	3	1	3	10.3	41	
	4	1	7	37.6	104	
	5	1	9	57.9	180	
	6	1	2	33.9	92	
LL	1	1	4	71.8	80	
LH	1	1	1	21.4	65	

At Government Point, 863 fractures were measured at six stations that extended over approximately 600 meters of coastline. Site 1 at Government Point, included two sub-horizontal outcrops (stations P1 and P2) and a long sub-vertical cliff section (station C1). Site 2 consisted of several vertical cliff sections and the two stations at site 3 were nearly flat-lying outcrops (stations P4,P5). Six sites spread over 1.5 km were used to measure 533 fractures at the Jalama Beach area. All sites at Jalama Beach were sub-vertical cliffs except for site 6 which was a sub-horizontal outcrop. Only one station was mapped in detail at Lions Head and one at Lompoc Landing.

As listed earlier there were several parameters collected for each observed discontinuity. These data were plotted in bar charts, box-plots, rose diagrams and lower hemisphere diagrams to determine if any general patterns exist between trace length, orientation, mineral infill, and large and small scale roughness. The areas and most sites were plotted separately so data from different structural positions would not obscure or create relationships.

Poles to fracture planes were plotted on lower hemisphere equal area plots for the four areas (shown in Figure 3.5). For Government Point and Jalama Beach, the fractures typically have steep dips, and even though there is a wide variability in the strike direction, the majority strike NE-SW. For the Lompoc Landing (LL) and Lions Head (LH) plots, the poles tend to cluster near the East-West line and indicate steep dips. A more detailed discussion of orientation is presented in section 3.3.1 and in Appendix C.

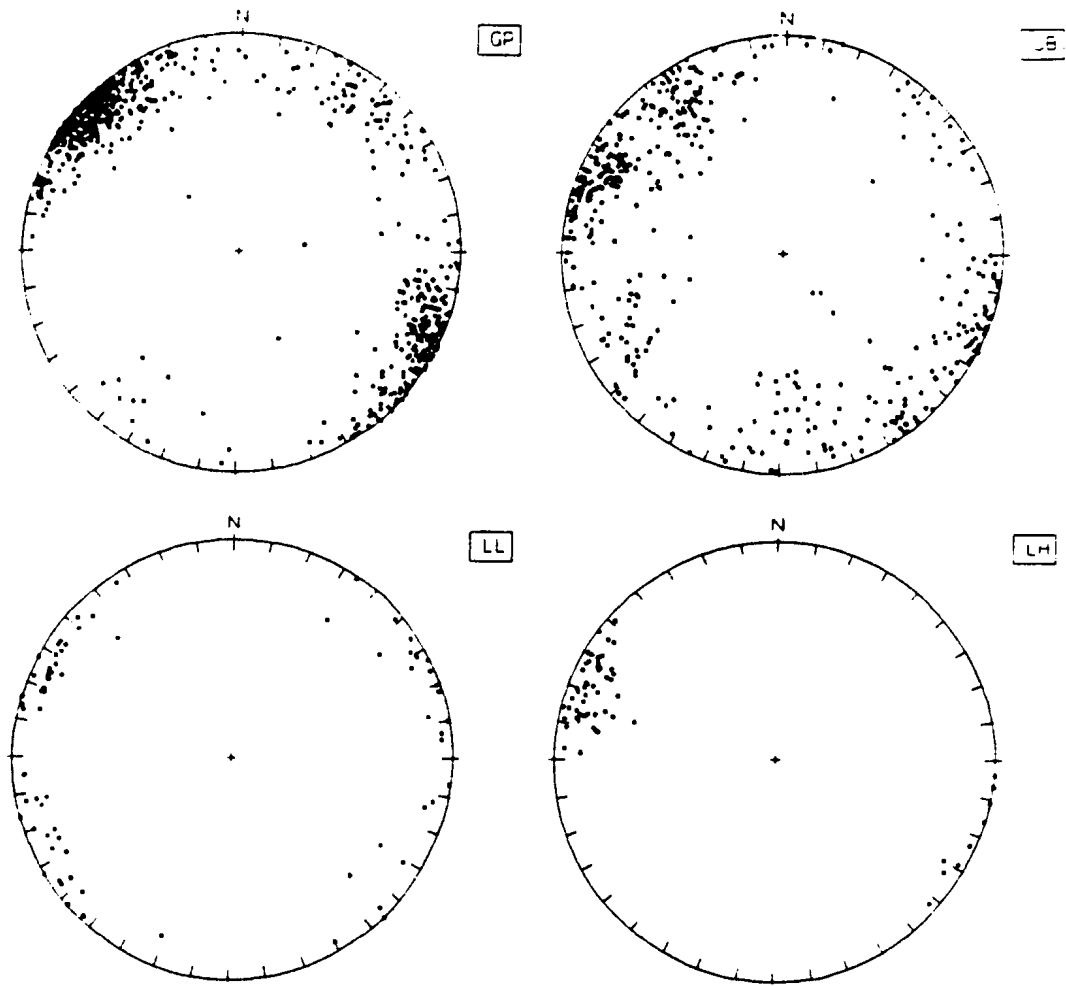


Figure 3.5. Lower hemisphere equal area plots of poles to fracture planes for GP - Government Point, JB - Jalama Beach, LL - Lompoc Landing, LH - Lions Head. Sample size for each area: GP(n=789), JB(n=445), LL(n=80), LH(n=65).

Table 3.2. Summary of fracture types and types of mineral infill for each site in the small-scale survey. N = total number of fractures measured, JT = joint, FZ = fracture zone, BZ = breccia zone, VN = vein; INFILL = predominate filling material.

SITE, STATION	N	TYPE				INFILL				
		JT	FZ	BZ	VN	TAR	FE	CAL	CLAY	GYP
GP,C1	181	176	5	0	0	50	0	0	1	21
GP,P1	226	215	11	0	0	52	0	0	0	0
GP,P2	203	201	2	0	0	54	29	0	14	0
GP2	136	95	41	0	0	97	0	0	1	1
GP,P4	43	33	9	1	0	35	0	0	0	0
GP,P5	74	58	15	1	0	60	7	0	0	0
JB1	49	35	14	0	0	0	49	0	0	0
JB2	31	31	0	0	0	0	26	1	3	0
JB3	41	40	1	0	0	0	0	0	0	0
JB4	104	83	21	0	0	0	60	0	0	0
JB5	180	167	13	0	0	0	0	0	13	0
JB6	92	84	0	0	8	0	0	32	0	30
LL	80	58	7	15	0	80	0	0	0	0
LH	65	65	0	0	0	0	0	0	0	0

Table 3.2 shows, by site and individual station, the break down of the observed fracture types, and the number of fractures per infill mineralization. Over 50% of all the measured fractures have some type of mineral infill, indicating that at some time the fracture was open as a pathway for fluid movement and, at the Government Point area, tar is infilling nearly 40% of the fractures. Fracture zones (FZ) (closely spaced and anastomosing joints) and breccia zones (BZ), at all sites, generally have longer trace lengths than the other fracture types, are tar-filled or iron-stained, and preferentially strike to the northeast.

Differences in mineralization in the fractures may be indicative of different stress regimes and/or distinct times of formation. It can be seen (Table 3.2) that at Government Point and

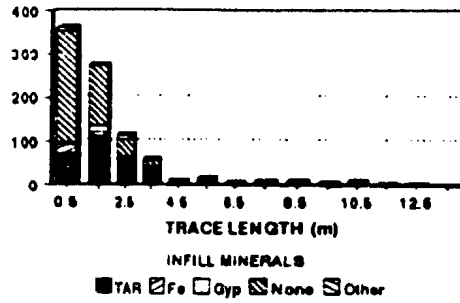
Lompoc Landing, of the fractures with mineralization, tar is the dominant infill. At Jalama Beach, mineralization is more variable from site to site, with Fe-staining dominant at sites 1, 2, 3, and 4, and there are equal amounts of carbonate and gypsum at site 6. The majority of observed fractures at Jalama Beach site 5, and the one mapped site at Lions Head have no visible mineralization. Table 3.3 summarizes the trace length statistics (based on a normal distribution) by mineralization for each site. Figure 3.6 shows the bar charts of trace length distribution and the associated mineralization for each of the four main areas. There is no definitive relationship, all types of mineralization seem to be ubiquitous to all trace lengths. Although, at Government Point, tar is present in a higher percentage of the longer fractures than the shorter length fractures. The differences in mineralization between the areas, are probably, in part, due to the differences in stratigraphic location (Figure 2.1). Especially, the presence of tar could be associated with the proximity to the phosphatic member, which has the highest organic content of the stratigraphic members in the Monterey Formation (MacKinnon, 1989). Box-plot diagrams in Figure 3.7 have been used to summarize and compare the distribution of trace length for each mineral infill. The box in this diagram represents the spread of the middle 50% of the data and the line inside the box is the median (central location) point of the trace lengths. The diagrams in Figure 3.7 represent the raw trace lengths of fractures and, although there may be censoring effects, the box-plots do show that for most sites the fractures with the relatively longer trace lengths are infilled with minerals.

Table 3.3. Raw trace length statistics by mineralization for small-scale survey sites. GP - Government Point, JB - Jalama Beach, LL - Lompoc Landing, LH - Lions Head. Mineral Infill is the dominant mineral in the fracture.

Location	Mineral	N	Raw Trace Length (m)				
	Infill		Mean	Std.	Min	Max	Median
GP Site 1	None	383	1.06	1.14	0.25	14.12	0.79
	Tar	156	1.93	1.79	0.25	12.80	1.44
	Fe	29	0.98	1.06	0.25	6.50	0.81
	Clay	15	1.64	2.11	0.35	8.00	0.73
	Gypsum	21	1.27	0.43	0.25	2.00	1.30
GP Site 2	None	37	1.41	0.60	0.67	3.00	1.40
	Tar	97	2.14	0.67	0.29	3.34	2.00
GP Site 3	None	15	1.48	1.44	0.25	6.20	0.95
	Tar	95	4.10	4.05	0.40	20.00	2.50
JB Site 1-4	None	87	1.89	1.48	0.25	5.00	1.43
	Fe	132	1.60	1.49	0.25	13.00	1.14
JB Site 5	None	165	1.94	1.00	0.32	4.87	1.70
	Clay	13	2.80	0.90	0.30	3.90	2.87
JB Site 6	None	30	2.52	2.23	0.61	8.22	1.43
	Calcite	32	2.94	1.77	0.69	8.00	2.47
	Gypsum	30	2.18	1.20	0.44	6.72	2.00
LL	Tar	80	5.43	9.05	0.25	48.50	2.23
LH	None	65	1.46	0.71	0.50	4.00	1.30

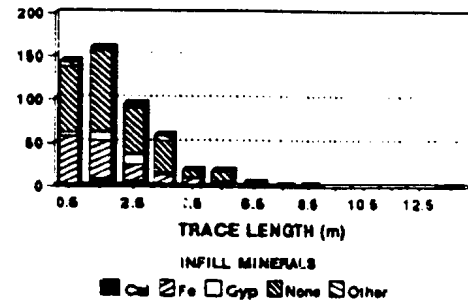
GOVERNMENT POINT

Raw Trace Lengths
by Infill Minerals



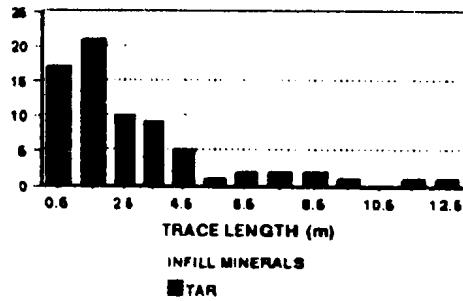
JALAMA BEACH

Raw Trace Lengths
by Infill Minerals



LOMPOC LANDING

Raw Trace Lengths
by Infill Minerals



LION'S HEAD

Raw Trace Lengths
by Infill Minerals

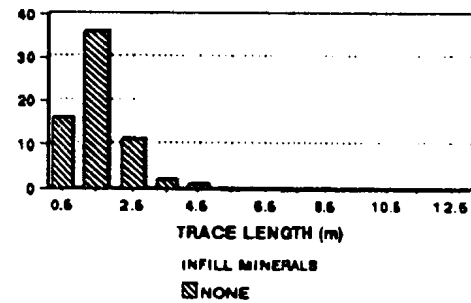


Figure 3.6. Bar charts of raw trace length by infill mineralization for each area in the small scale survey.

Lower hemisphere equal-area stereoplots were used to determine if there were any general grouping of poles to indicate a preferred orientation of fractures with the same mineral infilling. The stereoplots for Government Point and Jalama Beach are in Figure 3.8 and show that fractures with all types of infill material follow the general proportioning between groups and clustering seen in the stereoplots for all the fractures (in Figure 3.5).

Association of large scale roughness (trace shape) and small scale surface roughness with trace length may provide some indication of the timing and type of fracturing (shear, Type II or extensional, Type I; Paterson, 1978; Atkinson, 1987). Figure 3.9 presents box plots of the raw trace length distributions for each of the trace shapes recognized in this study. All of the fracture trace shapes have similar median trace lengths, except for fractures with the undulate shape (number 5 in the figure) at Jalama Beach and fractures with the planar trace shape (number 3 in the figure) at Lompoc Landing. To determine if the fractures with similar trace shapes have similar orientations, lower hemisphere equal area stereoplots of the poles to fracture planes were produced (Figure 3.10). No distinct groupings clearly show in the plots, but the planar shape is dominant. For the small scale roughness, box plots (Figure 3.11) and stereoplots (Figure 3.12) were also produced. The Government Point and Jalama Beach data have similar raw trace length distributions for each recognized surface roughness with no distinct grouping of poles to fracture planes. The Lompoc Landing data do show a difference, between fractures with smooth fracture surfaces and those with rough fracture surfaces, in raw trace length distributions and orientations. The fractures with rough surfaces have a slightly longer raw trace length and predominantly strike toward the northeast.

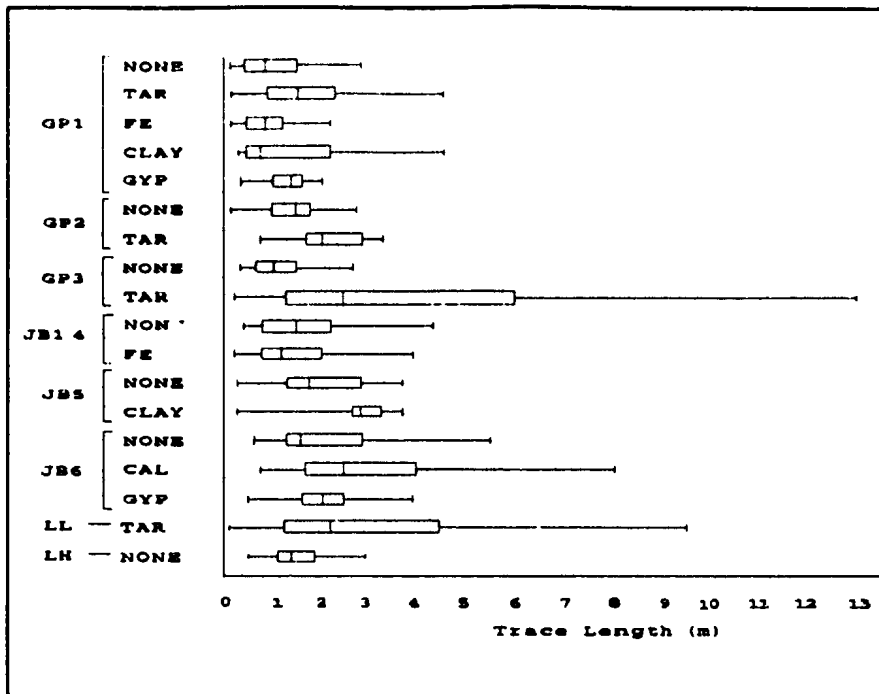


Figure 3.7. Box plot summary display of raw trace length distributions per mineral infill, for GP - Government Point sites 1, 2, & 3; JB - Jalama Beach sites 1-4, 5, & 6; LL - Lompoc Landing; and LH - Lions Head.

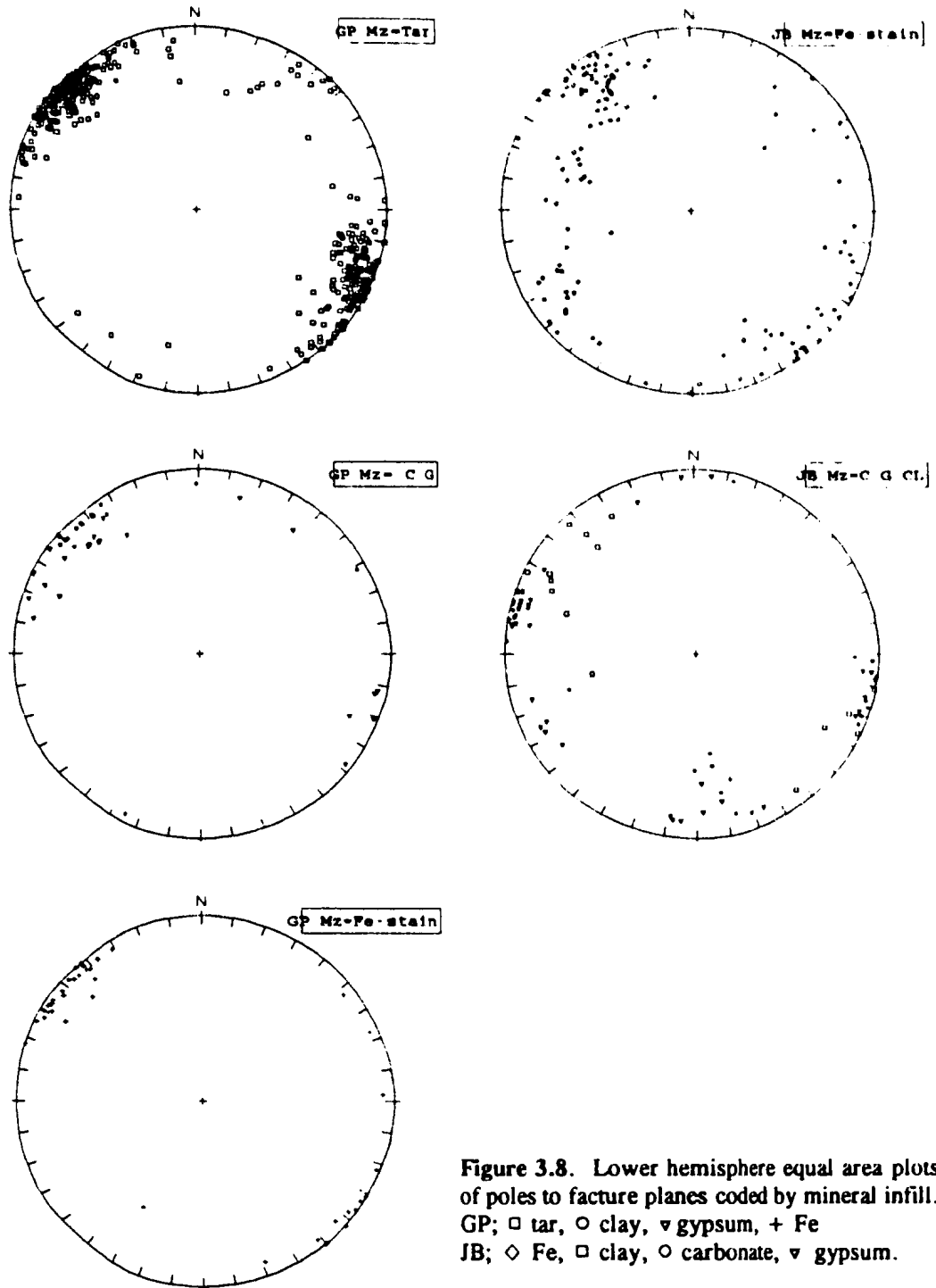


Figure 3.8. Lower hemisphere equal area plots of poles to fracture planes coded by mineral infill.
 GP; □ tar, ○ clay, ▽ gypsum, + Fe
 JB; ◇ Fe, □ clay, ○ carbonate, ▽ gypsum.

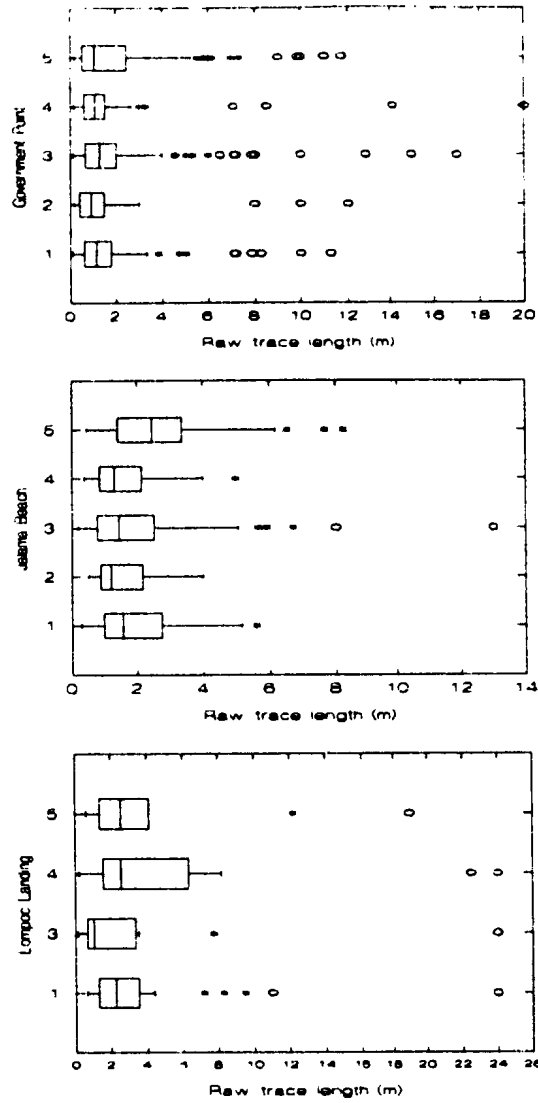


Figure 3.9. Box plots of raw trace length distributions for different trace shapes (large scale roughness) for the small-scale survey sites. Key to shapes (y-axis): 1 = curved, 2 = irregular, 3 = planar, 4 = stepped, 5 = undulate. Asterisks and ovals indicate outliers; data values larger (or smaller) than the value defined by, $1.5 \times$ the range of the values defining the box in the plot.

Government Point

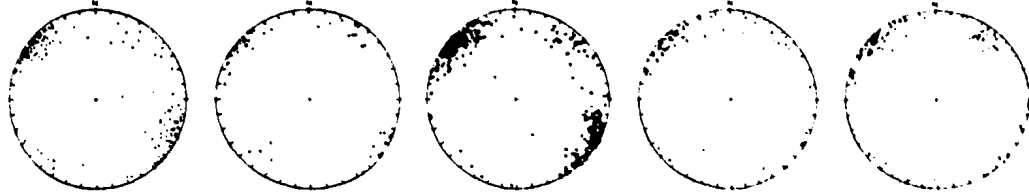
[C]
N=178

[I]
N=55

[P]
N=411

[S]
N=76

[U]
N=140



Jalama Beach

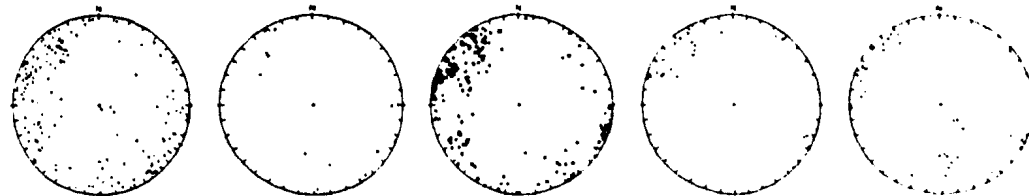
[C]
N=169

[I]
N=13

[P]
N=218

[S]
N=27

[U]
N=57



Lompoc Landing

[C]
N=27

[I]
N=0

[P]
N=21

[S]
N=22

[U]
N=10

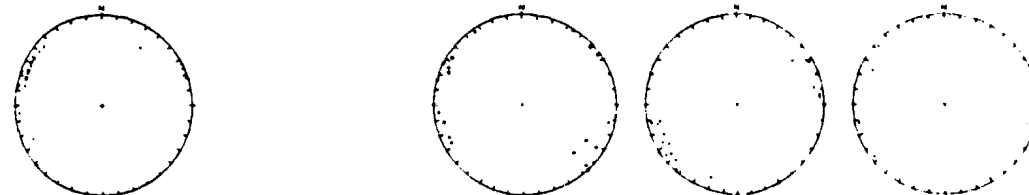


Figure 3.10. Lower hemisphere equal area plots of poles to fracture planes for different trace shapes (large scale roughness). [C] - curved, [I] - irregular, [P] - planar, [S] - stepped, [U] - undulate.

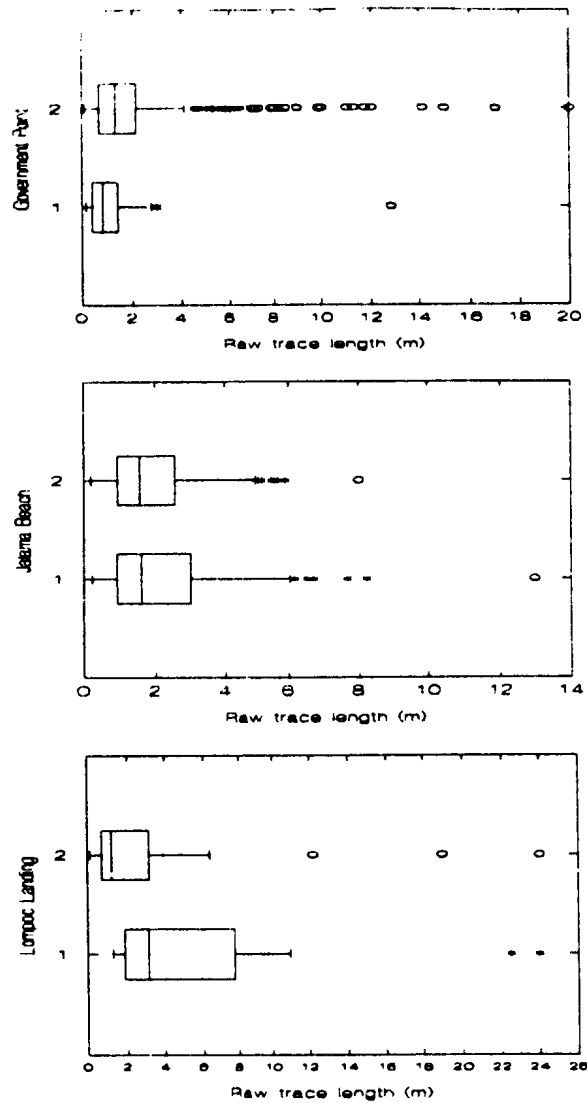
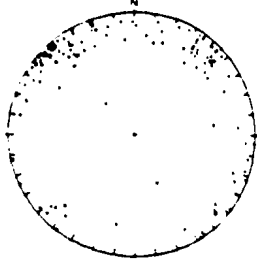
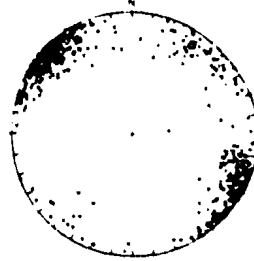


Figure 3.11. Box plots of raw trace length distributions for different fracture surface roughnesses, for the small-scale survey sites. Key: 1 = rough, 2 = smooth.

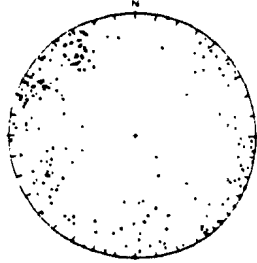
Government Point
[R]
N=143



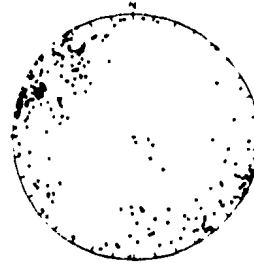
[S]
N=717



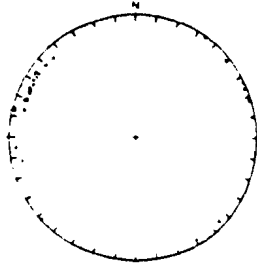
Jalama Beach
[R]
N=218



[S]
N=268



Lompoc Landing
[R]
N=38



[S]
N=42

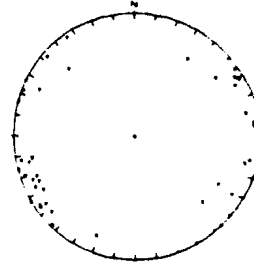


Figure 3.12. Lower hemisphere equal area plots to fracture planes for different fracture surface roughnesses. [R] - rough, [S] - smooth.

3.2.2 Large-scale fracture system

The large-scale survey measured fractures at two areas along the coast, one area with 4 mapped sites near Point Arguello (PA), and the other with two mapped sites near Purisma Point/Lompoc Landing (PP/LL)(Figure 1.1). For convenience, the mapped sites for the large-scale survey were named for the number of the air photo the site was located on, along with the initials NV or SV to designate if the site was located on the north (N) or south (S) part of Vandenberg (V) Air Force Base. NV and SV also correspond with sites that are located in two different structural domains (Figure 2.2). NV sites are in the Onshore Santa Maria domain and SV sites are in the Santa Barbara Channel domain. Table 3.4 summarizes the scanline data, and Table 3.5 shows the number of each fracture type, and types of mineralization, for each site. Examples of the large-scale fracture survey scanline maps are in Appendix B. Although mapped during the small-scale survey, data collected on 18 large-scale breccia zones along five scanlines between sites 2 and 3 at Government Point (GPBR) have been grouped with the other SV sites.

The 224 fractures measured are approximately equally divided between breccia zones (47%) and faults (53%). The breccia zones that were encountered typically cut through the bedding at high angles, had strikes sub-parallel to the general bedding dip direction, and are commonly extensional features. Geometrically the overall traces of the breccia zones are generally straight but composed of many anastomosing fractures so locally the boundary walls

Table 3.4. Scanline summary for each site in the large-scale fracture survey.

SITE	NUMBER OF LINES	TOTAL SCAN LENGTH(m)	TOTAL # OF FRACTURES
NV497	6	160.0	18
NV501	8	839.0	29
SV474	18	568.0	31
SV475	11	883.0	50
SV477	7	640.0	43
SV478	1	600.0	35
GPBR	5	410.5	18

Table 3.5. Summary of fracture types and infill for sites in the large-scale fracture survey. F - fault; BZ - breccia zone; Dom. Mnz. - dominant mineralization; Crb - carbonate; Cly - clay; Snd - Sand.

Location	Type		Dom.	Mnz.		
	F	BZ	Tar	Crb	Cly	Snd
NV497-8	18	0	6	0	0	0
NV501	8	21	12	3	5	0
SV474-5	55	26	26	13	10	0
SV477	20	23	15	0	11	0
SV478	17	18	12	0	4	2
GPBR	0	18	18	0	0	0

Table 3.6. Basic statistics of trace lengths for breccia zones and faults measured in the two mapped "large-scale" areas. Data in meters. BZ - Breccia zones, F - Faults, SKEW - skewness, KURT - kurtosis.

TYPE	N	MIN	MAX	MEAN	STD	MED	SKEW	KURT
NV BZ	21	5.0	100.0	56.4	38.6	70.0	-0.13	-1.65
NV F	26	3.0	34.0	11.1	8.4	8.0	1.78	2.33
SV BZ	82	3.0	90.0	17.9	17.1	10.0	1.96	4.13
SV F	93	3.0	90.0	18.3	18.3	12.0	2.59	7.16

are irregular. Clasts in the breccias, are usually large, of similar rock type as the local beds, are angular and show no indication of being crushed (Snyder, 1987; Viele, pers. comm. 1989). The primary cementing material in most breccias is tar, with minor amounts of carbonate, silica and clay. In a few locations, such as Purisma Point, vuggy carbonate and silica form the primary cement, and if tar was present, it has been removed. A few of the breccias were similar to the breccias described by Belfield et al. (1983) which they termed "stratigraphic breccias" in that they parallel bedding.

The other major fracture group mapped were termed faults, and showed horizontal and vertical separations that vary from a few centimeters to almost two meters. Characteristically the faults were planar in shape with steep dips except for the faults that parallel, then ramp through the bedding, changing from steep dips to shallower dips. Viele (pers. comm., 1989) notes that the planar shape is usually characteristic of rock failure at low temperature and pressure.

Comparison of the basic statistics for the measured trace lengths listed in Table 3.6 shows a wide distribution in trace lengths for the faults and the breccia zones in these two mapped areas. The maximum trace length measured was approximately 100 meters for both types and since the ends of most features were covered by alluvium the maximum trace length is unknown. Figure 3.13 shows four diagrams that are 3-dimensional scatter plots with the dip direction on the x-scale, dip in the y-direction, and trace length of the feature in the z-direction. The diagrams show that the observed faults and breccia zones, have the same

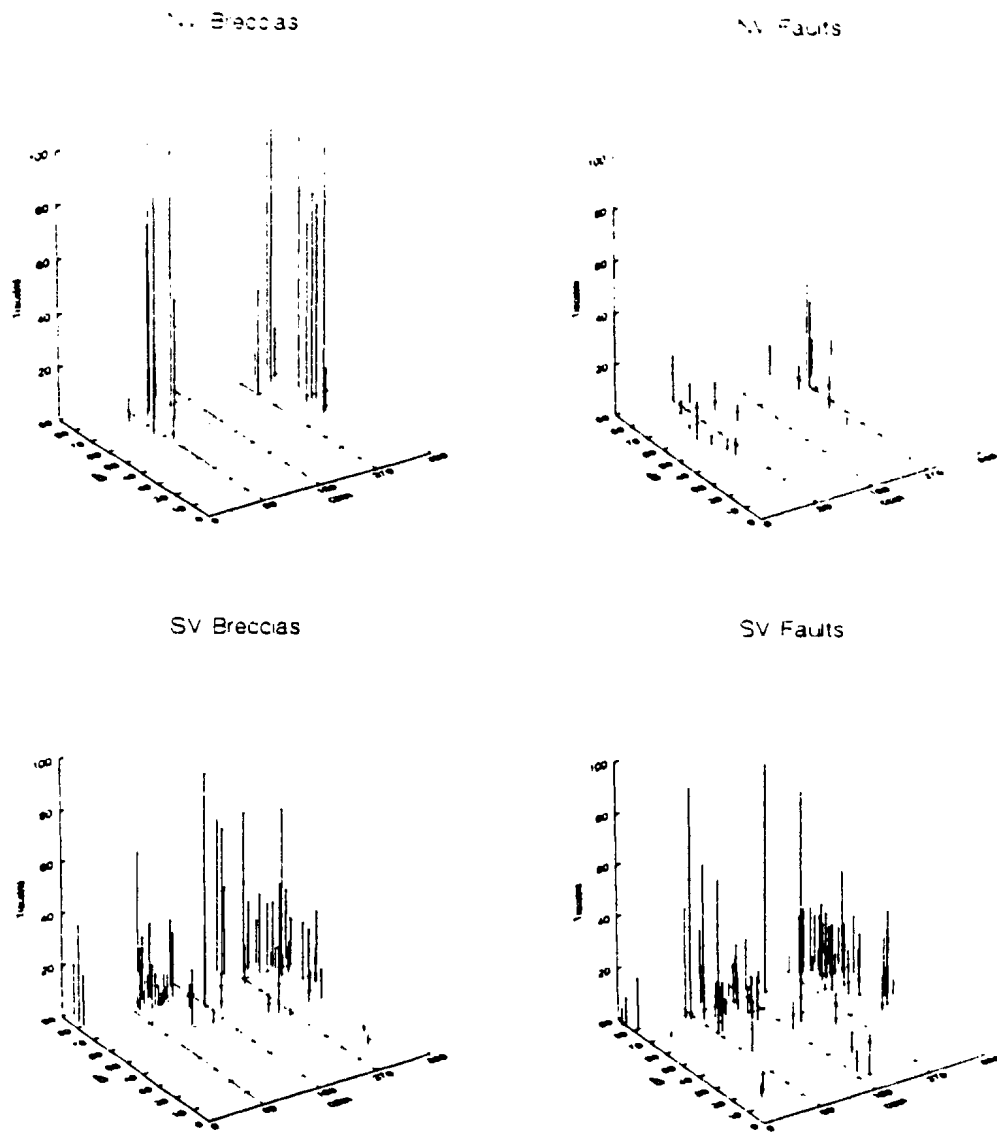


Figure 3.13. Three dimensional distribution of faults and breccia zones measured during the large-scale survey. NV - North Vandenberg, SV - South Vandenberg. z-axis = trace length (m), y-axis = dip, x-axis (DDR) = dip azimuth.

general grouping both within each structural domain and between the two structural domains. The majority of these features have steep dips oriented in a northwesterly or southeasterly direction. In the Onshore Santa Maria structural domain (NV), all but a few of the observed breccia zones had longer trace lengths than the faults but in the Santa Barbara Channel domain, breccia zones and faults had similar trace length statistics (Table 3.6).

3.2.3 Relationship to Structure

The discontinuities at the sites in the small-scale fracture survey are assumed to be related to the tectonic folding of the Monterey formation (Belfield et al., 1983), with some of the fractures being extended or enhanced by weathering. All of the large-scale features measured also appear to be related to the tectonic folding. Figure 3.14 shows strike rose diagrams for the fractures measured at each of the sites in both surveys and the major folds and faults mapped by Dibblee(1950) and other workers (Hall, 1981; Jennings, 1975). The arrows point to the sites the rose diagrams represent. The strikes are plotted in 10° intervals and are in percentage of total fractures for that site. Recall that the boundary between the two recognized structural domains is just north of Point Arguello at the Santa Ynez River fault. The data for the Santa Barbara Channel domain are presented in Figure 3.14a, and data for the Onshore Santa Maria domain are in Figure 3.14b.

Strikes oriented toward the northeast are very prevalent in all but two (SV-477C, NV-497) of the rose diagrams. The dominant direction ranges from an azimuth of 10° to 50°, and seems remarkably consistent regardless of position on the local structures. The variability in strike

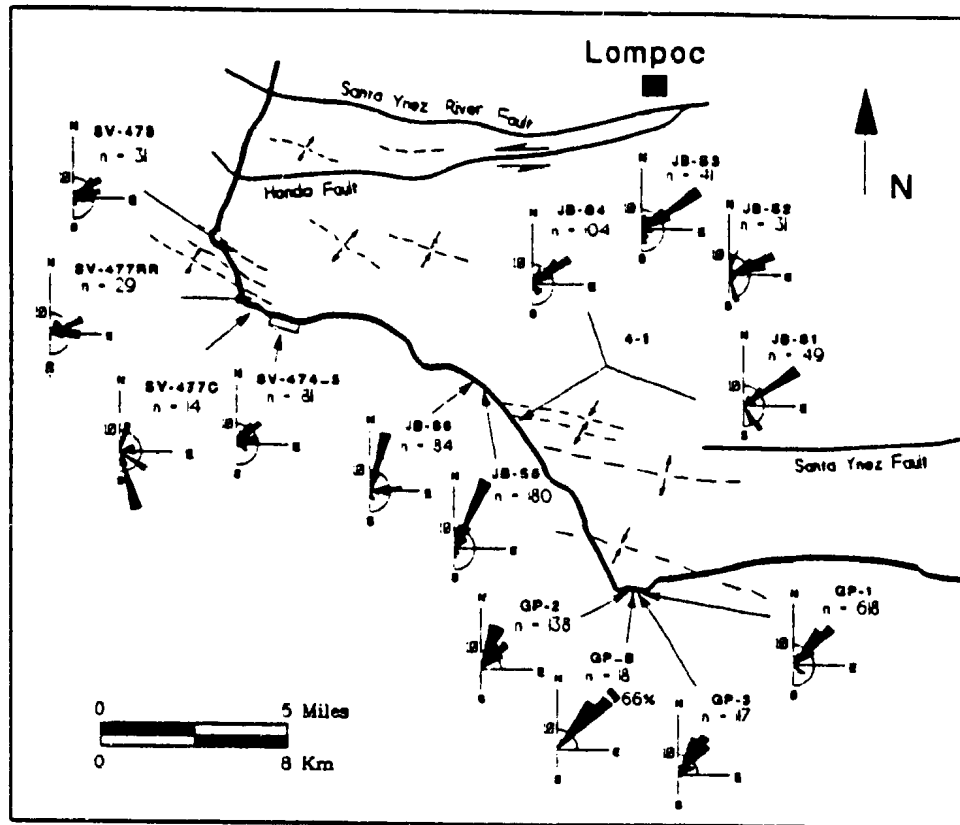


Figure 3.14a. Strike rose diagrams for features at each area from both surveys, relevant folds and faults are shown. Rose diagrams are shown as percent of total fractures measured at each site in 10° increments, the number to left of the diagrams indicates the number of features measured. Sites in the Santa Barbara Channel structural domain.

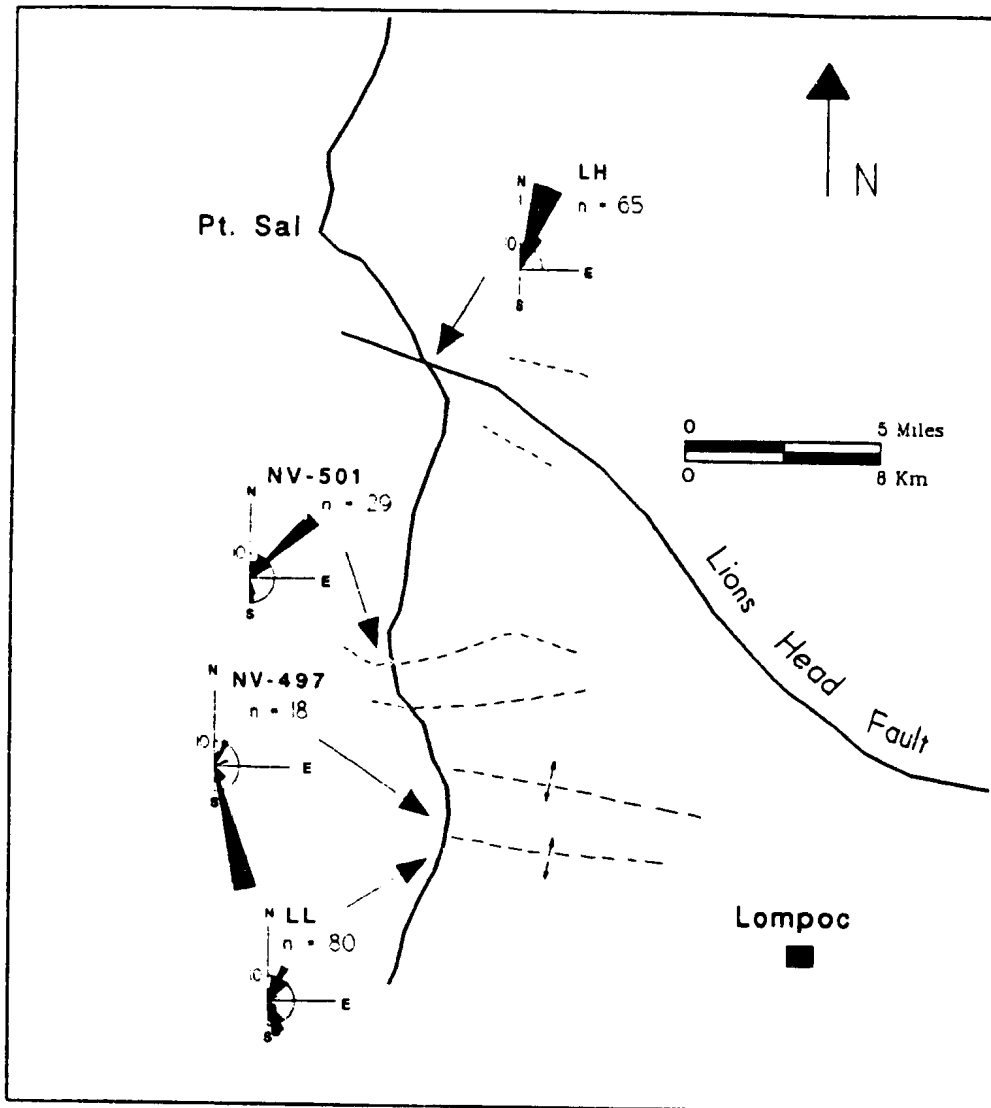
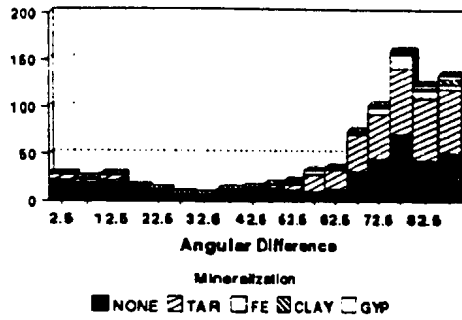
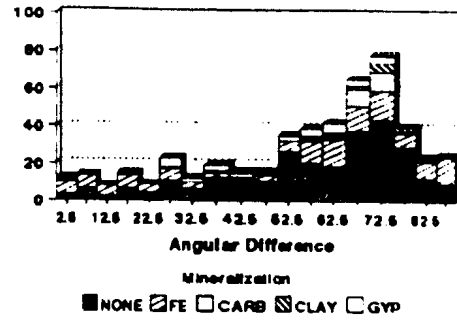


Figure 3.14b. Strike rose diagrams for features at each area from both surveys, relevant folds and faults are shown. Rose diagrams are shown as percent of total fractures measured at each site in 10° increments, the number to left of the diagrams indicates the number of features measured. Sites in the Onshore Santa Maria structural domain.

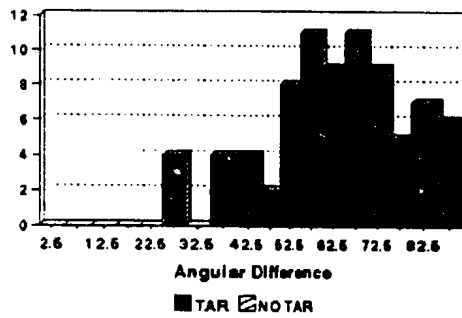
**Government Point
All Sites**



**Jalama Beach
All Sites**



**Lompoc Landing
Site 1**



**Lion's Head
Site 1**

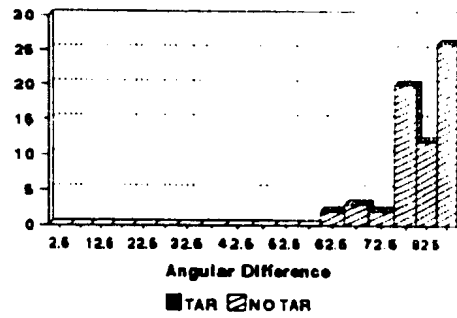


Figure 3.15. Histograms of angular difference between bedding strike and strike of discontinuities, for each area in the small-scale survey.

directions represented in the rose diagram for the SV477C site is due to the relatively small sample size but also to the fact that the scanline crossed the axis of a large anticline with steep, variable bedding.

Figure 3.15 shows the angular difference between bedding strike and the strike of the fracture for the small-scale survey sites. Fracture mineralization is also included in the histograms to determine any preference to fluid movement. The histograms show that the majority of fractures trend sub-perpendicular to bedding strike, as also shown by Belfield et al. (1983) for sites farther east in the Santa Barbara Channel structural domain. This sub-perpendicular trend is about 25° from what is expected for extensional fractures in pattern 1 of Stearns and Friedman (1972) (see Figure 1.6), and in some areas the differences in strikes are grouped closer to 60° than 90° . Those fractures could be interpreted as shear fractures of pattern 1, but there was no other clear evidence for shearing. A probable explanation for the discrepancy is that the bedding was rotated after the formation of the extensional fractures. This has also been noted by others (Dunham and Blake, 1987; Snyder, 1987), but it could be that only one of the conjugate shears developed at these sites (Snyder, 1987). Belfield et al. (1983) noted that if tar was present it is preferentially associated with the extension fractures. A similar but weaker association is also seen in this data set (Figure 3.15). Tar is present in all intervals of the histograms, but in a higher percentage in the sub-perpendicular (higher angular difference) fractures for the majority of sites where tar is present. At the Jalama Beach sites, tar is not present but the other infill minerals show a slightly stronger affinity for the extensional fractures.

3.3 FRACTURE ORIENTATION

Fracture orientation data were analyzed to determine the number of fracture sets at each site. Fracture orientations were plotted as lower hemisphere equal area projections of poles to fracture planes. Fracture sets were identified from clusters of pole points on the equal area projections using a computer program called CLUSTRAN (Gillett, 1987). Some adjustments were made to the selection of poles grouped into a cluster by CLUSTRAN, based on cross cutting relationships of fractures and other field observations. The procedure for determining the number of fracture sets is discussed in Appendix C, along with a discussion of the procedure used in correcting for orientation bias.

3.3.1 Small-scale Data

Two sets were found at each of the Government Point sites and at sites 1 through 4 at Jalama Beach, with 3 sets at Jalama Beach sites 5 and 6. Table 3.7 lists the mean orientation for each set, with the spherical variance presented in Appendix C (Table C.1). The pole of the mean orientation for each fracture set and the great circle for the bedding plane, at each site, are presented in Figures 3.16 to 3.18. These plots show a similar relationship, between bedding and the mean orientation of each fracture set, to that shown in the plots presented by Snyder (1987) for an area in the same structural domain but about 30km north-east of Government Point. The plots confirm the field observations, that there is a dominant fracture set that strikes roughly (within 30°) parallel to the bedding dip direction and a second set that is oriented 70° - 90° to the first set. There is a third set at Jalama Beach sites 5 and 6 that

Table 3.7. Mean fracture orientation and bedding orientation per site/station in the small-scale survey.

Site	Station	Set	N	Mean Orient.		Avg. Bedding	
				Dip Az.	Dip	Dip Az.	Dip
GP1	C1	1	20	220	72	15	15
		2	161	129	83		
GP1	P1	1	31	215	82	23	24
		2	154	128	82		
GP1	P2	1	23	223	83	35	20
		2	83	133	87		
GP2	C2	1	5	211	70	40	20
		2	131	301	83		
GP3	P4,P5	1	2	206	69	40	19
		2	113	129	89		
JB1	1	1	14	55	72	240	30
		2	33	141	90		
JB2	1	1	10	87	75	258	27
		2	9	155	81		
JB3	1	1	9	74	68	265	22
		2	29	146	73		
JB4	1	1	21	76	76	270	28
		2	57	152	82		
JB5	1	1	12	219	83	225	6
		2	134	112	83		
		3	24	329	87		
JB6	1	1	6	63	76	218	34
		2	47	105	89		
		3	39	356	68		
LL	1	1	38	120	86	353	5
		2	42	64	87		
LH	1	1	65	111	81	195	80

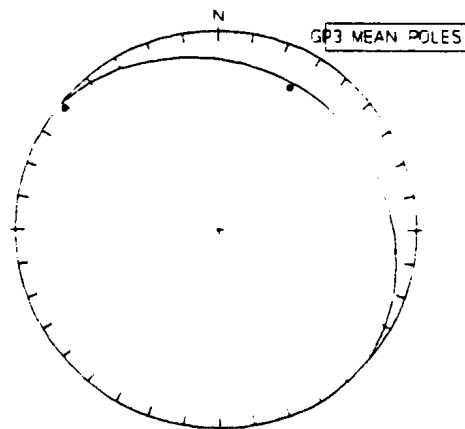
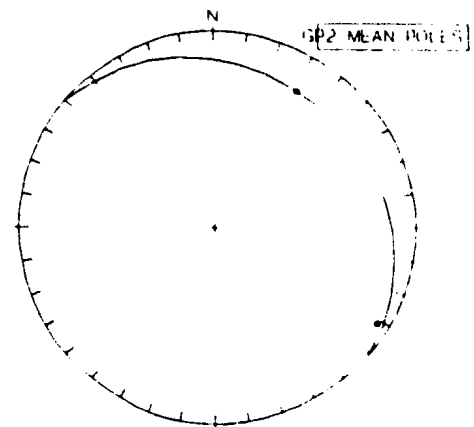
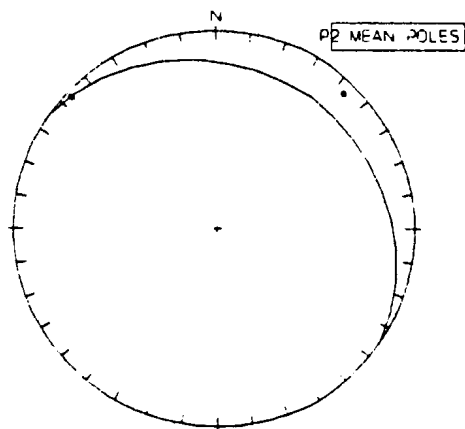
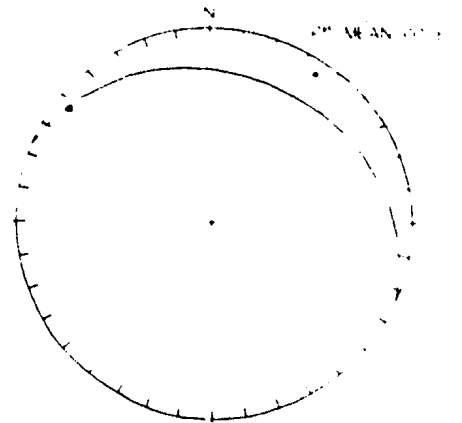
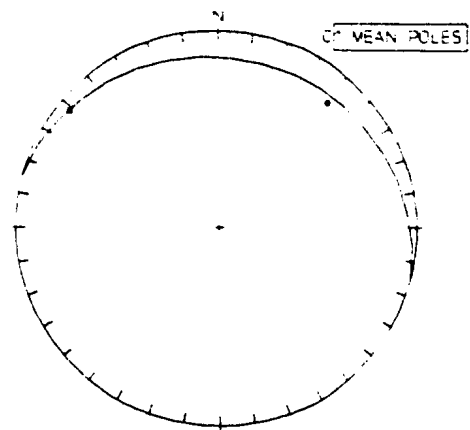


Figure 3.16. Lower hemisphere equal-area plots of poles to mean fracture planes with bedding plane as great circle for each Government Point station. Stations P4 and P5 are combined as GP3.

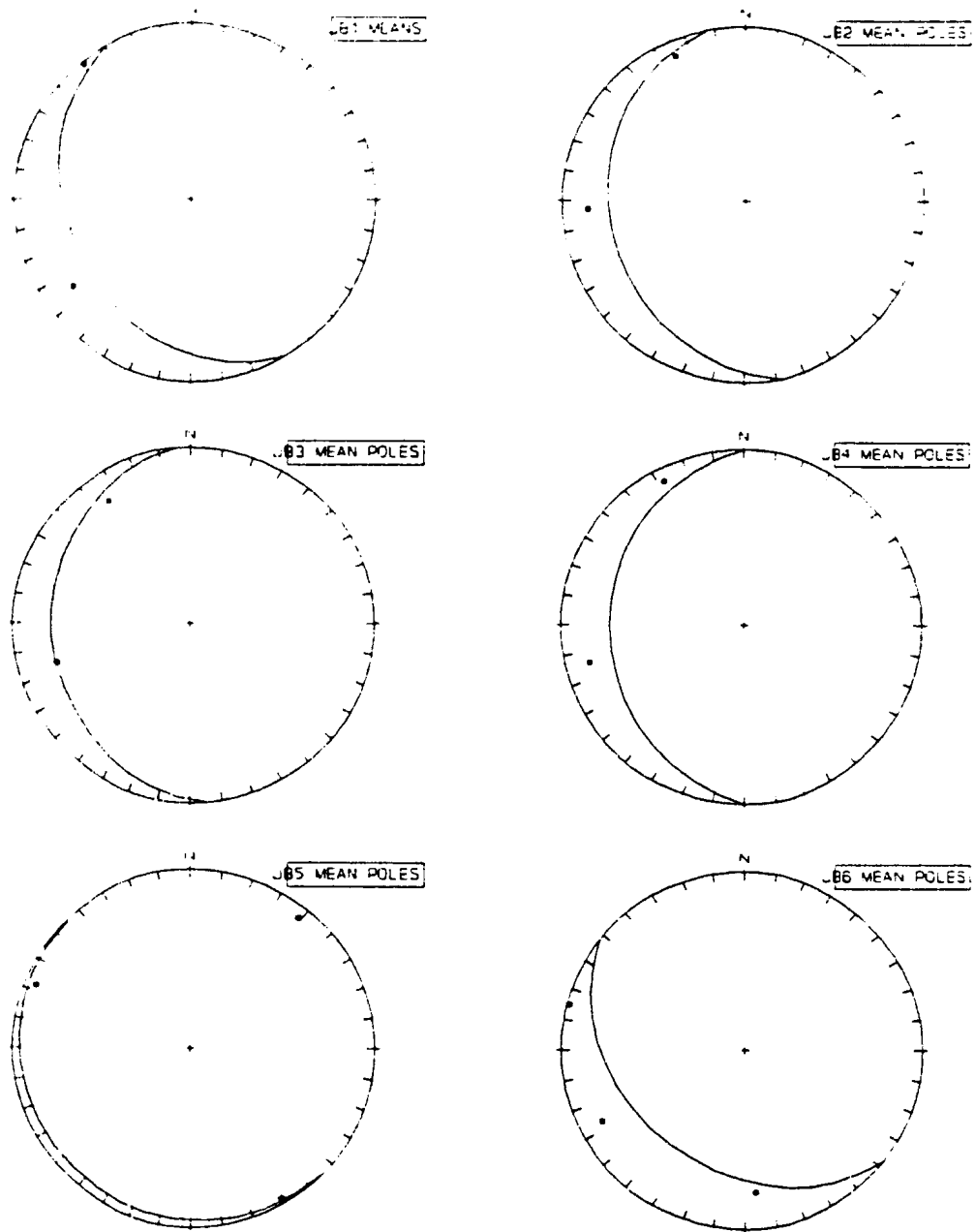


Figure 3.17. Lower hemisphere equal area plots of poles to mean fracture planes with bedding plane as great circle for each site at Jalama Beach.

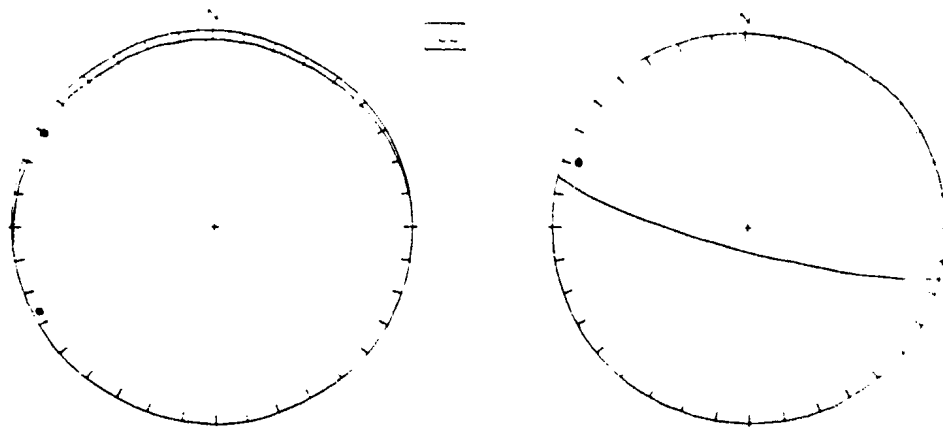


Figure 3.18. Lower hemisphere equal area plots of poles to mean fracture planes with bedding plane as great circle for the Lompoc Landing (LL) and Lions Head (LH) sites.

bisects the acute angle created by set 2 and set 1. The three sets and their cross-cutting relationships are quite evident in the flat-lying outcrops at site 6, but are not as evident at site 5 due to the near vertical cliff exposure.

In order to compare the mean orientation of the fracture sets between sites one should demonstrate that the data from different sites were sampled from populations with similar distributions. In addition from a geological perspective, one should compare sites of similar structural position and rock types. The orientation statistics are compared and discussed in Appendix C.

To correct for structural position, the fracture orientations are normalized by rotating the poles to the fracture planes along with the host bed about a vertical axis, until bedding has a north-south strike, then rotated to a horizontal (zero) dip. The average bedding attitude for each site/station is shown in Table 3.7. All of the original orientation data were rotated for each set and not just the mean orientations of the sets shown in Figures 3.16 to 3.18. The stereoplots of the rotated data are presented for each area in Figure 3.19, and the poles to the mean orientations for each set are plotted on stereonet in Figure 3.20. In the stereonet at the top of Figure 3.20, for each Government Point (GP) set, two mean poles are shown, in order to compare the two approaches used in rotating the data. The first approach, consisted of rotating the fracture orientation data using the average bed attitudes measured at each station then the data were combined and plotted (data shown in Figure 3.19a). In the second approach, orientation data from each station were combined then rotated using an average bed attitude of $40^{\circ}/20^{\circ}$ (dip direction/dip amount) for the area. This second approach was

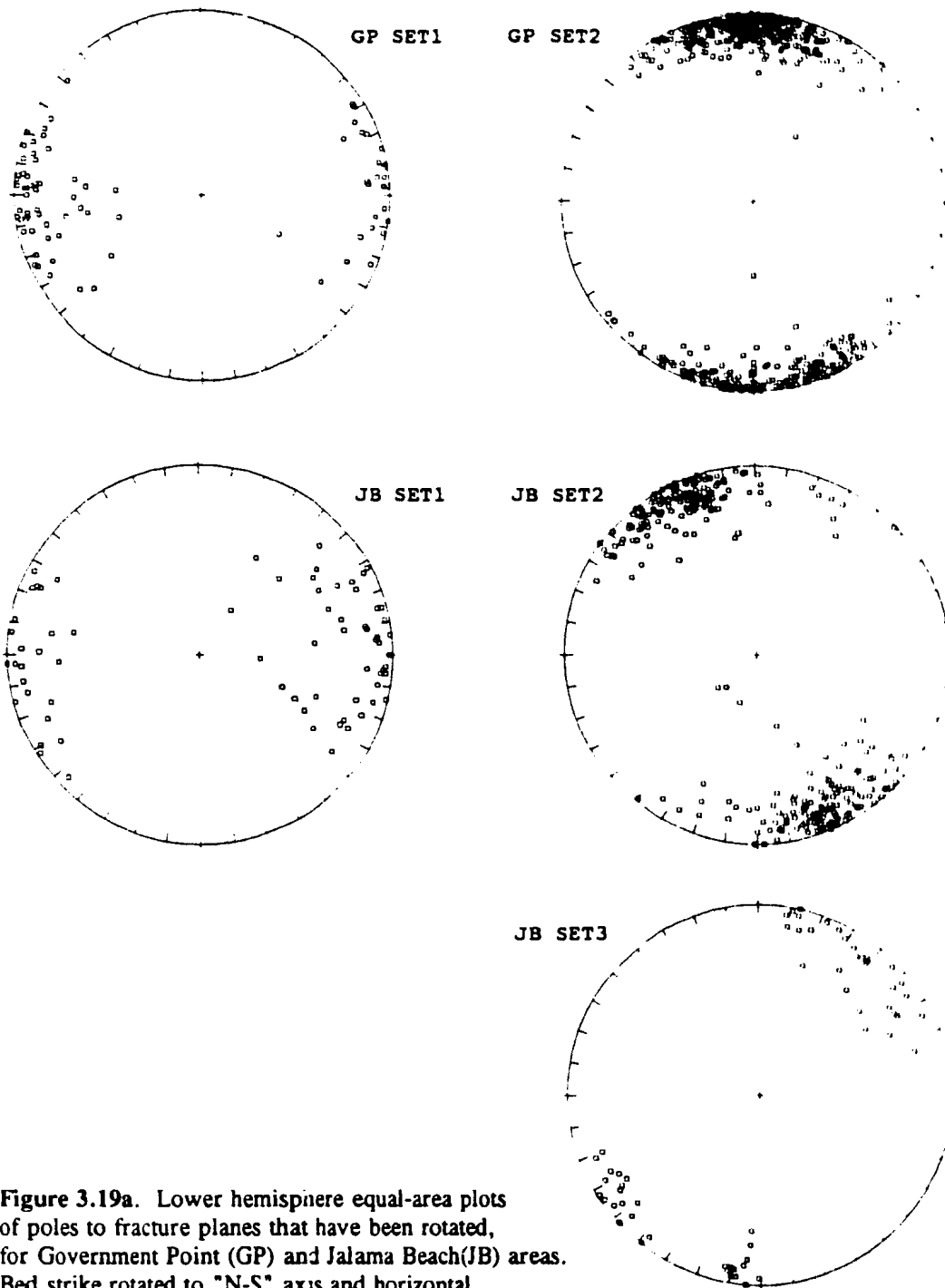


Figure 3.19a. Lower hemisphere equal-area plots of poles to fracture planes that have been rotated, for Government Point (GP) and Jalama Beach (JB) areas. Bed strike rotated to "N-S" axis and horizontal.

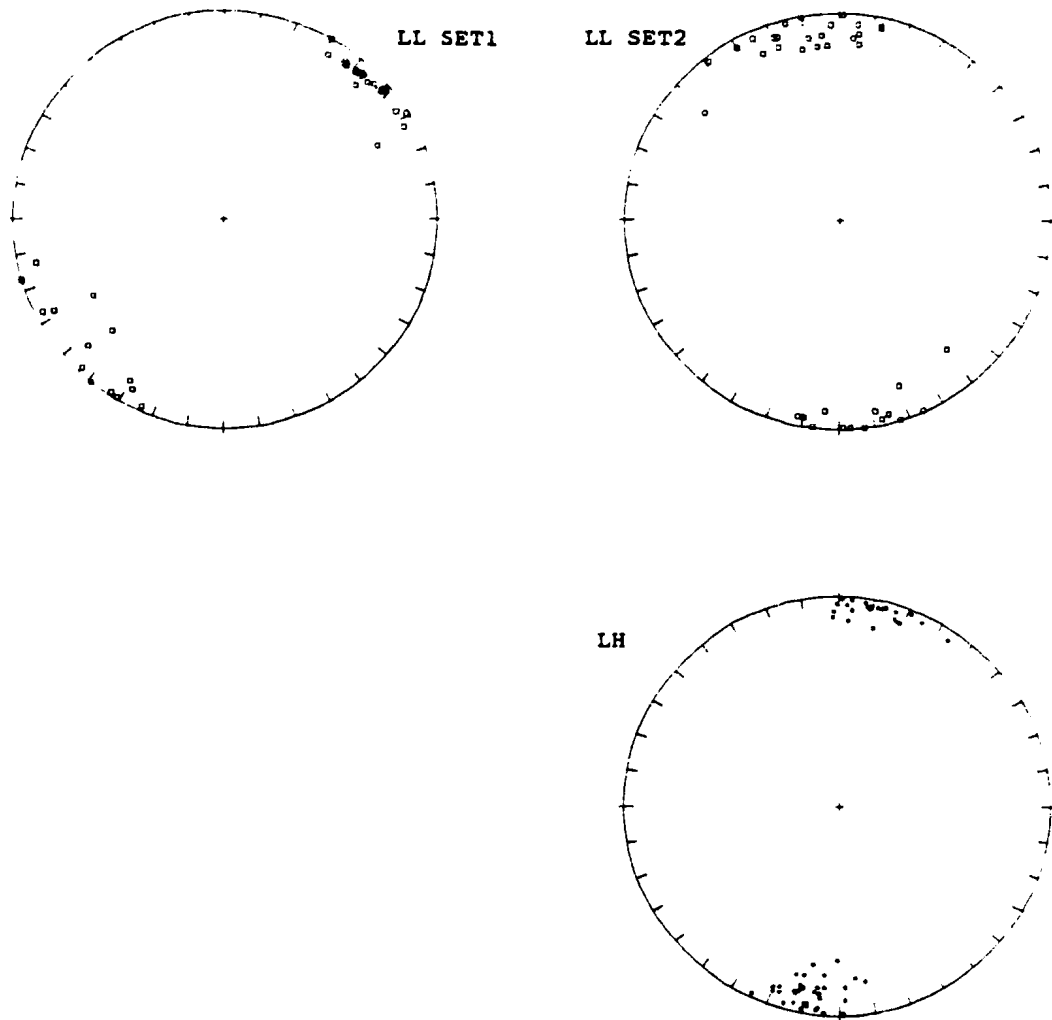
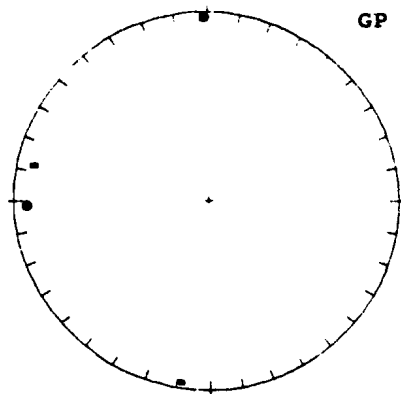
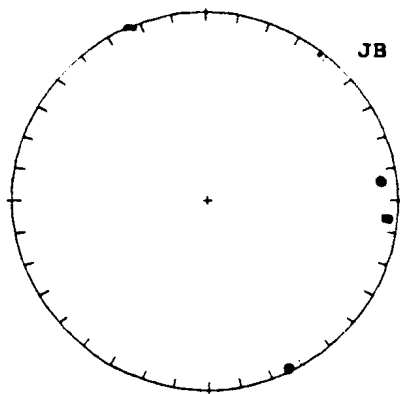


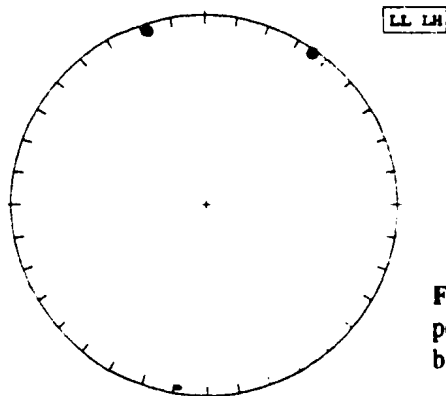
Figure 3.19b. Lower hemisphere equal area plots of poles to fracture planes that have been rotated, for Lompoc Landing and Lions Head fracture sets. Bed strike rotated to "N-S" axis and to a horizontal position.



Government Point area:
 Poles to mean orientation for
 Sets 1 and 2;
 - data rotated using ave. bed dir.
 for each site as shown in Table 3.7
 ● data rotated using an overall bed
 orientation of 40/20



Jalama Beach area:
 Poles to mean orientation for
 Sets 1 and 2;
 ● Sites 1 - 4 combined data
 - Sites 5 & 6 combined data
 ◆ Set 3 for sites 5 & 6



Lompoc Landing and Lions Head:
 Poles to mean orientation of sets
 ● Lompoc Landing sets 1 and 2
 - Lions Head one set

Figure 3.20. Lower hemisphere equal-area plots of mean poles for fracture sets shown in Figure 3.19a and b, bedding rotated data. Bed strike is on N-S axis.

employed to remove the effects of the local bedding attitudes created by any secondary folding which occurred after the formation of the fractures. As seen in the figure, both approaches produced similar mean orientations for each of the two fracture sets, with one set striking approximately parallel to the strike of bedding and the second set striking approximately parallel with bed dip direction.

The sites at Jalama Beach were separated into two groups; sites 1 through 4 forming one group (JB14) and sites 5 and 6 forming the other group (JB56). This division was performed because the JB14 sites and the JB56 sites were in different stratigraphic locations (Figure 2.1), and there were three recognized fracture sets at the JB56 sites and two fracture sets at the JB14 sites. Mean orientations for the fracture sets at JB14 and JB56 sites are shown in the middle stereonet of Figure 3.20. Set 1, at both JB14 and JB56, has the least number of fractures and strikes parallel with bed strike. The more abundant fractures of set 2, at both JB14 and JB56, have a mean strike 20-25° "left" (counterclockwise) of bedding dip direction. The average strike direction for set 3 fractures, present at JB56, perfectly bisects the acute angle between sets 1 and 2.

For the small-scale survey areas in the Onshore Santa Maria domain, the Lompoc Landing (LL) data show that the average strikes for the two sets are separated by approximately 55° and are bisected by the bedding dip direction (Figure 3.20). The fractures forming the one set mapped at Lions Head (LH) have a mean strike orientation that is within 10° of the bedding dip azimuth.

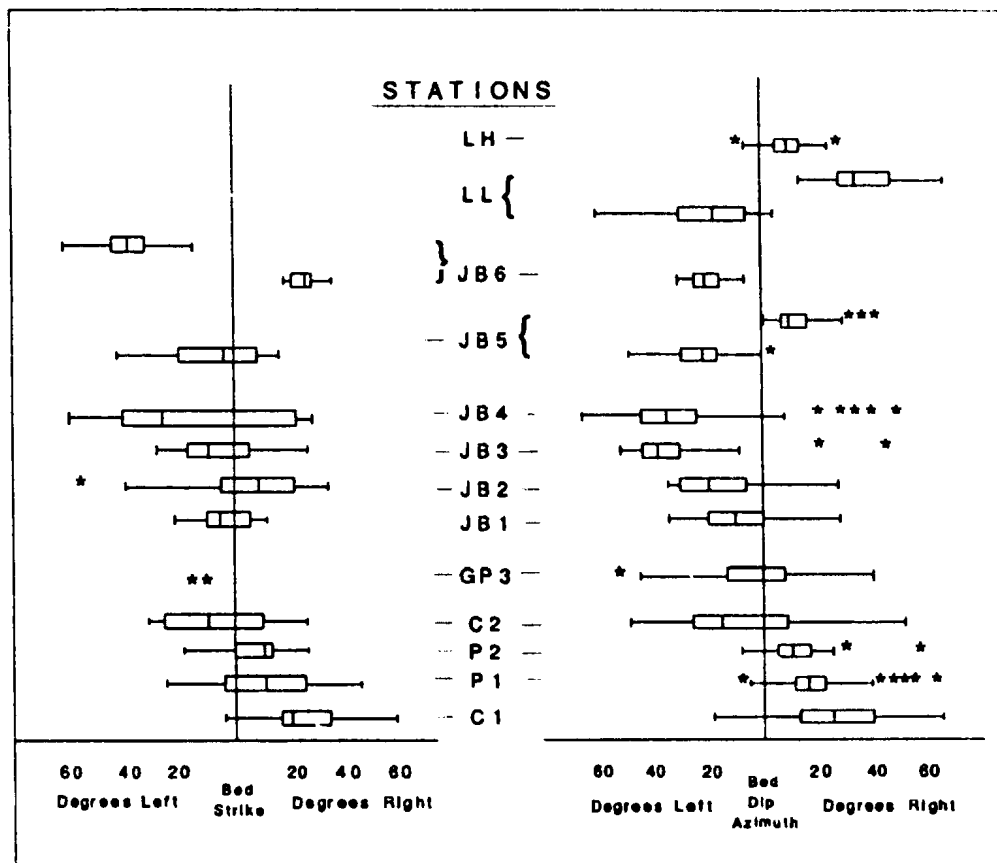


Figure 3.21. Box plot summary display, showing the spread and distributions of the bedding rotated orientation data. Boxes are placed according to relationship of the sets orientation to the bedding strike and bedding dip direction, which are represented by the vertical lines. Asterisks represent outliers.

The spread and distribution of the "bedding rotated" orientation data for each set at each site and/or station are presented as box-plots in Figure 3.21. The orientation data are shown in relationship to the bedding strike and bedding dip directions. These summary plots show the variability of the fracture trends from site to site and the wide spread of attitudes. It is interesting to note that the fractures of set 2 at three of the five stations at Government Point tend to be oriented to the "right" of the bed dip azimuth but the fractures of set 2 at Jalama Beach are to the "left". If the fractures are the result of local folding then set 2 at Government Point and set 2 at Jalama Beach would represent opposite "shear" fractures of the Stearns and Friedman (1972) pattern 1 model (Figure 1.6). If the set 2 fractures formed early before folding, the difference in the relationship of the fractures to bedding would probably be due to rotation or tilting of the local folds after formation of the fractures. The distinction could be important, in that, Type I (extension) fractures would be expected to be more open to fluid flow than the Type II (shear) fractures because of the mode of origin, if the fractures are under the influence of the same stress field that was active during folding.

3.3.2 Large-scale Data

The large-scale fractures were grouped into sets using a procedure similar to the one employed for the small-scale data; it is described in Appendix C. As the large-scale fractures were mapped over a large area and could not be grouped by specific outcrop, the orientation data were normalized and combined into two groups, one for the sites in the Onshore Santa Maria (OSM) structural domain and one for the Santa Barbara Channel (SBC) domain. In combining the data within the same structural domain it is assumed that the data are from features in similar rock types and have experienced similar stress histories. To normalize or standardize the orientations, the poles to fracture planes were rotated along with the bedding, as described in section 3.3.1 for the small-scale data.

Figure 3.22 presents stereoplots of the original data and the bedding rotated data for the two different structural domains. It can be seen that orientations are widely dispersed in all of the plots. The original orientations of the large-scale fractures in the OSM domain seem to define two sets with trends similar to the two sets found for the small-scale data at Lompoc Landing. When the poles are rotated so bedding is standardized, the two sets are not as well defined. From field observations, it was determined that there are three sets defined by these orientation data. The dominant set has an average strike which parallels the bedding dip direction, a subordinate set which strikes approximately 55° to the right of the first set, and the third set of only two fractures, strikes perpendicular to the first set (Table 3.8). These groupings should be considered preliminary, with more data needed to accurately define the sets in this domain.

More fractures were measured in the SBC domain and three sets are represented. Of the 155 fractures that orientations were collected for, 15% were sub-parallel to bedding, 23% on average strike parallel with bedding strike, and the largest group, 62%, show a mean strike parallel with the bedding dip direction (Table 3.8). Qualitatively these percentages fit with field observations, that the extensional fractures that are perpendicular to bedding strike are the predominant discontinuity, with fractures, parallel with the bedding plane and parallel to bedding strike being subordinate. These groupings are reasonable for these data and match published observations (Belfield et al., 1983; Snyder, 1987) but more sites need to be mapped to determine if these orientations and sets are pervasive in each structural domain.

Table 3.8. Mean orientations of sets for large-scale fractures that have been rotated so that all bedding have a common strike. STRIKE is the fractures strike in relationship to bedding strike, (-) indicates to the left of bedding strike, (+) to the right. DIP AZ. is mean dip azimuth for set represented in Figure 3.22, and SYMBOL is character representing poles within each set. N is the number of fractures in each set.

AREA	SET	N	STRIKE	DIP AZ.	DIP	SYMBOL
SV (SBC)	1	36	-15	255	75	□
	2	96	+94	4	87	○
	3	23	HORZ	108	4	▼
NV (OSM)	1	10	-38	232	87	□
	2	29	+94	4	87	○
	3	2	+5	92,277	59,58	+

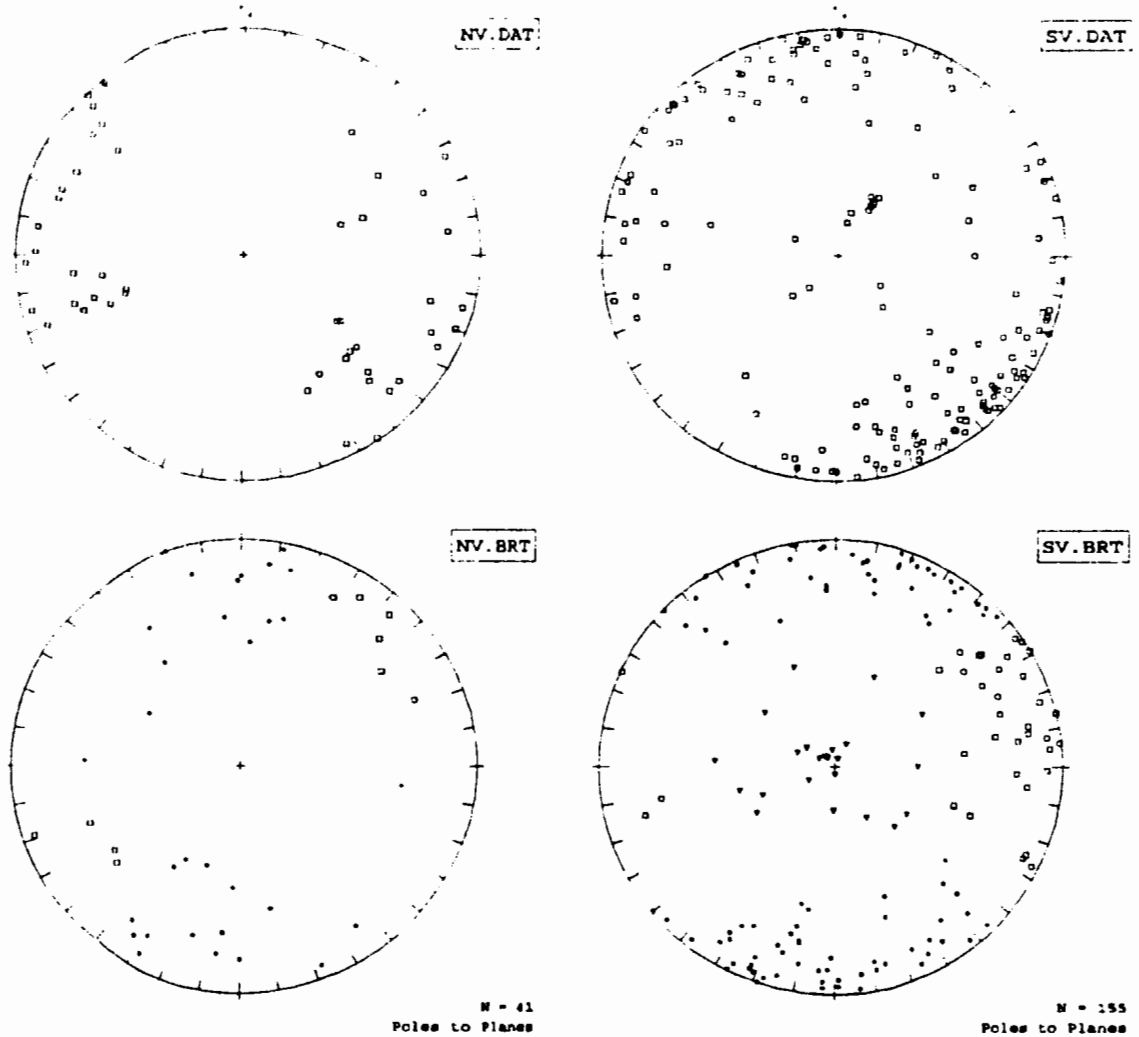


Figure 3.22. Lower hemisphere equal area stereoplots of poles to fracture planes for large scale survey data. NV - combined data from two sites in the Onshore Santa Maria domain, SV - combined data from all sites in the Santa Barbara Channel domain. Upper two stereoplots of original orientations, lower two plots of poles when bedding rotated to a N-S strike and horizontal (see text).

3.4 FRACTURE TRACE LENGTH

As with the generation of other fracture parameter statistics which are used in numerical models, careful analysis of trace lengths is needed in order to estimate the true fracture length distribution statistics. Some of the biases associated with the measurement of trace lengths have already been mentioned in section 3.1 and these biases and the procedures used to analyze fracture trace lengths are discussed by numerous workers, including, Call et.al.(1976), Baecher et.al.(1977), Cruden(1977), Baecher(1980), Pahl(1981), Priest and Hudson(1981), Laslett(1982), Rouleau(1984), and Kulatilake(1992). The main biases or sources of errors that are normally addressed in the analysis of fracture trace lengths collected from scanlines are truncation bias, censoring, size effect (the higher probability of sampling longer trace lengths), and the cut effect (that the trace length depends on the relative orientation between the fracture and the outcrop). To account for these biases the following procedures were used for analyzing the fracture trace lengths.

For each fracture set, the distribution of the raw trace lengths was determined by preparing bar charts, and calculating the basic statistics, including skewness and kurtosis, which provided a general description of the trace length distribution. A more rigorous graphical method, called probability plots or theoretical quantile-quantile plots (Chambers et.al., 1983), for censored data was used to determine the fit of the trace length distribution to the theoretical lognormal and exponential distributions. These two theoretical distributions are widely used to describe the trace length distribution and are available in the NAPSAC fracture flow modelling program used for this thesis.

To produce probability plots for progressively censored data, the data are ordered in ascending form and ranked 1 to n (n = total number in sample). Then for each uncensored length, calculate the plotting position (p_i), convert p_i to z_i , and plot the log trace versus z_i for the lognormal distribution or plot the trace length versus z_i for the exponential distribution.

Where, from Chambers et.al. (1983),

$$p_i = 1 - \frac{n+0.5}{n} \prod \frac{n-i+0.5}{n-i+1.5}$$

with i = the rank of the uncensored length. For the normal distribution convert p_i to z_i using,

$$z_i = 5.0633[p_i^{0.135} - (1-p_i)^{0.135}]$$

(Schemeiser, 1979). For the exponential distribution,

$$z_i = -\ln(1-p_i)$$

(Chambers et.al., 1983).

The probability plots provide a graphical estimation of the mean and standard deviation for the trace lengths. For a more analytical estimation of the distribution parameters for data that are truncated and progressively censored, a program by Chung (1988) called MULTI was used. MULTI assumes a lognormal distribution and uses the Kaplan-Meier product limit estimator, which is the same equation used in the plotting position formula for the probability

plots. A full explanation of the theory behind MULTI can be found in Chung (1988). The final step in analyzing the trace lengths was to determine the "true" underlying fracture length distribution from the trace length distribution. This step followed the procedure outlined by Herbert and Splawski (1990), which uses moment-estimating formulas assuming both distributions are lognormal and that the fractures have a rectangular shape. Herbert and Splawski provide a good discussion of the development of the moment estimators and of the consequences of using the above assumptions.

3.4.1 Small-scale Data

Figure 3.23 presents the bar charts for each set which are coded to indicate the degree of censoring, and Table 3.9 contains the basic trace length statistics for each set. The Government Point (GP) fracture sets were divided into traces that were collected from vertical outcrops (GP,1v and GP,2v) and from the horizontal outcrops (GP,1h and GP,2h). Since, at Government Point the horizontal exposures were nearly parallel to the bedding plane surfaces and the vertical cliff exposures were perpendicular to the bedding plane, it is assumed that the fracture traces in approximately orthogonal directions from outcrops, in close proximity, define the two dimensional nature of the fracture planes. It is interesting to note the differences in the mean raw trace lengths for the GP vertical and horizontal sections. The horizontal trace of set 1 (GP1,h) is considerable shorter than horizontal trace of set 2 (GP2,h), which is consistent with the higher percentage of terminations of set 1 against set 2 observed in the field. The mean lengths for the vertical traces of the two sets are similar in value and are probably controlled by the "mechanical" bed thickness. Due to the lack of vertical and

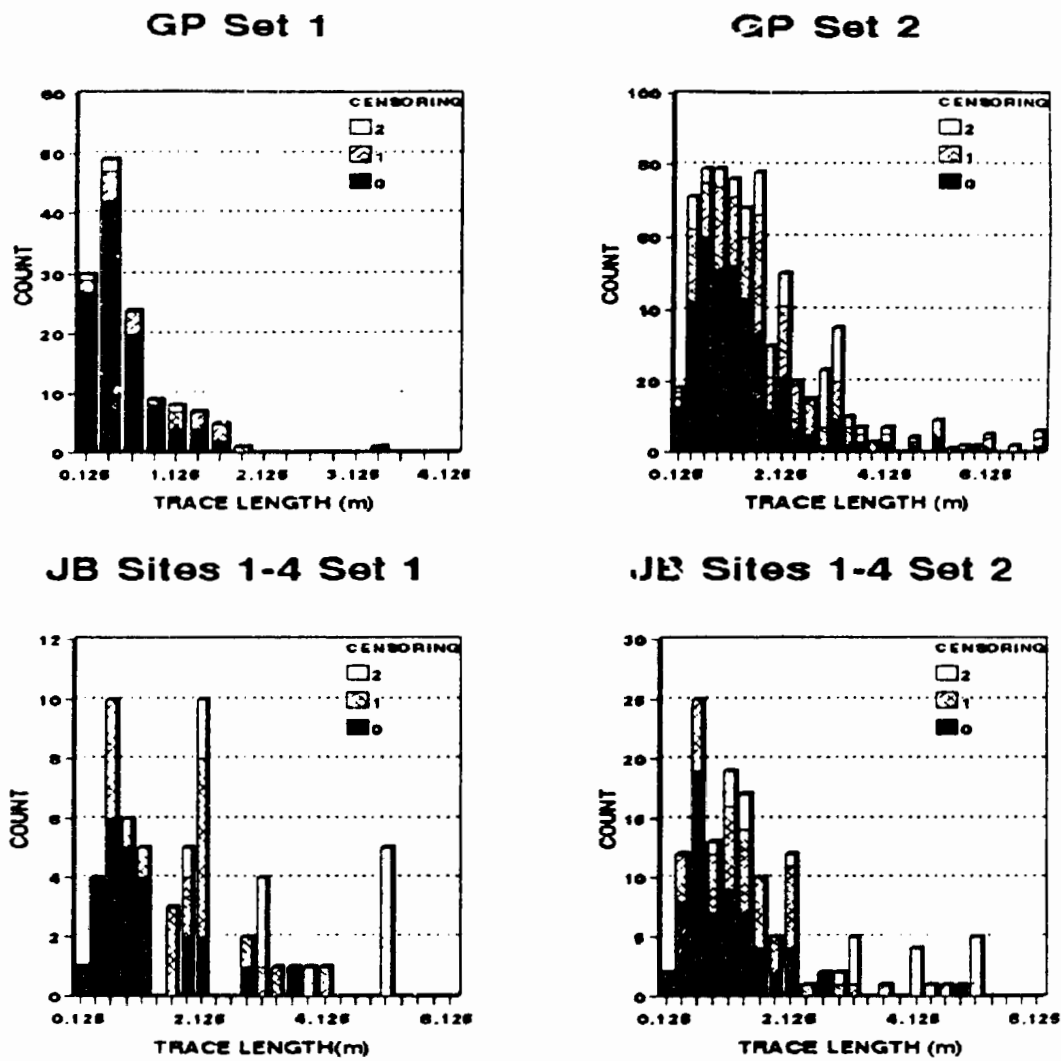
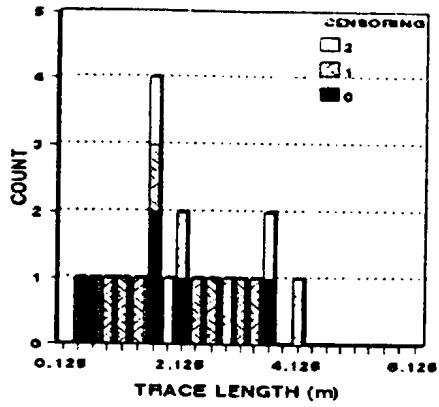
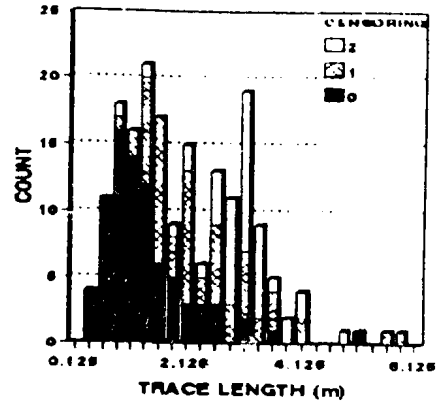


Figure 3.23a. Bar charts of trace length by censoring for each fracture set. GP - Government Point, JB - Jalama Beach sites 1-4.

JB Sites 5,6 Set 1



JB Sites 5,6 Set 2



JB Sites 5,6 Set 3

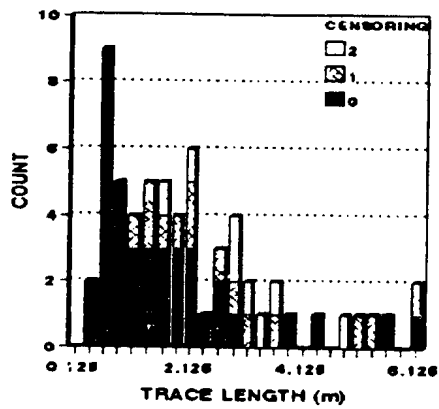


Figure 3.23b. Bar charts of trace length by censoring for each fracture set. JB - Jalama Beach sites 5 and 6.

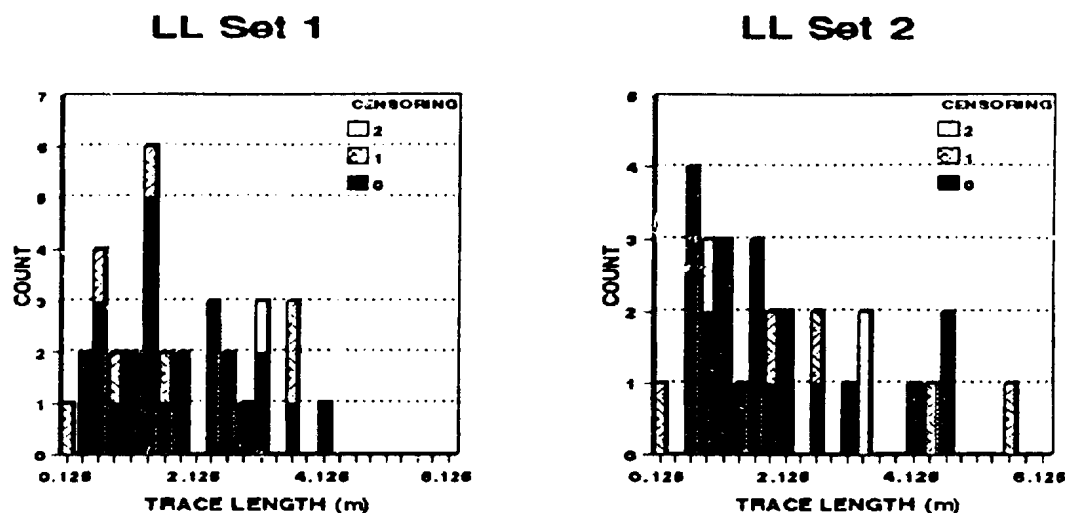


Figure 3.23c. Bar charts of trace length by censoring for each fracture set. LL - Lompoc Landing.

Table 3.9. General statistics of raw trace length for each set. N = number in sample, MIN = minimum length in meters (usually truncation value), MAX = maximum length measured, MEAN = arithmetic mean, S.D. = standard deviation, SKEW = skewness (= 0 for normal distribution), KURT = kurtosis (= 3 for normal distribution), MEDIAN = 50% point of data, %CENS = percent of sample that is censored.

SET	N	MIN (m)	MAX (m)	MEAN (m)	S.D.	MEDIA N (m)	SKEW	KURT	% CENS
GP,1	104	0.26	3.27	0.69	0.47	0.51	2.28	7.91	22
GP,1v	22	0.25	2.10	1.12	0.45	1.20	-0.04	-0.47	50
GP,1h	82	0.25	3.27	0.47	0.38	0.38	4.16	26.18	15
GP,2	706	0.25	20.00	1.98	2.14	1.41	3.59	17.51	49
GP,2v	289	0.35	5.00	1.74	0.94	1.53	1.43	2.32	43
GP,2h	417	0.25	20.00	2.07	2.64	1.17	3.00	11.07	53
JB14,1	59	0.27	13.00	2.10	1.97	1.81	3.12	14.05	58
JB14,2	137	0.32	5.00	1.57	1.17	1.22	1.54	1.76	54
JB56,1	20	0.40	4.00	2.11	1.03	1.96	0.20	-0.99	70
JB56,2	188	0.30	8.00	2.12	1.21	1.84	1.30	3.19	57
JB56,3	64	0.44	8.22	2.38	1.85	1.87	1.41	1.36	38
LL,1	37	0.37	24.00	3.07	4.25	1.85	3.63	14.45	24
LL,2	41	0.60	48.50	7.82	11.63	3.16	2.36	5.12	29

horizontal exposures in close proximity, a similar comparison of horizontal and vertical traces lengths can not be performed for the other areas. Overall the mean values of the trace lengths for set 1 fractures at all areas, except JB14, are shorter than those for set 2.

It can be seen from Table 3.9 that for all sets that contain more than 30 fractures there is a fairly strong positive skewness and a large value for kurtosis (strong peakness). These are properties of the lognormal and exponential distributions. Even though the shape of a bar chart is influenced by the number of intervals, the trace length bar charts in Figure 3.23 show a general lognormal shape for most of the sets. To graphically test how well the measured data fit these two distributions, the trace length data were plotted against the theoretical quantiles using probability plots (Figure 3.24). Probability plots give a good overall impression of the empirical distribution of censored data. The closer the plotted data points fit a straight line the better the theoretical distribution represents the measured data. A best fit line was drawn on the plots following the procedure in King (1971, p. 22). For most of the fracture sets both the lognormal and the exponential distributions fit the bulk of the central portion of the data. The deviation of points from the line at the lower end of the lognormal probability plots are an indication of the truncation bias, showing a clustering of points near the minimum length. This truncation bias also makes the exponential best fit line unreliable, since the true minimum is unknown. Curved deviation of data points from the straight line may be due to the mixing of trace length data from scanlines on different outcrops, rounding of trace length measurements, or mixing of data from an unrecognized fracture set. For this thesis, further in-depth analysis of the fracture trace lengths was not undertaken and it is felt that the trace length data are approximated well by the lognormal distribution.

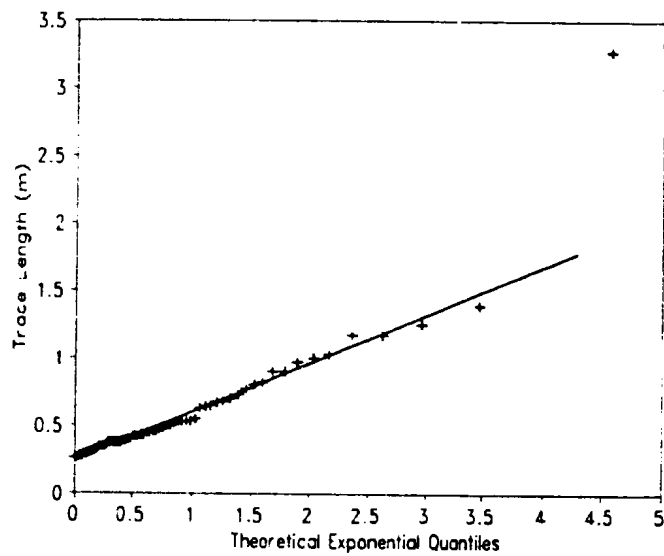
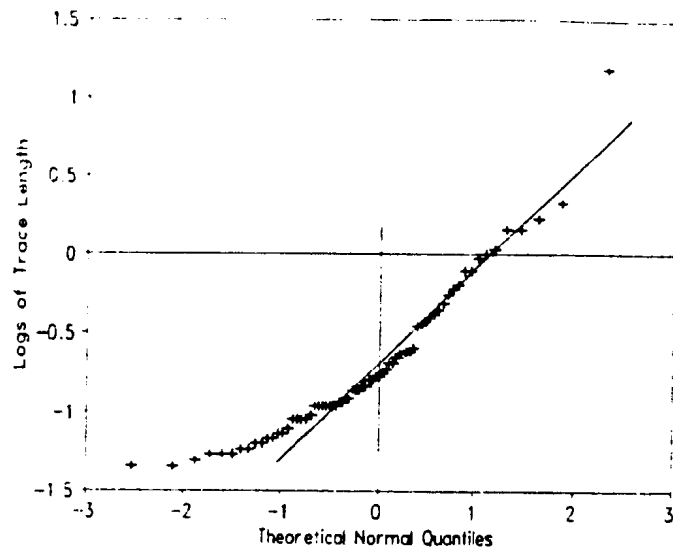


Figure 3.24. Probability plots using plotting position for censored data. Example shows comparison of trace length data for Government Point set 1h to the lognormal and exponential distributions.

Table 3.10. Means and standard deviations, in meters, for fracture sets. $MEAN_M = \ln$ mean from MULTI, $MEAN_{MB} =$ estimate of mean using Bury's(1975) equations, $MEAN_b = \ln$ mean of fracture length using equations from Herbert and Splawski (1990), $MEAN_B =$ estimate of true fracture mean using Bury's (1975) equations. S.D. = standard deviation for corresponding MEAN.

SET	N	MEAN _M	MEAN _{MB}	MEAN _b	MEAN _B	S.D. _M	S.D. _{MB}	S.D. _b	S.D. _B
GP,1	104	0.44	0.79	-1.04	0.42	0.64	0.56	0.59	0.27
GP,1v	22	0.34	1.65	-0.08	1.05	0.56	1.01	0.50	0.56
GP,1h	82	-0.65	0.59	-0.93	0.43	0.50	0.32	0.43	0.20
GP,2	706	0.85	4.28	-1.36	0.46	1.10	6.57	1.07	0.67
GP,2v	289	0.68	2.58	-0.19	1.05	0.74	2.19	0.69	0.82
GP,2h	417	1.00	6.59	-2.33	0.23	1.33	14.59	1.31	0.48
JB14,1	59	1.16	8.27	-2.43	0.22	1.38	19.76	1.36	0.51
JB14,2	137	0.74	3.56	-1.17	0.51	1.03	4.90	1.00	0.67
JB56,1	20	1.18	4.57	-0.30	1.10	0.92	5.73	0.88	1.20
JB56,2	188	1.13	5.49	-0.94	0.67	1.07	8.03	1.04	0.93
JB56,3	64	0.89	4.06	-0.94	0.63	1.01	5.40	0.98	0.80
LL,1	37	0.85	4.02	-1.10	0.55	1.04	5.61	1.01	0.74
LL,2	41	1.62	15.11	-2.55	0.23	1.48	42.57	1.46	0.62

Results of the maximum likelihood estimations of trace length using MULTI, correcting for truncation and censoring, are presented in Table 3.10. Means and standard deviations from MULTI are the natural logarithms of trace length, with the mean and standard deviation of the original distribution estimated by the following equations from Bury (1975, p.279).

$$\bar{\mu} = \exp\left[\mu_b + \frac{\sigma_b^2}{2}\right]$$

$$\bar{\sigma} = \sqrt{\exp(2\mu_b + \sigma_b^2) \cdot (\exp(\sigma_b^2) - 1)}$$

Estimations of the mean and standard deviation of the underlying fracture lengths for each set, using the Herbert and Splawski (1990) equations, are also shown in Table 3.10. Due to the large sample standard deviation for some of the sets, the estimation of the "true" fracture mean length is dramatically shorter than the trace length mean estimated by MULTI. The significance of this result will be discussed in Chapter 4.

3.4.2 Large-scale Data

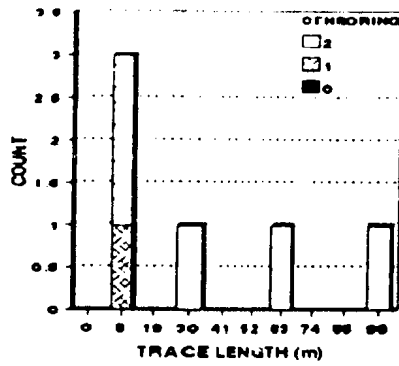
The general statistics for the large-scale trace length data are shown in Table 3.11. The truncation level for the large-scale trace lengths was set at 3.0 meters and the traces were measured to the nearest meter. Observations and comments about the large-scale trace lengths must be qualified, due to the small sample sizes for most of the sets and the high percentage of censored traces. For the bar charts (Figure 3.25), the data were grouped into nine, 10 meter, intervals starting at three meters and ending at 101 meters. All sets show an approximate lognormal distribution. Probability plots using the plotting position for censored data were not done, due to the fact that only a small percentage (< 10%) of the data points were uncensored and these would have to be used to estimate a fit to the distribution. For each set, the distribution of the measured traces was evaluated using all the trace lengths in probability plots with the commonly used plotting position, $p_i = (i-0.5)/n$, where i is the rank and n is the total sample size. As for the small-scale data, the traces were tested against the

lognormal and exponential distributions (Figure 3.26). These plots show that the distribution of the measured traces can be approximated by the lognormal distribution, but nothing can be said about the true uncensored trace length distribution. Also, because of the high degree of censoring, MULTI could not be used, and even though there is a strong bias, for completeness the underlying mean fracture length for each set was estimated using the formulas from Herbert and Splawski (1990). Results of these calculations are in Table 3.12.

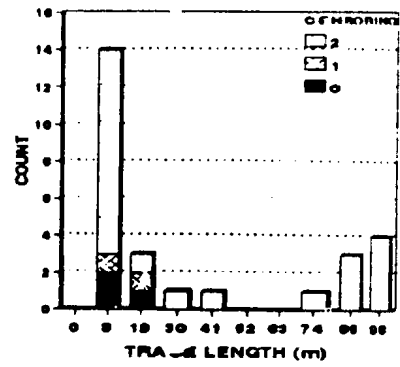
Table 3.11. General statistics of raw trace length for each set. N = number in sample, MIN = minimum length in meters (usually truncation value, 3.0 m), MAX = maximum length measured, MEAN = arithmetic mean, S.D. = standard deviation, SKEW = skewness (= 0 for normal distribution), KURT = kurtosis (= 3 for normal distribution), MED = 50% point of data, %CENS = percent of sample that is censored.

SET	N	MIN (m)	MAX (m)	MEAN (m)	S.D.	MED (m)	SKEW	KURT	% CENS
NV,1	6	7.0	100.0	38.2	38.9	22.0	0.69	-1.11	100
NV,2	27	3.0	100.0	34.7	37.8	13.0	0.88	-1.72	89
NV,3	2	45.0	100.0						100
SV,1	32	3.0	90.0	15.6	16.6	10.0	2.99	10.64	100
SV,2	106	3.0	90.0	18.6	17.1	12.0	2.12	5.06	91
SV,3	16	4.0	90.0	18.6	23.6	9.5	2.18	3.70	94

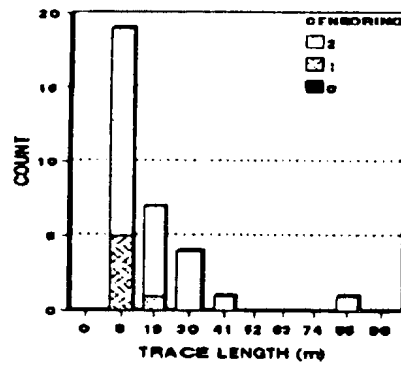
NV Set 1



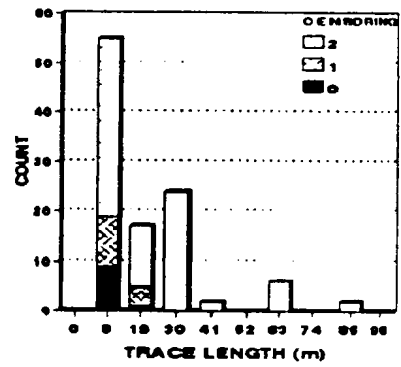
NV Set 2



SV Set 1



SV Set 2



SV Set 3

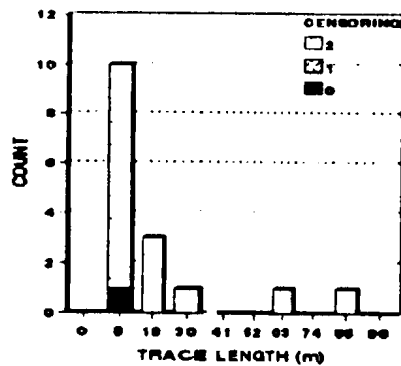


Figure 3.25. Bar charts of trace length by censoring for each fracture set. NV - North Vandenberg, SV - South Vandenberg.

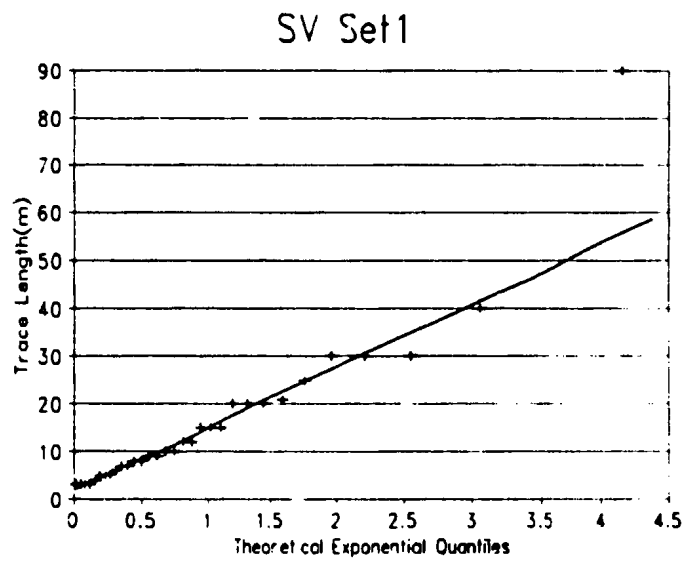
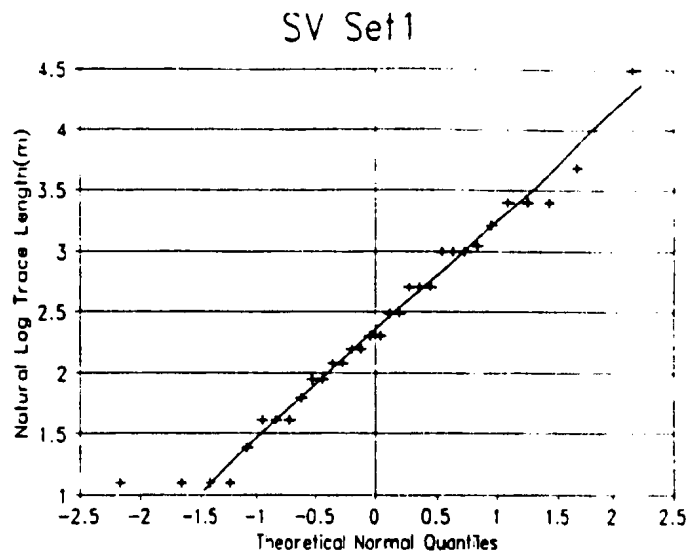


Figure 3.26. Probability plots using plotting position for censored data. Example shows comparison of trace length data for South Vandenberg set 1 to the lognormal and exponential distributions.

Table 3.12. Means and standard deviations, in meters, for each fracture sets. $MEAN_r$ = raw data ln mean, $MEAN_{rB}$ = estimate of mean using Bury's (1975) equations, $MEAN_{hB}$ = ln mean of fracture length using equations from Herbert and Splawski (1990), $MEAN_B$ = estimate of true fracture mean using Bury's (1975) equations. S.D. = standard deviation for corresponding MEAN.

SET	N	$MEAN_r$	$MEAN_{rB}$	$MEAN_{hB}$	$MEAN_B$	S.D. _r	S.D. _{rB}	S.D. _{hB}	S.D. _B
NV,1	6	3.11	45.0	0.54	3.3	1.18	78.2	1.15	5.6
NV,2	27	2.91	39.1	0.10	2.3	1.23	73.6	1.20	4.1
NV,3	2	-	-	-	-	-	-	-	-
SV,1	32	2.38	15.5	1.15	4.4	0.85	16.0	0.81	4.2
SV,2	106	2.59	18.5	1.49	6.0	0.81	17.8	0.77	5.4
SV,3	16	2.43	18.0	0.80	3.4	0.96	22.2	0.93	4.0

3.5 FRACTURE SPACING

Spacing of fractures in sedimentary rocks is believed to be influenced by a number of factors including rock type, bed thickness, contrast in mechanical properties between the fractured layer and unfractured confining layers, strain rate, in situ stresses, temperature and structural position. Stearns and Friedman(1972) state that fracture spacing in a brittle rock unit depends on the development of instabilities caused by different bed thicknesses and physical property differences in a multi-layered system. Others (Price, 1966; McQuillan, 1973; Narr, 1991) have shown that bed thickness is the dominant factor in determining fracture spacing in sedimentary rock in some localities. Pollard and Segall (1987) introduced a model for fracture spacing based on the premise that the perturbation of the stress field around a joint influences the development of an adjacent joint. Using field observations, they determined that the range of influence is based on the length of the joint which in turn is assumed to be determined by the thickness of the jointed layer. Several models consider the rock properties and strain, along with the bed thickness, in determining joint frequency (Price, 1966; Hobbs, 1967; and Sowers 1972). These models could not be utilized in this study to give an indication of the expected joint spacings, due to the lack of available data on the mechanical properties of the different rock types in the Monterey Formation.

The accuracy of the spacing analysis from fracture data collected using scanlines is affected by the lack of precision caused by the trace length truncation bias discussed earlier, errors introduced by the uneven surfaces of the outcrops, and the loss of data due to the finite length of the scanlines (no spacing data before the first fracture and after the last fracture). Even

with these limitations, fracture scanline mapping is sometimes the only available method (Priest and Hudson, 1976; Sen and Kazi, 1984; LaPointe and Hudson, 1985) to determine the fracture spacing distribution.

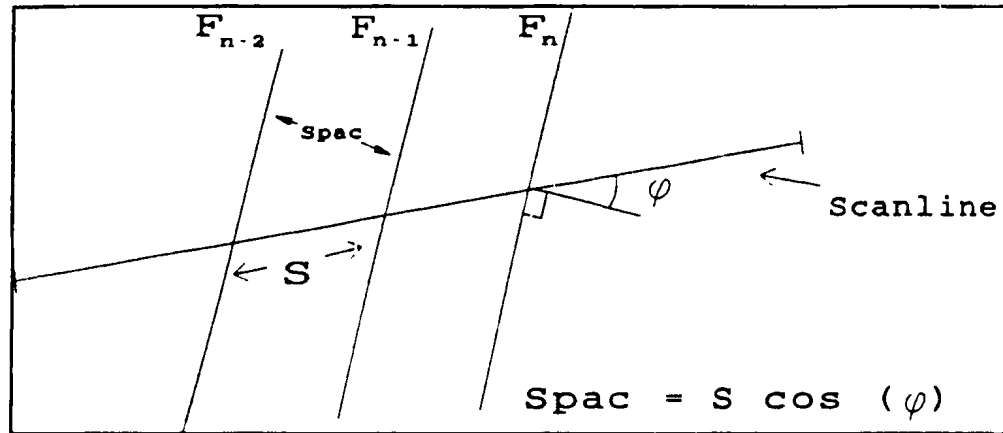


Figure 3.27. Scanline schematic illustrating correction for spacing. See text.

For this study, scanline maps were used to determine fracture spacings. Fracture spacing is defined as the distance between consecutive fractures of the same set that intersect a scanline, multiplied by the cosine of the angle between the scanline and the normal of the average plane for the set (Figure 3.27). To obtain the appropriate correction angle, the direction cosines were derived for the scanline and for the average pole of the fracture set, then $\cos \phi$ (see Figure 3.27) is derived using;

$$\cos(\phi) = l_s * l_f + m_s * m_f + n_s * n_f,$$

where subscript s = scanline and f = fracture, for the respective direction cosines (l, m, n).

Thus estimated spacing is, $Spac = s * \cos(\phi)$, assuming that all fractures of the same set are parallel and are oriented similar to the average orientation. After the individual spacings were estimated the basic statistics of spacing were calculated for each set. Bar charts, box plots

and probability plots were produced to graphically determine the distribution of the spacing data for each set.

3.5.1 Small-scale Data

Statistics for fracture spacing are given in Table 3.13, for the sets determined from the small-scale data. As in the evaluation of orientations, the outcrop areas, represented by the groupings of GP (for all sites at Government Point), JB14 (Jalama Beach sites 1 through 4), JB56 (Jalama Beach sites 5 and 6), and LL (Lompoc Landing, 1 site), were assumed to be homogeneous, and the spacing data from the different scanlines was combined. This assumption is consistent with the conclusions drawn by Narr and Suppe (1991). In addition, the groupings are in areas of similar structural position and rock types. The biggest exception to this, is for JB56, where the sites are separated by several hundred meters. The range of spacings within each set can be found in Table 3.13 and is graphically displayed in the box plots in Figure 3.28. The overall range is fairly large for most sets, but the spread of the middle 50 percent, represented by the rectangle in the box plots, is remarkably narrow; set 1 from the JB56 site with its low sample size being the only exception. Correction of spacings to account for short scanlines was checked using the graphs presented by Sen and Kazi (1984) for lognormally distributed spacings. Since over 85% of the scanlines were longer than three meters and the means and standard deviations of the spacings were relatively small compared to the scanline lengths, the relative error due to scanline length for these data will be less than five percent. The exception is set 1 from the JB56 site, where the relative error estimated from the graphs was near 50 percent.

The strong positive skewness to the spacing distributions is evident from the table and the box plots, possibly indicating a lognormal or exponential distribution. As with trace length, the distribution of spacings has been found to fit these two probability distributions by many workers (Priest and Hudson, 1976; Rouleau and Gale, 1985; Narr and Suppe, 1991). To compare the empirical spacing distributions to the theoretical lognormal and exponential distribution, probability plots were made using the statistical package, SYSTAT. Examples of the plots are shown in Figure 3.29, which show that the lognormal distribution is a good approximation for these spacing data.

Table 3.13. General statistics of corrected spacings for each set. N = number in sample, MIN = minimum spacing in meters, MAX = maximum, MEAN = arithmetic mean, S.D. = standard deviation, SKEW = skewness (= 0 for normal distribution), KURT = kurtosis (= 3 for normal distribution), MEDIAN = 50% point of data.

SET	N	MIN (m)	MAX (m)	MEAN (m)	S.D.	MEDIAN (m)	SKEW	KURT
GP,1	55	0.03	2.90	0.59	0.67	0.29	1.77	2.90
GP,1v	9	0.13	1.44	0.67	0.43	0.44	0.57	-0.85
GP,1h	46	0.03	2.90	0.57	0.71	0.25	1.81	2.73
GP,2	612	0.01	3.28	0.34	0.37	0.24	3.69	19.20
GP,2v	273	0.01	3.28	0.34	0.39	0.24	4.01	21.45
GP,2h	339	0.01	3.01	0.35	0.36	0.25	3.34	16.31
JB1-4,1	49	0.03	2.38	0.50	0.57	0.32	2.09	3.88
JB1-4,2	121	0.01	2.39	0.27	0.32	0.18	3.58	17.52
JB5-6,1	12	0.16	5.92	2.07	1.81	1.73	0.71	-0.36
JB5-6,2	167	0.02	2.58	0.44	0.38	0.33	1.92	5.64
JB5-6,3	63	0.01	1.57	0.30	0.28	0.20	1.76	4.84
LL,1	34	0.10	4.22	0.72	1.01	0.29	2.50	5.25
LL,2	39	0.03	5.12	0.89	1.12	0.57	2.57	6.58

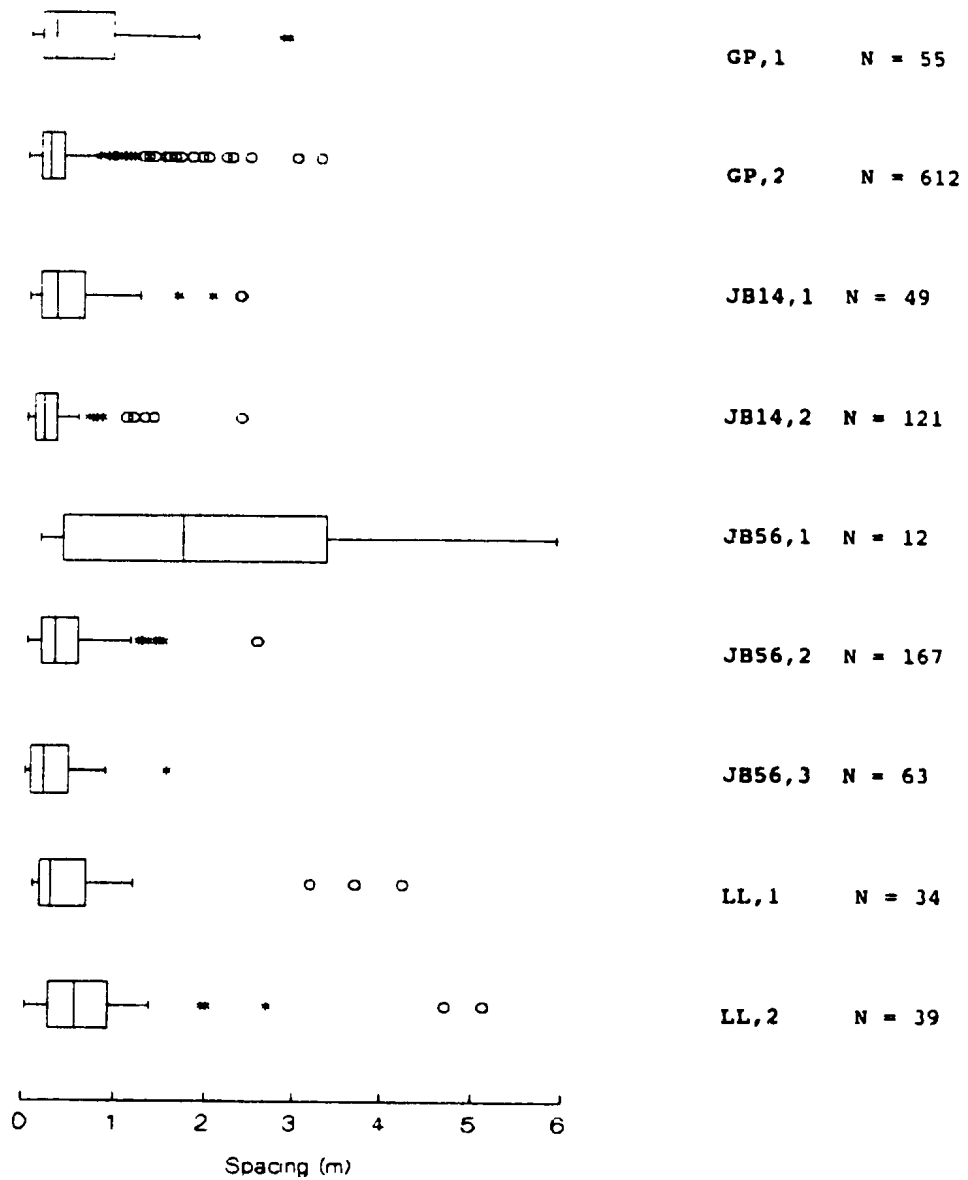


Figure 3.28. Box plot summary display for each set, showing the spread and distributions of spacing. GP,1 and GP,2 - Government Point sets 1 and 2, JB14 - Jalama Beach sites 1 through 4 sets 1 and 2, JB56 - Jalama Beach sites 5 and 6 sets 1, 2 and 3, LL - Lompoc Landing sets 1 and 2. N = sample size.

GP Set 1

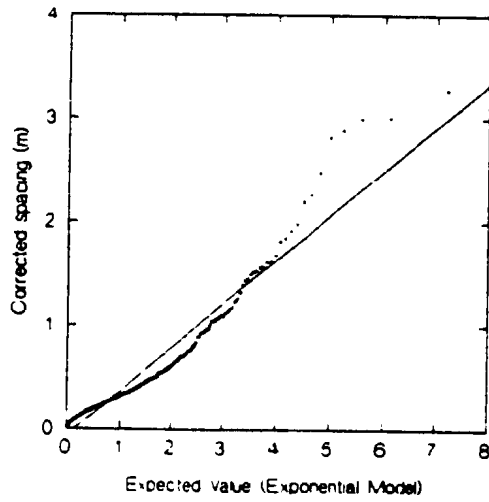
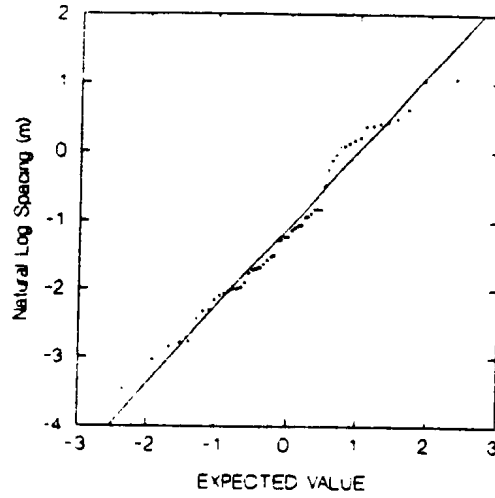


Figure 3.29. Example of probability plots showing comparison of spacing data to theoretical lognormal and exponential distributions, for Government Point (GP) set 1.

3.5.2 Large-scale Data

The general statistics for the large-scale sets are presented in Table 3.14, and the spacing distributions for each set are represented in box plots (Figure 3.30). Each individual spacing was corrected in a manner similar to that used for the small-scale data, except that the pole to each fracture orientation was used instead of the mean pole for the set. Since the scanlines were very long and traversed several outcrops which display varying bedding attitudes and structure, the measured spacings were evaluated using the tabulated scanline data (Appendix A) and the mapped photos. There is a great deal of variance to the spacings of fractures within each large-scale set. The box plots in Figure 3.30 show the central portion of the spacings for each set varying up to 20 meters and more for the small sample of NV set 1. Outliers range up to over 100 meters from the median spacing.

Table 3.14. General statistics of corrected spacing for each set. N = number in sample, MIN = minimum in meters, MAX = maximum, MEAN = arithmetic mean, S.D. = standard deviation, SKEW = skewness (= 0 for normal distribution), KURT = kurtosis (= 3 for normal distribution), MEDIAN = 50% point of data.

SET	N	MIN (m)	MAX (m)	MEAN (m)	S.D.	MEDIAN (m)	SKEW	KURT
NV,1	8	1.4	72.1	29.2	24.1	19.4	0.65	-0.86
NV,2	21	0.8	77.7	9.8	16.8	4.0	3.38	11.12
NV,3	1	-	24.3	-	-	-	-	-
SV,1	27	0.5	100.5	21.4	24.8	16.9	1.81	2.75
SV,2	102	0.1	80.6	14.9	18.6	6.8	1.99	3.36
SV,3	16	2.5	121.2	21.1	33.8	7.3	2.20	3.49

It is difficult to assess if there are physical factors that systematically control the spacings of the large-scale fractures at the study areas. Due to the extent of the fracture traces, it seems unlikely that bed thickness and rock type would have a strong influence on the frequency of these large-scale fractures. But structural position and fluid pressure seem to play a role in the development and could possibly influence the spacings of the large-scale fractures. All the mapped faults in this study were associated with the local folding, and other workers (Viele, 1984) have postulated that some of the large-scale breccias were a result of hydraulic fracturing with the source of the tar coming from the phosphatic member of the Monterey Formation.

Examples of the probability plots used to evaluate graphically the fit of the empirical spacing data to the theoretical lognormal and exponential model are shown in Figure 3.31. As with the small-scale spacing data, the lognormal distribution is a good approximation of the large-scale fracture spacings.

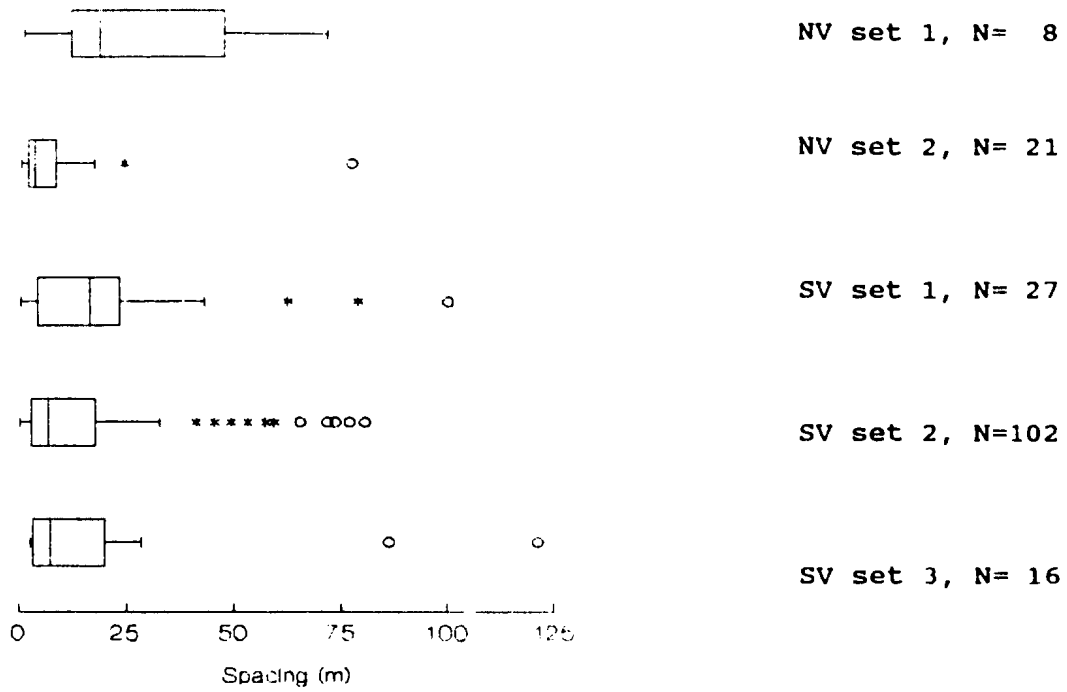


Figure 3.30. Box plot summary display for each set, showing the spread and distributions of spacing. From the top; NV - North Vandenberg, SV - South Vandenberg.

S / Set 1

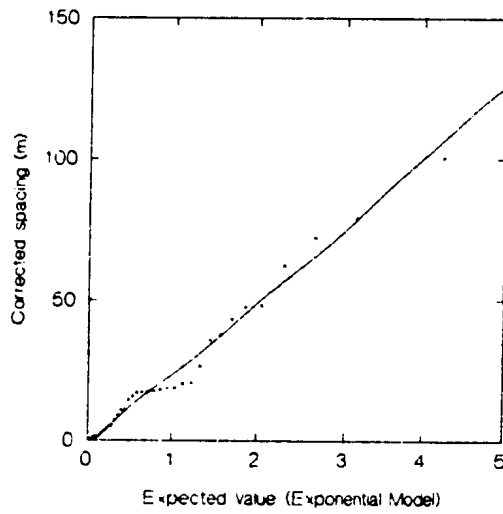
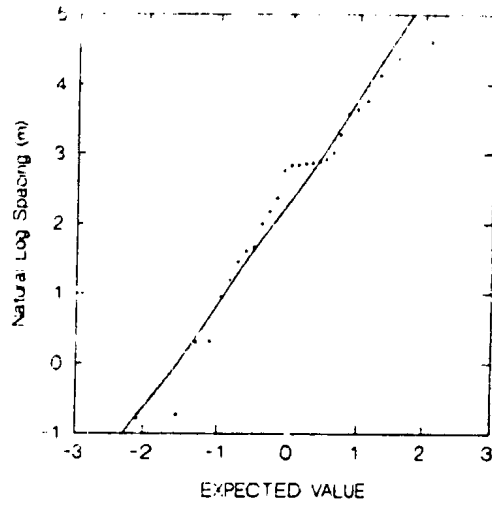


Figure 3.31. Example of probability plots showing comparison of spacing data to theoretical lognormal and exponential distributions, for South Vandenberg set 1.

CHAPTER 4. NUMERICAL SIMULATION

4.1 INTRODUCTION

There are basically two approaches used in numerically modeling fluid flow through the passageways created by interconnected fractures. One approach assumes that at some scale the fractures are continuous (of infinite extent) and the second approach, used here, recognizes that within the rock mass the discrete fractures are discontinuous within the region modeled. To model the discontinuous nature of fractures in a fractured rock mass, several parameters or characteristics of the fractures are needed, such as orientation, length, spacing, and aperture. The detailed mapping of fractures in outcrops described earlier, provided data for some of these fracture parameters for each set of fractures in selected parts of the Monterey section. Chapter 3 reported on the statistical characteristics of these parameters, for the mapped areas, which have been used to determine the effects of fracture geometry (orientation, trace length and spacing) on the preferred directions of flow through the Monterey reservoirs. Two dimensional fracture networks were generated by the computer modeling program NETWRK/NETFLO (Rouleau, 1984; Rouleau and Galc, 1987) which was used early in the Chevron fracture study, and is presented here for comparison to the 3-D simulations. Some of the results from the two-dimensional modeling have been presented earlier (Gale et al., 1991). Modeling of flow through a three dimensional discrete fracture network was accomplished using the computer program NAPSAC (Herbert et al. 1990). A brief discussion follows of the methods for generating the 2-D and 3-D fracture networks and solving for steady state fluid flow through the networks, along with the input statistics and results.

4.2 TWO DIMENSIONAL SIMULATION

4.2.1 Model Description

NETWRK/NETFLO is a modular computer program that generates a two-dimensional line network using the Monte-Carlo method, and solves for the steady-state fluid flow in the network assuming an impermeable matrix. The computer codes were primarily written by A. Rouleau (1984) and site tested on the Stripa project in Sweden (Rouleau and Gale, 1987).

The geometry of the model can be rectangular or circular (only one quadrant is used in the solution), with inner and outer boundary dimensions specified by the user. Lines are generated within the outer boundary but the inner boundary defines the solution region. The buffer zone between the inner and outer boundaries reduces the edge effects of reduced lines near the boundary of the model. Lines are produced for each fracture set in the following manner. The program NETWRK first generates a number of random points based on the fracture density, which is the total length of the fracture traces per unit surface area [L^{-1}]. A line segment is assigned to each point, with a fixed orientation or one randomly selected from the input statistics of the normal distribution. A length is also assigned, either as a single (constant) value or as a randomly selected value from the lognormal distribution based on the trace length statistics. This line generation process is continued until the prescribed line density (L^{-1}) is reached. All the lines cutting across the inner model boundary are terminated at the boundary, correcting for any changes in the length distribution. In addition, if from field observations it is determined that one set preferentially terminates against another, the

"fracture" of the terminated set is trimmed at the intersection point, if it is found to extend beyond the line defining the "dominant" set. The extra length of fracture is then added to the other end of the line segment, maintaining the correct trace length distribution.

In the second step, NETWRK locates the line intersections present in the generated line network and records the coordinates of the effective intersections, called nodes. An intersection is determined to be effective if it contributes to continuous flow through the system. Many intersections will be found ineffective because they are not located along any possible flow paths. The computer defines as an "element" every line segment between two consecutive nodes. During this final step, an aperture is assigned to each line segment according to a single value or from the statistics of the lognormal distribution and the "fracture porosity" (total and effective) of each fracture set is computed. The output of the program NETWRK is then used directly as input for the program NETFLO. Several scenarios with different apertures can be run by calling the aperture generator program, APEGEN, after NETWRK and before NETFLO, to change the apertures in the simulated fracture network.

The program NETFLO uses the finite element method to solve the equations for steady-state laminar flow of an incompressible viscous fluid. NETFLO first reads in the boundary flow conditions, with a boundary being labeled either no flow or having a fixed head value that is constant, linearly varying, or logarithmical varying. Then the generated network geometry data of nodal coordinates, element length, orientation, and aperture are read. The program assigns the head values for the nodes located on the boundaries and then calculates the fluid

pressure at each node in the network. Then the flow rate, velocity, and Reynold's number in each element are calculated, and finally the total flux through the model.

4.2.2 Input and Results

Since one of the primary goals in this numerical simulation of flow through computer generated fracture networks is to determine whether fracture geometry imparts a preferred direction to fluid flow through the Monterey reservoirs, an arbitrary (25m)² rectangular model geometry was chosen. In addition, since the network model is a two dimensional representation of a three dimensional network, simulations were run with the fracture system generated in a horizontal plane, with boundaries oriented North-South and East-West, and generated in two vertical sections, one the East-West section and the other the North-South section. To evaluate the effects of geometry on flux, all of the generated fracture elements were assigned the same aperture value of 5 μ m, and in all simulations the hydraulic gradient was set at 0.8 (Δ head/ Δ length = 20m/25m). To determine flow rate as a function of direction, the generated fracture network plane was rotated in 15° increments relative to the flow boundaries, with total flux calculated for each increment.

The trace length and spacing statistics used in the models for the Government Point and Jalama Beach areas are presented in Table 4.1, and are from the preliminary analysis of the fracture data by Gale et al. (1991). It should be pointed out that in the process of analyzing the fracture data for this thesis the set numbers were redesignated for the Government Point and Jalama Beach data. The set designated number 1 in this thesis corresponds to the set 2

Table 4.1. Trace length and spacing statistics for each fracture set, used in 2-D simulation. Mean and Mean_u (and standard deviation) for uncorrected (raw) trace data, Mean_u(corrected) for data corrected for censoring and truncation. Est. Mean and Est. Std. deviation are the estimates of the statistics using Burys' equations.

Trace Length	Government Point		Jalama	Beach
	1	2	1	2
Set	1	2	1	2
No. of Observations	601	97	297	47
Minimum length (m)	0.12	0.14	0.30	0.47
Maximum length (m)	17.00	7.34	8.00	5.00
Mean (m)	1.64	0.67	1.80	2.26
Std. deviation (m)	1.67	0.64	1.19	1.29
Skewness	3.73	5.82	1.67	0.47
Mean _u	0.16	-0.73	0.39	0.62
Std. dev. _u	0.82	0.72	0.64	0.67
Mean _u (corrected)	0.82	-0.82	0.92	-1.19
Std. dev. _u	1.24	1.07	1.07	4.75
Est. Mean (m)	4.90	0.77	4.44	-
Est. Std dev. (m)	9.40	1.12	6.50	-
Spacing				
No. of Observations	355	38	297	28
Minimum value (m)	0.01	0.08	0.01	0.04
Maximum value (m)	2.98	2.08	3.19	2.56
Mean _u	-1.53	-0.93	-1.27	-0.72
Est. mean spacing(m)	0.34	0.70	0.45	0.89
Std. dev. _u	0.95	1.07	0.97	1.10
Est. std. dev. (m)	0.42	1.03	0.56	1.37

reported by Gale et al. (1991) and vice versa for the other set. The orientations were input as normally distributed data with meanstrike and dip of $N41^{\circ}/82^{\circ}SE$ for set 1 and $N130^{\circ}/77^{\circ}SW$ for set 2 at Government Point. For the Jalama Beach area, set 1 mean orientation was $N36^{\circ}/82^{\circ}SE$ and $N145^{\circ}/84^{\circ}NE$ for set 2.

The three diagrams in Figure 4.1 show the model geometry for the horizontal section and the two vertical sections for the Government Point area. Represented in these diagrams are the angles formed by the projection of the average plane of each fracture set, into the plane of each section, i.e. the trace of the strike line in the horizontal section and the trace of the apparent dip on each vertical plane. On each of the model geometries the trace of the average bedding plane is shown. Figure 4.2 shows the representative model geometries for the Jalama Beach area.

Figures 4.3 and 4.4 show the relative flow rates for the three orthogonal planes for each area, Government Point and Jalama Beach, respectively. Each open circle represents the flow rate calculated for each 15° increment. The inner oblong form is for uncorrected trace length data the larger outline for the trace data corrected for truncation and censoring. At the time of these model simulations, the large number of censored trace lengths for set 2 at Jalama Beach made it impossible to make the needed truncation and censoring corrections for this fracture set. Two more flux diagrams are shown in Figure 4.5 which show the effects on permeability when a third set is added to the network. This third set represents bedding plane shears with a single input value of 30 meters for trace length and a mean spacing of two meters. Figure 4.6 compares flow rates obtained from using the horizontal generated fracture plane at

Government Point, with fracture aperture held constant at $20\mu\text{m}$ for one series of simulations and, for the other series, the aperture was set proportional to length and distributed lognormally with a $5\mu\text{m}$ mean. More discussion of the 2-D results and comparison with the 3-D results are presented in Chapter 5.

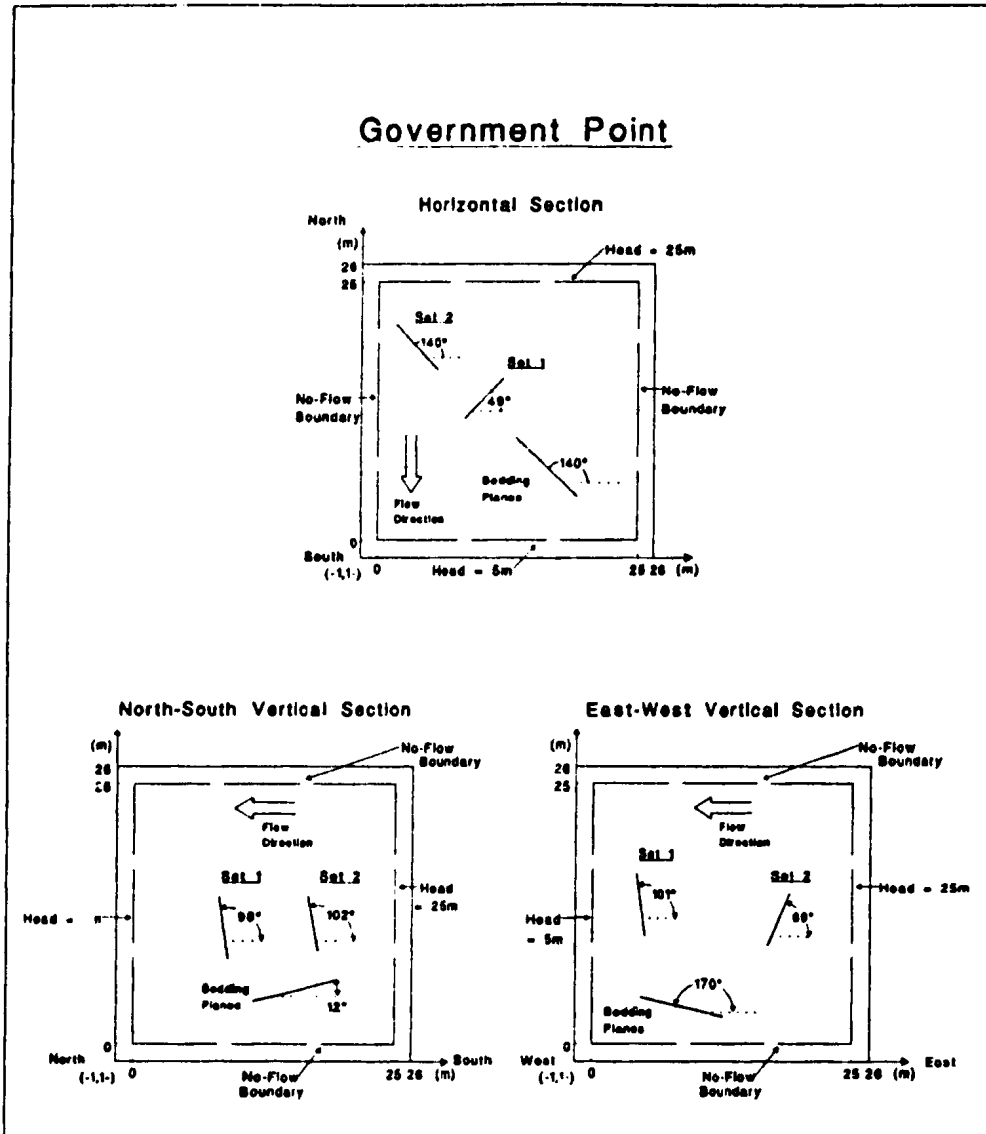


Figure 4.1. Diagrams showing input parameters for modeling fluid flow through generated fracture network from Government Point data, (a) horizontal plane, (b) N-S vertical section, (c) E-W vertical section.

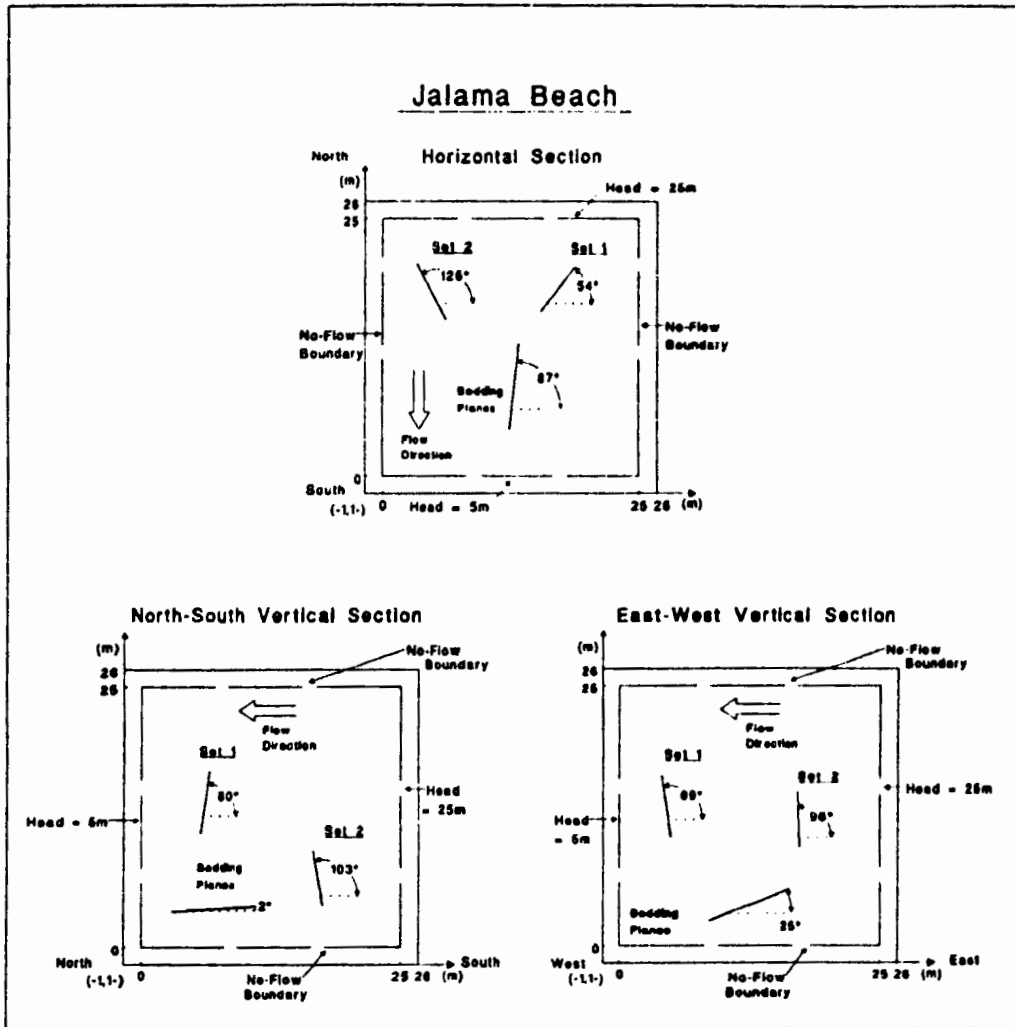


Figure 4.2. Diagrams showing input parameters for modeling fluid flow through generated fracture network from Jalama Beach data, (a) horizontal plane, (b) N-S vertical section, (c) E-W vertical section.

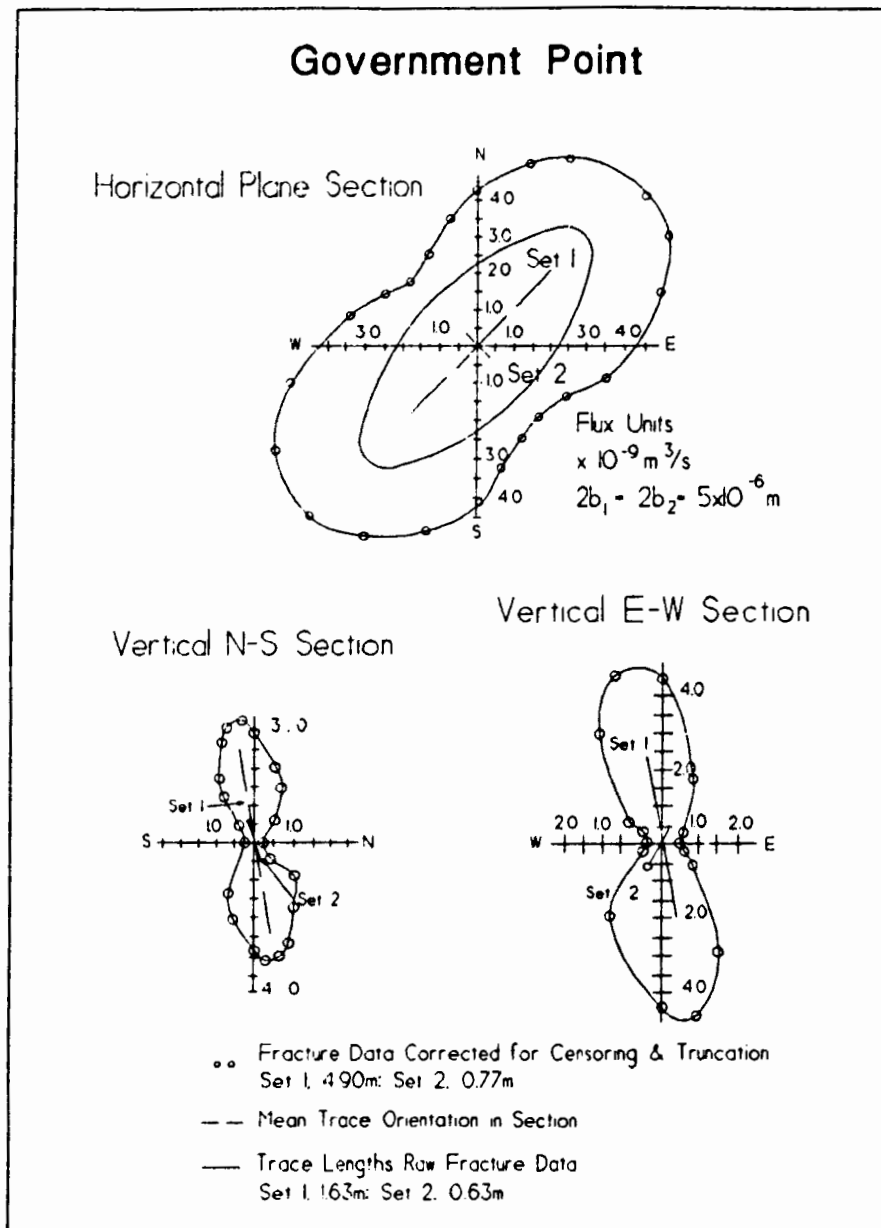
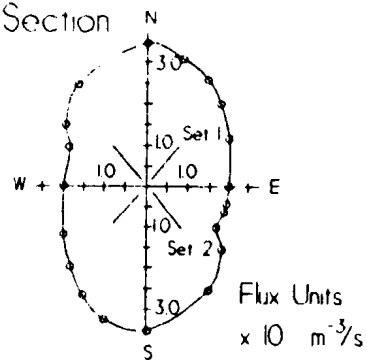


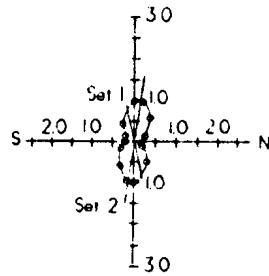
Figure 4.3. Diagrams of relative flux as a function of direction for uncorrected and corrected trace lengths from Government Point data, (a) horizontal plane, (b) N-S vertical section, (c) E-W vertical section.

Jalama Beach

Horizontal Plane Section



N-S Vertical Plane



E-W Vertical Plane

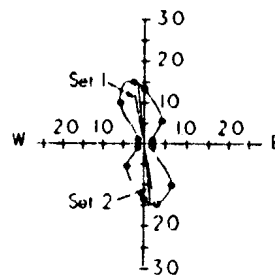


Figure 4.4. Diagrams of relative flux as a function of direction for uncorrected trace lengths from Jalama Beach data, (a) horizontal plane, (b) N-S vertical section, (c) E-W vertical section.

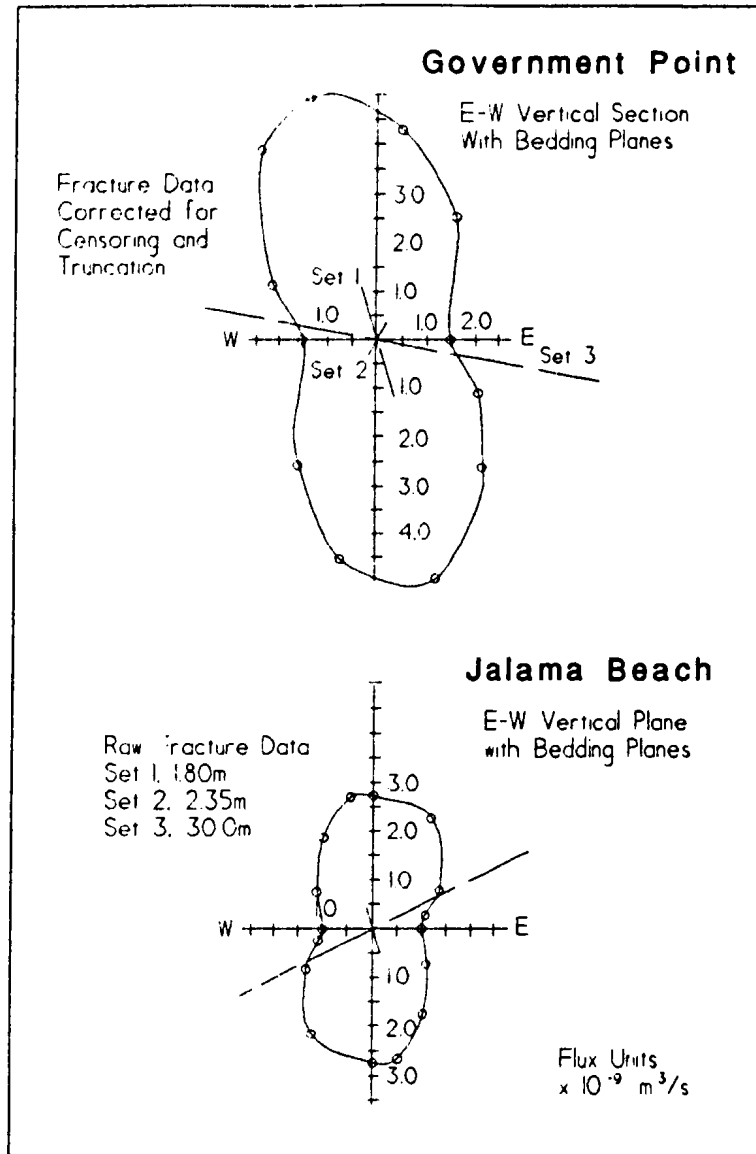


Figure 4.5. Relative flux as a function of direction in the E-W vertical section at (a) Government Point for the corrected fracture trace length data and, (b) Jalama Beach for the raw fracture trace length data. Both networks include the bedding plane shears as a third fracture set with a mean trace length of 30m.

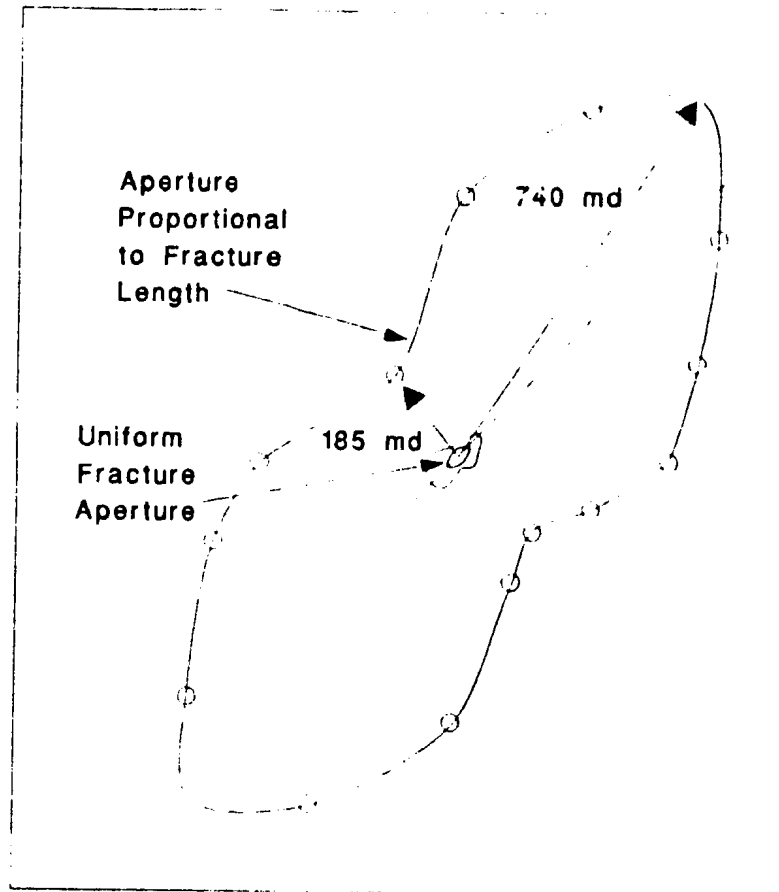


Figure 4.6. Relative flux as a function of direction in the horizontal plane at Government Point for the corrected fracture trace length data and variable aperture.

4.3 THREE DIMENSIONAL SIMULATION

4.3.1 Model Description

NAPSAC is a computer program developed to determine fluid flow and the transport of dissolved chemicals through a three dimensional stochastically generated discrete fracture network. The computer code was developed at the UK Atomic Energy Authority's Harwell Laboratory during the 1980's and site tested at the Stripa Mine in Sweden (Herbert et al., 1990). NAPSAC is similar to NETWRK/NETFLO in that both generate a fracture network based on probability distributions of the fracture parameters that are input by the user and solve for steady-state laminar flow of an incompressible viscous fluid through the generated fracture network with an impermeable matrix. However, the NAPSAC program, besides being a 3-D code, is larger and offers more flexibility in describing the distributions of the fracture geometry along with capabilities of calculating the basic transport properties and an extensive range of options for output of the results.

The network generation stage produces rectangular planar fractures in a cuboid region that has dimensions assigned by the user. The centers for the "fracture" planes are randomly placed within the cuboid following the uniform distribution and the densities (number of centers/cubic meter) for each fracture set. The planes are created around these centers according to the mean and spread of the input probability distributions. The geometric parameters needed, are the half-lengths of the fracture, effective aperture, and three angles that describe the orientation of the fracture. These three angles are designated as orientation

angle, dip angle and dip direction. The orientation angle corresponds to the degrees the fracture is allowed to rotate within its own plane. Dip angle and dip direction are self-explanatory. The probability distributions that are available for these variables are the uniform, normal, lognormal, and two-parameter exponential. Six sets of randomly placed fractures can be used along with up to 20 "known" fractures whose geometric properties are explicitly set by the user. The solution region within the cuboid can be the union of irregularly shaped hexahedra and should be smaller than the outer domain to avoid the edge effect of reduced density of fractures near the outer boundaries. By default each face of the solution domain is considered impermeable, so the user must designate the non-hydrostatic component of the pressure to the desired permeable boundaries. The pressure distribution can be set to a uniform value on the surface, specified at a particular point on the surface along with a linear pressure gradient, or by specifying several points of assigned pressure in a lattice layout and interpolating between points.

To solve for steady-state laminar flow, each "fracture" in the generated network is divided into a number of triangular elements with four elements grouped together to form rectangles, and solved using a finite element method. Fluid flux along any fracture plane is assumed to follow the fracture flow law and mass conservation equations.

4.3.2 Input and Results

The statistics, derived in Chapter 3 for the fracture sets deemed representative at each of the four small-scale sites and the two large-scale sites, were used to assess the impact of fracture

orientation and aperture on the directional permeability. This assessment, using the 3-D modeling program NAPSAC on a SUN SPARC2 workstation, was completed in several steps. The first step was to determine the largest model block size that could be run on the SPARC2 for each individual site and how permeability changed with the increase in block size. The next step compared model length and spacing output to the input statistics and evaluated the effect of using the fracture length statistics derived from using the approach presented by Herbert and Splawski (1990) as compared to using the trace length statistics. After choosing the model input statistics and model size for each site, simulations were run to determine permeability, in the bedding dip direction (parallel to the x-axis in the model), parallel to bedding strike (along the y-axis), and vertically (along the z-axis). Three series of simulations were made, one with constant orientation/constant aperture, the second with variable orientation/constant aperture, and the third with variable orientation/variable aperture. The fourth step was to assess if the permeability of the chosen model block size could be described by a permeability tensor and thus approximate an equivalent porous medium. The directional permeability was determined every 22.5°, from 0° to 157.5°, by rotating the two flow boundaries relative to the fracture network with the other four faces being impermeable. The last step was to check the variability in the permeability in the x and z directions for selected sites, by running over 30 realizations for each model with different random seed numbers.

For the first step, two models were made for each of the four small-scale sites; titled GP for the Government Point data, JB14 for the Jalama Beach sites 1 through 4, JB56 for the Jalama Beach sites 5 and 6, and LL for the Lompoc Landing data, with suffix "A" designating use of the fracture length statistics, and "B" for the trace length statistics. Models in all realizations

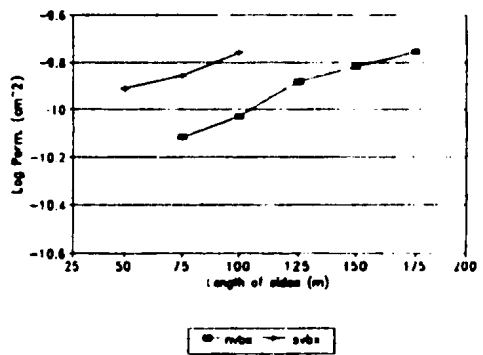
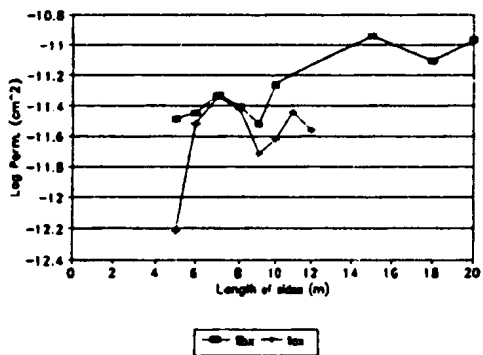
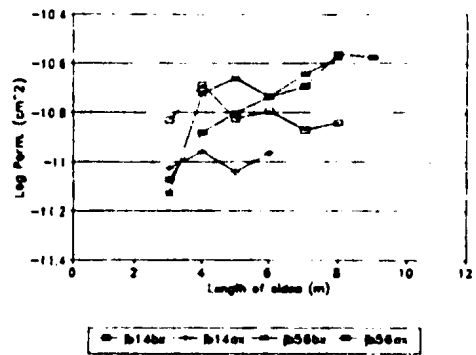
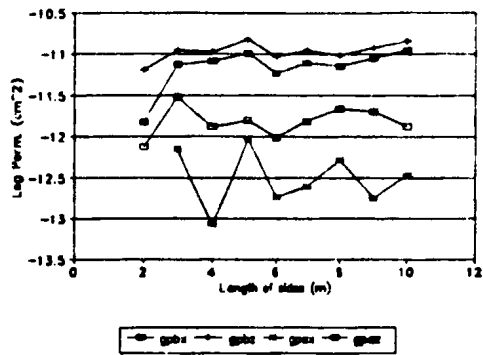


Figure 4.7. Graphs showing the relationship of permeability to block size. gp - Government Point; jb14 - Jalama Beach sites 1-4; jb56 - Jalama Beach sites 5&6; ll - Lompoc Landing; nv - North Vandenberg; sv - South Vandenberg. b is for "B" model input, a for "A" model input, x and z indicate direction of gradient.

were cubes, starting at 2 meters per side for the solution region for most of the small-scale sites, and 50 meters per side for the large-scale models (SV and NV). Side length for the generation region was approximately 20 to 25% longer than the solution region sides. The X-Y graphs shown in Figure 4.7 show the relationship of permeability to block size. For the JB models, stable percolation started with the 3 meter block, at 5 meters for the LL model, and 75 meters for the NV model. Stable percolation would be dependent on an adequate number of intersecting fractures that connect the two flow boundaries, and is also a function of fracture orientation, length and density. The maximum block size for each model that would successfully execute on the SUN SPARC2 with 32 megabytes of memory and 1 gigabyte of disk storage, was controlled by the number of intersections, and it was found that the maximum limit for intersections was in the 6500 to 7000 range. Several realizations were completed successfully with over 8000 intersections but took over 13 hours to complete. Each point on the graphs (Figure 4.7) represents one realization, with variable orientation and constant aperture equal to $20\mu\text{m}$. For most of the models, using the trace length statistics, there is a steady but relatively small increase in permeability with increase in block size. The permeabilities for the models using the fracture length statistics ("A" models) are more variable and consistently lower than the "B" model permeabilities. This is probably a result of the shorter fracture plane dimensions that are generated from the input fracture length statistics, because "A" model realizations had 10 to 100% more fracture planes, but a similar degree of interconnection as a "B" model of comparable size. The block size in these realizations was increased until the limits of the SUN SPARC2 were reached, with more realizations needed at each block size to determine the "true" relationship between block size and permeability. The size of the solution region chosen for each "B" model is listed in

Table 4.2, along with the probabilities of a generated fracture exceeding a certain length for each set. An attempt was made to balance the largest possible block size for each model with a reasonable execution time. For most of the "B" models the block dimensions were close to two times the average trace lengths and more than ten times the average spacing, with exceptions for the JB14-B and LL-B models. Due to this limitation in block size, it was of interest to see what the probability would be of a generated plane exceeding a particular length or, in other words, how many planes could be expected to be connected to both flow boundaries. These probabilities give an indication of whether the permeability was due to the number of long fractures or to the interconnection of the fracture network. Table 4.2 shows that for most of the tested model block sizes, there was less than a 10% probability that a fracture could connect to both flow boundaries. The probabilities were slightly higher for set 2 at Government Point (GP,2v and GP,2h), and between 10 and 20% probability for set 1 at Jalama Beach sites 1-4 (JB14,1), all sets at Jalama Beach sites 5 and 6, and set 2 at Lompoc Landing.

It was also of interest to evaluate the impact on directional permeability of the estimated fracture lengths from the trace length statistics, using the formulas presented by Herbert and Splawski (1990, see section 3.4). There was a concern that the dramatic reduction in estimated mean fracture length from the mean trace length for most of the sets, would not adequately represent the observed field data and relationships. This reduction in length is probably due, to the assumption that the fractures are square in shape and free to rotate within their own plane, and that there is a fairly large standard deviation to the trace length distributions. From observations, the extensional fractures usually have a shorter vertical

Table 4.2. Probabilities of a generated fracture exceeding a certain length for a given mean and standard deviation (S.D.) from the lognormal distribution. Numbers are average from 10 Monte Carlo simulations of 1000 generated lengths per simulation.

Set	Lognorm. Distr.		Prob. frac. > length.(m)			Model size (m)		
	Mean	S.D.	50%	20%	10%	X	Y	Z
GP,1v	0.34	0.59	1.40	2.25	2.90	10	10	6
GP,1h	-0.65	0.50	0.50	0.80	1.00			
GP,2v	0.68	0.74	2.00	3.70	5.00			
GP,2h	1.00	1.33	2.70	8.30	14.90			
JB14,1	1.16	1.38	3.20	10.20	18.70	8	8	8
JB14,2	0.74	1.03	2.10	5.00	7.90			
JB56,1	1.18	0.92	3.25	4.10	10.60	8	8	8
JB56,2	1.13	1.07	3.10	7.60	12.20			
JB56,3	0.89	1.01	2.40	5.70	8.90			
LL,1	0.85	1.04	2.40	5.60	8.80	18	18	18
LL,2	1.62	1.48	5.00	17.50	33.50			
NV,1	3.11	1.18	22.00	60.00	100.00	150	150	150
NV,2	2.91	1.23	18.00	52.00	88.00			
NV,3	4.21	0.56	67.00	108.00	138.00			
SV,1	2.38	0.85	11.00	22.00	32.00	100	100	100
SV,2	2.59	0.81	13.00	26.00	38.00			
SV,3	2.43	0.96	11.00	25.00	39.00			

Table 4.3. Comparison of corrected trace length and spacing means, from realizations, with the input statistics for the GP A and B models.

Model	Set	Input (m)	Corrected Output (m)	% Difference
GP A trace	1h	0.43	0.52	22
	1v	1.05	1.22	16
	2h	0.23	0.29	27
	2v	1.05	1.31	25
	spacing	1	0.59	0.55
	2	0.34	0.38	11
GP B trace	1h	0.59	0.69	17
	1v	1.65	1.83	11
	2h	6.59	7.78	18
	2v	2.58	2.99	16
	spacing	1	0.59	0.60
	2	0.34	0.35	2

extent than horizontal extent and the cross fractures which usually terminate against the extensional set have longer vertical length than horizontal length, thus neither would be square. Due to the large trace length standard deviation, which is used in the formulas to estimate the fracture length, the above field observations are not maintained in the fracture length statistics (see Table 3.10).

Checking the consistency of the generated fracture length and spacing was done by simulating planes, called mapping planes, through the solution region and "running" scanlines across these mapping planes. The NAPSAC program determines for each generated fracture that crosses the scanline; trace length, distance from start of the scanline, and angle between the fracture and the scanline. Comparison of the output means and the input statistics are shown in Table 4.3 for the GP-A and GP-B models, based on three realizations and three orthogonal planes through each realization. Between 400 and 700 generated fractures were sampled for each fracture set. It can be seen in the table that the sampled trace length output for each model is consistently slightly longer than the input values, but the mean spacing for each set compared very well. The difference in mean trace length is due to the bias introduced by sampling longer traces and the deletion by NAPSAC of unconnected fractures, which are probably the shortest generated lengths.

Table 4.4 presents the input statistics for the models chosen to evaluate the directional permeability. Density is the number of fracture centers per cubic meter and is determined by the inverse of the product of mean spacing and mean area for each set. In NAPSAC, lengths are entered as half lengths and for all sets are lognormally distributed. For these sets, dip

Table 4.4. Input statistics for the models chosen to evaluate directional permeability. See text for discussion.

Model		GP A		GP B	
Set		1	2	1	2
Density	(cntrs/m ³)	2.97	4.11	1.741	0.173
Lengths	mean(ln,m)	-1.62,-0.77	-3.02,-0.88	-1.34,-0.35	0.31,-0.01
	s.d.(ln,m)	0.43, 0.50	1.31, 0.69	0.50, 0.56	1.33, 0.74
Dip dir.	mean(m)	88	179	88	179
	s.d.(m)	15.8	15.4	15.8	15.4
Dip	mean(m)	82	87	82	87
	s.d.(m)	15.3	9.4	15.3	9.4

Model		JB14 B		JB56 B			LL B	
Set		1	2	1	2	3	1	2
Density	(cntrs/m ³)	0.029	0.292	0.02	0.075	0.202	0.086	0.005
Lengths	mean(ln,m)	0.47	0.05	0.49	0.44	0.20	0.16	0.93
	s.d.(ln,m)	1.38	1.03	0.92	1.07	1.01	1.04	1.48
Dip dir.	mean(m)	264	334	276	157	218	216	162
	s.d.(m)	12.8	24.8	7.1	12.1	11.5	13.6	14.9
Dip	mean(m)	81	89	83	90	88	89	86
	s.d.(m)	13.7	18.0	5.8	7.7	8.2	6.6	5.8

Model		NV B			SV B		
Set		1	2	3	1	2	3
Density	(cntrs/m ³)	2.35E-5	8.47E-5	7.83E-6	1.92E-4	1.94E-4	1.37E-4
Lengths	mean(ln,m)	2.42	2.22	3.52	1.69	1.90	1.74
	s.d.(ln,m)	1.18	1.23	0.56	0.85	0.81	0.96
Dip dir.	mean(m)	232	4	95	255	4	108
	s.d.(m)	13.95	13.83	0.0	17.24	14.84	34.87
Dip	mean(m)	87	87	59	75	87	4
	s.d.(m)	9.18	15.45	0.0	9.81	12.34	7.90

direction (Dip dir.) is the azimuth of the fracture's dip after rotation (see section 3.3) and dip is the vertical angle in degrees. The third orientation angle, discussed earlier, for all models in this study was set at 0 degrees, thus the fractures were not allowed to rotate within their own plane. The NAPSAC program makes the simplifying assumption that dip direction and dip are independent, and thus can follow separate distributions. Although, in section 3.3 and Appendix C the fracture orientation was determined as a two dimensional distribution, the difference to the fracture network and the flow field should not be significant (Herbert et al., 1991). Along with the parameters listed in Table 4.4, aperture is entered for each set. There are no quantitative aperture data available from the field surveys, so a mean aperture equal to $20\mu\text{m}$ was used for the small-scale fractures and $100\mu\text{m}$ for the large-scale fractures. When the apertures were allowed to vary, they followed the lognormal distribution, with standard deviations of $15\mu\text{m}$ and $75\mu\text{m}$ for the small-scale and large-scale fractures, respectively.

The first sequence of tests to evaluate the effect of orientations and aperture on the permeability were run with the trace length statistics (the "B" models) for all the models. Permeability was determined from unit gradients along the x-axis, then the y-axis, and then the z-axis, with the appropriate opposite faces open to flow and all others impermeable. For the first series of realizations, aperture and orientation were held constant, and length was allowed to vary according to a lognormal distribution. Thus this first series could be considered a lower limiting case in respect to the number of intersections the geometry could produce. The second series of realizations held aperture constant, while orientation and length varied. In the third series, all parameters were allowed to vary according to their respective probability distributions. A summary of the output from these realizations is given

Table 4.5. Summary of output from realizations used in evaluating the effect of fracture orientation and aperture on permeability. Models used trace length statistics. The xx, yy, zz, signify gradient in respective direction, with all other faces impermeable. Percent change explained in the text.

Model	Dimension	constant orientation			variable orientation			variable orientation			percent change		
		constant aperture			constant aperture			variable aperture			1&2	2&3	1&3
		Q(m ³ /s)	k(cm ²)	k(md)	Q(m ³ /s)	k(cm ²)	k(md)	Q(m ³ /s)	k(cm ²)	k(md)			
gp _{xx}	10x10x6m	5.67E-11	9.44E-12	0.95	5.99E-11	9.99E-12	1.01	3.27E-10	5.45E-11	5.51	6	446	477
gp _{yy}	10x10x6m	1.64E-12	2.73E-13	0.03	1.28E-11	2.13E-12	0.22	1.75E-11	2.91E-12	0.29	680	37	967
gp _{zz}	10x10x6m	2.11E-10	1.26E-11	1.27	1.38E-10	1.38E-11	1.39	3.29E-10	3.29E-11	3.32	9	139	161
jb14 _{xx}	8x8x8m	9.09E-11	1.42E-11	1.43	1.29E-10	2.01E-11	2.03	5.68E-10	8.88E-11	8.96	42	341	525
jb14 _{yy}	8x8x8m	7.22E-11	1.13E-11	1.14	1.20E-10	1.87E-11	1.89	7.99E-10	1.25E-10	12.61	66	568	1006
jb14 _{zz}	8x8x8m	2.10E-10	3.29E-11	3.32	2.26E-10	3.53E-11	3.57	1.07E-09	1.67E-10	16.89	8	373	409
jb56 _{xx}	8x8x8m	1.12E-10	1.75E-11	1.77	1.73E-10	2.7E-11	2.72	3.56E-10	5.56E-11	5.62	54	106	218
jb56 _{yy}	8x8x8m	7.13E-11	1.11E-11	1.13	8.51E-11	1.33E-11	1.34	1.72E-10	2.69E-11	2.71	19	102	141
jb56 _{zz}	8x8x8m	2.28E-10	3.56E-11	3.59	2.77E-10	4.33E-11	4.37	7.13E-10	1.11E-10	11.25	22	157	213
ll _{xx}	18x18x18m	2.32E-10	7.16E-12	0.72	2.25E-10	6.95E-12	0.70	5.89E-10	1.82E-11	1.83	-3	161	154
ll _{yy}	18x18x18m	7.45E-11	2.3E-12	0.23	9.50E-11	2.93E-12	0.30	5.94E-10	1.83E-11	1.85	27	525	697
ll _{zz}	18x18x18m	4.84E-10	1.49E-11	1.51	4.34E-10	1.34E-11	1.35	9.20E-10	2.84E-11	2.87	-10	112	90
nv _{xx}	150x150x150m	3.63E-07	1.61E-10	16.28	3.41E-07	1.52E-10	15.32	1.36E-06	6.04E-10	61.05	-6	299	275
nv _{yy}	150x150x150m	1.25E-07	5.57E-11	5.62	1.39E-07	6.16E-11	6.22	3.89E-07	1.73E-10	17.46	11	181	211
nv _{zz}	150x150x150m	4.64E-07	2.06E-10	20.82	4.52E-07	2.01E-10	20.27	1.22E-06	5.42E-10	54.76	-3	170	163
sv _{xx}	100x100x100m	1.78E-07	1.78E-10	18.02	1.74E-07	1.74E-10	17.57	4.73E-07	4.73E-10	47.77	-2	172	165
sv _{yy}	100x100x100m	1.06E-07	1.06E-10	10.69	1.12E-07	1.12E-10	11.28	4.32E-07	4.32E-10	43.63	5	287	308
sv _{zz}	100x100x100m	2.48E-07	2.48E-10	25.09	2.61E-07	2.61E-10	26.32	9.77E-07	9.77E-10	98.68	5	275	293

in Table 4.5 with the calculated flux in m^3/s and permeability in both cm^2 and millidarcies. The last three columns in the table compare the difference in permeabilities between each of the orientation/aperture setups. For each progressive realization the calculated permeability in the tested directions gets larger, except for a few very small negative changes, for the Lompoc Landing (llxx, llzz) data and the large-scale data (nvxx, nvzz, svxx). The variable orientation/constant aperture simulations produced 160 to 200% more intersections than the constant orientation/constant aperture simulations. The corresponding change in permeabilities was variable, but most model permeabilities increased by less than 70%. This seems to indicate that the fracture geometries, with no variability to fracture orientation, produce a fairly well connected network at the modeled scales. The largest percentage increase in permeability occurred in the "yy" models where the gradient and flow are parallel to the y-axis. For most of the models the fracture set with shorter trace lengths strikes sub-parallel with the y-direction, thus the permeability in the y-direction benefits from the increased interconnections due to the variability of fracture orientations.

The number of intersections and the generated fracture geometry is the same for the second and third orientation/aperture setups, thus the increase in permeability is due to the variability in aperture between members of the same set. Allowing the aperture to vary lognormally with a standard deviation approximately 0.75 times the mean, had a dramatic effect on the permeabilities in the three directions tested. For several of the variable orientation/variable aperture realizations, the generated aperture data were extracted. All showed a lognormal distribution and for the small-scale data the apertures ranged between $4\mu m$ and $154\mu m$ with means and standard deviations approximately $23\mu m$ and $16\mu m$, respectively. For the large-

scale realizations, all the means were approximately $118\mu\text{m}$ and standard deviations of around $74\mu\text{m}$ to $77\mu\text{m}$, with minimums around $15\mu\text{m}$ and maximums near $600\mu\text{m}$, but for all the realizations 90% of the apertures were less than $220\mu\text{m}$. As stated earlier there are no quantitative aperture field data, but the generated values seem reasonable.

In determining if permeability of these models can be approximated by a tensor, the standard test procedure of rotating the flow boundaries in relation to the network, was followed. A unit gradient was applied in all realizations, which were rotated 22.5° from 0° to 157.5° , with only the two opposite faces, perpendicular to the gradient direction being permeable. Since the permeability should be the same for flows 180° apart (Scheidegger, 1954), the 8 directions should be adequate. As a check, several extra realizations with gradients 180° from another realization were produced, and in all cases the permeabilities were found to be equal. For the realizations with variable orientation/constant aperture and a unit gradient, the calculated permeabilities (in millidarcies) for each 22.5° increment is plotted on the left, for each model, in Figures 4.8 through 4.14. The plot on the right is one over the square root of permeability ($1/k^M$), and should approximate an ellipse if the permeability can be characterized by a tensor (Scheidegger, 1954; Long et al., 1982). The top pair of plots is the horizontal section, where bedding strike is in the y-direction. The other two pairs represent the two vertical sections, one parallel to the zy plane, the other the zx plane, and vertically up is toward the top of the plots. Most of the permeability plots for the horizontal sections show the characteristic shape of a modified figure 8 with the major principal permeability axis, which is approximately (within 25°) in the direction of bedding dip and follows the strike of the predominant extensional set. The major exception is for the JB14-B (Figure 4.10) model

where the major permeability is 40° from the bedding dip direction and parallels the shorter but more numerous fracture set. At Lompoc Landing (LL-B, Figure 4.12) the major permeability is also in the general direction of the shorter but more numerous generated fracture set. For these two sites (JB14-B, LL-B), the generated dominant set does not conform to the observed dominant set. This is due to the fact that density is inversely proportional to the size of the fracture in these models, it is also a reflection on the scanline mapping technique and its bias towards longer fractures. As pointed out earlier, when the generated fracture network is sampled using a scanline technique, the calculated spacings for each set match the input spacings used in calculating the input density. For the vertical sections, the plots of permeability are elongated ellipses to ovals in shape, showing a slightly less anisotropy to flow than in the horizontal sections. In general, the zy plane shows a greater anisotropy to flow than the zx plane, mainly because the zy plane is sub-parallel to the shorter fracture set. Figure 4.9 show the plots of the permeabilities from the realizations for the GP-A model using the fracture length statistics (Table 4.4). These plots show more variability in directional permeability and are strikingly different from the GP-B (Figure 4.8) model plots using the trace length statistics. The only difference in the input between the "A" and "B" models is the reduced fracture lengths for the GP-A model, which also increases the densities for each set. Realizations for the GP-A model have more than 2.5 times the number of planes than the realizations for the GP-B model, but about an equal number of intersections (> 5000). The shorter, and more numerous fractures in the GP-A models allow the variability in the orientations to become more of a factor in the directional permeabilities. Figures 4.15 and 4.16 are the permeability and $1/k^h$ plots for the GP-B and SV-B models, respectively, generated with variable orientation and variable aperture, for the same block

sizes as the other orientation/aperture model setups. The variable aperture dramatically increases the permeability and the anisotropy for both models. Allowing the aperture to vary within each set also adds more variability to the directional permeabilities than is seen in the constant aperture case, and thus the $1/k^h$ plots show a more irregular elliptical shape than those shown in Figures 4.8 and 4.14.

For all the B models, simulated with variable orientation and constant aperture, except the LL-B plots, the $1/k^h$ plots show a good approximation to an ellipse. To calculate the principal directions and magnitude of the ellipse, in the 2-D planes, the equations presented by Scheidegger (1954) were used. Since permeability was determined in 22.5 degree increments(α) it is possible to solve for the components of the inverse permeability tensor(κ) using the following equations;

$$\kappa_{11} = \left(\frac{3}{8}\right) \Sigma \frac{1}{k_i} \cos^2 \alpha_i - \left(\frac{1}{8}\right) \Sigma \frac{1}{k_i} \sin^2 \alpha_i ,$$

$$\kappa_{22} = \left(\frac{3}{8}\right) \Sigma \frac{1}{k_i} \sin^2 \alpha_i - \left(\frac{1}{8}\right) \Sigma \frac{1}{k_i} \cos^2 \alpha_i ,$$

$$\kappa_{12} = \left(\frac{1}{2}\right) \Sigma \frac{1}{k_i} \cos \alpha_i \sin \alpha_i .$$

The position of the principal axes can be calculated from,

$$\tan\phi = [\kappa_{22} - \kappa_{11} \pm ((\kappa_{11} - \kappa_{22})^2 + 4\kappa_{12}^2)^{\frac{1}{2}}] / (2\kappa_{12})$$

where ϕ is the angle of the principal axis. Once the components of the matrix are found, the eigenvalues were calculated to obtain the magnitudes of the principal axes. Scheidegger (1954) gave a simple formula for this calculation;

$$\lambda = \left(\frac{1}{2}\right) \left[\kappa_{11} + \kappa_{22} \pm ((\kappa_{11} - \kappa_{22})^2 + 4\kappa_{12}^2)^{\frac{1}{2}}\right].$$

The eigenvalues obtained from the above equation are in md^{-1} , which are converted to millidarcies (for cm^2 , $\text{cm}^2 = 9.87 \times 10^{-12}(\text{md})$) and listed in Table 4.6. The values for the principal permeabilities can be compared to the plots in Figures 4.8 through 4.16. The match between the measured (from the realizations) and the calculated values is good for the bulk of the plots. Some expected exceptions are the GP-A (Figure 4.9) model plots, the LL-B (Figure 4.12) horizontal section, the GP-Bv (v for variable aperture) horizontal section plot and the SV-Bv model plots. These plots show a greater variability in the directional permeabilities, and for the variable aperture models there is a strong anisotropy. From this inspection of the directional permeabilities for these models, it seems that these fracture networks could be considered an anisotropic porous medium at the scale of the models. As these permeability plots are based on one realization for each direction and as an anisotropic porous medium equivalent for a fracture network is probably dependent on the size and shape of the tested model block, more realizations for different shapes are needed to describe quantitatively the directional permeability. However, based on this series of realizations, only a slight change in the principal permeability direction would be expected with a possibly greater adjustment to the magnitude.

To determine the spread in permeability values due to the variability in the input statistics, over 30 realizations were made for the GP-B and the SV-B models with constant and variable aperture, for unit gradients in the x (parallel to bedding dip) and z (vertical) directions. The statistics from the realizations are summarized in Table 4.7. Flows and thus the permeabilities from these realizations follow the normal distribution with relatively small standard deviations. Considering the variabilities in the input parameters, especially fracture orientations and trace lengths, the range in permeabilities from these models is quite narrow.

Table 4.6. Position and magnitude (in millidarcies) of principal axes calculated using equations from Scheidegger (1954). Angles are in degrees from the positive y-axis with (-) counterclockwise. Horz. is the horizontal plane, zy and zx are the vertical planes.

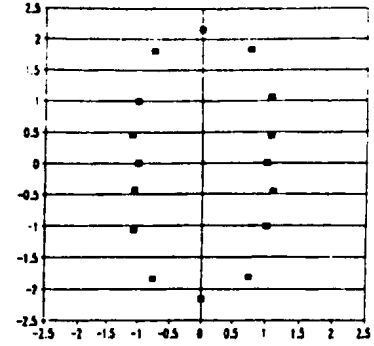
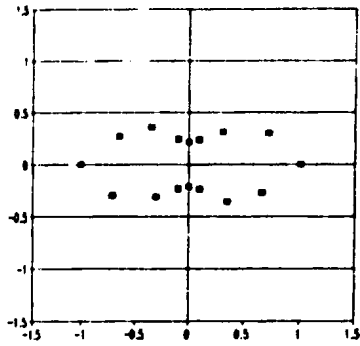
		Principal axes				Principal axes	
		Position	Magnitude			Position	Magnitude
Model	Plane	angle	perm.(md)	Model	Plane	angle	perm.(md)
GPB	horz.	89, -1	1.38,0.23	GPBv	horz.	82, -8	9.30,0.34
	zy	5,-85	1.52,0.61		zy	-1, 89	3.39,1.05
	zx	-13, 77	1.41,0.67		zx	-17, 73	4.75,0.91
GPA	horz.	66,-24	0.67,0.01	NVB	horz.	-77, 13	17.3, 6.9
	zy	65,-25	0.14,0.08		zy	-2, 88	19.5, 7.4
	zx	-33, 57	0.13,0.10		zx	18,-72	20.8,15.4
JB14B	horz.	50,-40	3.26,1.24	SVB	horz.	-67, 23	20.4,10.4
	zy	-3, 87	4.64,1.12		zy	-1, 89	28.1,12.2
	zx	-7, 83	3.51,2.19		zx	-16, 74	26.9,14.2
JB56B	horz.	-69, 21	3.26,1.25	SVBv	horz.	-62, 28	58.4,41.3
	zy	8,-82	4.41,1.63		zy	-1, 89	230,16.8
	zx	-3, 87	4.61,2.72		zx	-27, 63	110,49.7
LLB	horz.	-69, 21	2.00,0.29				
	zy	0, 90	2.04,0.39				
	zx	-12, 78	1.42,1.03				

Table 4.7. Statistical summary of realizations used to determine variability in the magnitude of permeability in the x and z directions for Government Point and South Vandenberg B models. Plns = number of generated planes, Ints = number of intersections, Q = flux, k = permeability, Cnst ap = constant aperture model, and Var ap = variable aperture model.

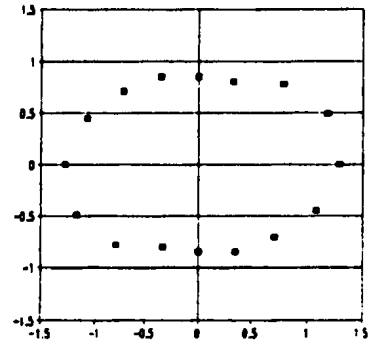
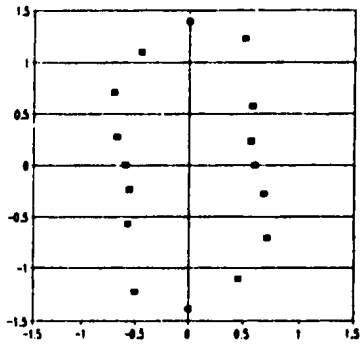
Rlz.		Plns	Ints	Cnst ap			Var ap		
				Q(m ³ /s)	k(cm ²)	k(md)	Q(m ³ /s)	k(cm ²)	k(md)
GPBx N=32	avg	1647	5049	5.79E-11	9.65E-12	1.0	1.81E-10	3.02E-11	3.1
	std	32	389	1.10E-11	1.83E-12	0.2	1.14E-10	1.90E-11	1.9
	min	1597	4385	4.07E-11	6.78E-12	0.7	7.26E-11	1.21E-11	1.2
	max	1712	5973	7.99E-11	1.33E-11	1.3	6.79E-10	1.13E-10	11.4
GPBz N=31	avg	1647	5061	1.27E-10	1.27E-11	1.3	2.39E-10	2.39E-11	2.4
	std	26	357	1.70E-11	1.70E-12	0.2	7.01E-11	7.01E-12	0.7
	min	1580	4385	9.35E-11	9.35E-12	0.9	1.58E-10	1.58E-11	1.6
	max	1699	5973	1.71E-10	1.71E-11	1.7	4.22E-10	4.22E-11	4.3
SVBx N=30	avg	671	4007	1.98E-07	1.98E-10	20.0	5.61E-07	5.61E-10	56.7
	std	15	410	2.52E-08	2.52E-11	2.5	1.51E-07	1.51E-10	15.3
	min	653	3225	1.41E-07	1.41E-10	14.2	3.22E-07	3.22E-10	32.5
	max	716	4693	2.50E-07	2.50E-10	25.3	8.40E-07	8.40E-10	84.8
SVBz N=30	avg	664	3878	2.67E-07	2.67E-10	27.0	9.01E-07	9.01E-10	91.0
	std	9	421	3.64E-08	3.64E-11	3.7	2.19E-07	2.19E-10	22.2
	min	653	3225	2.01E-07	2.01E-10	20.3	4.67E-07	4.67E-10	47.1
	max	683	4693	3.35E-07	3.35E-10	33.8	1.50E-06	1.50E-09	151.5

GP B Model

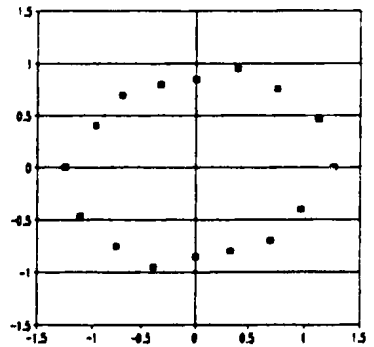
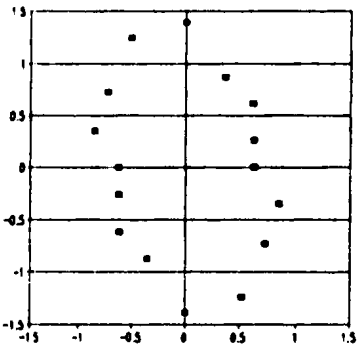
Horizontal Plane



Vertical ZY Plane



Vertical ZX Plane



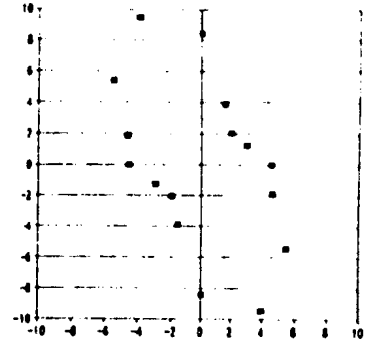
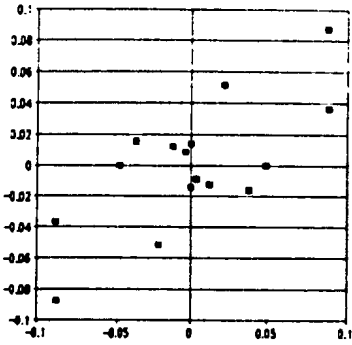
k (md)

$1/k^h$

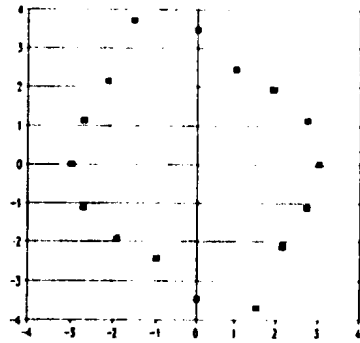
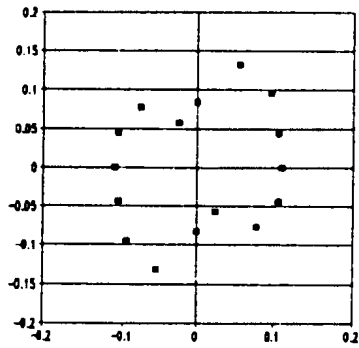
Figure 4.8. Directional permeability and $1/k^h$ plots for Government Point B model. Horizontal and vertical scales are in same units.

GP A Model

Horizontal Plane



Vertical ZY Plane



Vertical ZX Plane

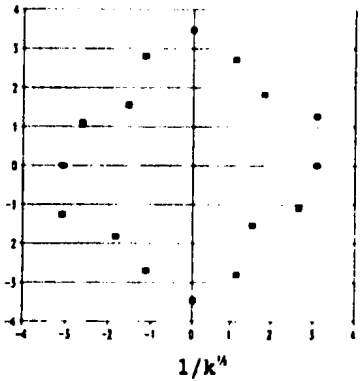
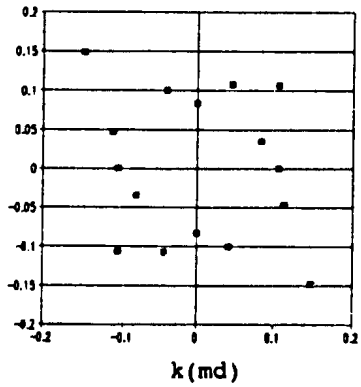
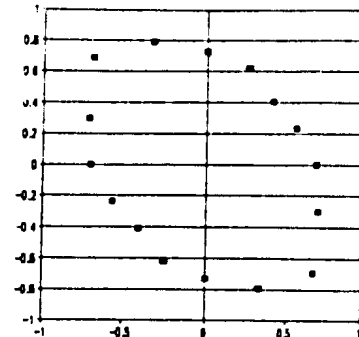
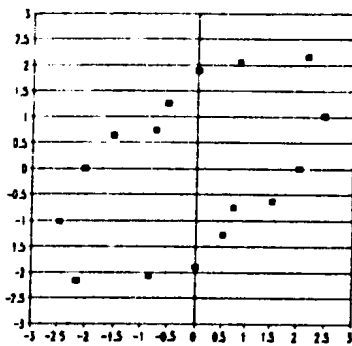


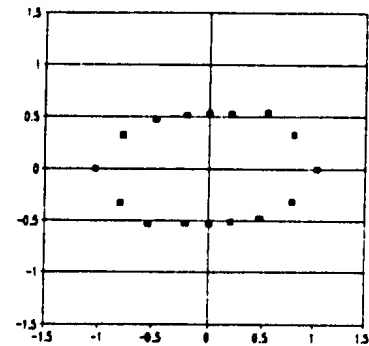
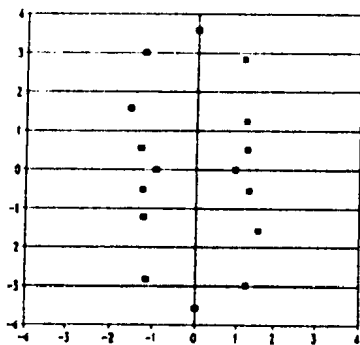
Figure 4.9. Directional permeability and $1/k^2$ plots for Government Point A model. Horizontal and vertical scales are in same units.

JB14 B Model

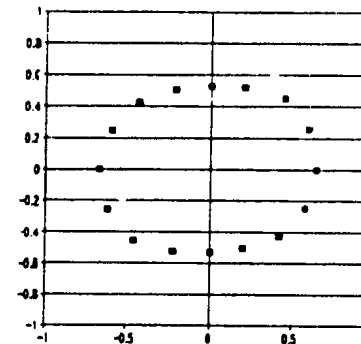
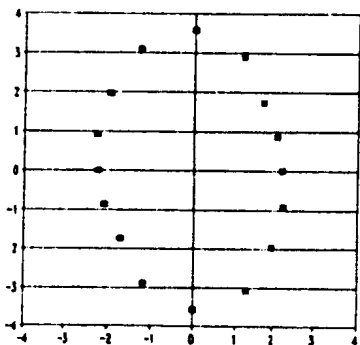
Horizontal
Plane



Vertical
ZY Plane



Vertical
ZX Plane



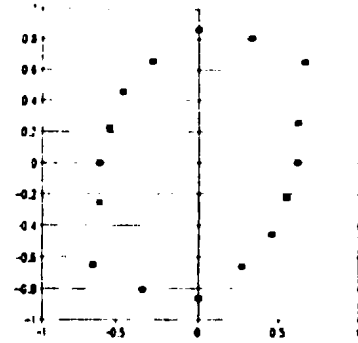
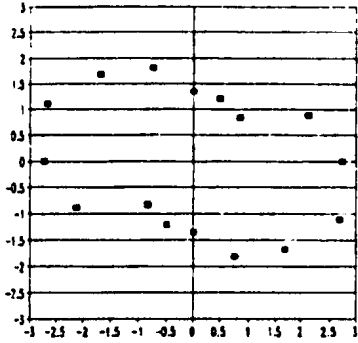
k (md)

1/k^k

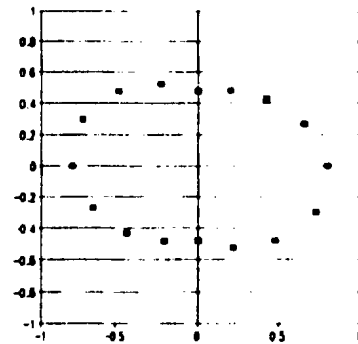
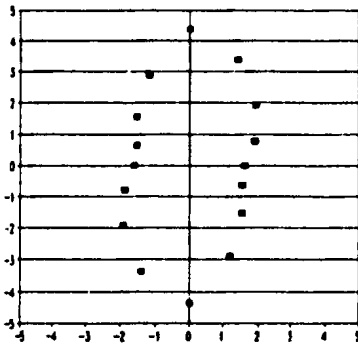
Figure 4.10. Directional permeability and 1/k^k plots for Jalama Beach sites 1-4 B model. Horizontal and vertical scales are in same units.

JB56 B Model

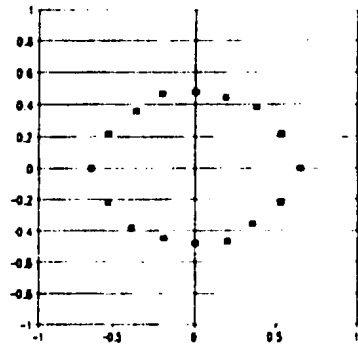
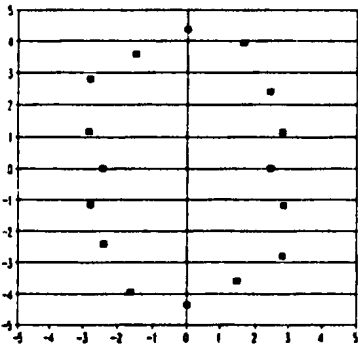
Horizontal
Plane



Vertical
ZY Plane



Vertical
ZX Plane



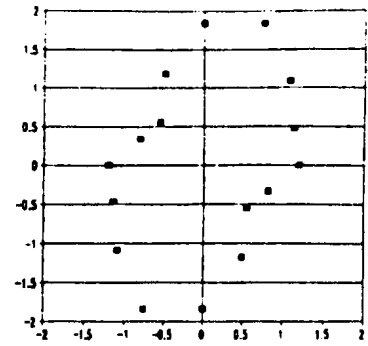
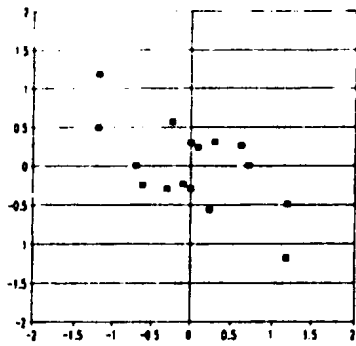
k(md)

1/k^h

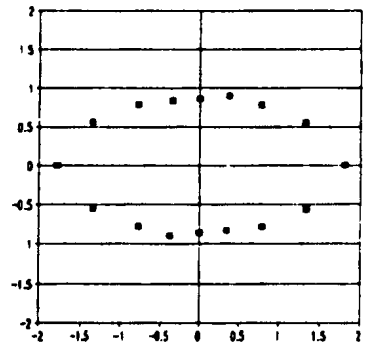
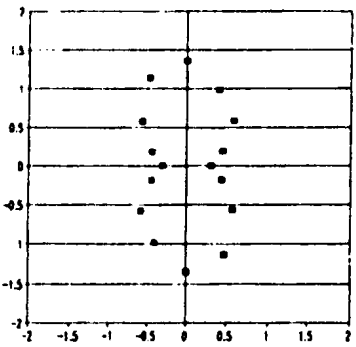
Figure 4.11. Directional permeability and 1/k^h plots for Jalama Beach sites 5&6 B model. Horizontal and vertical scales are in same units.

LL B Model

Horizontal Plane



Vertical ZY Plane



Vertical ZX Plane

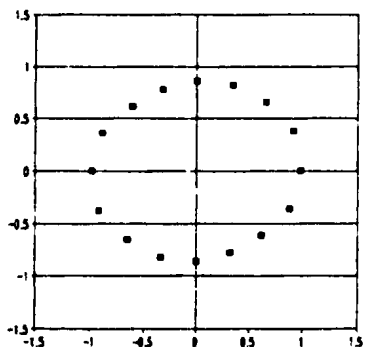
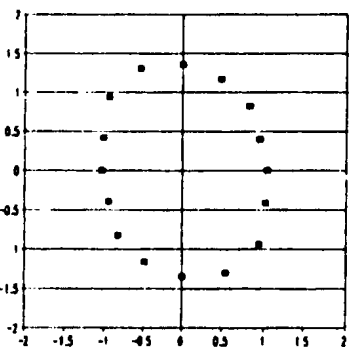
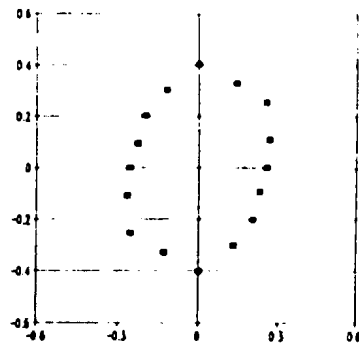
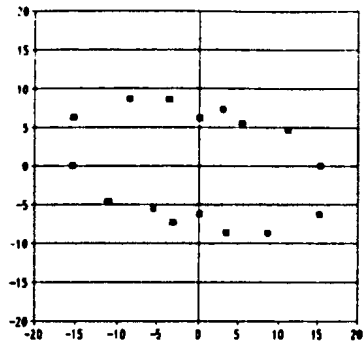


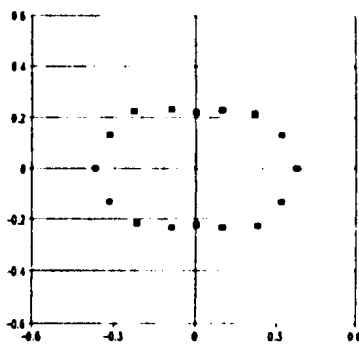
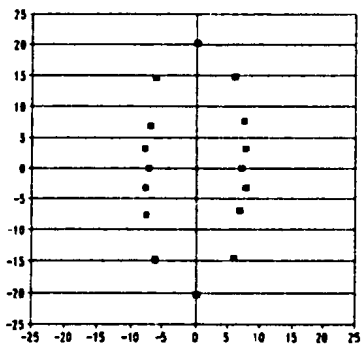
Figure 4.12. Directional permeability and $1/k^h$ plots for Lompoc Landing B model. Horizontal and vertical scales are in same units.

NV B Model

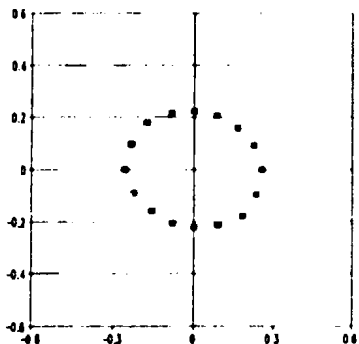
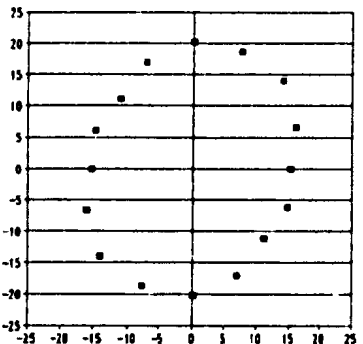
Horizontal Plane



Vertical ZY Plane



Vertical ZX Plane



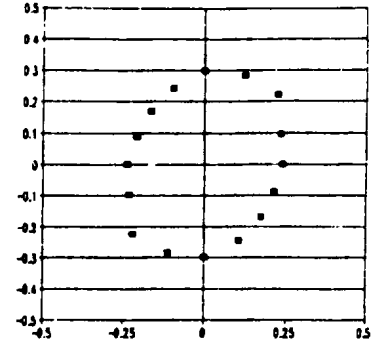
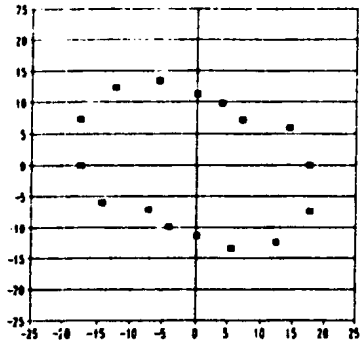
k (md)

$1/k^h$

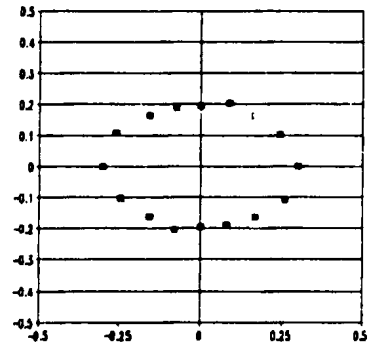
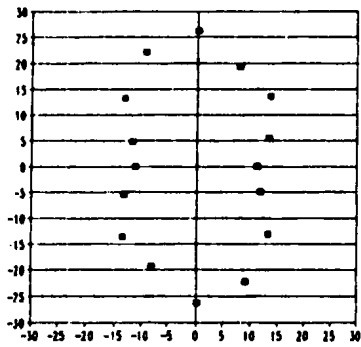
Figure 4.13. Directional permeability and $1/k^h$ plots for North Vandenberg B model. Horizontal and vertical scales are in same units.

SV B Model

Horizontal Plane



Vertical ZY Plane



Vertical ZX Plane

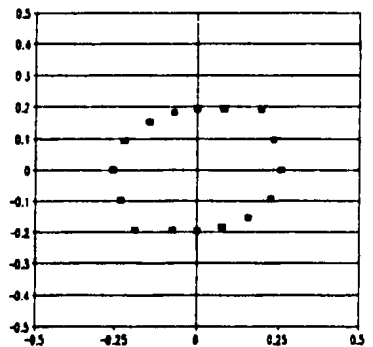
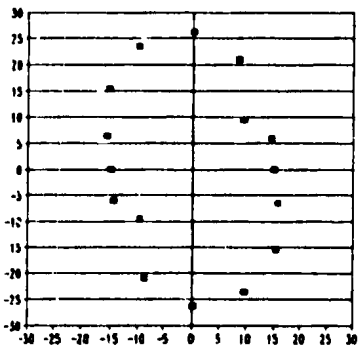


Figure 4.14. Directional permeability and $1/k^{0.5}$ plots for South Vandenberg B model. Horizontal and vertical scales are in same units.

GP B Model Variable Aperture

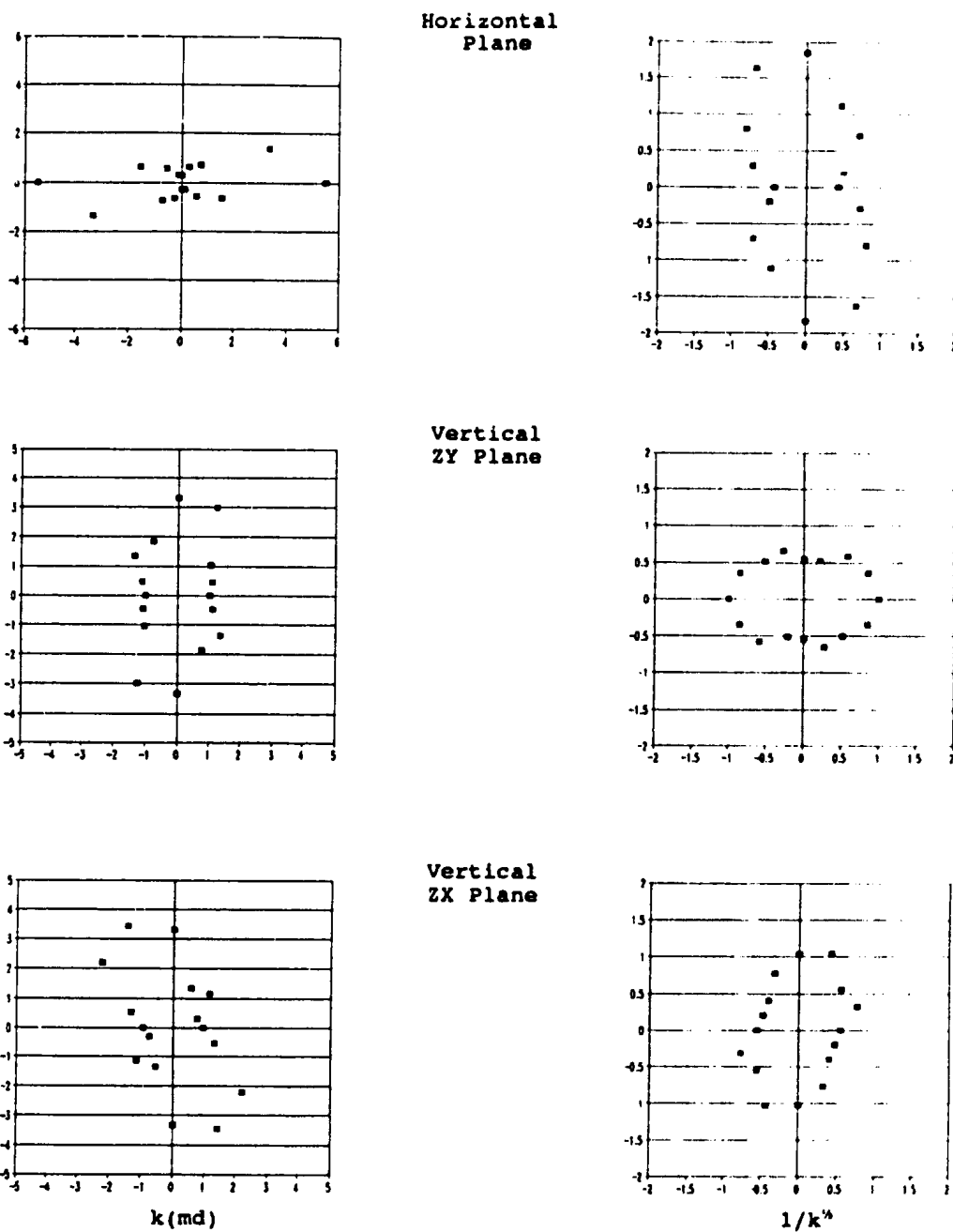


Figure 4.15. Directional permeability and $1/k^2$ plots for Government Pt. B variable aperture model. Horizontal and vertical scales in same units.

SV B Variable Aperture Model

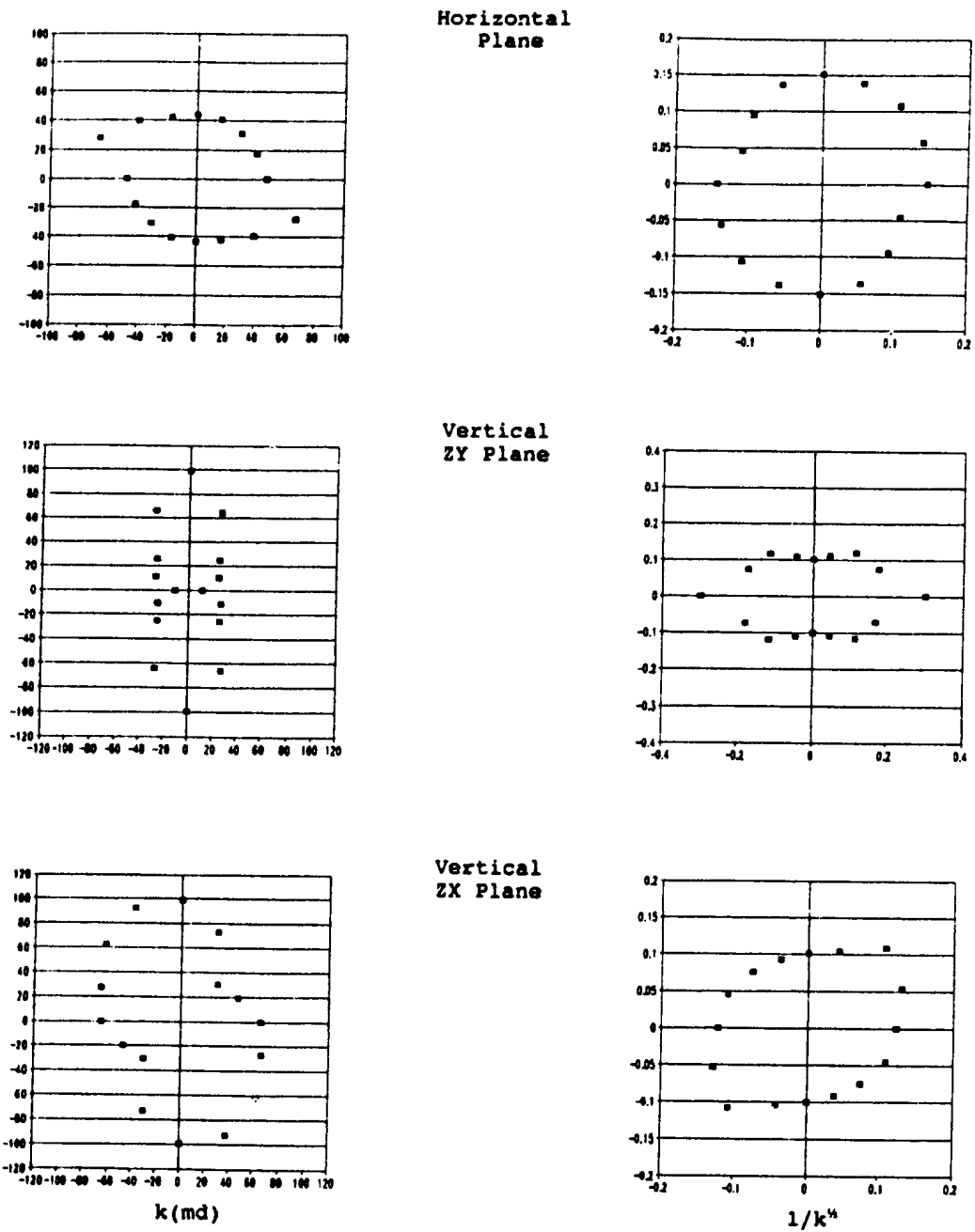


Figure 4.16. Directional permeability and $1/k^4$ plots for S. Vandenberg variable aperture B model. Horizontal and vertical scales in same units.

CHAPTER 5. DISCUSSION, SUMMARY AND CONCLUSIONS

The two major objectives of this study were to characterize the fracture geometry and evaluate the impact of the fracture geometry on fluid flow in the Monterey Formation. The Monterey Formation is a folded and fractured sedimentary rock mass with low matrix permeability (Crain et al., 1985; MacKinnon, 1989). Thus, fluid flow through the formation is predominantly in discrete fractures, and it is recognized that these fractures are discontinuous within the rock mass. The fracture network modeling used in this study directly simulates the flow process through the interconnected discrete fractures. The interconnectivity of the fracture system is controlled by the number of fracture sets and the orientations, lengths and spacings of the fractures within each set. Since it is not possible to describe every fracture in the rock mass, areal and scanline mapping surveys were conducted to sample the rock mass for the above fracture parameters, along with other fracture characteristics, at two distinct scales of fracturing. As mentioned in Chapter 1, it is believed that at a "small-" scale, the fracture (joint) system provides the fluid pathways to the "large-" scale fractures (breccia zones and faults) which, with the dilation openings in the fold hinges (Figure 1.4), are the major permeability conduits within the Monterey Formation. From the sampled fracture parameters, a stochastic description of the fracture geometry was obtained and used as input for 2-D and 3-D discrete fracture flow models. The following sections summarize: (a) the assumptions, inferences, biases and errors associated with, the fracture sampling process, the statistical fracture analysis, and in the determination of the input parameters for the 2-D and 3-D models; (b) a preliminary comparison of the 2-D and 3-D flow modeling results; and (c) the results of the 3-D discrete fracture modeling of the impact of the fracture geometry on

fluid flow in the Monterey Formation. Conclusions and recommendations are presented in the last section of this chapter.

5.1 FRACTURE MAPPING AND STATISTICS

The coastal outcrops of the Monterey Formation, with vertical cliff and horizontal "bench" exposures, allowed for the detailed areal and scanline sampling of the fracture system in close areal proximity (< 6 km) to the offshore oil reservoirs. In a folded sedimentary sequence, such as the Monterey Formation, lithology, bed thickness and structural position may influence the development and characteristics of the fractures and fracture system. As discussed in Chapter 2, most of the mapped sites were located on the limbs of large anticlines or synclines with only the Lions Head area being located near a major fault (Figures 2.2 and 3.12). Figure 2.1 shows that the sample sites were in the upper two members of the Monterey Formation which included all the major rock types: porcelanites, siliceous mudstones, mudstones, dolostones, and some cherts. The distinction between some of the rock types, especially between porcelanites and siliceous mudstones, is gradational and in many places difficult to differentiate in the field.

As with all field fracture studies, there is always some degree of uncertainty that the number of sampled fractures adequately represents the "true" population of fractures. This will always be the case unless the whole formation can be sampled. For this particular fracture study of the Monterey Formation, which was based on data from coastal outcrops, confidence could be increased on the applicability of these data for modeling offshore oil reservoir

behavior: by sampling the fractures in oriented core from offshore wells; and/or by demonstrating that rock composition and structural geometry are similar. This would increase confidence in using the fracture orientations and spacings, determined from data collected in this study, in characterizing the nature of the fracture system in the offshore oil reservoirs. In one of the few published core and field studies on the Monterey Formation, Narr (1991) found that almost all the fractures in cores from offshore oil wells, had orientations similar to the extensional fracture set found in surface outcrops. These orientations are also similar to the extensional set found in this study with fracture strikes being sub-parallel to the bedding dip direction. Narr(1991) concluded that the fracture densities were higher in the surface outcrops than in the subsurface, possibly due to enhancement by weathering and unloading. It was observed in this study, and from the literature (see Chapter 2), that the lithology and style of folding in the Monterey Formation are similar throughout this study area, and that the dominance of extensional fractures is also prevalent. It, therefore, seems reasonable that, if a similar deformational style is exhibited offshore in the Monterey Formation, fracture sets with similar characteristics as the sets seen at the surface, especially the dominant extensional set, would exist in the offshore reservoirs.

The scanline mapping technique, used to sample the rock mass for fracture characteristics, provided data on the key parameters of fracture trace length, orientation, and spacing. In addition, a qualitative description of fracture aperture and roughness was obtained. Due to the dimensions and orientations of the rock outcrops, along with the length of the scanlines (< 30 m) used in the small-scale survey, the orientation bias on the small-scale fracture data was minimal (see Appendix C). However, for the large-scale survey the length of the

scanlines (100 m to 1400 m) and the lack of rock exposures of suitable extent in two dimensions, precluded the use of orthogonal sampling lines. Therefore, fracture sets with strikes sub-parallel to the scanline directions, if they exist, will not be well represented at this larger scale.

The orientation bias was also accounted for during the statistical analysis (Appendix C and Chapter 3) when determining the number of fracture sets and their orientation statistics. There is no well defined quantitative method for determining the number of fracture sets in a given rock mass, and this is an area of fracture analysis where there can be a good deal of uncertainty. The method employed in this study was to objectively determine the mode of clustering of poles to fracture planes for each mapped site, using the computer program CLUSTRAN (Gillett, 1987). The poles to the fracture planes were also plotted on lower hemisphere equal area stereonet, with fracture sets visually determined by the clustering of poles. In these stereonet, there was a relatively strong clustering of points in two to four or five groups along the perimeter of the stereonet, with each group showing some degree of scatter in dip but more so in dip direction. The "fringe" areas (created by the scattered poles) of the clusters can overlap and make it difficult to determine the boundaries of each set. The sets determined visually and by CLUSTRAN were compared and where there were discrepancies, the field notes and maps were consulted for other fracture characteristics, such as termination mode or cross cutting relationships, that would determine which set was appropriate for the fracture in question. Structural differences were corrected and the fracture sets were compared between sites to determine the final groupings. Two to three sets were recognized at the sites mapped during the small-scale fracture survey, and three fracture sets

were determined from the large-scale fracture survey data. Fracture data were not combined between the major mapped areas of Government Point (GP), Jalama Beach (JB14, JB56), Lompoc Landing (LL), and Lions Head, mainly because the areas are located in different parts of the stratigraphic section, but similarities in orientations can be seen (Table 5.1). The Lions Head data are not presented in Table 5.1 because only one fracture set was identified and the data were not used in the modeling phase of this thesis. The large-scale fracture data were combined into two groups according to location within one of the two structural domains, the Onshore Santa Maria domain (NV) or the Santa Barbara Channel domain (SV). As with the small-scale fracture data, there are similarities in orientations for corresponding fracture sets located in the two structural domains. Table 5.1 also presents the mean and standard deviation for the trace lengths and spacings for each fracture set, assuming both follow a lognormal distribution.

The proper choice of distributional models for each fracture parameter is critical to reducing the uncertainties when using the estimated distributional statistics in the flow modeling. How the empirical distribution differs from the theoretical distribution is important and a sufficient sample size (usually > 30) will help in reducing the uncertainty in determining if the sample data follow a given distribution. For most sites, the sample size is large (see Table 5.1), and robust statistical techniques of maximum likelihood estimation and probability plots were used. Probability plots for censored data (Chambers et al., 1983) are well suited for evaluating the fit of the empirical trace length distribution to a theoretical distribution. Using probability plots, the lognormal distribution was judged to be a good approximation of the measured trace length data for these study sites. On most of the probability plots a lognormal

model fits the central portion of the data well, but may slightly underestimate the longer trace lengths. The probability plots also show the effects of the truncation bias introduced by selectively ignoring traces less than .25 m in length. The truncation bias is shown by a grouping of data points at the cutoff value thus the lower tail of the plot flattens out. For the trace length data the truncation bias was corrected using the computer program MULTI (Chung, 1989), but this bias also affects the spacing analysis. It is difficult to estimate the influence the truncation bias has on the spacings of a set, since there is no proven correlation between spacing and trace length. But, as some of the fractures are ignored due to their short trace lengths (<0.25 m) there will be some impact on the distribution of fracture spacings. Based on fractured core studies, where the spacing between every fracture is measured, many workers including Rouleau and Gale (1985), found fracture spacings follow the exponential distribution. In this study, using scanlines, fracture spacings were found to follow the lognormal distribution. The difference in distributional type could be, in part, due to the truncation bias associated with fracture scanline surveys. It is assumed that the contribution to the rock mass permeability, of the fractures associated with trace lengths shorter than the mean fracture spacing, is not significant.

From the field work and subsequent statistical analysis of the fracture data, the parameters that describe the fracture geometry were estimated. Mean fracture orientation was estimated for each set, with dip and dip direction assumed to follow independently a normal distribution. Means and standard deviations were estimated for the fracture trace lengths and spacings, with both parameters being shown to follow the lognormal distribution. A qualitative assessment was also made of fracture aperture and surface roughness. These data,

except surface roughness, were used as input to the 2-D and 3-D discrete fracture flow models to determine the impact of fracture geometry on fluid flow in the Monterey Formation.

Table 5.1. Summary of mean orientation, trace length and spacing for each set. N = number of fractures in each set, Mean Orient. = mean dip azimuth and mean dip of normalized fracture orientations, Trace Length = corrected trace length in meters, Spacing = corrected fracture spacings in meters. GP = Government Point, JB14 = Jalama Beach sites 1-4, JB56 = Jalama Beach sites 5 and 6, LL = Lompoc Landing, NV = sites on North Vandenberg Air Force Base in the Onshore Santa Maria structural domain, SV = South Vandenberg Air Force Base in the Santa Barbara Channel structural domain.

Site	Set	N	Mean Orient.	Trace Length (m)		Spacing (m)	
			DipAz/Dip	Mean	Std.	Mean	Std.
GP	1(v)	81	88/82	1.65	1.01	0.59	0.67
	1(h)			0.59	0.32		
	2(v)	642	179/87	2.58	2.19	0.34	0.37
	2(h)			6.59	14.59		
JB14	1	54	264/81	8.27	19.76	0.50	0.57
	2	128	334/89	3.56	4.90	0.27	0.32
JB56	1	18	276/83	4.97	5.73	2.07	1.81
	2	181	157/90	5.49	8.03	0.44	0.38
	3	63	218/88	4.06	5.40	0.30	0.28
LL	1	38	216/89	4.02	5.61	0.72	1.01
	2	42	162/86	15.11	42.57	0.89	1.12
NV	1	10	232/87	45.0	78.2	29.2	24.1
	2	29	4/87	39.1	73.6	9.8	16.8
	3	2	95/59	73.0	--	24.3	--
SV	1	36	255/75	15.5	16.0	21.4	24.8
	2	96	4/87	18.5	17.8	14.9	18.6
	3	23	108/04	18.0	22.2	21.1	33.8

5.2 NUMERICAL MODELING

The first step in modeling a fractured rock mass at the discrete fracture level is to determine a representative elemental volume (REV) whose properties, can be described as an equivalent porous medium. This REV is determined by many factors with fracture frequency and fracture size and shape being important parameters. It is also important that the model size be sufficiently large so as to minimize the number of generated fractures that cut across the modeled volume and that provide hydraulic connection from flow boundary to flow boundary. For highly skewed distributions like the lognormal distribution, depending on the standard deviation, models should have dimensions 3 to 5 times the mean trace length to have less than 10% of the generated fractures potentially longer than the modeled region (Table 4.3).

When modeling the fracture networks based on the statistics for the Monterey data, several key points arose. One was concerned with the creation of intersections within the realization that possibly would not occur in the rock mass. Due to the wide variability in orientation for each set it is possible for members of the same set to intersect. This is seldom seen in the outcrops of the Monterey, but regularly occurs in the realizations. The set of realizations with constant orientation/constant aperture were compared to the realizations with variable orientation/constant aperture to determine if the increased number of intersections had a great impact on the permeability. It was found that there were 60% to 100% fewer intersections in the realizations where orientation was held constant at the mean value than when orientation was allowed to vary, but the effect on the permeability was slight. This indicates that fracture lengths for each set were sufficient in size to create a well connected network and at the tested

scale the intersections created between members of the same set did not have a major affect on the permeability.

Another aspect of the intersections that should be tested further is the predominance of one set terminating against the other set, which is seen in the study areas. This termination of one set against another was accounted for in the 2-D simulations but not in the 3-D simulations. No direct comparison on the impact of termination mode can be made between the 2-D and 3-D results. At this point in the study of fracture network permeability in the Monterey Formation, some qualitative comparisons between the 2-D simulations and the 3-D simulations for Government Point (GP) and Jalama Beach (JB) can be made. It should be noted that the numbering of the sets at GP and JB changed between the 2-D and 3-D analysis. Thus 2-D set 1 and the 3-D set 2 are essentially the same extensional set, and similarly for the other set. Also for the 2-D realizations, fracture orientation was not corrected for changes in bedding between stations as for the 3-D data. Fracture orientations for the 2-D simulations are the true measured azimuths while the 3-D orientations are related to bedding (see section 3.3). Even with these differences some comparisons can be drawn.

The 2-D flux diagrams shown in Figure 4.4 for the Government Point data show the importance and influence of correcting the trace length statistics for truncation and censoring. There is approximately a doubling of flux due to the increase of fracture trace length. These 2-D realizations used a constant aperture of $5\mu\text{m}$ but when permeability is calculated, the values are the same order of magnitude as the permeability calculated for the 3-D realizations, based on a constant $20\mu\text{m}$ aperture. The direction of the principal permeabilities are

essentially the same for the 2-D and 3-D models, with both having maximum flow parallel to the strike of the dominant extensional fracture set. The 2-D model showed the same dramatic increase in flux, as the 3-D model, when aperture was allowed to vary. Both models show a strong vertical flux, with the 2-D vertical flux just slightly less than the horizontal flux but the 3-D model had a slightly larger vertical flux than horizontal. These observations point out the relative importance of the third dimension in determining the permeability perpendicular to bedding or parallel to the fracture dip. More realizations with realistic aperture distributions would determine if 2-D fracture networks can be used to simulate a 3-D environment.

Realizations that used apertures estimated from field data would also allow one to determine if the generated network produces realistic porosities. A preliminary analysis of the 3-D simulations, based on the total number of planes that formed the interconnected network and the average fracture size and mean aperture (20 μ m and 100 μ m, for the small and large-scale fractures, respectively) for each set, resulted in a fracture porosity in the range of 0.02% to 0.2% for the different sites. This range is slightly less than the range of porosities calculated from tests on oil wells in the offshore Monterey Formation (Carpenter - pers. comm., 1992), but Grivetti (1983) reported fracture porosities that were at least a magnitude larger for fractures measured in outcrops. Grivetti didn't explain his method for estimating the fracture porosity, but a major source for the difference in estimated fracture porosity would come from the enhanced fracture apertures due to weathering of the surface outcrops.

Another area where differences exist is in how the boundary conditions are applied when determining the permeability of a discrete fracture network (Dershowitz, 1984). The

approach used in this study was to have constant head boundaries on two opposing faces with all other faces assigned as no-flow boundaries. This method requires multiple realizations, as the network is rotated within the solution region, with the flow calculated at each interval of rotation and then used to compute a permeability tensor. With this method there is a possibility of changing the connectivity of the network and, due to the anisotropic nature of the network, producing gradients that will not be uniform throughout the solution region. A second approach (Long et al., 1982; Herbert et al., 1991) used to apply boundary conditions, is to assign linear pressure boundaries and allowing all faces to flow. According to Long et al. (1982) this is necessary to produce a uniform linear gradient in an anisotropic flow field. This second approach to applying boundary conditions, is assumed to allow three of the permeability tensor components to be calculated from one 3-D realization (Herbert et al., 1991). Thus only three simulations are needed to determine the permeability tensor. This second method was attempted using the Government Point data. There were three realizations with flow parallel to the x, y, and z axis, respectively. Flows through opposing faces were not equal but the total mass flux was conserved. The solution region was the same as the one for the simulations discussed in section 4.3.2, but the derived permeabilities did not form a symmetric matrix. One conclusion from using this second approach on the Government Point data could be that the fracture network does not approximate a porous medium at the modeled scale. However, the results of the realizations that used the no-flow boundary conditions of the first method did produce a symmetric matrix, and thus at the modeled scale, the fracture network is assumed to be an equivalent porous media.

5.3 CONCLUSIONS AND RECOMMENDATIONS

Conclusions that can be drawn from the work conducted in this study include:

- field scanline surveys can provide fracture geometry data from outcrops at different fracture scales.
- the fracture system in the Monterey Formation can be defined using the scanline fracture data, with appropriate corrections for the orientation, truncation and censoring biases associated with scanline sampling.
- there are two to three fracture sets in the Monterey Formation at the study sites, with the mean strike of the dominant set sub-parallel with the bedding dip direction.
- the fracture patterns do not match theoretical fracture pattern model proposed by Stearns.
- fracture geometry produces a well connected network.
- varying fracture apertures logarithmically within fractures of the same set has a strong impact on the magnitude of directional permeability, but only a slight affect on the direction of the principal permeabilities.

Recommendations for further study include:

- a further in-depth analysis of the fracture trace lengths could be undertaken using the probability plots to help ascertain if there is a physical or structural reason for deviation of data points from the assumed theoretical model.

- simulate larger model sizes to determine if REV exists at all sites and both fracture scales.
- produce realizations of models using the linear pressure boundary and the constant head boundary methods at varying model sizes to evaluate the differences, if any, between these methods.
- additional modeling is needed to evaluate if and/or how the large-scale fractures form the hydrodynamic boundaries for the small-scale fracture system, and if one can merge the permeabilities of the small and large-scale fracture systems.

REFERENCES

- Andersson, J., Shapiro, A. M., and J. Bear, 1984. A stochastic model of a fractured rock conditioned by measured information, *Water Resour. Res.*, 20(1), 79-88.
- Asfari, A., and P. A. Witherspoon, 1973. Numerical Simulation of Naturally Fractured Reservoirs, SPE paper 4290 for the 3rd Numerical Simulation of Reservoir Performance Symposium of SPE, Houston, TX, 7p.
- Atkinson, B. K., 1987. Introduction to Fracture mechanics and its Geophysical Applications, in Fracture Mechanics of Rock, B. K. Atkinson ed., Academic Press Inc., London, 1-25.
- Baecher, G. B., 1980. Progressively Censored Sampling of Rock Joint Traces, *Math. Geology*, Vol.12, No.1, 33-40.
- Baecher, G. B., N. A. Lanney, H. H. Einstein, 1977. Statistical Description of Rock Properties and Sampling, 19th U.S. Sym. on Rock Mech., 5C1-1 - 5C1-8.
- Barton, C. C., and E. Larsen, 1985. Fractal geometry of two-dimensional fracture networks at Yucca Mountain, southwestern Nevada, *Proc. Fundz. Rock Joints*, O. Stephansson, ed., 77-84.
- Belfield, W. C., Helwig, J., La Pointe, P., and W. K. Dahleen, 1983. South Elwood oil field, Santa Barbara Channel, California, a Monterey Formation fractured reservoir, In Isaacs, C., and R. E. Garrison, eds., *Petroleum Generation and Occurrence in the Miocene Monterey Formation, California: Pacific Section SEPM*, 201-212.
- Blake, M. C., Jr., Campbell, R. H., Dibblee, T. W., Jr., Howell, D. G., Nilsen, T. H., Normark, W. R., Vedder, J. C., and E. A. Silver, 1978. Neogene basin formation in relation to plate-tectonic evolution of San Andreas fault system, California, *AAPG Bulletin*, v. 62, 344-372.
- Caldwell, J. A., 1971. The Theoretical Determination of the Fluid Potential Distribution in Jointed Rocks, M.Sc. thesis, University of the Witwatersrand, Johannesburg, South Africa.
- Call, R. D., J. P. Savely, and D. E. Nicholas, 1976. Estimation of Joint Set Characteristics from Surface Mapping Data, in 17th Proceedings U.S. Sym. on Rock Mech., 2B2-1 - 2B2-9.
- Carpenter, A. B., 1992. Personal communication, Chevron Oil Field Research Company, La Habra, CA.
- Chambers, J. M., W. S. Cleveland, B. Kleiner, and P. A. Tukey, 1983. Graphical Methods for Data Analysis, Wadsworth and Brooks, Pacific Grove, CA, 395p.

- Chilès, J. P., 1988. Fractal and Geostatistical Methods for Modeling of a Fracture Network, *Math. Geo.*, 20(6), 631-654.
- Chung, C.-J. F., 1988. Statistical Analysis of Truncated Data in Geosciences, *Sciences de la Terre-Serie Informatique Geologic*.
- Crain, W. E., Mero, W. E., and D. Patterson, 1985. Geology of the Point Arguello Discovery, *The A.A.P.G. Bull.*, 69(4), 537-545.
- Cruden, D. M., 1977. Describing the Size of Discontinuities, *Int. J. Rock Mech. Min. Sci. & Geomech. Abstr.*, Vol. 14, 133-137.
- Dershowitz, W. S., 1984. Rock Joint Systems, PhD Thesis, Massachusetts Institute of Technology, Cambridge, MA.
- Dershowitz, W. S., Gordon, B. M., J. C. Kafritsas, and H. Herda, 1985. A New Three Dimensional Model for Flow in Fractured Rock, *Mem. Int. Assoc. Hydrogeol.*, 17, 441-448.
- Dibblee T. W., 1950. Geology of southwestern Santa Barbara County, California, *Cal. Div. of Mines Geology Bulletin* 150, 95p.
- Duguid, J. O., and P. C. Y. Lee, 1977. Flow in Fractured Porous Media, *Water Resour. Res.*, 13(3), 558-566.
- Dunham, J. B., and G. H. Blake, 1987. Guide to coastal outcrops of the Monterey Formation of western Santa Barbara County, California, *Pacific Section SEPM book* 53, 36p.
- Ernst, W. G. ed., 1981. The Geotectonic Development of California, Rubey Volume I, Prentice-Hall, New Jersey, 706p.
- Gale, J. E., 1975. A Numerical, field, and laboratory study of flow in rocks with deformable fractures, Ph.D. dissertation, University of California, Berkeley.
- Gale, J. E., 1981. Fracture and hydrology data from field studies at Stripa, Sweden, Lawrence Berkeley Lab. Rep. LBL-13101, SAC-46.
- Gale, J. E., and A. Stråhle, 1988. Site Characterization and Validation - Drift and Borehole Fracture Data, Stage 1, Stripa Project IR 88-10, SKB, Stockholm, Sweden
- Gale, J. E., MacLeod, R., Stråhle, A., and S. Carlsten, 1990. Site Characterization and Validation - Drift and Borehole Fracture Data, Stage 3, Stripa Project IR 90-02, SKB, Stockholm, Sweden.

- Gale, J. E., Schaefer, R. A., Carpenter, A. B., and A. Herbert, 1991. Collection, Analysis, and Integration of discrete fracture data from the Monterey Formation for fractured reservoir simulations, SPE paper 022741 for the 66th Annual Technical Conference and Exhibition of SPE, Dallas, TX, 11p.
- Garrison, R. E., and R. G. Douglas, eds., 1981. The Monterey Formation and Related Siliceous Rocks of California, Pacific Section, SEPM, 327p.
- Gillett, S. L., 1987. Extract clusters from axial data sets using the algorithm of Shanley and Mahtab, Unpublished IBM-PC computer program.
- Gorham, F. D., et.al., 1979. Fractures in Cretaceous Rocks from Selected Areas of San Juan Basin, New Mexico - Exploration Implications, AAPG Bulletin, 63(4), 598-607.
- Grivetti, M. C., 1982. Aspects of stratigraphy, diagenesis, and deformation in the Monterey Formation near Santa Maria - Lompoc, California, M.A. Thesis, University of California, Santa Barbara, California
- Hall, C. A. Jr., 1981. Evolution of the Western Transverse Ranges Microplate: Late Cenozoic faulting and basinal development, in The Geotectonic Development of California, Rubey Volume I, Ernst, W. G. ed., Prentice-Hall, New Jersey, 559-582.
- Hancock, P. L., 1985. Brittle microtectonics: principles and practice, Journal of Structural Geology, Vol. 7, 437-457.
- Herbert, A., Dershowitz, W., Long, J., and D. Hodgkinson, 1990. Validation of fracture flow models in the Stripa project, Proc. GEOVAL-90, Swe. Nuc. Power Inspec., Stockholm, Sweden, 15p.
- Herbert, A., and B. Splawski, 1990. Prediction of Inflow into the D-Holes at the Stripa Mine, Stripa project TR 90-14, SKB, Stockholm, Sweden.
- Herbert, A., J. Gale, G. Lanyon, and R. Macleod, 1991. Modelling for the Stripa Site Characterization and Validation Drift Inflow: Prediction of Flow Through Fractured Rock, Stripa project TR 91-35, SKB, Stockholm, Sweden.
- Hobbs, D. W., 1967. The Formation of Tension Joints in Sedimentary Rocks: An Explanation, Geol. Mag., 104, 550-556.
- Hodgson, R. A., 1961. Regional study of jointing in Com Ridge, Navajo mountain area, Arizona and Utah, AAPG Bull. 45(1), 1- 37.
- Hornafuis, J. S., Luyendyk, B. P., Terres, R. R., and M. J. Kamerling, 1986. Timing and extent of Neogene tectonic rotation in the western Transverse Ranges, California, GSA Bull., 97, 1475-1487.

- Hudson, J. A., and P. R. La Pointe, 1980. Printed circuits for studying rock mass permeability, *Int. Jour. of Rock Mech., Min. Sci. and Abs.*, v.17, 297-301.
- Huskey, W. L., and P. B. Crawford, 1967. Performance of petroleum reservoirs containing vertical fractures in the matrix, *Soc. Pet. Engr. Jour.*, 7(2), 221-228.
- Ingersoll, R. V., and W. G. Ernst, eds., 1987. Cenozoic Basin Development of Coastal California, Rubey Volume VI, Prentice-Hall, New Jersey, 496p.
- International Society for Rock Mechanics Commission on Standardization of Laboratory and Field Tests (1978). Suggested Methods for the Quantitative Description of Discontinuities in Rock Masses. *Int. J. Rock. Mech. Min. Sci. and Geomech. Abstr.*, vol. 15, 319-368.
- Isaacs, C. M., 1981. Guide to the Monterey Formation in the California coastal area, Ventura to San Luis Obispo, Pacific Section, AAPG, v. 52, 91p.
- Isaacs, C. M., and R. E. Garrison, eds., 1983. Petroleum Generation and Occurrence in the Miocene Monterey Formation, California, Pacific Section, SEPM, 228p.
- Jaroszewski, W., 1984. Fault and Fold Tectonics. John Wiley and Sons, New York.
- Jennings, C. W., 1975. Fault map of California, with locations of volcanoes, thermal springs and thermal wells: Calif. Div. of Mines & Geology, Calif., Calif. Geol. Data Map Series, Map No. 1.
- King, J. R., 1971. Probability Charts for Decision Making, Industrial Press Inc., New York, 290p.
- Kulatilake, P. H. S. W., 1992. State-of-the-art in stochastic joint geometry modeling, Key Questions in Rock Mechanics, 29th U.S. Sym. on Rock Mech., Cundal et al. (eds.), 215-229.
- La Pointe, P. R., and J. A. Hudson, 1985. Characterization and Interpretation of Rock Mass Joint Patterns. Special Paper 199, GSA, 37p.
- Laslett, G. M., 1982. Censoring and Edge Effects in Areal and Line Transect Sampling of Rock Joint Traces, *Math. Geology*, Vol.14, No.2, 125-140.
- Lee, W. H. K., Yerkes, R. F., and M. Simirenko, 1979. Recent earthquake activity and focal mechanisms in the Western Transverse Ranges, USGS Circular 799-A, 27p.
- Litvak, B. L., 1986. Simulation and Characterization of Naturally Fractured Reservoirs, in Reservoir Characterization, L. Lake, and H. Carroll, Jr., eds, Academic Press, 561-584.

- Long, J.C.S., Remer, J.S., Wilson, C.R., and P. A. Witherspoon, 1982. Porous Media Equivalents for Network of Discontinuous Fractures, *Water Resources Res.*, vol. 18, no.3, 645-658.
- Long, J.C.S., and P. A. Witherspoon, 1985. The relationship of the degree of interconnection and permeability in a fracture network, *J. Geophys. Res.*, v.90, 3087-3098.
- Long, J.C.S., Gilmour, P., and P. A. Witherspoon, 1985. A Model for Steady Fluid Flow in Random Three-Dimensional Networks of Disc-Shaped Fractures, *Water Resour. Res.*, 21(8), 1105-1115.
- Long, J.C.S., and D. M. Bilaux, 1987. From field data to fracture network modeling: and example incorporating spatial structure, *Water Resour. Res.*, 23(7), 1207-1216.
- Luyendyk, B. P., 1991. A model for Neogene crustal rotations, transtension, and transpression in southern California, *GSA Bull.*, v.103, 1528-1536.
- MacKinnon, T. C., ed., 1989. Oil in the California Monterey Formation, 28th Int. Geol. Congress guidebook T311 vol. 1, Am. Geophys Union, 55p.
- Mardia, K. V., 1972. Statistics of Directional Data, Academic Press, 357p.
- McQuillan, H., 1973. Small-Scale Fracture Density in Asmari Formation of Southwest Iran and its Relation to Bed Thickness and Structural Setting, *AAPG Bull.*, 57(12), 2367-2385.
- Murray, G.H., 1968. Quantitative Fracture Study-Sanish Pool, McKenzie Co., North Dakota, *AAPG Bull.*, v.52, 57-65.
- Narr, W., 1991. Fracture Density in the Deep Subsurface: Techniques with Application to Point Arguello Field, *AAPG Bull.*, 75(8), 1300-1323.
- Narr, W., and J. Suppe, 1991. Joint Spacing in sedimentary rocks, *Jour. of Struct. Geol.*, 13(9), 1037-1048.
- Noorishad, J., M. S. Ayatollahi, and P. A. Witherspoon, 1982. A Finite-Element Method for Coupled Stress and Fluid Flow Analysis in Fractured Rock Masses, *Int. J. Rock Mech. Min. Sci. & Geomech. Abstr.*, Vol. 19, 185-193.
- Pahl, P. J., 1981. Estimation of the Mean Length of Joint Traces, *Int. J. Rock Mech. Min. Sci. & Geomech. Abstr.*, Vol. 18, 221-228.
- Paterson, M. S., 1978. Experimental Rock Deformation - The Brittle Field, Springer-Verlag, New York, 254pp.

- Pisciotta, , 1981. Notes on Monterey rocks near Santa Maria, California, in Guide to the Monterey Formation in the California coastal area, Ventura to San Luis Obispo, Pacific Section, Isaacs, C. M., ed., AAPG, v. 52, 73-81.
- Polishook, B., and A. Flexer, 1985. Joint parameters and their relation to structural history (Sa'ad anticline Central Negev, Israel), Fundamentals of Rock Joints, Proceedings.
- Pollard, D., and P. Segall, 1987. Theoretical displacements and stresses near fracture in rock: with applications to faults, joints, veins, dikes, and solution surfaces, in Fracture Mechanics of Rock, Atkinson, B.K., ed, Academic Press, London, 277-349.
- Price N. J., 1966. Fault and Joint Development, in Brittle and Semi-brittle Rock. Pergamon Press,.
- Priest, S. D., and J. A. Hudson, 1976. Discontinuity Spacings in Rock, Int. J. Rock. Mech. Min. Sci. and Geomech. Abstr., v. 13, 135-148.
- Priest, S. D., and J. A. Hudson, 1981. Estimation of Discontinuity Spacing and Trace Length Using Scanline Surveys, Int. J. Rock. Mech. Min. Sci. and Geomech. Abstr., v. 18, 183-197.
- Priest, S. D., 1985. Hemispherical Projection Methods in Rock Mechanics, George Allen & Unwin, 126p.
- Quillan, J. A., and D. W. Stearns, 1986. Field Study of Fracture Characteristics as Function of Bed Curvature in Folded Dolomites, AAPG Bull. 70(5), 636.
- Ramsay, J. G., and M. I. Huber, 1987. The Techniques of Modern Structural Geology, Vol. 2: Folds and Fractures, Academic Press Limited, 700p.
- Reches, Z., 1976. Analysis of joints in two monoclines in Israel. Bull. Geol. Soc. Am. 87, 1654-1662.
- Rouleau, A., 1984. Statistical characterization and numerical simulation of a fracture system - application to groundwater flow in the Stripa granite, Ph.D. thesis, Univ. of Waterloo, Canada, 416p.
- Rouleau, A., and J.E. Gale, 1985. Statistical Characterization of the Fracture System in the Stripa Granite, Sweden, Int. J. Rock. Mech. Min. Sci. and Geomech. Abstr., 22(6), 353-367.
- Rouleau, A., and J.E. Gale, 1987. Stochastic discrete fracture simulation of groundwater flow into an underground excavation in granite, Int. J. Rock. Mech. Min. Sci. and Geomech. Abstr., 24(2), 99-112.

- Samaniego, J. A., and S. D. Priest, 1984. The prediction of water flow through discontinuity networks into underground excavations, Paper 19, Design and performance of underground excavations, ISRM/BGS, Cambridge, 157-164.
- Scheidegger, A. E., 1954. Directional Permeability of Porous Media to Homogeneous Fluids, *Geofisica Pura & Applicata*, vol. 28, 75-90.
- Schemeiser, B. W., 1979. Approximation to the inverse normal function for use on hand calculators, *Applied Statistics*, 28, 175-176.
- Sen, Z., and Kazi, A., 1984. Discontinuity Spacing and RQD Estimates from Finite Length Scanlines, *Int. J. Rock. Mech. Min. Sci. and Geomech. Abstr.*, v. 21(4), 203-212.
- Shanley, R. J., and M. A. Mahtab, 1976. Delineation and analysis of clusters in orientation data, *Math. Geol.*, v. 8, 9-23.
- Snow, D. T., 1969. Anisotropic Permeability of Fractured Media, *Water Resour. Res.*, 5(6), 1273-1289.
- Snyder, W. S., Brueckner, H. K., and R. A. Schweickert, 1983. Deformational Styles in the Monterey Formation and other Siliceous Sedimentary Rocks, in Petroleum Generation and Occurrence in the Miocene Monterey Formation, California, Isaacs, C. M., and R. E. Garrison, eds., Pacific Section, SEPM, 151-170.
- Snyder, W. S., 1987. Structure of the Monterey Formation: stratigraphic, diagenetic, and tectonic influences on style and timing, in Cenozoic Basin Development of Coastal California, Rubey Volume VI, Ingersoll, R. V., and W. G. Ernst, eds., Prentice-Hall, New Jersey, 321-347.
- Sowers, G. M., 1972. Theory of spacing of extension fractures, *Engng. Geol. Case Hist.* 9, 27-53.
- Stearns, D. W., 1968. Certain aspects of fractures in naturally deformed rocks, in NSF Advanced science seminar in Rock Mechanics: Spec. Pubs. Air Force Cambridge Labs, R. Riecker ed., Bedford, MA, 97-118.
- Stearns, D. W., and M. Friedman, 1972. Reservoirs in fractured rock, in stratigraphic oil and gas field. *AAPG Bull.* 16, 82-106.
- Sylvester, A. G., and A. C. Darrow, 1979. Structure and Neotectonics of the Western Santa Ynez Fault System in Southern California, *Tectonophysics*, vol. 52, 389-405.
- Terzaghi, R. D., 1965. Sources of Errors in Joint Surveys, *Geotechnique*, 15(3), 287-304.
- Turcotte, D. L., 1986. A Fractal Model for Crustal Deformation, *Tectonophysics*, v. 132, 261-269.

- USGS, 1974. Geology and Reservoir Characteristics of the Santa Ynez Unit, Santa Barbara Channel, off California. U. S. Geological Survey FES 74-20, in Petroleum Generation and Occurrence in the Miocene Monterey Formation, California, Isaacs, C. M., and R. E. Garrison, eds., Pacific Section, SEPM, 111-130.
- van Everdingen, D. A., J. A. M. van Gool, and R. L. M. Vissers, 1992. Quickplot: A microcomputer-based program for processing of orientation data, *Computers and Geosciences*, 18(2/3), 183-287.
- van Golf-Racht, T.D., 1982. *Fundamentals of Fractured Reservoir Engineering*, Elsevier, 710p.
- Vetter, J. G., Wagner, H. C., and J.E. Schoellhamer, 1969. Geologic Framework of the Santa Barbara Channel Region, in Geology, Petroleum Development, and Seismicity of the Santa Barbara Channel Region, California, USGS Professional Paper 679-A, 1-11.
- Viele, G. W., 1984. Jointing and folding of the Monterey Formation in the area of the Santa Maria Basin and the western Santa Ynez Mountains, Tech. Memorandum, Chevron Oil Field Research Company.
- Viele, G. W., 1991. Personal Communication.
- Wang, J. S. Y., 1991. Flow and Transport in Fractured Rocks, *Reviews of Geophysics supplement*, Am. Geophys. Union, 254-262.
- Wilson, C. R., and P. A. Witherspoon, 1970. An Investigation of Laminar Flow in Fractured Rocks, Geotechnical Report No. 70-6, Univ. of California, Berkeley.
- Winsor, C. N., 1979. The correlation of fracture directions with sediment anisotropy in folded rocks of the Delamerian fold belt at Port Germein gorge, South Australia, *Journal of Structural Geology*, Vol. 1, 245-254.
- Wishart, D., 1968. Mode analysis: A generalization of nearest neighbor which reduces chaining effects, *Numerical Taxonomy*, 282-309.
- Wittke, W., 1970. Three-Dimensional Percolation of Regularly Fissured Rock, *Proc. of Symp. on the Theoretical Background of the Planning of Open Pit Mines with Special Reference to Slope Stability*, Johannesburg.
- Woodring, W. P., and M. N. Bramlette, 1950. Geology and Paleontology of the Santa Maria district, California, USGS Professional Paper 222, 185p.

APPENDIX A. Fracture Mapping Data Files

KEY:

Site - location; station number.scanline number.
NNum - number of feature.
Space- distance at which feature intersected scanline.
Type - feature type.
Ddr - dip direction.
DI - dip.
Trace- trace length.
Cen - censoring type of feature.
Mz - mineral infill.
Lsr - large scale roughness (shape).
Ssr - small scale roughness (surface roughness).
RkT - rock type.
Trm - termination type of feature.

*other abbreviations defined in Figure 3.3.

CHEVRON Fracture Data:

Site	NNum	Space	Type	Ddr	DI	Trace	Cen	Mz	LaR	Sar	RkT	Trm
GP1.01	001.0	0.00	JT	138	71	1.50	0	G	P	S	SM	2
GP1.01	003.0	0.45	JT	133	74	1.30	0	G	U	S	SM	2
GP1.01	004.0	0.80	JT	137	71	0.80	0	G	P	S	SM	1
GP1.01	005.0	0.90	JT	137	75	0.80	0	G	P	S	SM	1
GP1.01	007.0	2.35	JT	102	80	0.35	0	G	U	S	SM	2
GP1.02	008.0	2.50	JT	144	79	0.60	0	G	U	S	SM	1
GP1.02	009.0	2.52	JT	308	86	1.30	0	G	U	S	SM	2
GP1.02	010.0	2.60	JT	108	86	2.00	1	G	U	S	SM	1
GP1.02	012.0	2.75	JT	283	84	0.80	0	G	U	S	SM	2
GP1.02	013.0	3.05	JT	134	74	1.70	1	G	U	R	SM	0
GP1.02	014.0	3.55	JT	149	64	1.30	0	G	C	S	SM	0
GP1.02	015.0	4.00	JT	125	88	1.70	0	G	U	S	SM	2
GP1.02	016.0	4.55	JT	116	89	1.45	0	G	S	S	SM	1
GP1.02	017.0	5.10	JT	291	88	1.48	0	G	U	S	SM	2
GP1.02	019.0	5.50	JT	289	79	1.10	0		P	S	SM	2
GP1.02	020.0	5.60	FZ	290	86	2.00	1		P	S	SM	1
GP1.02	021.0	5.82	FZ	286	84	2.00	0		P	S	SM	2
GP1.02	022.0	6.15	JT	264	24	0.65	0		C	S	SM	2
GP1.02	023.0	6.34	JT	110	87	1.05	0		S	S	SM	2
GP1.02	024.0	6.65	JT	289	85	0.80	0		C	S	SM	2
GP1.02	025.0	7.10	JT	129	78	0.90	0		S	S	SM	3
GP1.02	026.0	7.60	JT	212	76	0.50	0		P	S	SM	2
GP1.02	027.0	7.90	FZ	107	85	2.50	1		S	S	SM	1
GP1.02	028.0	8.30	JT	109	87	2.00	1		S	S	SM	1
GP1.02	029.0	9.04	JT	148	85	1.37	0		S	S	SM	2
GP1.02	031.0	9.68	JT	104	89	1.10	0		P	S	P	2
GP1.02	032.0	9.95	JT	130	79	0.90	0		C	S	P	2
GP1.02	033.0	10.80	JT	106	85	0.90	0		U	S	P	2
GP1.02	034.0	11.12	JT	109	85	1.20	0		U	S	P	2
GP1.02	035.0	11.12	JT	196	65	0.90	0		U	S	P	2
GP1.02	037.0	13.10	JT	167	84	0.75	0		S	S		2
GP1.02	039.0	15.20	JT	137	84	2.65	0		S	S		2
GP1.02	040.0		JT	129	66				P	S		
GP1.02	041.0		JT	236	89				U	S		
GP1.02	042.0		JT	274	85				P	S		
GP1.02	043.0		JT	273	88				U	S		
GP1.02	044.0		JT	197	87				U	S		
GP1.03	001.0	1.20	JT	217	70	1.00	1		P	S	SM	1
GP1.03	002.0	3.15	JT	144	69	1.60	1		S	S	SM	1
GP1.03	021.0	2.50	JT	146	68	0.90	0		P	R	SM	0
GP1.04	003.0	5.55	JT	149	69	0.70	0		P	S	SM	1
GP1.04	004.0	5.50	JT	335	36	1.00	0		P	R	SM	0
GP1.04	005.0	6.22	JT	145	78	1.00	1		P	R	SM	1
GP1.04	006.0	8.08	JT	137	28	1.20	0		P	R	SM	0
GP1.04	007.0	8.48	JT	333	76	0.80	1		S	R	SM	0
GP1.04	008.0	9.67	JT	156	68	0.68	0		U	R	SM	0
GP1.04	009.0	9.80	JT	328	89	0.52	0		U	R	SM	0
GP1.04	010.0	10.70	JT	214	70	1.00	2		P	R	SM	4
GP1.05	011.0	0.10	JT	192	83	1.41	0		S	R	SM	2
GP1.05	012.0	0.10	JT	217	72	1.50	0	G	U	R	SM	1
GP1.05	013.0	0.58	JT	141	71	0.80	0		P	R	SM	1
GP1.05	014.0	1.65	JT	142	82	1.00	0		S	S	SM	1
GP1.05	015.0	3.20	JT	135	62	1.20	0		P	S	SM	3
GP1.05	016.0	4.15	JT	135	78	2.00	0		P	S	SM	3
GP1.06	017.0	4.95	JT	320	72	1.59	0		P	S		3
GP1.06	018.0	5.76	JT	142	64	0.78	0		P	S		1
GP1.06	019.0	6.08	JT	135	74	1.00	0		S	S		1
GP1.06	020.0	7.78	JT	145	70	0.97	0		P	S		1
GP1.06	022.0	50.00	JT	145	67	1.13	0		P	R		2
GP1.06	023.0	50.00	JT	140	62	0.64	0		U	R		3

Site	NNum	Space	Type	Ddr	DI	Trace	Can	Mz	LaR	Ssr	RkT	Trm
GP1.07	001.0	0.00	JT	244	70	1.50	1		U	R	M	0
GP1.07	002.0	0.50	JT	159	87	1.30	0		S	R	M	0
GP1.07	003.0	0.70	JT	120	75	1.24	0	FE	P	R	M	0
GP1.07	004.0	1.05	FZ	125	79	2.00	0	GCL	S	R	M	1
GP1.07	005.0	1.40	JT	112	71	1.30	0	G	P	S	M	1
GP1.07	006.0	1.90	FZ	132	77	2.20	0		P	S	M	1
GP1.07	007.0	2.03	JT	295	81	1.40	0		C	S	M	0
GP1.07	008.0	2.21	JT	307	83	1.20	0		P	S	M	0
GP1.07	009.0	2.24	JT	294	75	0.80	0		C	S	M	1
GP1.07	010.0	2.37	JT	299	80	1.00	0		U	S	M	1
GP1.07	011.0	2.48	JT	129	89	1.30	0	T	U	S	M	1
GP1.07	012.0	2.74	JT	288	83	1.00	0		U	S	M	1
GP1.07	013.0	3.00	JT	284	86	1.50	0		C	S	M	0
GP1.07	014.0	3.21	JT	124	77	0.70	0		S	S	M	0
GP1.07	015.0	3.41	JT	130	88	1.00	0		U	S	M	0
GP1.07	016.0	3.52	JT	110	82	1.40	0		C	S	M	0
GP1.07	017.0	3.53	JT	124	78	1.30	0		U	S	M	0
GP1.07	019.0	4.82	JT	122	87	1.52	0	T	P	S	M	1
GP1.07	020.0	5.00	JT	127	88	1.03	0	T	P	S	M	1
GP1.07	021.0	5.05	JT	121	87	2.00	0	T	P	S	M	1
GP1.07	022.0	5.30	JT	94	85	2.00	0	T	P	S	M	1
GP1.07	023.0	5.40	JT	112	85	2.00	0	T	P	S	M	0
GP1.07	024.0	5.69	JT	109	84	1.13	0		S	S	M	1
GP1.08	025.0	6.20	JT	131	82	4.00	0	T	P	S		1
GP1.08	026.0	6.70	JT	129	84	2.04	0	T	P	R		1
GP1.08	027.0	6.88	JT	119	80	0.72	0	T	S	R		1
GP1.08	028.0	6.97	JT	282	85	1.15	0	G	C	R		2
GP1.08	029.0	7.09	JT	267	89	1.24	0	T	P	S		1
GP1.08	030.0	7.35	JT	299	88	1.10	0		S	S		1
GP1.08	031.0	7.52	JT	292	89	1.58	0	T	P	S		2
GP1.08	032.0	7.63	JT	130	87	1.16	0	T	P	S		2
GP1.08	033.0	7.83	JT	122	86	1.10	0		P	S		0
GP1.08	034.0	8.38	JT	124	81	0.93	0	T	P	S		1
GP1.08	035.0	8.07	JT	122	89	1.72	0		P	S		1
GP1.08	036.0	8.33	JT	127	85	2.00	0		P	S		1
GP1.08	037.0	8.55	JT	128	85	0.57	0	T	P	S		1
GP1.08	038.0	8.58	JT	120	87	1.20	0	T	P	S		1
GP1.08	039.0	8.67	JT	128	80	0.73	0	T	P	S		0
GP1.08	040.0	8.72	JT	136	84	1.98	0	T	P	S		1
GP1.08	041.0	9.12	JT	126	85	0.48	0	T	P	S		0
GP1.08	042.0	9.19	JT	128	84	1.90	0	T	P	S		2
GP1.08	043.0	9.25	JT	126	81	4.00	0	T	P	S		1
GP1.08	044.0	9.64	JT	125	78	1.65	0		U	S		1
GP1.08	045.0	10.02	JT	125	85	1.27	0		C	S		1
GP1.08	046.0	10.65	JT	274	89	1.04	0	T	U	R		2
GP1.08	047.0	10.75	JT	129	80	1.42	0	T	P	S		1
GP1.08	048.0	11.11	JT	133	80	3.00	0	T	P			1
GP1.09	049.0	0.14	JT	298	80	0.50	0	T	P	S		1
GP1.09	050.0	0.25	JT	119	75	2.00	0	T	P	S		3
GP1.09	051.0	0.60	JT	127	76	2.00	0	T	P	S		1
GP1.09	052.0	0.97	JT	126	85	1.00	0	T	P	S		3
GP1.09	053.0	1.29	JT	284	81	1.50	0	T	P	S		2
GP1.09	054.0	1.29	JT	299	90	0.50	0	T				3
GP1.09	055.0	1.68	JT	124	70	1.50	0	T	P	S		2
GP1.09	056.0	1.85	JT	122	86	1.00	0		C	S		3
GP1.09	057.0	1.94	JT	124	87	1.50	0		C	S		2
GP1.09	058.0	2.19	JT	148	71	1.00	0	T	P	S		2
GP1.09	059.0	2.42	JT	114	80	1.00	0	G	P	S		2
GP1.09	060.0	2.82	JT	293	74	1.53	0	G	P	S		3
GP1.09	061.0	3.20	JT	131	88	1.87	0	T	P	S		3
GP1.09	062.0	3.58	JT	121	80	2.00	0	T	P	S		0

Site	NNum	Space	Type	Ddr	DI	Trace	Cen	Mz	LaR	Ssr	RkT	Trm
GP1.09	063.0	3.57	JT	127	86	4.00	1	T	P	S		1
GP1.09	064.0	3.82	JT	122	78	5.00	1	T	P	S		1
GP1.09	065.0	3.89	JT	320	83	5.00	1	T	P	S		1
GP1.09	066.0	4.06	JT	130	80	5.00	1	T	P	S		1
GP1.09	067.0	4.12	JT	124	82	4.50	0	T	P	S		2
GP1.10	001.0	4.22	JT	136	76	3.00	0	T	P	S		2
GP1.10	002.0	4.38	JT	142	76	0.95	0	T	C	S		2
GP1.10	003.0	4.89	JT	126	75	1.67	0	T	P	S		2
GP1.10	004.0	5.38	JT	122	86	1.67	0	T	P	S		2
GP1.10	005.0	5.62	JT	144	74	0.89	1		P	S		1
GP1.10	006.0	6.10	JT	132	84	4.00	0	T	P	S		2
GP1.10	007.0	6.18	JT	125	86	1.60	0	T	P	S		2
GP1.10	008.0	6.29	JT	292	80	5.00	0	T	P	S		2
GP1.10	009.0	6.27	JT	286	82	5.00	1		C	S		1
GP1.10	010.0	6.54	JT	126	88	1.37	0		I	S		
GP1.10	011.0	6.79	JT	317	84	1.00	0	T	P	S		2
GP1.10	012.0	7.22	JT	316	67	0.50	0	T	R	S		2
GP1.10	013.0	7.56	JT	306	82	5.00	0	T	P	S		2
GP1.10	014.0	7.39	JT	160	80	0.55	0	T	P	R		2
GP1.10	015.0	8.09	JT	137	88	4.50	0	T	P	S		2
GP1.10	016.0	8.57	JT	288	85	0.55	0		P	S		3
GP1.10	017.0	8.57	JT	326	86	5.00	0		P	S		3
GP1.10	018.0	8.90	JT	145	89	0.65	0		C	S		2
GP1.10	019.0	9.60	JT	298	89	0.60	0	T	P	S		2
GP1.10	020.0	10.22	JT	135	87	1.40	0	T	P	S		2
GP1.11	001.0	20.30	JT	331	86	0.80	0		P	S	M	0
GP1.11	002.0	20.80	JT	148	70	1.35	1		P	S	M	1
GP1.11	003.0	20.83	JT	151	75	1.35	1		P	S	M	1
GP1.11	004.0	21.55	JT	158	65	1.40	1		S	S	M	1
GP1.11	005.0	21.80	JT	153	67	0.83	0		P	S	M	1
GP1.11	006.0	22.18	JT	141	85	1.14	1	G	S	S	M	0
GP1.11	007.0	22.45	JT	263	54	0.95	0		C	R	M	1
GP1.11	008.0	23.13	JT	144	70	1.50	1		C	S	M	1
GP1.11	009.0	24.90	JT	226	75	1.40	1		U	R		0
GP1.12	010.0	26.85	JT	144	70	1.35	0		S	R		1
GP1.12	011.0	27.02	JT	144	74	1.40	1		S	R		0
GP1.12	012.0	27.35	JT	174	67	1.35	1		S	R		0
GP1.12	013.0	27.45	JT	164	73	1.12	1		C	R		0
GP1.12	014.0	27.40	JT	220	80	0.65	1		C	S		0
GP1.12	015.0	28.10	JT	162	77	1.65	1		P	S		1
GP1.12	016.0	28.40	JT	215	76	1.40	0		I	S		1
GP1.12	017.0	28.70	JT	213	74	1.35	1		I	S		1
GP1.12	018.0	30.90	JT	213	86	1.50	0		I	R		0
GP1.12	019.0	31.50	JT	156	80	2.00	1		P	S		1
GP1.12	020.0	31.70	JT	150	86	1.45	0		P	S		1
GP1.12	021.0	31.75	JT	146	89	1.35	0		S	S		0
GP1.12	022.0	32.20	JT	141	80	1.00	0		C	S		1
GP1.12	023.0	32.45	JT	150	76	1.00	0		C	S		1
GP1.12	024.0	31.80	JT	217	69	2.10	1		P	R		1
GP1.12	025.0	32.80	JT	150	68	0.75	0		P	R		1
GP1.12	026.0	33.55	JT	136	87	0.55	0		P	R		1
GP1.12	027.0	34.50	JT	137	89	1.70	0		P	S		0
GP1.12	028.0	35.80	JT	147	89	1.40	0		P	S		0
GP1.12	029.0	35.10	JT	213	66	1.60	1		P	S		1
GP1.12	030.0	36.10	JT	208	81	0.70	0		P	S		1
GP1.12	031.0	37.30	JT	149	76	1.55	0		P	S		1
GP1.12	032.0	37.50	JT	151	75	1.10	0		P	R		1
GP1.12	033.0		JT	151	84	0.70	1		S	S		0
GP1.12	034.0		JT	261	83	0.70	0		S	S		1
GP1.12	035.0		JT	149	75	0.85	1		P	S		1
GP2.01	001.0	0.00	JT	296	82	1.75	2	T	P	S		4

Site	NNum	Space	Type	Ddr	DI	Trace	Cen	Mz	LaR	Ssr	RkT	Trm
GP2.01	002.0	0.28	JT	287	77	1.70	0	T	P	S		0
GP2.01	003.0	0.44	JT	292	81	1.10	0	T	C	S		0
GP2.01	004.0	0.55	JT	284	76	1.70	2	T	P	S		4
GP2.01	005.0	0.71	FZ	291	75	1.76	2	T	P	R		4
GP2.01	006.0	0.85	FZ	278	78	1.68	2	T	P	S		4
GP2.01	007.0	1.18	JT	281	77	1.57	2	T	C	S		4
GP2.01	008.0	1.37	FZ	286	89	1.57	2	T	P	S		4
GP2.01	009.0	1.38	FZ	266	74	1.63	2	T	C	C		4
GP2.01	010.0	1.64	FZ	280	80	1.62	2	T	P	S		4
GP2.01	011.0	1.85	JT	185	67	0.19	2		P	S		4
GP2.01	012.0	2.12	FZ	284	80	1.56	2	T	P	S		4
GP2.01	013.0	2.22	FZ	303	86	1.66	2	T	C	S		4
GP2.01	014.0	2.73	JT	293	76	1.78	2	T	P	S		4
GP2.01	015.0	2.93	JT	313	88	1.95	2	T	C	S		4
GP2.01	016.0	3.10	FZ	301	72	1.85	2	T	C	S		4
GP2.01	017.0	3.40	JT	325	82	1.52	1	T	P	S		1
GP2.01	018.0	3.34	JT	276	71	2.15	2	T	P	S		4
GP2.01	019.0	3.47	JT	280	66	1.85	2	T	P	S		4
GP2.01	020.0	3.67	JT	284	64	2.10	2	T	P	S		4
GP2.01	021.0	4.23	JT	315	80	1.83	1		P	S		1
GP2.01	022.0	4.07	FZ	265	70	1.83	2	T	P	S		4
GP2.01	023.0	4.58	FZ	299	85	2.05	2	T	P	S		4
GP2.01	024.0	4.75	JT	279	70	1.56	1	T	C	S		1
GP2.01	025.0	5.01	JT	296	82	1.05	0	T	C	S		2
GP2.01	025.A	4.51	JT	249	56	1.26	1		P	S		0
GP2.01	026.0	5.13	FZ	284	66	1.84	2	T	P	S		4
GP2.01	027.0	5.38	JT	285	73	1.52	1	T	C	S		1
GP2.01	028.0	5.83	FZ	286	77	1.93	2	T	P	S		4
GP2.01	029.0	5.96	JT	276	74	2.00	2	T	C	S		4
GP2.01	030.0	6.45	FZ	293	73	2.08	2	T	P	S		4
GP2.01	031.0	6.54	JT	294	76	0.98	1		P	S		1
GP2.01	032.0	6.72	JT	281	72	2.12	2		P	S		4
GP2.01	033.0	7.21	FZ	299	82	2.10	2	T	P	S		4
GP2.02	001.0	7.48	FZ	302	80	3.10	2	T	P	S		4
GP2.02	002.0	7.50	FZ	308	87	2.75	2	T	P	S		4
GP2.02	003.0	8.00	FZ	309	89	1.74	1	T	C	S		1
GP2.02	004.0	8.18	FZ	294	81	1.72	1	T	P	S		1
GP2.02	005.0	8.35	FZ	300	83	1.50	1	T	C	S		1
GP2.02	006.0	8.64	FZ	286	79	2.75	2	T	C	S		4
GP2.02	007.0	8.75	FZ	295	76	0.78	0	T	P	S		2
GP2.02	008.0	8.88	FZ	294	76	1.54	1	T	P	S		1
GP2.02	009.0	9.02	JT	298	77	2.96	2	T	C	S		4
GP2.02	010.0	9.36	JT	298	70	2.75	2	T	C	S		4
GP2.02	011.0	9.72	FZ	291	79	2.87	2	T	P	S		4
GP2.02	012.0	9.92	FZ	280	76	2.74	2	T	P	S		4
GP2.02	013.0	10.12	JT	301	80	2.24	1	T	C	S		1
GP2.02	014.0	10.23	JT	297	87	2.84	2	T	P	S		4
GP2.02	015.0	10.29	JT	291	74	2.61	1	T	P	S		1
GP2.02	016.0	10.51	JT	287	67	2.77	2	T	P	S		4
GP2.02	017.0	10.67	FZ	290	78	3.01	2	T	P	S		4
GP2.02	018.0	10.83	JT	300	71	1.38	2	T	P	S		4
GP2.02	019.0	10.92	JT	304	55	1.72	1	T	C	S		1
GP2.02	020.0	11.05	FZ	300	87	2.10	1	T	C	S		0
GP2.02	021.0	11.18	JT	307	75	2.24	1	T	C	S		1
GP2.02	022.0	11.38	JT	306	65	1.55	1	T	C	S		1
GP2.02	023.0	11.53	JT	301	75	2.88	2	T	P	S		4
GP2.02	024.0	11.72	JT	291	70	2.40	1	T	C	S		1
GP2.02	025.0	11.86	FZ	304	86	2.77	1	T	P	S		1
GP2.02	026.0	12.04	FZ	283	74	2.93	2	T	P	S		4
GP2.02	027.0	12.30	JT	289	88	2.91	2	T	P	S		4
GP2.02	028.0	12.48	JT	286	81	1.72	0	T	C	S		2

Site	NNum	Space	Type	Ddr	DI	Trace	Cen	Mz	LSR	Ser	RkT	Trm
GP2.02	029.0	12.55	JT	290	65	2.05	0	T	C	S		2
GP2.02	030.0	12.63	JT	296	80	2.98	2	T	P	S		4
GP2.02	031.0	12.72	FZ	284	73	3.00	2	T	P	S		4
GP2.02	032.0	13.08	FZ	279	72	2.98	2	T	C	S		4
GP2.02	033.0	13.42	JT	298	85	3.19	2	T	P	S		4
GP2.02	034.0	13.65	JT	281	67	1.61	0	T	C	S		2
GP2.02	035.0	13.83	JT	287	68	2.90	2	T	P	S		4
GP2.02	036.0	13.96	JT	285	70	1.96	0	T	P	S		2
GP2.02	037.0	14.39	JT	284	80	2.94	2	T	P	S		4
GP2.02	038.0	14.66	JT	291	82	1.77	1	T	C	S		1
GP2.02	039.0	14.72	FZ	286	81	2.23	1	T	C	S		1
GP2.02	040.0	14.89	FZ	292	89	2.97	2	T	P	S		4
GP2.02	041.0	15.11	FZ	281	82	3.09	2	T	P	S		4
GP2.02	042.0	15.21	FZ	288	77	2.95	2	T	P	S		4
GP2.02	043.0	15.30	JT	300	85	3.14	2	T	C	S		4
GP2.02	044.0	15.45	JT	286	80	1.96	1	T	P	S		1
GP2.02	045.0	15.68	JT	280	65	1.96	1	T	P	S		1
GP2.02	046.0	15.92	FZ	281	72	3.09	2	T	P	S		4
GP2.02	047.0	16.24	FZ	283	80	3.06	2	T	P	S		4
GP2.02	048.0	16.56	FZ	296	89	3.13	2	T	P	S		4
GP2.02	049.0	16.70	JT	296	90	3.22	2	T	C	S		4
GP2.02	050.0	16.97	JT	295	87	3.34	2	T	C	S		4
GP2.02	051.0	17.10	JT	294	83	2.44	1	T	P	S		1
GP2.02	052.0	17.20	JT	295	90	1.40	0	T	C	S		2
GP2.02	053.0	17.55	JT	274	81	1.16	0	T	C	R		2
GP2.02	054.0	17.80	JT	294	77	1.34	2	T	P	S		4
GP2.05	001.0	0.00	JT	128	87	1.30	0	T	P	S		0
GP2.05	002.0	0.31	FZ	121	89	3.00	1	T	I	R		0
GP2.05	003.0	0.61	JT	295	79	3.00	1		I	R		0
GP2.05	004.0	0.79	JT	326	89	2.00	1		I	R		0
GP2.05	005.0	1.22	JT	138	84	2.00	1		U	R		0
GP2.05	006.0	1.65	JT	133	84	3.00	1		C	R		0
GP2.05	007.0	2.07	JT	141	70	1.60	1		C	R		1
GP2.05	008.0	2.53	JT	137	89	1.28	0		I	R		1
GP2.05	009.0	2.62	JT	108	79	1.45	0		I	R		0
GP2.05	010.0	2.84	JT	146	77	1.40	0		I	R		0
GP2.05	011.0	2.90	JT	146	81	0.72	0		P	R		0
GP2.05	012.0	2.99	JT	145	85	0.82	0		P	R		0
GP2.05	013.0	3.23	JT	151	89	1.58	1		I	R		0
GP2.05	014.0	3.58	JT	135	81	1.28	0		I	R		0
GP2.05	015.0	3.96	JT	139	79	1.90	0	T	P	R		1
GP2.05	016.0	4.36	JT	147	82	1.40	0	T	S	S		1
GP2.05	017.0	4.72	JT	138	78	1.52	1	T	C	S		1
GP2.05	018.0	5.03	JT	136	78	2.00	1	T	P	S		1
GP2.05	019.0	5.41	JT	139	81	1.60	2	T	P	S		4
GP2.05	020.0	5.76	JT	140	89	2.00	0	T	S	S		0
GP2.06	021.0	0.38	JT	130	85	2.80	1	T	C	S		1
GP2.06	022.0	0.69	JT	138	74	1.45	1		P	S		0
GP2.06	023.0	1.07	JT	146	80	0.98	1	CL	P	S		0
GP2.06	024.0	1.91	FZ	134	84	3.00	1	T	I	R		0
GP2.06	025.0	2.21	JT	141	78	3.00	2	T	P	S		4
GP2.06	026.0	2.53	JT	134	76	0.98	1	T	P	S		0
GP2.07	001.0	0.00	JT	136	82	1.60	1		S	S		1
GP2.07	002.0	0.27	JT	139	89	1.65	1		U	R		1
GP2.07	003.0	0.38	JT	181	78	2.60	0		U	R		2
GP2.07	004.0	0.61	JT	224	84	0.74	0		U	R		1
GP2.07	005.0	0.61	JT	138	86	0.74	0		U	R		2
GP2.07	006.0	1.07	JT	314	81	1.67	0		U	R		2
GP2.07	007.0	1.86	JT	320	86	1.24	0		P	S		1
GP2.07	008.0	2.07	JT	320	89	1.47	1		S	R		0
GP2.07	009.0	1.83	JT	209	69	1.60	1		U	R		0

Site	NNum	Space	Type	Ddr	DI	Trace	Cen	Mz	LSR	Ssr	RkT	Trm
GP2.07	010.0	2.44	JT	315	80	0.91	0		P	S		1
GP2.07	011.0	2.90	FZ	327	89	1.34	1		P	S		1
GP2.07	012.0	3.35	JT	150	87	0.90	0		P	S		1
GP2.07	013.0	3.66	FZ	321	85	0.95	0	T	P	S		1
GP2.07	014.0	4.57	JT	195	76	1.20	1	S	I	R		0
GP2.07	015.0	4.45	JT	128	89	0.67	0	T	P	R		1
GP2.07	016.0	4.66	JT	142	87	1.76	1		I	R		0
GP2.07	017.0	4.88	JT	315	80	0.93	0		I	R		1
GP2.07	018.0	5.09	JT	300	85	0.68	0		I	R		1
GP2.07	019.0	5.21	JT	326	86	0.84	0		P	R		1
GP2.07	020.0	5.41	JT	311	75	1.00	0		P	R		0
GP2.07	021.0	5.56	JT	158	81	1.10	0		P	R		1
GP2.07	022.0	5.64	JT	314	78	1.71	1		P	R		0
GPP1.00	081.0		JT	125	85	1.41	2		P	S	M	4
GPP1.00	082.0		JT	135	75	1.68	1		C	S	M	0
GPP1.00	083.0		JT	114	80	2.67	1		P	S	M	1
GPP1.00	084.0		JT	108	90	3.44	2		P	S	M	4
GPP1.00	085.0		JT	211	86	0.47	2		I	S	M	4
GPP1.00	086.0		JT	132	84	0.35	1		I	S	M	1
GPP1.00	087.0		JT	127	85	2.04	1		U	S	M	0
GPP1.00	088.0		JT	131	88	1.23	0		C	S	M	0
GPP1.00	089.0		JT	138	88	2.15	0	T	C	S	M	2
GPP1.00	090.0		FZ	132	77	14.12	1		S	S	M	0
GPP1.00	091.0		JT	110	83	1.45	1		P	S	M	1
GPP1.00	092.0		JT	214	79	0.97	0		S	S	M	2
GPP1.00	093.0		JT	147	90	0.67	0		P	S	M	1
GPP1.00	094.0		JT	135	70	2.45	1	T	U	S	M	0
GPP1.00	095.0		JT	112	86	0.78	1		P	S	M	1
GPP1.00	096.0		JT	137	80	0.33	1	T	S	S	M	1
GPP1.00	097.0		JT	78	88	0.22	0		P	R	M	2
GPP1.00	098.0		JT	202	84	0.35	0		I	R	M	2
GPP1.00	099.0		JT	130	85	1.39	0		P	S	M	1
GPP1.00	100.0		JT	35	80	0.82	1		P	S	M	0
GPP1.00	101.0		JT	216	70	0.67	0		C	S	M	1
GPP1.00	102.0		JT	302	86	0.90	2	T	S	S	M	4
GPP1.00	103.0		JT	128	78	1.12	1	T	S	S	M	1
GPP1.00	104.0		JT	213	70	0.32	1	T	U	S	M	1
GPP1.00	105.0		JT	128	80	1.34	1	T	S	S	M	1
GPP1.00	106.0		JT	121	85	0.98	1	T	U	S	M	1
GPP1.00	107.0		JT	133	75	1.44	0	T	U	S	M	0
GPP1.00	108.0		JT	61	83	0.33	0		C	S	M	2
GPP1.00	109.0		JT	248	80	0.31	0		C	S	M	2
GPP1.00	110.0		JT	173	59	0.60	0	T	C	S	M	2
GPP1.00	111.0		JT	202	80	0.38	0		U	S	M	1
GPP1.00	112.0		JT	19	85	0.32	0	T	U	S	M	1
GPP1.00	113.0		JT	123	81	0.67	0		C	S	M	0
GPP1.00	114.0		JT	129	81	0.89	0		U	S	M	0
GPP1.00	115.0		JT	129	76	2.00	1	T	P	S	M	0
GPP1.00	116.0		JT	315	84	1.59	1		U	S	M	1
GPP1.00	117.0		FZ	141	80	2.30	2	T	P	S	M	4
GPP1.00	118.0		JT	210	72	0.38	0		U	S	M	2
GPP1.00	119.0		JT	66	89	0.53	0		U	R	M	1
GPP1.00	120.0		JT	213	75	0.77	0		U	R	M	2
GPP1.00	121.0		JT	219	73	3.27	0		S	S	M	1
GPP1.01	001.0	3.12	JT	124	83	0.80	0		C	S	M	1
GPP1.01	002.0	3.19	JT	126	75	1.65	0		C	S	M	0
GPP1.01	003.0	3.20	JT	121	75	0.26	0		U	S	M	0
GPP1.01	004.0	3.38	JT	119	84	3.80	1	T	P	S	M	1
GPP1.01	005.0	3.45	JT	212	79	0.19	0		U	S	M	2
GPP1.01	006.0	3.80	JT	116	74	0.45	0		P	S	M	0
GPP1.01	007.0	4.00	JT	232	64	0.27	0		U	R	M	2

Site	NNum	Space	Type	Ddr	DI	Trace	Cen	Mz	LaR	Ssr	RkT	Trm
GPP1.01	008.0	4.11	JT	124	70	0.45	1		P	S	M	1
GPP1.01	009.0	4.20	JT	228	73	0.20	0		P	R	M	2
GPP1.01	010.0	4.33	JT	123	59	0.50	0		P	R	M	0
GPP1.01	011.0	4.58	JT	140	75	1.30	0		P	R	M	0
GPP1.01	012.0	4.66	JT	115	71	0.35	0		P	S	M	0
GPP1.01	013.0	4.88	JT	127	79	0.54	0		P	S	M	0
GPP1.01	014.0	5.10	JT	127	65	1.10	0		C	S	M	1
GPP1.01	015.0	5.32	JT	197	67	0.38	0		P	R	M	2
GPP1.01	016.0	5.43	JT	132	80	0.43	0		P	S	M	0
GPP1.01	017.0	5.50	JT	129	66	0.90	0	T	P	S	M	0
GPP1.01	018.0	5.51	JT	133	76	1.00	0		P	S	M	0
GPP1.01	019.0	5.82	JT	127	88	3.25	0	T	P	S	M	0
GPP1.01	020.0	6.25	JT	125	78	0.65	1		P	S	M	0
GPP1.01	021.0	6.54	JT	109	74	1.80	0	T	P	S	M	2
GPP1.01	022.0	6.60	FZ	125	80	3.20	2	T	P	S	M	4
GPP1.01	023.0	6.72	JT	238	80	0.30	0		P	R	M	2
GPP1.01	024.0	6.78	JT	126	82	0.30	2		P	S	M	4
GPP1.01	025.0	6.80	JT	124	76	0.30	0		P	S	M	0
GPP1.01	026.0	6.90	JT	131	89	2.70	1		P	S	M	0
GPP1.01	027.0	7.06	FZ	126	84	3.20	0		P	S	M	0
GPP1.01	028.0	7.52	JT	124	89	3.00	1		P	S	M	0
GPP1.01	029.0	7.78	JT	138	75	0.48	0		P	S	M	1
GPP1.01	030.0	8.29	JT	145	75	0.22	2		P	S	M	4
GPP1.01	031.0	8.57	JT	130	85	1.16	1		P	S	M	0
GPP1.01	032.0	9.34	JT	135	76	0.90	1		P	S	M	0
GPP1.01	033.0	9.66	JT	128	85	3.16	0		P	S	M	0
GPP1.01	034.0	9.90	JT	124	85	1.80	1		C	S	M	0
GPP1.01	035.0	10.00	JT	126	80	0.85	0		C	S	M	0
GPP1.01	036.0	10.20	JT	232	76	0.16	0		P	S	M	2
GPP1.01	037.0	10.23	JT	149	79	0.90	1	T	P	S	M	1
GPP1.01	038.0	10.38	JT	127	69	2.60	0	T	C	S		0
GPP1.02	001.0	0.18	JT	129	89	1.55	0		P	S		0
GPP1.02	002.0	0.64	FZ	131	85	0.82	0		P	S		1
GPP1.02	003.0	0.77	JT	121	74	0.38	2		C	S		4
GPP1.02	004.0	0.99	JT	134	87	0.68	0		I	R		1
GPP1.02	005.0	1.05	JT	187	70	0.35	0		I	R		2
GPP1.02	006.0	1.09	JT	100	81	0.53	0		I	R		3
GPP1.02	007.0	1.20	JT	115	85	0.88	0		I	R		0
GPP1.02	008.0	1.27	JT	128	82	0.41	0		C	R		0
GPP1.02	009.0	1.35	JT	192	65	0.24	0		S	R		2
GPP1.02	010.0	1.53	JT	119	79	1.61	1	T	S	S		0
GPP1.02	011.0	1.56	JT	122	87	0.47	0		S	S		1
GPP1.02	012.0	1.75	JT	134	85	0.53	0		P	S		1
GPP1.02	013.0	1.75	JT	119	88	0.42	0		C	S		1
GPP1.02	014.0	1.88	JT	126	85	0.31	0		P	S		0
GPP1.02	015.0	1.95	JT	166	80	0.22	0		P	R		0
GPP1.02	016.0	2.12	JT	159	84	0.25	0		S	R		1
GPP1.02	017.0	2.37	JT	121	89	0.32	0		C	R		1
GPP1.02	018.0	2.48	JT	308	89	0.28	0		I	R		1
GPP1.02	019.0	2.70	JT	134	82	2.75	0	T	C	R		0
GPP1.02	020.0	2.86	JT	137	84	1.05	0	T	C	R		2
GPP1.02	021.0	3.09	JT	224	70	0.28	0		I	R		2
GPP1.02	022.0	3.17	JT	127	80	0.55	0		P	S		0
GPP1.02	023.0	3.23	JT	131	84	1.47	0	T	C	S		0
GPP1.02	024.0	3.26	JT	125	89	0.28	0		P	S		0
GPP1.02	025.0	3.39	JT	125	89	0.17	0		P	S		1
GPP1.02	026.0	3.46	JT	124	88	1.25	0		I	S		0
GPP1.02	027.0	3.69	JT	126	85	1.80	1	T	P	S		0
GPP1.02	028.0	3.75	JT	126	87	0.32	0		C	S		1
GPP1.02	029.0	3.96	JT	128	86	0.47	0	T	S	S		1
GPP1.02	030.0	4.13	JT	126	85	1.01	0	T	C	S		1

Site	NNum	Space	Type	Ddr	DI	Trace	Cen	Mz	LaR	Ssr	RkT	Trm
GPP1.02	031.0	4.20	JT	121	84	0.97	0		C	S		1
GPP1.02	032.0	4.40	JT	126	89	0.27	0		C	S		2
GPP1.02	033.0	4.52	JT	211	71	0.42	0		I	S		2
GPP1.02	034.0	4.65	JT	133	87	0.44	0		P	S		1
GPP1.02	035.0	4.95	JT	139	89	1.06	0		I	S		0
GPP1.02	036.0	5.24	JT	127	86	0.58	0		P	S		0
GPP1.02	037.0	5.28	JT	125	89	0.67	0		U	S		0
GPP1.02	038.0	5.49	JT	130	88	0.64	0		C	S		1
GPP1.02	039.0	5.61	JT	135	69	0.23	0		C	S		1
GPP1.02	040.0	5.68	JT	122	79	1.44	0	T	C	S		0
GPP1.02	041.0	5.90	JT	124	82	1.76	0	T	I	S		1
GPP1.02	042.0	5.93	JT	138	78	1.70	0	T	C	S		1
GPP1.02	043.0	6.18	JT	128	85	0.60	0		P	S		0
GPP1.02	044.0	6.32	JT	133	82	0.42	0		C	S		1
GPP1.02	045.0	6.35	JT	168	61	0.12	0		P	S		2
GPP1.02	046.0	6.49	JT	132	79	0.35	0		I	S		0
GPP1.02	047.0	6.56	JT	133	86	1.07	0	FE	I	R		0
GPP1.02	048.0	6.65	JT	247	85	0.15	0	FE	P	S		1
GPP1.02	049.0	6.75	JT	127	84	0.16	0	FE	S	S		1
GPP1.02	050.0	6.80	JT	152	77	0.55	0	T	I	S		1
GPP1.02	051.0	7.08	JT	128	86	0.18	0	FE	C	S		1
GPP1.02	052.0	7.15	JT	310	86	1.80	0	T	C	S		1
GPP1.02	053.0	7.32	JT	133	72	0.83	0	FE	I	S		0
GPP1.02	054.0	7.51	JT	123	86	0.70	0	FE	C	S		0
GPP1.02	055.0	7.77	JT	124	87	0.40	0	FE	I	R		1
GPP1.02	056.0	7.97	JT	29	55	0.54	0	FE	S	S		0
GPP1.02	057.0	8.01	JT	120	88	0.82	0	FE	I	S		0
GPP1.02	058.0	8.43	JT	12	64	0.24	0	T	C	R		2
GPP1.02	059.0	8.48	JT	105	86	4.00	1	T	P	S	M	1
GPP1.03	00A.0	2.65	JT	136	80	0.94	1		P	S	M	1
GPP1.03	00B.0	3.10	JT	299	88	2.30	0		P	S	M	1
GPP1.03	00C.0	3.45	JT	4	86	0.46	0		P	S	M	1
GPP1.03	00D.0	3.52	JT	122	81	1.70	1		P	S	M	0
GPP1.03	00E.0	3.62	JT	134	86	0.88	0		C	S	M	0
GPP1.03	00F.0	3.75	JT	135	80	0.90	1		C	S	M	0
GPP1.03	00G.0	3.78	JT	140	75	0.49	1		U	S	M	0
GPP1.03	00H.0	3.81	JT	241	75	0.38	0		C	S	M	1
GPP1.04	001.0	0.16	JT	300	85	0.33	1	T	C	S	M	0
GPP1.04	002.0	0.35	JT	153	86	1.30	0	T	P	S	M	1
GPP1.04	003.0	0.55	JT	316	90	0.14	0	T	P	S	M	1
GPP1.04	004.0	0.65	JT	196	77	0.09	0		C	S	M	2
GPP1.04	005.0	0.73	JT	32	80	0.38	0		C	S	M	2
GPP1.04	006.0	0.84	JT	122	85	3.22	0	T	P	S	M	1
GPP1.04	007.0	0.86	JT	200	80	0.26	0		S	S	M	1
GPP1.04	008.0	1.01	JT	205	89	0.24	0		S	S	M	2
GPP1.04	009.0	1.35	FZ	141	80	1.54	1		U	S		0
GPP1.04	010.0	1.58	JT	133	77	0.48	0		P	S	SP	0
GPP1.04	011.0	1.71	JT	135	78	0.21	0		P	S	SP	0
GPP1.04	012.0	2.12	JT	150	54	2.60	0		U	S	SP	3
GPP1.04	013.0	2.18	JT	138	79	0.20	0		P	S	SP	1
GPP1.04	014.0	2.41	JT	135	70	0.54	0		P	S	SP	0
GPP1.04	015.0	2.55	JT	127	72	0.72	0		U	S	SP	0
GPP1.04	016.0	3.13	JT	144	83	0.27	0		P	S	SP	1
GPP1.04	017.0	3.18	JT	144	85	0.33	0		C	S	SP	0
GPP1.04	018.0	3.42	FZ	236	76	0.64	0		U	S	SP	0
GPP1.04	019.0	4.80	FZ	129	78	3.55	0	T	P	S	P	0
GPP1.04	020.0	4.90	JT	222	85	0.14	1		P	S	M	0
GPP1.04	021.0	5.10	FZ	122	85	7.14	1	T	P	S	P	0
GPP1.04	022.0	5.70	JT	237	76	0.30	0		C	S	P	2
GPP1.04	023.0	5.75	JT	140	79	0.36	0		C	S	P	1
GPP1.04	024.0	5.86	JT	2	79	0.90	0		U	S	P	1

Site	NNum	Space	Type	Ddr	DI	Trace	Cen	Mz	LsR	Ssr	RkT	Trm
GPP1.04	025.0	6.16	JT	128	78	0.98	0	T	U	S		3
GPP1.04	026.0	6.22	JT	213	80	0.28	0		U	S		2
GPP1.04	027.0	7.22	JT	126	77	1.56	0		U	S	AP	3
GPP1.04	028.0	8.13	JT	130	77	0.80	0	T	S	S	AP	0
GPP1.04	029.0	8.18	JT	214	80	0.14	0	T	S	S	AP	2
GPP1.04	030.0	8.45	JT	208	76	0.22	0		P	S	AP	2
GPP1.04	031.0	8.36	FZ	133	81	5.64	0		U	S	AP	3
GPP1.04	032.0	8.58	FZ	133	83	3.52	1	T	U	S	AP	1
GPP1.04	033.0	9.60	JT	134	85	0.16	1			S	AP	0
GPP1.04	034.0	10.00	JT	136	84	0.41	1		S	S	AP	1
GPP1.04	035.0	10.05	JT	243	83	0.18	0		U	S	AP	2
GPP1.04	036.0	10.80	JT	116	80	0.37	1		P	S	AP	0
GPP1.04	037.0	11.21	JT	209	89	0.21	0		C	S		2
GPP1.04	038.0	11.42	JT	312	85	1.08	1		P	S		3
GPP1.04	039.0	12.69	JT	128	81	0.41	2		U	R		4
GPP1.04	040.0	12.75	JT	223	82	0.24	0		U	S		2
GPP1.05	041.0	0.00	JT	298	90	0.63	1	T	P	S	AP	0
GPP1.05	042.0	0.36	JT	311	87	0.56	1	T	P	S	AP	1
GPP1.05	043.0	0.84	JT	128	87	1.86	0	T	P	S	AP	1
GPP1.05	044.0	0.94	JT	118	85	3.34	0	T	U	S	AP	1
GPP1.05	045.0	1.03	JT	110	89	4.12	2	T	U	S	AP	4
GPP1.05	046.0	1.15	JT	215	85	1.04	1		U	R	AP	1
GPP1.05	047.0	1.38	JT	114	86	0.32	1		I	S	AP	1
GPP1.05	048.0	1.72	JT	295	86	0.99	1		C	S	AP	0
GPP1.05	049.0	1.98	JT	293	87	0.79	1	T	P	S	AP	1
GPP1.05	050.0	2.30	JT	127	88	0.62	1		P	S	AP	0
GPP1.05	051.0	2.65	JT	123	86	0.65	0		U	S	AP	0
GPP1.05	052.0	4.72	JT	288	85	1.17	1	T	U	R	AP	0
GPP1.05	053.0	4.79	JT	223	75	0.31	1		S	R	AP	0
GPP1.05	054.0	4.83	JT	133	87	0.39	1		P	S	AP	0
GPP1.05	055.0	4.88	JT	106	87	5.50	2	T	U	S	AP	4
GPP1.05	056.0	4.91	JT	105	84	0.86	0	T	U	S	AP	1
GPP1.05	057.0	5.08	JT	323	89	0.53	0		U	S	AP	2
GPP1.05	058.0	5.15	JT	136	82	0.41	1		P	S	AP	0
GPP1.05	059.0	5.17	JT	108	88	5.22	1	T	U	S	AP	0
GPP1.05	060.0	5.31	JT	138	83	0.52	1		C	S	AP	1
GPP1.05	061.0	5.61	JT	123	82	0.88	2		C	S	AP	4
GPP1.05	062.0	5.86	JT	133	90	0.55	2		U	S	AP	4
GPP1.05	063.0	6.25	JT	115	86	0.88	0		C	S	AP	0
GPP1.05	064.0	6.52	JT	124	90	0.73	1		C	S	AP	0
GPP1.05	065.0	7.17	JT	132	84	1.09	2		U	S	AP	4
GPP1.05	066.0	7.56	JT	129	82	0.99	1		P	S	AP	0
GPP1.05	067.0	8.16	JT	120	90	0.41	1		U	S	AP	1
GPP1.05	068.0	8.24	JT	140	82	0.29	1		S	S	AP	1
GPP1.05	069.0	8.32	JT	130	80	0.14	1		P	S	AP	0
GPP1.05	070.0	8.42	JT	104	80	0.14	1		P	S	AP	1
GPP1.05	071.0	9.38	JT	134	86	1.48	2		S	S	AP	4
GPP1.05	072.0	9.59	JT	124	90	3.35	1		U	S	AP	0
GPP1.05	073.0	9.83	JT	124	80	0.52	1		P	S	AP	0
GPP1.05	074.0	10.05	JT	126	85	0.56	1		S	S	AP	0
GPP1.05	075.0	10.26	JT	128	77	0.33	1		U	S	AP	0
GPP1.05	076.0	10.45	JT	126	80	1.62	0		U	S	AP	0
GPP1.05	077.0	10.63	JT	125	79	3.35	1		P	S	AP	0
GPP1.05	078.0	11.00	JT	118	78	2.14	0		S	S	AP	0
GPP1.05	079.0	11.20	JT	114	85	0.39	1		P	S	AP	1
GPP1.05	080.0	11.60	JT	130	86	7.10	0		S	S	AP	0
GPP2.00	001.0		JT	126	77	3.58	1		P	S	M	0
GPP2.00	002.0		JT	134	85	2.40	1	T	P	S	M	0
GPP2.00	003.0		JT	132	89	2.75	0		P	S	M	0
GPP2.00	004.0		JT	212	75	0.43	0		U	S	M	2
GPP2.00	005.0		JT	136	85	2.45	1		P	S	M	0

Site	NNum	Space	Type	Ddr	DI	Trace	Cen	Mz	LsR	Ssr	RkT	Trm
GPP2.00	006.0		JT	319	85	0.65	0		P	S	M	0
GPP2.00	007.0		JT	130	85	3.28	1	T	C	S	M	0
GPP2.00	008.0		JT	310	89	1.26	1		U	S	M	0
GPP2.00	009.0		JT	48	75	0.63	0		P	S	M	1
GPP2.00	00A.0		JT	135	89	0.44	1	T	P	S	M	0
GPP2.00	00B.0		JT	293	88	0.32	1	T	C	S	M	0
GPP2.00	00C.0		JT	130	87	0.74	1	T	P	S	M	0
GPP2.00	00D.0		JT	144	85	1.15	1	T	C	S	M	0
GPP2.00	00E.0		JT	315	75	1.54	1	T	P	S	M	0
GPP2.00	00F.0		JT	138	71	1.47	2	T	C	S	M	4
GPP2.00	00G.0		JT	136	73	0.54	1	T	P	S	M	0
GPP2.00	00H.0		JT	140	82	2.00	2	T	P	S	M	4
GPP2.00	00I.0		JT	140	82	1.50	0	T	P	S	M	0
GPP2.00	00J.0		JT	143	85	2.00	2	T	P	S	M	4
GPP2.00	00K.0		JT	228	88	0.50	0	T	P	S	M	2
GPP2.00	00L.0		JT	207	63	0.52	0	T	P	S	M	2
GPP2.00	00M.0		JT	205	60	0.40	0	T	C	S	M	1
GPP2.00	00N.0		JT	217	80	0.28	0	T	P	S	M	2
GPP2.00	010.0		JT	310	88	1.56	0		P	S	M	0
GPP2.00	011.0		JT	230	75	0.65	0		U	S	M	2
GPP2.00	012.0		JT	135	88	2.00	1		P	S	M	0
GPP2.00	013.0		JT	227	80	0.73	0		S	S	M	2
GPP2.00	014.0		FZ	143	75	3.00	0		S	S		0
GPP2.00	015.0		JT	136	85	1.53	1		P	S		0
GPP2.00	016.0		JT	143	85	1.51	1		C	S		0
GPP2.00	017.0		JT	231	80	0.50	0		S	S		2
GPP2.00	018.0		JT	140	85	1.40	1		P	S		0
GPP2.00	019.0		JT	155	85	1.05	1		P	S	M	0
GPP2.00	020.0		JT	325	90	1.00	1	T	P	S		0
GPP2.00	021.0		JT	50	76	1.03	0	T	C	S		1
GPP2.00	022.0		JT	55	85	1.39	0		S	S		1
GPP2.00	023.0		JT	314	85	2.64	1		P	S	AP	0
GPP2.00	024.0		JT	220	89	0.65	1		I	R		1
GPP2.00	025.0		JT	138	85	1.34	1		P	S		1
GPP2.00	026.0		JT	138	84	1.44	0		P	S		1
GPP2.00	027.0		JT	213	79	0.38	0		C	R		2
GPP2.00	028.0		JT	215	88	0.45	0		U	R		2
GPP2.00	029.0		JT	133	90	1.57	1		U	S		1
GPP2.00	030.0		JT	121	85	1.80	0		C	S		1
GPP2.00	031.0		JT	123	87	2.00	0		P	S		1
GPP2.00	032.0		JT	315	85	2.53	1		P	S		1
GPP2.00	033.0		JT	318	86	1.65	0		P	S		1
GPP2.00	034.0		JT	213	82	0.32	0		U	R		2
GPP2.00	035.0		JT	224	78	0.40	0		U	R		2
GPP2.00	036.0		JT	213	73	0.48	0		U	R		2
GPP2.00	037.0		JT	325	83	2.93	1		P	S	M	0
GPP2.00	038.0		JT	145	84	3.33	1	T	P	S		0
GPP2.00	039.0		JT	225	90	0.46	0		U	R		2
GPP2.00	040.0		JT	44	85	1.17	0		S	S		0
GPP2.00	041.0		JT	224	86	0.90	0	T	S	R		2
GPP2.00	042.0		JT	140	85	2.30	1		S	S		0
GPP2.00	043.0		JT	228	83	0.70	0		P	S		2
GPP2.00	044.0		JT	319	90	1.00	1	T	S	S		0
GPP2.00	045.0		JT	142	85	1.20	0		P	S		0
GPP2.00	046.0		JT	316	90	2.30	1	T	P	S		0
GPP2.00	047.0		JT	38	89	0.45	0		U	R		2
GPP2.00	048.0		JT	143	87	2.22	1		P	S		0
GPP2.00	049.0		JT	316	90	2.22	1		P	S		0
GPP2.00	050.0		JT	51	85	0.38	0		U	R		2
GPP2.00	051.0		JT	216	75	0.35	0		U	R		2
GPP2.00	052.0		JT	47	84	0.47	0		U	R		2

Site	NNu	Space	Type	Ddr	DI	Trace	Cen	Mz	LSR	Ssr	RkT	Trm
GPP2.00	053.0		JT	138	86	3.00	1	T	P	S		0
GPP2.00	054.0		JT	143	89	2.30	1		C	S		0
GPP2.00	055.0		JT	222	63	0.24	0		U	R		2
GPP2.00	056.0		JT	138	99	1.59	1		S	S		0
GPP2.00	057.0		JT	38	89	0.29	0		U	R		2
GPP2.00	058.0		JT	225	74	0.53	0		U	R		2
GPP2.00	059.0		JT	140	80	2.37	1		P	S		0
GPP2.00	060.0		JT	140	88	0.68	0		S	S		1
GPP2.00	061.0		JT	68	90	0.55	0		C	S		2
GPP2.00	062.0		JT	140	79	2.00	1		P	S		0
GPP2.00	063.0		JT	224	70	0.68	1		U	R		1
GPP2.00	064.0		JT	221	85	0.47	1		U	R		1
GPP2.00	065.0		JT	147	85	1.25	1		C	S	AP	0
GPP2.00	066.0		FZ	133	87	6.00	1		P	S		0
GPP2.00	067.0		JT	131	80	3.09	0		P	S	M	0
GPP2.00	068.0		JT	38	80	0.42	0		U	S	M	2
GPP2.00	069.0		JT	131	89	0.67	1		P	R		0
GPP2.00	070.0		JT	48	77	0.23	0		I	R		2
GPP2.00	071.0		JT	308	75	0.91	1	T	I	S		0
GPP2.00	072.0		JT	310	88	1.53	2		I	S		4
GPP2.00	073.0		JT	133	82	1.20	0	T	P	S		0
GPP2.00	074.0		JT	228	85	1.00	0	T	U	R		1
GPP2.00	075.0		JT	145	84	1.42	1	T	U	S		0
GPP2.00	076.0		JT	207	85	0.26	0		U	R		2
GPP2.00	077.0		JT	215	35	1.17	0	T	U	S		2
GPP2.00	078.0		JT	217	80	0.82	0		U	S		1
GPP2.00	079.0		JT	316	89	0.88	0	T	P	S		0
GPP2.00	080.0		JT	228	75	0.80	0		U	S		3
GPP2.00	081.0		JT	131	87	1.40	0		P	S		0
GPP2.00	082.0		JT	250	90	0.39	0		U	S		2
GPP2.00	083.0		JT	172	82							
GPP2.01	001.0	0.00	JT	138	84	0.37	2		P	S		4
GPP2.01	002.0	0.51	JT	135	87	0.85	2	T	P	S		4
GPP2.01	003.0	0.70	JT	217	70	0.30	1		P	S		1
GPP2.01	004.0	0.89	JT	137	84	0.53	1		P	S		1
GPP2.01	005.0	1.15	JT	226	80	0.45	1		P	S		1
GPP2.01	006.0	1.25	JT	134	90	0.68	2		P	S		4
GPP2.01	007.0	1.49	JT	136	88	0.81	1		P	S		0
GPP2.01	008.0	1.64	JT	222	79	0.55	1		P	S		0
GPP2.01	009.0	1.98	JT	135	84	0.26	1		P	S		0
GPP2.01	010.0	2.15	JT	128	85	8.00	2	CL	P	S		4
GPP2.01	011.0	2.48	JT	234	81	0.42	0		P	S		2
GPP2.01	012.0	2.47	JT	179	81	0.56	0	CL	P	R		0
GPP2.01	013.0	2.80	JT	137	85	0.68	0	CL	P	S		1
GPP2.01	014.0	3.03	JT	241	84	0.43	0	CL	P	S		2
GPP2.01	015.0	3.14	JT	137	81	3.67	0	T	P	S		0
GPP2.01	016.0	3.34	JT	142	84	0.73	2	CL	P	S		4
GPP2.01	017.0	3.56	JT	137	86	0.25	2	CL	P	R		4
GPP2.01	018.0	3.62	JT	130	79	1.10	2	CL	P	S	M	4
GPP2.01	019.0	3.72	JT	131	85	0.34	2	CL	P	S		4
GPP2.01	020.0	3.98	JT	146	87	0.33	2	CL	P	S		4
GPP2.01	021.0	4.22	JT	135	86	4.59	2	CL	P	S		4
GPP2.01	022.0	5.07	JT	124	85	7.87	0	T	P	S		3
GPP2.01	023.0	5.88	JT	130	85	0.73	0	CL	P	S		0
GPP2.01	024.0	6.07	JT	127	85	1.70	0	T	P	R		0
GPP2.01	025.0	6.13	JT	132	85	0.95	0	T	C	R		0
GPP2.01	026.0	6.42	JT	109	88	0.40	2		C	R		4
GPP2.01	027.0	5.63	JT	110	89	0.61	2		C	R		4
GPP2.01	028.0	7.11	JT	46	75	0.36	2		C	R		4
GPP2.01	029.0	7.39	JT	132	89	1.05	2	T	C	R	M	4
GPP2.01	030.0	10.77	JT	126	86	12.80	2	T	P	R		4

Site	NNum	Space	Type	Ddr	PI	Trace	Cap	Mz	LsR	Sar	RkT	Trm
GPP2.01	031.0	10.79	JT	25	85	0.54	0	CL	P	S		2
GPP2.01	032.0	11.00	JT	138	78	0.60	0		P	S		2
GPP2.01	033.0	11.08	JT	133	85	0.32	0		C	S		2
GPP2.01	034.0	11.21	JT	116	88	0.83	0	FE	C	S		2
GPP2.01	035.0	11.40	JT	108	90	0.70	0	FE	C	S		2
GPP2.01	036.0	11.65	JT	268	84	0.55	0	FE	P	S		2
GPP2.01	037.0	11.95	JT	138	78	0.45	0	FE	P	S		2
GPP2.01	038.0	12.15	JT	149	85	0.56	0	FE	P	S		2
GPP2.01	039.0	12.45	JT	139	84	0.50	0	FE	C	R		2
GPP2.01	040.0	12.66	JT	138	88	1.38	0	FE	C	R		2
GPP2.01	041.0	12.82	JT	132	88	0.35	0	FE	S	R		2
GPP2.01	042.0	12.92	JT	292	88	0.59	0	FE	P	R		2
GPP2.01	043.0	13.26	JT	301	90	0.81	0	FE	P	S		2
GPP2.01	044.0	13.50	JT	313	84	0.41	0	FE	C	S		2
GPP2.01	045.0	13.63	JT	122	87	0.86	0	FE	P	S		2
GPP2.01	046.0	14.04	JT	138	89	0.40	0	FE	S	S		2
GPP2.01	047.0	14.29	JT	143	85	0.48	0	FE	S	S		2
GPP2.01	048.0	14.52	JT	339	82	0.34	0	FE	C	S		2
GPP2.01	049.0	14.85	JT	143	86	0.48	0	FE	P	S		2
GPP2.01	050.0	15.30	JT	321	85	1.41	0	FE	P	S		2
GPP2.01	051.0	15.35	JT	138	85	6.50	1	FE	P	S		1
GPP2.01	052.0	15.45	JT	138	88	1.24	1	FE	P	S	M	1
GPP2.01	053.0	15.52	JT	135	86	1.21	1	FE	P	S		1
GPP2.01	054.0	17.75	JT	320	90	0.92	0	FE	C	S		2
GPP2.01	055.0	17.90	JT	232	83	1.25	0	FE	C	S		1
GPP2.01	056.0	18.50	JT	138	90	1.19	0	FE	C	S		2
GPP2.01	057.0	18.81	JT	118	85	2.96	1	FE	C	S	M	1
GPP2.01	058.0	21.36	JT	133	85	7.20	2	T	P	S		4
GPP2.01	059.0	21.80	JT	303	88	1.06	0	FE	C	S	M	2
GPP2.01	060.0	22.05	JT	308	86	0.44	0	FE	P	S		2
GPP2.01	061.0	22.20	JT	136	90	0.83	0	FE	P	S		2
GPP2.01	062.0	22.29	JT	312	90	1.02	0	FE	P	S		2
GPP2.01	063.0	22.68	JT	138	88	2.52	0	FE	S	S		2
GPP2.01	064.0	23.00	JT	130	90	2.32	0	T	S	S		2
GPP2.01	065.0	23.54	JT	131	90	1.08	0	T	P	S	M	2
GPP2.01	066.0	23.95	JT	123	90	1.46	0	T	C	S		2
GPP2.01	067.0	25.00	JT	132	85	2.48	0		C	S		2
GPP2.01	068.0	25.20	JT	222	80	0.35	0	T	P	S		2
GPP2.01	069.0	25.40	JT	138	88	2.19	0	T	P	S		2
GPP2.01	070.0	25.70	JT	130	90	2.15	0	CL	C	S		2
GPP2.01	071.0	26.01	JT	136	88	8.26	1	T	C	S		1
GPP2.01	072.0	26.17	JT	130	88	2.49	0	CL	C	S		2
GPP2.01	073.0	27.00	JT	143	85	1.50	0	T	P	S		2
GPP2.01	074.0	27.19	JT	128	80	1.79	0	T	P	S		2
GPP2.01	075.0	27.58	JT	149	82	2.06	0	T	C	S		2
GPP2.01	076.0	27.85	JT	134	89	3.31	2	T	C	S		4
GPP2.01	077.0	28.19	JT	138	88	2.53	1	T	C	S		1
GPP2.01	078.0	28.53	JT	135	88	3.07	1	T	C	S		1
GPP2.01	079.0	28.70	JT	131	89	2.30	1	T	P	S		1
GPP2.02	050.0	0.00	JT	135	84	0.69	0		P	S		0
GPP2.02	051.0	0.35	JT	215	60	0.39	0		C	S		2
GPP2.02	052.0	0.68	JT	214	60	0.23	0		P	R		2
GPP2.02	053.0	0.82	JT	224	85	0.31	0		C	R		2
GPP2.02	054.0	1.12	JT	39	75	0.29	0		C	R		2
GPP2.02	055.0	1.52	JT	225	74	0.17	0		I	R		1
GPP2.02	056.0	1.61	JT	227	78	0.19	0		P	R		2
GPP2.02	057.0	1.67	JT	135	89	0.33	0		P	S		1
GPP2.02	058.0	1.75	JT	228	65	0.23	0		P	R		1
GPP2.02	059.0	1.94	JT	43	69	0.36	0		I	R		1
GPP2.02	060.0	2.00	JT	32	69	0.20	0		I	S		1
GPP2.02	061.0	2.13	JT	42	55	0.23	0		I	S		2

Site	NNum	Space	Type	Ddr	DI	Trace	Cen	Mz	LSR	Ser	RkT	Trm
GPP2.02	062.0	2.23	JT	233	71	0.22	0		C	S		2
GPP2.02	063.0	2.23	JT	314	89	0.15	0		C	S		2
GPP2.03	001.0	0.55	JT	134	82	1.32	1	T	P	S	MD	0
GPP2.03	002.0	2.16	JT	308	82	0.77	0	T	P	S		0
GPP2.03	003.0	2.30	JT	140	80	1.93	1	T	P	S		0
GPP2.03	004.0	2.53	JT	141	85	0.75	0	T	P	S		0
GPP2.03	005.0	3.27	JT	325	85	0.24	1	T	C	S		1
GPP2.03	006.0	3.64	JT	313	80	0.64	0	T	P	S		0
GPP2.03	007.0	4.05	JT	132	80	0.38	1	T	P	S		0
GPP2.03	008.0	4.60	JT	135	78	0.30	1	T	P	S		0
GPP2.03	009.0	4.90	JT	195	55	0.15	1	T	C	S		0
GPP2.03	010.0	5.18	JT	315	75	0.24	0	T	P	S		0
GPP2.03	011.0	5.21	JT	237	60	0.20	0	T	P	S		2
GPP2.03	012.0	5.65	JT	35	72	0.17	0	T	C	S		2
GPP2.03	013.0	5.81	JT	140	85	7.20	2	T	C	S		4
GPP4.01	001.0	0.00	JT	314	89	3.54	2	T	U	S	AP	4
GPP4.01	002.0	0.23	JT	156	86	0.56	0		U	S	AP	1
GPP4.01	003.0	0.66	JT	137	89	1.10	1		S	S	AP	1
GPP4.01	004.0	0.88	JT	136	89	0.89	1		S	S	AP	0
GPP4.01	005.0	1.08	JT	132	89	1.10	1		U	S	AP	0
GPP4.01	006.0	1.35	JT	143	89	1.43	2		U	S	AP	4
GPP4.01	007.0	1.90	JT	225	90	7.34	1	T	U	S	AP	0
GPP4.01	008.0	2.36	JT	133	88	0.59	0		U	S	AP	2
GPP4.01	009.0	3.07	JT	141	88	1.85	0	T	U	S	AP	1
GPP4.01	010.0	3.45	FZ	136	89	10.00	1	T	C	S	AP	1
GPP4.01	011.0	3.95	JT	140	87	3.00	0	T	U	S	AP	0
GPP4.01	012.0	4.48	JT	204	71	0.68	0		C	S	AP	2
GPP4.01	013.0	4.55	JT	134	88	3.48	1	T	U	S	AP	3
GPP4.01	014.0	4.68	FZ	138	90	3.86	1	T	U	S	AP	0
GPP4.01	015.0	5.75	FZ	150	84	6.07	1	T	U	S	AP	1
GPP4.01	016.0	6.44	JT	136	82	9.00	1	T	U	S	AP	0
GPP4.01	017.0	7.20	JT	135	86	7.00	0	T	U	S	AP	3
GPP4.01	018.0	7.60	FZ	155	89	11.27	0	T	C	S	AP	1
GPP4.01	019.0	8.65	JT	146	80	6.00	0	T	U	S	AP	1
GPP4.01	020.0	9.00	JT	140	80	10.00	1	T	U	S	AP	1
GPP4.01	021.0	9.50	JT	171	73	5.85	0	T	U	S	AP	3
GPP4.01	022.0	10.30	JT	157	86	9.85	1	T	U	S	AP	3
GPP4.01	023.0	11.55	JT	171	77	10.00	1	T	U	S	AP	3
GPP4.01	024.0	12.05	BZ	150	85	1.62	1	T	C	R	AP	1
GPP4.01	025.0	12.50	FZ	336	84	7.14	1	T	C	S	AP	3
GPP4.01	026.0	13.20	FZ	160	86	7.88	2	T	C	S	AP	4
GPP4.01	027.0	14.25	FZ	139	88	4.70	1	T	C	S	AP	1
GPP4.01	028.0	15.35	JT	151	80	9.99	2	T	U	S	AP	4
GPP4.01	029.0	16.05	JT	153	87	1.93	1	T	U	S	AP	0
GPP4.01	030.0	17.00	FZ	137	85	11.72	2	T	U	S	AP	4
GPP4.01	031.0	17.10	JT	173	82	2.98	1	T	U	R	AP	0
GPP4.01	032.0	18.20	JT	161	84	6.20	2		U	S	AP	4
GPP4.01	033.0	19.09	FZ	142	89	5.24	0	T	U	S	AP	2
GPP4.01	034.0	19.65	JT	139	86	5.80	0	T	U	S	AP	0
GPP4.01	035.0	19.95	JT	136	90	2.47	1	T	U	S	AP	0
GPP4.01	036.0	20.22	JT	137	89	11.00	2	T	U	S	AP	4
GPP4.01	037.0	21.15	JT	149	89	4.00	2	T	P	S	AP	4
GPP4.01	038.0	21.70	JT	151	87	3.00	2	T	P	S	AP	4
GPP4.01	039.0	22.30	JT	137	88	3.00	2	T	U	S	AP	4
GPP4.01	040.0	22.64	JT	139	87	1.00	2	T	U	S	AP	4
GPP4.01	041.0	23.30	JT	135	90	3.00	2	T	U	S	AP	4
GPP4.01	042.0	23.95	JT	160	84	2.50	1	T	U	S	AP	1
GPP4.01	043.0	24.50	JT	133	88	3.00	1	T	U	S	AP	1
GPP5.01	001.0	0.00	JT	127	89	2.26	0		P	R	DM	0
GPP5.01	002.0	0.21	JT	135	85	0.63	0	T	P	S	DM	1
GPP5.01	003.0	0.50	JT	110	82	0.45	0		C	S	DM	1

Site	NNum	Space	Type	Ddr	DI	Trace	Cen	Mz	LaR	Ssr	RkT	Trm
GPP5.01	004.0	0.83	JT	304	88	2.24	0		P	S	DM	0
GPP5.01	005.0	1.24	JT	131	79	2.28	0	T	P	S	DM	0
GPP5.01	006.0	1.71	JT	316	88	0.53	0		C	S	DM	0
GPP5.01	007.0	1.85	JT	121	84	0.81	1	FE	C	S	DM	1
GPP5.01	008.0	2.11	JT	306	89	0.86	1	FE	C	S	DM	0
GPP5.01	009.0	2.29	JT	134	80	1.36	0		P	S	DM	0
GPP5.01	010.0	2.23	JT	136	77	0.39	0		P	S	DM	0
GPP5.01	011.0	3.21	JT	308	89	1.27	0		P	S	DM	0
GPP5.01	012.0	3.42	JT	127	88	0.29	0		I	S	DM	0
GPP5.01	013.0	3.88	JT	131	80	1.40	0		I	S	DM	0
GPP5.01	014.0	3.90	JT	118	89	0.69	0		I	S	DM	0
GPP5.01	015.0	4.09	JT	131	89	0.68	0		I	S	DM	0
GPP5.01	016.0	4.27	JT	129	89	2.61	1		I	S	DM	0
GPP5.01	017.0	4.48	JT	123	88	0.33	0	T	P	S	M	2
GPP5.01	018.0	4.76	JT	116	88	0.52	1	T	P	S	M	1
GPP5.01	019.0	4.97	JT	120	89	0.48	1	T	P	S	M	1
GPP5.01	020.0	5.22	FZ	294	86	3.83	1	T	C	S	M	0
GPP5.01	021.0	5.50	9T	310	90	0.47	0	T	C	S	M	0
GPP5.01	022.0	5.76	JT	304	84	1.43	0	T	P	S	M	1
GPP5.01	023.0	5.80	JT	126	84	0.22	1	T	P	S	M	0
GPP5.01	024.0	5.92	JT	129	75	0.24	0	T	P	S	M	0
GPP5.01	025.0	6.48	JT	260	62	1.00	0	T	P	S	M	1
GPP5.01	026.0	6.86	JT	280	90	1.20	1	T	C	S	M	0
GPP5.01	027.0	7.21	FZ	295	87	1.60	1	T	C	S	M	0
GPP5.01	028.0	7.55	FZ	302	83	5.30	2	T	P	S	M	4
GPP5.01	029.0	8.08	JT	286	83	2.10	1	T	C	S	M	0
GPP5.01	030.0	8.73	JT	299	87	6.50	1	T	P	S	M	0
GPP5.01	031.0	8.98	JT	310	74	3.00	1	T	C	S	M	0
GPP5.01	032.0	9.27	JT	133	64	1.50	0	T	C	S	M	0
GPP5.01	033.0	10.68	FZ	121	81	3.10	1	T	C	S	M	0
GPP5.01	034.0	11.23	FZ	303	86	2.35	1	T	P	S	M	0
GPP5.01	035.0	12.19	JT	290	81	2.33	1	T	P	S	M	0
GPP5.01	036.0	12.90	FZ	288	77	2.00	1	T	P	S	M	0
GPP5.01	037.0	13.66	JT	128	73	3.20	0	T	C	S	M	0
GPP5.01	038.0	13.87	JT	290	88	1.22	1	T	P	S	M	1
GPP5.01	039.0	14.20	JT	128	75	1.32	1	T	P	S	M	0
GPP5.01	040.0	14.31	JT	299	88	2.00	1	T	P	S	M	1
GPP5.01	041.0	15.09	FZ	299	90	3.56	2	T	P	S	M	4
GPP5.01	042.0	15.58	JT	122	84	0.75	2	T	P	S	M	4
GPP5.01	043.0	15.96	JT	290	81	1.64	2	T	P	S	M	4
GPP5.01	044.0	16.52	JT	287	88	1.63	2	T	P	S	M	4
GPP5.02	001.0	7.65	JT	120	90	0.85	1	T	C	S		0
GPP5.02	002.0	9.05	JT	292	78	0.66	0	T	C	S		1
GPP5.02	003.0	9.30	JT	288	64	1.53	0	T	C	S		1
GPP5.02	004.0	10.16	JT	208	66	0.20	0	T	U	S		2
GPP5.02	005.0	11.05	JT	293	80	0.80	0	T	P	S		0
GPP5.02	006.0	14.50	JT	296	89	1.20	2	T	P	S		4
GPP5.03	001.0	0.10	JT	108	80	0.50	1	T	S	S		1
GPP5.03	002.0	0.50	JT	126	86	1.30	2	T	I	S		4
GPP5.03	003.0	0.95	FZ	296	74	1.60	1	T	I	S		0
GPP5.03	004.0	1.64	FZ	294	88	10.00	2	T	I	S		4
GPP5.03	005.0	2.00	JT	293	85	8.50	0	T	S	S		1
GPP5.03	006.0	2.80	FZ	296	87	8.00	1	T	I	S		1
GPP5.03	007.0	3.50	FZ	301	86	12.00	1	T	I	S		0
GPP5.03	008.0	4.12	JT	126	84	3.50	0	T	P	S		1
GPP5.03	009.0	5.00	FZ	130	81	10.00	2	T	P	S		4
GPP5.03	00A.0	15.21	JT	277	84	0.31	2	T	C	S		4
GPP5.03	00B.0	13.96	JT	295	80	1.09	1	T	P	S		0
GPP5.03	00C.0	13.28	JT	301	75	0.93	0	T	P	S		0
GPP5.03	00D.0	13.08	JT	115	85	0.75	0	T	P	S		0
GPP5.03	00E.0	12.88	JT	110	83	1.32	2	T	P	S		4

Site	NNum	Space	Type	Ddr	DI	Trace	Cen	Mz	LsR	Ssr	RkT	Trm
GPP5.03	00F.0	12.71	JT	110	85	0.90	1	T	P	S		0
GPP5.03	00G.0	12.01	JT	295	84	0.84	2	T	P	S		4
GPP5.03	00H.0	11.41	JT	290	85	1.03	1	T	P	S		0
GPP5.03	00I.0	10.12	JT	302	90	17.00	1	T	P	S		0
GPP5.03	00J.0	9.41	JT	134	80	0.93	1	T	P	R		0
GPP5.03	00K.0	6.43	JT	318	86	1.55	1	T	C	S		1
GPP5.03	00L.0	6.00	BZ	135	80	3.00	1	T	U	S		0
GPP5.03	010.0	5.35	FZ	126	84	6.00	1	T	P	S		0
GPP5.03	011.0	6.00	FZ	125	88	15.00	1	T	P	S		0
GPP5.03	012.0	7.21	FZ	126	90	20.00	2	T	S	S		4

JALAMA BEACH

Site	NNum	SPACE	TYPE	DDR	DI	TRACE	CEN	MZ	LSR	SSR	RKT	TRM
JB1.601	001.0	0.30	FZ	113	88	1.56	1	FE	P	S		0
JB1.601	002.0	0.90	JT	304	84	1.25	1	FE	C	S		1
JB1.601	003.0	1.15	JT	131	88	1.40	2	FE	U	S		4
JB1.601	004.0	1.29	JT	57	60	2.00	1	FE	P	S		1
JB1.601	005.0	1.42	JT	142	52	0.70	1	FE	C	S		1
JB1.601	007.0	1.35	JT	223	89	0.47	0	FE	P	S		2
JB1.601	008.0	2.48	JT	138	80	1.10	2	FE	P	S		4
JB1.601	009.0	2.48	JT	51	74	0.65	0	FE	P	S		2
JB1.601	010.0	3.50	JT	298	89	1.00	1	FE	S	S		1
JB1.601	011.0	3.80	JT	163	54	0.80	0	FE	P	S		2
JB1.601	012.0	4.70	JT	73	58	3.55	0	FE	UP	R		1
JB1.601	013.0	4.58	JT	148	70	1.14	1	FE	U	S		1
JB1.601	015.0	4.95	JT	47	86	0.50	1	FE	P	S		1
JB1.601	016.0	5.90	JT	285	74	2.38	2	FE	U	S		4
JB1.601	017.0	6.80	FZ	294	85	2.18	1	FE	U	S		0
JB1.601	018.0	7.20	FZ	339	64	2.60	0	FE	U	S		1
JB1.601	019.0	8.00	FZ	322	80	2.00	1	FE	SU	S		1
JB1.601	020.0	7.50	FZ	349	69	0.80	1	FE	U	S		0
JB1.601	021.0	8.50	FZ	335	55	1.90	0	FE	P	S		0
JB1.601	022.0	10.60	FZ	308	80	2.80	2	FE	C	S		4
JB1.601	023.0	11.50	FZ	323	85	3.00	2	FE	P	S		4
JB1.601	024.0	12.86	JT	138	80	1.80	0	FE	U	S		1
JB1.601	026.0	13.61	JT	131	88	3.00	2	FE	P	S		4
JB1.601	027.0	13.78	JT	146	59	1.80	1	FE	C	S		1
JB1.602	025.0	12.95	JT	146	84	1.50	1	FE	P	S		0
JB1.602	028.0	14.43	JT	145	79	1.60	1	FE	P	S		0
JB1.602	029.0	14.70	JT	50	75	2.08	0	FE	P	R		2
JB1.602	030.0	1.47	JT	149	71	2.00	1	FE	P	S		0
JB1.602	031.0	15.55	FZ	148	89	3.00	1	FE	P	S		1
JB1.602	032.0	15.80	JT	67	64	4.00	1	FE	P	R		1
JB1.602	033.0	15.80	FZ	320	88	3.00	2	FE	U	S		4
JB1.602	034.0	16.05	JT	127	89	2.00	1	FE	P	S		1
JB1.602	035.0	16.40	JT	320	86	1.10	0	FE	C	S		0
JB1.602	036.0	16.70	JT	314	79	1.20	0	FE	C	S		0
JB1.602	037.0	17.55	FZ	144	77	3.00	2	FE	P	S		4
JB1.602	038.0	17.75	JT	64	64	3.00	2	FE	P	R		4
JB1.602	039.0	18.20	JT	65	66	3.00	2	FE	P	R		4
JB1.602	040.0	18.30	JT	147	64	1.37	1	FE	C	S		0
JB1.602	041.0	18.73	JT	165	74	1.00	0	FE	P	S		0
JB1.602	042.0	19.22	JT	56	68	2.00	2	FE	P	R		4
JB1.602	043.0	18.75	JT	37	75	0.75	0	FE	P	R		2
JB1.602	044.0	18.80	FZ	130	88	0.88	0	FE	P	S		2
JB1.602	045.0	19.43	JT	54	69	0.80	0	FE	C	S		1
JB1.602	046.0	19.46	JT	327	69	1.46	0	FE	P	S		0
JB1.602	047.0	19.70	JT	328	65	1.00	0	FE	P	S		0
JB1.602	048.0	20.08	JT	332	74	2.00	0	FE	P	S		0
JB1.603	049.0	20.38	FZ	323	72	2.50	0	FE	P	S		0

Site	NNUM	SPACE	TYPE	CDR	DI	TRACE	CEN	MZ	LSR	SSR	RKT	TRM
JB1.603	050.0	21.30	FZ	65	75	3.00	2	FE	P	R		4
JB1.603	051.0	20.65	JT	51	85	2.00	0	FE	C	S		0
JB1.401	001.0	0.00	JT	230	44	0.64	0	FE	C	R		2
JB1.401	002.0	0.28	JT	139	76	0.40	0	FE	F	S		2
JB1.401	003.0	0.43	JT	147	80	1.10	1	FE	P	R		0
JB1.401	004.0	1.05	JT	147	65	0.75	0	FE	P	R		2
JB1.401	006.0	2.60	JT	149	55	1.55	0	FE	C	R		1
JB1.401	007.0	2.70	JT	94	65	0.70	1	FE	C	R		1
JB1.401	008.0	2.75	JT	94	65	0.35	0	FE	C	R		1
JB1.401	009.0	2.80	JT	15	87	0.23	0	FE	R	P		1
JB1.401	010.0	3.28	JT	81	55	0.38	0	FE	C	R		2
JB1.401	011.0	3.46	JT	281	75	1.61	1	FE		R		1
JB1.401	012.0	3.56	JT	287	82	0.60	1	FE	P	R		1
JB1.402	013.0	4.12	JT	275	79	1.80	1	FE	C	R		3
JB1.402	014.0	4.36	JT	79	45	0.23	0	CL	P	R		2
JB1.402	015.0	4.58	JT	74	36	1.00	0	FE	C	R		1
JB1.402	016.0	4.82	JT	325	89	1.38	1	FE	C	R		3
JB1.402	017.0	4.87	JT	151	79	0.50	0	FE	P	R		2
JB1.402	018.0	5.12	JT	345	84	1.65	0	FE	C	R		1
JB1.402	019.0	5.08	JT	74	58	0.27	0	C	P	R		1
JB1.402	020.0	5.58	JT	337	86	1.70	1	FE	C	R		0
JB1.402	021.0		JT	338	60	1.05	0	LT	C	R		1
JB1.402	022.0		JT	147	66	0.45	1	FE	C	R		0
JB1.402	023.0		JT	151	71	0.54	1	FE	C	R		1
JB1.402	024.0		JT	149	74	0.42	1	FE	C	R		1
JB1.402	025.0		JT	65	61	1.20	1	LT	C	R		1
JB1.402	026.0		JT	139	66	0.47	1	CL	P	R		1
JB1.402	027.0		JT	150	75	0.32	0	CL	C	R		1
JB1.402	028.0		JT	151	72	0.47	0	FE	C	R		0
JB1.402	029.0		JT	259	72	0.68	0	FE	C	R		1
JB1.402	030.0		JT	285	79	0.56	0	FE	P	R		2
JB1.402	031.0		JT	108	49	0.90	1	FE	P	R		1
JB1.402	032.0		JT	144	64	0.69	1	FE	P	R		0
JB1.301	001.0	0.00	JT	260	71	2.17	1		P	S		0
JB1.301	002.0	0.66	JT	130	65	2.39	1		C	S		1
JB1.301	003.0	1.01	JT	140	60	0.65	1		P	S		1
JB1.301	004.0	1.30	JT	140	55	0.59	0		C	S		2
JB1.301	005.0	1.26	FZ	70	60	2.10	1		C	R		1
JB1.301	006.0	1.59	JT	155	80	2.85	1		P	R		1
JB1.301	007.0	2.00	JT	75	60	2.93	0		C	S		2
JB1.301	008.0	2.28	JT	150	70	2.15	0		P	R		2
JB1.301	009.0	3.14	JT	100	35	1.81	0		C	R		2
JB1.302	010.0	2.68	JT	70	75	2.03	1		C	R		1
JB1.302	011.0	2.84	JT	125	80	0.70	0		P	S		2
JB1.302	012.0	3.55	JT	150	60	1.85	1		C	S		1
JB1.302	013.0	3.54	JT	140	65	1.31	0		P	S		2
JB1.302	014.0	3.38	JT	285	65	0.86	0		C	S		2
JB1.302	015.0	3.65	JT	150	70	1.31	0		C	S		2
JB1.302	016.0	3.82	JT	145	70	0.66	0		C	R		2
JB1.302	017.0	4.11	JT	135	70	1.55	0		C	R		2
JB1.302	018.0	4.40	JT	135	70	1.68	1		C	S		1
JB1.302	019.0	4.64	JT	80	60	0.98	0		P	R		2
JB1.302	020.0	4.63	JT	195	90	1.17	2		C	R		4
JB1.302	021.0	5.03	JT	140	55	1.96	1		P	S		1
JB1.302	022.0	5.38	JT	140	70	0.96	1		C	R		1
JB1.302	023.0	5.40	JT	195	90	0.83	2		C	R		4
JB1.303	00A.0	5.68	JT	143	70	0.55	0		P	S		0
JB1.303	00B.0	5.82	JT	137	82	0.70	0		S	S		0
JB1.303	00C.0	5.98	JT	142	83	0.55	0		S	S		0
JB1.303	00D.0	6.28	JT	127	66	0.45	0		P	R		0
JB1.303	00E.0	6.38	JT	153	89	0.50	0		S	S		0

Site	NNUM	SPACE	TYPE	DDR	DI	TRACE	CEN	MZ	LSR	SSR	RKT	TRM
JB1.303	00F.0	6.45	JT	58	56	2.20	2		C	R		4
JB1.303	00G.0	6.82	JT	147	67	0.90	0		S	R		0
JB1.303	00H.0		JT	40	75	0.50	1		P	K		1
JB1.303	00I.0	7.15	JT	147	72	0.40	1		S	S		0
JB1.303	00J.0	7.70	JT	139	65	1.15	1		I	R		0
JB1.303	00K.0		JT	140	75	0.80	1		C	R		1
JB1.303	00L.0	8.15	JT	143	69	0.50	1		P	R		1
JB1.303	00M.0	8.20	JT	56	73	0.65	0		P	S		2
JB1.303	00N.0	8.57	JT	319	76	2.10	2		P	R		4
JB1.303	00O.0	8.76	JT	338	4	2.10	1		C	S		0
JB1.303	00P.0	9.40	JT	280	10	1.10	0		C	S		0
JB1.303	00Q.0	9.00	JT	294	14	1.10	0		C	S		0
JB1.303	00R.0	10.13	JT	122	84	2.00	1		P	B		1
JB1.201	001.0	0.40	JT	31	85	1.13	1		P	S		1
JB1.201	002.0	0.00	JT	166	74	1.29	2		P	S		4
JB1.201	003.0	0.87	JT	164	73	1.07	2		P	R		4
JB1.201	004.0	1.56	JT	121	61	0.98	0		P	R		1
JB1.201	005.0	1.69	JT	272	54	1.97	2		C	S		4
JB1.201	006.0	1.52	JT	13	71	1.44	2		P	R		4
JB1.201	007.0	1.94	JT	118	54	3.80	2		C	R		4
JB1.201	008.0	1.86	JT	215	87	4.10	2		P	R		4
JB1.201	009.0	2.29	JT	116	57	0.93	1		P	S		1
JB1.201	010.0	2.59	JT	118	56	0.73	1		P	S		1
JB1.201	011.0	2.80	JT	130	60	1.48	1		C	S		1
JB1.202	012.0	2.92	JT	237	87	1.68	1		C	R		1
JB1.202	013.0	3.09	JT	56	62	5.00	2		F	R		4
JB1.202	014.0	3.24	JT	24	89	1.57	1		P	R		0
JB1.202	015.0	3.48	JT	149	61	2.14	1		C	R		1
JB1.202	016.0	4.63	JT	36	71	2.20	1		C	R		1
JB1.202	017.0	5.00	JT	143	57	5.00	2		P	R		4
JB1.202	018.0	4.88	JT	25	66	5.00	2		C	R		4
JB1.202	019.0	5.18	JT	154	66	1.43	1		P	R		1
JB1.202	020.0	5.61	JT	142	46	5.00	2		P	S		4
JB1.202	021.0	5.60	JT	225	66	1.53	1		P	R		1
JB1.202	022.0	6.22	JT	134	44	0.90	1		F	S		1
JB1.202	023.0	6.36	JT	127	49	1.82	1		P	S		1
JB1.202	024.0	7.80	JT	142	64	5.00	2		P	R		4
JB1.202	025.0	5.94	JT	73	62	5.00	2		C	R		4
JB1.202	026.0	6.48	JT	62	71	5.00	2		P	R		4
JB1.202	027.0	6.95	JT	62	71	3.14	1		C	R		1
JB1.202	028.0	7.36	JT	74	66	5.00	2		C	R		4
JB1.202	029.0	8.08	JT	66	45	5.00	2		C	R		4
JB1.202	030.0	8.30	JT	221	82	5.00	2		C	R		4
JB1.202	031.0	8.50	FZ	126	82	3.50	1		C	R		1
JB1.203	001.0	0.30	JT	245	84	3.34	1	FE	C	S		0
JB1.203	003.0	0.55	JT	17	69	1.00	0	FE	C	S		1
JB1.203	004.0	1.21	JT	240	84	1.82	0	FE	C	R		1
JB1.203	005.0	1.54	JT	64	78	2.86	1	FE	P	R		1
JB1.203	006.0	1.73	JT	151	72	0.52	0	FE	P	R		0
JB1.203	007.0	2.18	JT	153	85	0.57	0		C	R		0
JB1.203	008.0	2.50	JT	318	29	1.43	0		U	S		1
JB1.203	009.0	2.77	JT	322	18	0.83	0		U	S		2
JB1.203	010.0	3.16	JT	146	86	4.04	2		C	S		4
JB1.203	011.0	3.45	JT	151	68	0.71	0		P	R		3
JB1.203	012.0	3.20	JT	49	86	0.55	0		C	R		2
JB1.203	013.0	3.69	JT	325	86	1.27	0		P	R		1
JB1.203	014.0	3.73	FZ	324	89	1.14	1	FE	C	R		0
JB1.203	015.0	3.79	JT	237	70	1.01	0	FE	P	S		1
JB1.203	016.0	3.80	JT	163	71	1.35	1	FE	C	S		0
JB1.203	017.0	4.18	JT	144	81	1.02	1	FE	P	R		0
JB1.203	018.0	4.49	JT	145	68	1.33	1	FE	C	R		0

Site	NNUM	SFACE	TYPE	DDR	DI	TRACE	CEN	MZ	LSR	SSR	RKT	TRM
JB1.203	019.0	4.79	JT	142	88	0.72	0	FE	P	R		0
JB1.203	020.0	4.92	JT	153	74	1.05	0	FE	P	S		0
JB1.203	021.0	5.07	JT	158	75	1.72	0	FE	P	S		0
JB1.203	022.0	5.27	FZ	154	84	0.62	0	FE	P	R		J
JB1.203	023.0	5.73	JT	150	87	1.22	0	FE	P	R		1
JB1.203	024.0	5.95	JT	137	85	0.78	0	FE	P	R		0
JB1.203	025.0	6.12	JT	305	89	4.44	2	FE	P	R		4
JB1.203	026.0	6.51	JT	317	59	0.49	0		C	R		0
JB1.203	027.0	7.01	JT	141	59	4.64	2		P	R		4
JB1.203	028.0	7.28	JT	133	80	0.47	0	FE	U	R		0
JB1.204	029.0	7.62	FZ	138	86	0.53	0	FE	C	S		0
JB1.204	030.0	8.05	JT	108	60	0.69	0	FE	P	S		0
JB1.204	031.0	8.05	JT	358	84	0.52	0	FE	I	R		0
JB1.204	032.0	8.07	JT	112	64	0.81	0	FE	P	S		1
JB1.204	033.0	8.64	JT	133	75	0.43	0		P	S		0
JB1.204	035.0	8.80	FZ	104	56	0.39	0	FE	P	S		0
JB1.204	036.0	9.70	FZ	115	55	0.40	0	FE	P	S		0
JB1.204	037.0	8.89	JT	34	76	0.68	0	FE	C	R		0
JB1.204	038.0	9.25	FZ	330	31	0.59	0		C	R		0
JB1.204	039.0	9.92	FZ	115	55	0.70	0		P	S		0
JB1.204	040.0	10.80	FZ	106	50	0.86	0	FE	P	S		0
JB1.204	041.0	11.25	JT	58	80	4.00	2	FE	P	R		4
JB1.204	042.0	11.78	FZ	215	71	0.58	0	FE	C	R		0
JB1.204	043.0	12.44	JT	321	85	1.45	0	FE	C	S		2
JB1.205	044.0	13.20	JT	144	85	2.07	0	FE	P	S		0
JB1.205	045.0	13.47	JT	136	82	0.45	0	FE	P	S		0
JB1.205	046.0	13.68	JT	285	65	2.04	1	FE	U	S		0
JB1.206	047.0	0.97	JT	141	65	1.28	0	FE	C	R		1
JB1.206	048.0	0.50	FZ	315	20	4.90	0		U	R		2
JB1.206	049.0	0.95	FZ	314	47	0.63	0		C	R		1
JB1.206	050.0	1.13	JT	138	74	0.56	0	FE	P	S		0
JB1.206	051.0	2.43	JT	145	74	0.57	0	FE	P	S		1
JB1.206	052.0	2.57	JT	148	83	0.50	0	FE	S	S		1
JB1.206	053.0	3.20	FZ	54	65	13.00	1	FE	P	R		1
JB1.207	054.0	3.90	FZ	140	74	1.14	0	FE	C	R		2
JB1.207	055.0	3.68	FZ	1	89	0.70	0	FE	C	R		2
JB1.207	056.0	4.13	JT	152	72	0.46	0		P	S		2
JB1.207	057.0	4.60	JT	138	62	0.82	0	FE	I	S		2
JB1.207	058.0	4.70	JT	120	56	1.36	0	FE	I	R		2
JB1.207	059.0	5.50	JT	315	89	4.00	2	FE	S	R		4
JB1.207	060.0	6.20	FZ	151	73	0.20	0	FE	P	S		1
JB1.207	061.0	8.65	JT	323	86	2.10	0	FE	U	S		2
JB1.207	062.0	9.40	JT	131	59	0.60	0	FE	P	S		1
JB1.207	063.0	10.25	FZ	307	76	4.00	2	FE	I	S		4
JB1.207	064.0	10.30	FZ	93	60	0.30	0	FE	C	S		1
JB1.207	065.0	10.96	JT	135	56	1.50	0	FE	P	S		0
JB1.207	066.0	11.25	JT	144	63	0.90	0	FE	S	S		0
JB1.207	067.0	11.70	JT	106	46	1.67	0	FE	C	S		1
JB1.207	068.0	12.15	JT	113	53	0.78	0	FE	P	S		2
JB1.207	069.0	12.47	JT	117	58	0.69	0	FE	S	S		1
JB1.207	070.0	12.65	JT	112	64	0.95	0	FE	P	S		1
JB1.207	071.0	12.73	JT	139	54	1.00	1	FE	C	S		0
JB1.207	072.0	12.30	JT	222	60	4.00	2	FE	P	R		4
JB1.207	073.0	14.15	FZ	143	81	6.00	2	FE	U	R		4
JB1.207	074.0	14.45	FZ	141	60	5.00	0	FE	S	S		0
JB1.207	075.0	15.85	FZ	146	84	4.00	2	FE	U	S		4
JB5.ONF	001.0		JT	44	70	2.40						
JB5.ONF	002.0		JT	282	89	0.70						
JB5.ONF	003.0		JT	106	81	0.94						
JB5.ONF	004.0		JT	309	90	0.65						
JB5.ONF	005.0		JT	110	77	0.98						

Site	NNUM	SPACE	TYPE	DDR	DI	TRACE	CEN	MZ	LSR	SSR	RKT	TRM
JB5.ONF	006.0		JT	50	89	3.09						
JB5.ONF	007.0		JT	295	90	0.72						
JB5.ONF	008.0		JT	332	81	0.68						
JB5.ONF	009.0		JT	269	89	0.38						
JB5.ONF	010.0		JT	111	77	0.32						
JB5.101	001.0	0.00	JT	135	75	3.18		1	U	S		1
JB5.101	002.0	0.44	JT	317	68	0.99		0	C	S		2
JB5.101	003.0	0.59	JT	316	61	0.64	0	LD	P	S		2
JB5.101	004.0	0.71	JT	319	76	0.74	0	LD	C	S		2
JB5.101	005.0	0.83	JT	139	75	0.30	0	CL	C	S		2
JB5.101	006.0	1.61	JT	138	79	2.74	0		C	S		2
JB5.101	007.0	1.80	JT	272	81	3.11	0		C	S		2
JB5.101	008.0	2.46	JT	298	68	2.84	2		C	S		4
JB5.101	009.0	2.83	JT	106	87	1.59	0		P	S		2
JB5.101	010.0	3.03	JT	326	80	2.76	1		C	S		1
JB5.101	011.0	2.81	JT	214	81	1.91	2		S	R		4
JB5.101	012.0	3.24	JT	219	83	2.98	2		S	R		4
JB5.102	001.0	3.43	JT	117	88	2.74	2	CL	C	R		4
JB5.102	002.0	3.98	JT	308	79	1.24	0		C	R		2
JB5.102	003.0	3.87	JT	294	78	2.93	2		S	R		4
JB5.102	004.0	4.47	JT	115	71	3.16	1	CL	P	S		0
JB5.102	005.0	4.67	JT	304	64	1.45	1		P	S		0
JB5.102	006.0	4.96	JT	296	90	1.23	0		C	S		2
JB5.102	007.0	5.18	JT	286	89	2.94	2		S	S		4
JB5.102	008.0	5.45	JT	120	76	2.79	1	CL	C	S		1
JB5.102	009.0	5.80	JT	231	77	3.28	1		C	R		0
JB5.102	010.0	5.63	JT	291	89	2.11	2		S	S		4
JB5.102	011.0	6.16	JT	291	79	2.67	1	CL	C	S		1
JB5.102	012.0	5.10	JT	86	84	1.34	1		P	S		1
JB5.102	013.0	6.67	JT	118	74	3.34	2	CL	P	S		4
JB5.102	014.0	7.75	JT	137	85	1.77	1	CL	P	S		1
JB5.102	015.0	7.64	JT	98	79	0.98	0		C	S		2
JB5.102	016.0	8.12	JT	277	66	1.02	0		C	S		2
JB5.102	017.0	8.33	JT	299	70	3.90	2	CL	C	S		4
JB5.102	018.0	8.18	JT	94	87	1.54	0		C	S		2
JB5.102	019.0	9.00	JT	296	88	3.88	2	CL	C	S		4
JB5.103	001.0	9.41	JT	106	81	0.84	0		P	S		2
JB5.103	002.0	9.63	JT	323	81	3.33	2	CL	C	S		4
JB5.103	003.0	9.09	JT	53	73	2.20	2		C	R		4
JB5.103	004.0	9.85	JT	81	75	2.38	0		C	S		2
JB5.103	005.0	10.81	JT	119	86	1.38	1		C	S		1
JB5.103	006.0	11.06	JT	296	84	2.82	2		P	S		4
JB5.103	007.0	11.19	JT	108	60	2.60	2	CL	P	S		4
JB5.103	008.0	11.40	JT	116	83	1.47	1		C	S		1
JB5.103	009.0	11.91	JT	110	89	3.06	2	CL	C	S		4
JB5.103	010.0	12.13	JT	131	54	2.17	1		C	S		1
JB5.103	011.0	12.66	JT	292	81	0.87	0		S	R		2
JB5.104	001.0	13.03	JT	281	89	2.87	1	CL	C	S		1
JB5.104	002.0	13.64	JT	96	86	0.96	1		P	R		0
JB5.104	003.0	13.86	JT	174	85	2.06	1		C	S		1
JB5.104	004.0	14.91	JT	110	83	2.04	1		P	S		1
JB5.104	005.0	15.24	JT	95	77	3.29	2		C	S		4
JB5.104	006.0	15.91	JT	289	89	2.15	1		C	S		1
JB5.104	007.0	15.84	JT	126	81	3.43	1		C	S		1
JB5.104	008.0	16.03	JT	90	87	3.73	1		C	S		1
JB5.104	009.0	16.88	JT	260	88	3.42	2		C	S		4
JB5.104	010.0	17.75	JT	118	70	2.74	1		C	R		1
JB5.104	011.0	17.73	JT	161	89	1.01	1		S	R		1
JB5.104	012.0	18.17	JT	81	85	3.32	2		P	S		4
JB5.104	013.0	19.28	JT	282	89	3.50	2		P	R		4
JB5.104	014.0	20.08	JT	114	74	3.46	2		C	R		4

Site	NUM	SPACE	TYPE	DDR	DI	TRACE	CEN	MZ	LSR	SSR	RKT	TRM
JB5.105	001.0	20.60	JT	295	89	4.00	2		U	R		4
JB5.105	002.0	20.70	JT	295	85	1.40	1		U	R		1
JB5.105	003.0	21.35	JT	171	81	0.60	0		C	S		1
JB5.105	004.0	22.15	JT	107	80	3.00	2		U	R		4
JB5.105	005.0	22.68	JT	132	86	0.86	0		U	R		1
JB5.105	006.0	22.70	JT	96	76	3.00	2		U	R		4
JB5.105	007.0	22.80	JT	220	74	3.50	2		U	R		4
JB5.105	008.0	23.10	JT	80	81	3.00	2		P	R		4
JB5.105	009.0	23.40	JT	150	79	1.80	1		U	R		1
JB5.105	010.0	23.80	JT	74	74	2.00	1		C	R		1
JB5.106	011.0	24.85	JT	111	82	1.50	1		P	R		1
JB5.106	012.0	25.60	JT	295	72	3.20	2		U	R		4
JB5.106	013.0	26.25	JT	323	85	1.45	1		C	R		1
JB5.106	014.0	26.40	JT	316	86	1.50	2		C	R		4
JB5.106	015.0	26.50	JT	112	76	0.85	2		C	R		4
JB5.106	016.0	27.10	JT	304	80	1.40	2		C	R		4
JB5.106	017.0	27.10	FZ	263	65	3.40	2		C	R		4
JB5.106	018.0	27.10	JT	235	76	4.00	2		U	R		4
JB5.106	019.0	27.25	JT	116	84	4.00	2		U	R		4
JB5.106	020.0	27.85	JT	113	87	2.80	2		U	R		4
JB5.106	021.0	28.35	JT	116	80	2.10	1		U	R		0
JB5.106	022.0	29.05	FZ	110	85	3.10	1		U	R		1
JB5.106	023.0	29.20	FZ	100	72	3.00	1		U	R		1
JB5.106	024.0	30.52	FZ	117	85	3.20	2		U	R		4
JB5.106	025.0	30.60	JT	120	84	1.25	0		C	R		2
JB5.106	026.0	30.80	JT	313	70	1.00	0		C	R		1
JB5.107	027.0	31.22	JT	121	76	3.30	1		P	R		1
JB5.107	028.0	32.00	JT	320	89	1.90	0		P	R		1
JB5.107	029.0	32.24	JT	120	78	0.65	0		P	R		1
JB5.107	030.0	32.30	JT	97	76	0.80	0		P	R		0
JB5.107	031.0	33.40	FZ	112	70	1.50	1		C	R		0
JB5.107	032.0	33.40	FZ	122	74	2.50	1		P	R		1
JB5.107	033.0	33.40	FZ	325	82	3.00	2		U	K		4
JB5.107	034.0	33.70	JT	88	88	1.15	0		U	R		1
JB5.107	035.0	33.80	JT	275	86	1.00	0		U	R		1
JB5.107	036.0	34.50	JT	277	88	2.80	2		C	R		4
JB5.107	037.0	35.20	JT	120	73	1.00	0		P	S		0
JB5.107	038.0	35.65	JT	320	78	3.00	1		C	S		1
JB5.107	039.0	36.40	JT	352	80	1.40	0		C	R		1
JB5.107	040.0	36.50	JT	324	80	2.80	1		C	R		0
JB5.107	041.0	36.80	JT	146	80	2.10	0		C	R		1
JB5.107	042.0	37.35	JT	325	85	0.90	0		I	R		1
JB5.107	043.0	37.80	JT	110	88	0.70	0		P	F		0
JB5.107	044.0	36.50	JT	225	82	1.10	1		P	R		0
JB5.107	045.0	37.95	JT	105	81	1.80	0		P	R		0
JB5.107	046.0	38.30	JT	100	50	0.80	0		P	S		0
JB5.107	047.0	38.50	JT	255	60	1.20	0		P	R		1
JB5.107	048.0	38.65	JT	120	67	0.85	0		S	R		1
JB5.107	049.0	39.10	JT	123	80	2.20	0		S	S		0
JB5.107	050.0	39.30	JT	120	74	1.00	0		P	S		0
JB5.107	051.0	39.50	JT	14	80	0.70	0		P	S		2
JB5.107	052.0	39.75	JT	2	38	0.40	0		P	S		2
JB5.107	053.0	39.70	JT	123	68	0.95	0		C	R		2
JB5.107	054.0	39.85	JT	94	84	2.20	0		P	R		1
JB5.107	055.0	40.00	JT	120	70	0.65	0		P	R		1
JB5.107	056.0	40.13	JT	119	71	1.20	0		P	R		1
JB5.108	057.0	40.40	JT	119	72	1.70	1		P	R		1
JB5.108	058.0	40.70	JT	120	70	1.65	1		P	R		0
JB5.108	059.0	40.85	JT	117	78	2.10	1		U	R		1
JB5.108	060.0	41.22	JT	120	75	1.30	1		P	R		0
JB5.108	061.0	41.30	JT	116	76	1.50	1		P	S		0

Site	NNUM	SPACE	TYPE	DDR	DI	TRACE	CEN	MZ	LSR	SSR	RKT	TRM
JB5.108	062.0	41.60	JT	121	85	2.72	2		C	S		4
JB5.108	063.0	42.13	JT	127	76	3.14	2		C	S		4
JB5.108	064.0	42.66	JT	119	74	1.04	1		P	S		0
JB5.108	065.0	42.70	JT	116	77	0.54	0		P	S		1
JB5.108	066.0	42.84	JT	116	80	1.55	1		P	S		1
JB5.108	067.0	44.22	JT	197	64	0.88	1		C	R		1
JB5.108	068.0	45.80	JT	232	86	1.50	1		U	R		0
JB5.108	069.0	44.35	JT	294	89	2.16	1		I	R		1
JB5.108	070.0	44.20	FZ	265	71	4.87	2		C	R		4
JB5.108	071.0	45.06	JT	114	70	2.30	0		P	S		1
JB5.108	072.0	45.34	JT	114	72	1.60	0		S	S		0
JB5.108	073.0	45.70	JT	112	72	1.50	1		P	S		0
JB5.108	074.0	46.30	JT	109	69	2.64	1		C	S		0
JB5.108	075.0	46.60	JT	146	89	1.72	0		C	S		2
JB5.108	076.0	47.40	JT	110	78	1.50	0		C	S		0
JB5.108	077.0	47.68	JT	112	73	1.30	0		S	S		0
JB5.108	078.0	47.90	FZ	121	75	3.20	2		P	R		4
JB5.109	001.0	7.84	JT	106	74	1.80	1		C	S		1
JB5.109	002.0	8.02	JT	108	87	1.27	0		P	S		1
JB5.109	003.0	8.15	JT	113	86	0.97	0		P	S		2
JB5.109	004.0	8.43	JT	118	70	0.75	0		P	S		2
JB5.109	005.0	8.59	JT	119	71	0.61	0		C	S		2
JB5.109	006.0	8.80	JT	113	72	3.10	1		P	S		1
JB5.109	007.0	9.04	JT	119	80	0.61	0		P	S		2
JB5.109	008.0	9.18	JT	93	75	0.85	0		P	R		2
JB5.109	009.0	9.70	JT	301	84	0.37	0		P	S		2
JB5.109	010.0	9.97	JT	121	86	0.69	0		P	R		2
JB5.109	011.0	10.28	JT	116	75	2.77	1		C	S		1
JB5.109	012.0	10.47	JT	115	72	1.59	1		P	S		0
JB5.109	013.0	10.66	JT	107	88	1.80	0		S	S		2
JB5.109	014.0	10.84	JT	115	78	0.73	0		P	S		2
JB5.109	015.0	11.14	JT	113	80	1.20	0		C	S		1
JB5.109	016.0	11.32	JT	113	79	2.05	1		S	S		1
JB5.109	017.0	11.82	JT	103	76	1.45	0		C	S		0
JB5.109	018.0	13.60	JT	241	76	1.67	2		U	R		4
JB5.109	019.0	12.32	JT	154	82	2.50	0		I	R		2
JB5.109	020.0	13.04	FZ	148	87	3.85	2		I	R		4
JB5.109	021.0	12.50	JT	144	86	0.83	0		P	S		2
JB5.109	022.0	12.60	JT	170	70	2.15	1		S	R		1
JB5.109	023.0	13.10	JT	109	79	3.45	2		P	S		4
JB5.109	024.0	13.15	JT	114	79	3.50	1		P	R		1
JB5.109	025.0	13.61	FZ	109	79	3.20	2		P	R		4
JB5.109	026.0	13.74	JT	108	81	1.70	1		C	S		1
JB5.109	027.0	14.83	JT	109	85	1.33	1		S	P		1
JB5.109	027.0	14.15	JT	110	87	1.08	1		S	S		0
JB5.109	028.0	14.48	FZ	299	89	3.05	2		U	R		4
JB5.109	030.0	15.40	FZ	296	75	3.12	2		C	R		4
JB5.109	031.0	15.62	JT	113	85	1.70	1		P	S		0
JB5.109	032.0	15.85	JT	117	72	3.34	2		P	S		4
JB5.109	033.0	19.22	JT	110	76	1.45	1		P	S		0
JB5.109	034.0	17.10	JT	114	75	2.65	1		P	S		0
JB5.109	035.0	17.65	JT	328	89	2.50	1		P	S		0
JB5.109	036.0	17.73	JT	113	76	2.87	2		P	S		4
JB6.901	001.0	0.00	JT	276	81	2.60	2	G	P	S		4
JB6.901	002.0	0.76	JT	278	89	2.20	2	G	C	S		4
JB6.901	003.0	2.13	JT	107	80	2.00	1	G	P	S		0
JB6.901	004.0	2.13	JT	74	78	1.50	0	G	C	S		2
JB6.901	005.0	2.31	JT	358	60	3.60	1	G	C	S		1
JB6.901	006.0	3.16	JT	277	89	2.00	1	C	P	R		1
JB6.901	007.0	4.13	JT	285	86	2.50	1	C	P	R		1
JB6.901	008.0	4.29	JT	60	70	2.50	1		C	S		1

Site	NNUM	SPACE	TYPE	DDR	DI	TRACE	CEN	MZ	LSR	SSR	RKT	TRM
JB6.901	009.0	4.71	JT	192	85	4.90	2	C	C	S		4
JB6.901	010.0	5.17	JT	100	77	2.34	1	G	C	S		1
JB6.901	011.0	5.81	JT	105	85	2.84	2	G	P	S		4
JB6.901	012.0	6.96	JT	101	86	1.50	1		P	S		0
JB6.901	013.0	7.08	JT	100	85	1.84	1	G				0
JB6.901	014.0	7.33	JT	185	86	0.48	0	G	P	S		2
JB6.901	015.0	7.60	JT	99	87	1.70	2	G	P	S		4
JB6.901	016.0	8.36	JT	8	80	2.32	0	G	C	S		2
JB6.901	017.0	9.12	JT	120	80	0.93	0	G	P	S		2
JB6.901	018.0	9.27	JT	9	78	2.20	0	G	P	S		2
JB6.901	019.0	9.52	JT	16	85	0.88	0		C	S		2
JB6.901	020.0	10.43	JT	62	78	1.56	0	G	P	S		2
JB6.901	021.0	10.37	JT	341	80	0.44	0	G	P	S		2
JB6.901	022.0	10.49	JT	328	80	0.70	0		P	S		2
JB6.901	023.0	10.67	JT	351	70	2.06	0	G	C	S		2
JB6.901	024.0	11.07	JT	65	75	1.43	1	G	P	S		1
JB6.901	025.0	11.73	JT	336	80	1.56	0	G	C	S		2
JB6.901	026.0	12.16	JT	276	86	1.46	0	G	C	S		2
JB6.901	027.0	12.49	JT	55	74	2.01	0	G	C	S		2
JB6.901	028.0	12.62	JT	120	80	1.20	0		P	S		2
JB6.901	029.0	12.80	JT	122	88	1.26	0		P	S		2
JB6.901	030.0	13.53	JT	291	83	1.74	0	G	P	S		2
JB6.901	031.0	13.92	JT	102	67	1.88	0	G	P	S		2
JB6.901	032.0	14.14	JT	5	80	1.50	1	G	C	R		1
JB6.901	033.0	14.14	JT	111	88	0.77	0		P	S		2
JB6.901	034.0	14.56	JT	289	84	2.42	1	G	P	S		1
JB6.901	035.0	14.59	JT	176	85	0.93	0	G	C	S		2
JB6.901	036.0	14.84	JT	284	85	2.47	2	G	P	S		4
JB6.901	037.0	15.50	JT	358	75	4.34	0	G	C	S		2
JB6.901	038.0	15.96	JT	291	76	1.41	0		C	S		2
JB6.901	039.0	15.96	JT	347	80	1.24	0		P	S		2
JB6.901	040.0	16.39	JT	64	79	3.52	0	G	C	S		2
JB6.901	041.0	16.78	JT	107	81	0.78	0		P	S		2
JB6.901	042.0	16.99	JT	160	76	2.84	2	G	C	S		4
JB6.901	043.0	17.88	JT	286	86	1.38	0		P	S		2
JB6.901	044.0	18.82	JT	109	80	6.72	2	G	P	R		4
JB6.901	045.0	20.22	JT	2	70	5.58	0		C	S		2
JB6.902	001.0	0.20	JT	270	84	1.80	2		I	R		4
JB6.902	002.0	0.30	JT	10	46	1.21	0		I	R		1
JB6.902	003.0	1.71	VN	102	86	1.44	0	C	C	S		1
JB6.902	004.0	1.70	VN	347	78	2.00	1	C	C	R		1
JB6.902	005.0	1.95	VN	287	88	3.01	2	C	P	S		4
JB6.902	006.0	2.00	JT	351	65	5.48	1	C		S		1
JB6.902	007.0	2.40	JT	22	74	1.54	0		UC	R		1
JB6.902	008.0	3.62	JT	353	51	5.19	1	C	C	S		0
JB6.902	009.0	3.84	JT	1	53	0.71	0	C	C	S		0
JB6.902	010.0	4.11	JT	346	59	0.69	0	C	I	S		1
JB6.902	011.0	4.12	JT	271	76	1.14	0	C	I	R		1
JB6.902	012.0	4.40	JT	272	86	1.24	0	C	P	R		2
JB6.902	013.0	4.59	JT	10	50	0.61	0		UI	S		0
JB6.902	014.0	4.85	JT	351	56	6.05	2		UP	P		4
JB6.902	015.0	5.40	JT	345	80	1.44	1		UI	R		1
JB6.902	016.0	5.51	JT	107	85	3.19	0	C	P	S		1
JB6.902	017.0	6.10	JT	107	85	4.12	1	C	P	S		1
JB6.902	018.0	6.25	JT	108	85	1.84	0	C	P	R		1
JB6.902	019.0	6.42	JT	354	60	7.68	1		UP	R		0
JB6.902	020.0	7.17	JT	353	45	1.85	0	C	P	R		0
JB6.902	021.0	8.19	VN	293	86	4.02	1	C	P	S		1
JB6.902	022.0	8.40	JT	354	60	8.22	2		UP	R		4
JB6.902	023.0	8.82	VN	110	89	1.72	0	C	P	S		2
JB6.902	024.0	9.21	JT	106	80	5.91	1	C	P	S		0

Site	NNUM	SPACE	TYPE	DDR	DI	TRACE	CEN	MZ	LSR	SSR	RKT	TRM
JB6.902	025.0	9.43	JT	106	85	5.66	1	C	P	S		0
JB6.902	026.0	9.52	JT	94	89	2.55	0	C	P	S		0
JB6.902	027.0	9.60	JT	357	46	2.92	0		UP	R		1
JB6.902	028.0	9.85	JT	2	48	0.66	0		UP	S		1
JB6.902	029.0	10.30	JT	354	49	1.38	0		UP	S		0
JB6.902	030.0	10.35	VN	111	86	2.43	0	C	P	S		0
JB6.902	031.0	10.70	VN	290	86	1.95	0	C	P	S		0
JB6.902	032.0	10.86	JT	351	56	6.18	0		UP	R		2
JB6.902	033.0	11.22	JT	344	52	2.51	0		UP	R		2
JB6.902	034.0	11.38	JT	357	69	1.37	0		UP	R		1
JB6.902	035.0	11.48	JT	358	74	1.88	0		UP	R		1
JB6.902	036.0	11.67	JT	106	89	8.00	1	C	P	S		0
JB6.902	037.0	11.82	JT	111	86	2.57	0	C	P	S		1
JB6.902	038.0	12.11	JT	342	69	6.54	0		UI	R		0
JB6.902	039.0	12.38	JT	103	86	3.53	1	C	P	S		1
JB6.902	040.0	12.55	JT	103	86	5.08	0	C	P	S		0
JB6.902	041.0	12.73	VN	103	86	1.27	0	C	P	S		0
JB6.902	042.0	12.92	JT	9	66	3.54	0		UI	R		2
JB6.902	043.0	13.97	JT	107	89	3.52	0	C	P	S		0
JB6.902	044.0	13.20	JT	107	89	2.04	0	C	P	S		0
JB6.902	045.0	13.22	JT	1	61	1.25	0		UI	R		1
JB6.902	046.0	13.43	JT	101	89	1.28	0	C	P	S		0
JB6.902	047.0	13.60	JT	104	88	1.31	0	C	P	S		1

LOMPOC LANDING Fracture data

Site	Nnum	Space	Type	Ddr	DI	Trace	Cen	Mz	LSR	SSR	Rkt	Trm
LL1.01	001.0	1.85	FZ	229	86	3.40	2	T	P	R		0
LL1.01	002.0	2.15	FZ	214	89	3.40	2	T	P	R		0
LL1.01	003.0	2.95	JT	236	87	1.07	0	T	P	S		0
LL1.01	004.0	3.88	JT	243	89	1.36	0	T	C	R		0
LL1.01	005.0	4.00	BZ	246	88	8.30	1	T	C	R		1
LL1.01	006.0	5.40	BZ	252	88	7.20	0	T	C	R		1
LL1.01	007.0	6.38	BZ	260	89	6.80	0	T	S	R		1
LL1.01	008.0	7.05	BZ	250	88	22.50	0	T	S	R		1
LL1.01	009.0	8.20	BZ	260	89	8.20	0	T	S	R		0
LL1.01	010.0	8.35	JT	113	80	2.35	0	T	P	R	CH	1
LL1.01	011.0	8.60	JT	135	80	1.33	0	T	C	R		2
LL1.01	012.0	8.90	JT	124	84	1.29	1	T	C	R		1
LL1.01	013.0	9.11	JT	124	81	3.60	1	T	C	R		1
LL1.01	014.0	9.33	JT	110	80	3.50	1	T	C	R		1
LL1.01	015.0	9.60	JT	114	81	3.20	0	T	C	R		2
LL1.01	016.0	9.95	JT	109	80	2.90	0	T	C	R		2
LL1.01	017.0	10.18	JT	85	85	4.40	1	T	C	R		1
LL1.01	018.0	10.18	JT	123	84	3.55	0	T	P	R		0
LL1.01	019.0	11.24	JT	115	82	2.70	0	T	C	R	CH	0
LL1.01	020.0	11.48	JT	122	81	1.30	0	T	C	R	CH	1
LL1.01	021.0	11.78	JT	130	81	1.65	0	T	C	R	CH	0
LL1.01	022.0	12.40	JT	116	82	1.28	0	T	P	R		0
LL1.01	023.0	12.80	JT	118	80	1.50	0	T	C	R		0
LL1.01	024.0	12.95	JT	110	81	1.45	0	T	C	R		1
LL1.01	025.0	13.20	JT	120	82	2.55	0	T	C	R		0
LL1.01	026.0	13.83	JT	115	80	2.30	0	T	C	R		0
LL1.01	027.0	14.18	JT	104	80	1.85	0	T	C	R		0
LL1.01	028.0	14.60	JT	113	81	2.30	0	T	C	R		0
LL1.01	029.0	14.95	BZ	48	89	24.00	1	T	C	R		1
LL1.01	030.0	15.38	BZ	109	82	11.00	1	T	C	R		1
LL1.02	001.0	21.10	FZ	277	89	7.75	0	T	P	R		0
LL1.02	002.0	25.53	BZ	103	88	9.50	1	T	C	R		1
LL1.02	003.0	26.90	JT	104	99	3.10	J	T	C	R		2
LL1.03	001.0	1.20	JT	21	75	1.00	0	T	S	S		2

Site	Nnum	Space	Type	Ddr	DI	Trace	Cen	Mz	LsR	SsR	Rkt	Trm
LL1.03	002.0	1.70	BZ	85	84	1.70	0	T	P	R		1
LL1.03	003.0	2.00	JT	78	75	4.50	0	T	S	S		3
LL1.03	004.0	2.20	BZ	78	80	48.50	1	T	P	R		1
LL1.03	005.0	2.27	JT	112	88	1.20	0	T	C	S	P	3
LL1.03	006.0	3.30	JT	67	80	0.70	0	T	P	S	P	1
LL1.03	007.0	3.35	JT	60	75	0.72	0	T	S	S	P	2
LL1.03	008.0	3.80	JT	282	83	0.62	0	T	P	S	P	3
LL1.03	009.0	4.35	JT	116	75	1.40	0	T	U	S	P	2
LL1.03	010.0	4.85	BZ	330	85	1.90	0	T	U	R	P	3
LL1.03	011.0	5.95	JT	300	67	1.00	0	T	P	S	M	3
LL1.03	012.0	8.06	JT	284	80	0.90	0	T	U	S		1
LL1.03	013.0	8.47	JT	54	85	1.83	0	T	S	S		2
LL1.03	014.0	8.72	JT	234	70	1.76	2	T	S	S		0
LL1.03	015.0	9.63	JT	43	88	24.00	0	T	S	S		0
LL1.03	016.0	10.10	JT	48	80	4.71	0	T	S	S		3
LL1.03	017.0	10.14	JT	53	85	4.14	0	T	U	S		3
LL1.03	018.0	10.96	JT	239	83	1.57	0	T	S	S		3
LL1.03	019.0	11.30	JT	53	80	2.50	0	T	S	S		3
LL1.03	020.0	11.45	JT	53	80	3.16	0	T	S	S		3
LL1.03	021.0	12.74	JT	78	85	2.15	0	T	U	S		3
LL1.03	022.0	13.30	BZ	241	85	5.35	1	T	S	S		1
LL1.03	023.0	14.10	BZ	330	85	3.00	2	T	U	R		0
LL1.03	024.0	14.94	JT	301	80	0.50	0	T	P	S		3
LL1.04	001.0	0.09	JT	68	75	0.19	1	T	S	S	P	1
LL1.04	002.0	0.10	JT	316	90	0.12	1	T	P	S		1
LL1.04	003.0	0.40	BZ	78	80	48.50	1	T	P	R		0
LL1.04	004.0	1.65	JT	314	65	0.37	0	T	P	S		1
LL1.04	005.0	1.93	JT	132	85	0.63	1	T	U	S		1
LL1.04	006.0	2.00	JT	265	85	0.60	0	T	S	S		2
LL1.04	007.0	2.65	BZ	315	85	24.00	1	T	P	R		0
LL1.04	008.0	5.60	FZ	136	65	4.00	0	T	U	S		1
LL1.04	009.0	5.70	JT	258	80	0.78	1	T	S	S		1
LL1.04	010.0	10.67	FZ	78	85	1.67	0	T	S	S		0
LL1.04	011.0	11.75	FZ	70	85	19.00	0	T	U	S		0
LL1.04	012.0	12.45	FZ	243	80	12.20	0	T	U	S		0
LL1.04	013.0	13.67	JT	76	78	24.00	0	T	S	S	P	0
LL1.04	014.0	15.20	JT	65	75	1.21	0	T	C	S		1
LL1.04	015.0	15.25	JT	74	90	0.81	0	T	C	S		0
LL1.04	016.0	15.40	JT	214	65	0.67	0	T	C	S		1
LL1.04	017.0	15.96	JT	63	80	0.95	0	T	P	S		1
LL1.04	018.0	17.00	JT	263	85	2.12	0	T	S	S	P	1
LL1.04	019.0	16.10	JT	146	86	0.48	0	T	P	S		2
LL1.04	020.0	17.20	JT	58	90	6.34	1	T	S	S		0
LL1.04	021.0	17.90	JT	63	80	2.67	1	T	S	S	P	0
LL1.04	022.0	17.60	JT	106	90	0.70	0	T	P	S		0
LL1.04	023.0	20.40	JT	117	90	0.82	1	T	P	S		0

LIONS HEAD Fracture data

Site	Nnum	Space	Type	Ddr	DI	Trace	Cen	Mz	LsR	SsR	Rkt	Trm
LH1.01	1.0	0.35	JT	104	76	0.5	1		PS	S	CH	0
LH1.01	2.0	0.73	JT	281	90	0.9	2		PS	S		0
LH1.01	3.0	1.05	JT	277	90	0.50	2		PS	S		0
LH1.01	4.0	1.22	JT	104	86	1.00	2		PS	S		0
LH1.01	5.0	1.63	JT	101	87	3.17	2		PS	S		0
LH1.01	6.0	2.03	JT	116	74	1.20	2		PS	S		0
LH1.01	7.0		BD	195	80	4.00	2		P	S		0
LH1.01	8.0	2.48	JT	102	81	1.70	2		PS	S		0
LH1.01	9.0	2.70	JT	112	82	0.80	2		PS	S		0
LH1.01	10.0	2.90	JT	99	85	1.60	2		PS	S		0
LH1.01	11.0	3.08	JT	119	81	1.30	2		PS	S		0

Site	Nnum	Space	Type	Ddr	DI	Trace	Cen	Mz	LsR	SsR	Rkt	Trm
LH1.01	12.0	3.34	JT	103	80	1.20	2		PS	S		0
LH1.01	13.0	3.45	JT	117	86	1.10	2		PS	S		C
LH1.01	14.0	3.60	JT	118	79	0.60	2		PS	S		0
LH1.01	15.0	3.78	JT	120	86	0.75	2		PS	S		0
LH1.01	16.0	4.06	JT	115	86	0.60	2		PS	S		0
LH1.01	17.0	4.25	JT	110	85	0.75	2		PS	S		0
LH1.01	18.0	4.60	JT	109	84	0.50	2		PS	S		0
LH1.01	19.0	5.00	JT	111	75	0.50	2		PS	S		0
LH1.01	20.0	5.55	JT	121	81	1.40	1		PS	S		0
LH1.01	21.0	5.90	JT	119	74	1.00	2		PS	S		0
LH1.01	22.0	6.28	JT	118	72	0.50	2		PS	S		0
LH1.01	23.0	6.51	JT	120	82	1.40	2		PS	S		0
LH1.01	24.0	6.63	JT	131	86	1.30	2		PS	S		0
LH1.01	25.0	6.69	JT	118	80	2.00	2		PS	S		0
LH1.01	26.0	7.18	JT	299	86	1.40	2		PS	S		0
LH1.01	27.0	7.54	JT	293	87	1.00	2		PS	S		0
LH1.01	28.0	7.51	JT	92	77	0.90	2		PS	S		0
LH1.01	29.0	7.98	JT	104	82	1.55	1		PS	S		0
LH1.01	30.0	8.35	JT	111	82	2.20	1		PS	S		0
LH1.01	31.0	8.70	JT	112	81	1.60	1		PS	S		1
LH1.01	32.0	9.22	JT	274	90	3.50	2		PS	S		0
LH1.01	33.0	9.22	JT	126	89	1.70	0		PS	S		0
LH1.01	34.0	9.49	JT	110	85	1.89	0		PS	S		0
LH1.01	35.0	9.88	JT	118	80	1.65	0		PS	S		0
LH1.01	36.0	10.10	JT	126	80	2.20	2		PS	S		0
LH1.01	37.0	10.44	JT	117	79	2.20	2		PS	S		0
LH1.01	38.0	10.63	JT	107	80	1.40	2		PS	S		0
LH1.01	39.0	10.80	JT	103	77	2.60	2		PS	S		0
LH1.01	40.0	11.17	JT	104	73	2.10	2		PS	S		0
LH1.01	41.0	11.48	JT	286	89	1.24	2		PS	S		0
LH1.01	42.0	11.59	JT	118	85	1.00	1		PS	S		0
LH1.01	43.0	11.80	JT	110	85	0.83	1		PS	S		0
LH1.01	44.0	12.20	JT	105	65	2.30	2		PS	S		0
LH1.01	45.0	12.70	JT	120	88	1.90	1		PS	S		0
LH1.01	46.0	13.08	JT	126	83	1.86	2		PS	S		0
LH1.01	47.0	13.28	JT	120	88	1.07	1		PS	S		0
LH1.01	48.0	13.65	JT	300	79	1.26	2		PS	S		0
LH1.01	49.0	13.95	JT	312	86	1.31	2		PS	S		0
LH1.01	50.0	14.15	JT	105	56	1.30	2		PS	S		0
LH1.01	51.0	14.50	JT	109	80	1.50	2		PS	S		0
LH1.01	52.0	15.71	JT	112	66	1.00	2		PS	S		0
LH1.01	53.0	15.90	JT	116	72	1.10	1		PS	S		0
LH1.01	54.0	16.10	JT	103	78	0.79	1		PS	S		0
LH1.01	55.0	16.50	JT	104	89	0.90	1		PS	S		0
LH1.01	56.0	16.90	JT	106	69	0.90	1		PS	S		0
LH1.01	57.0	18.10	JT	101	80	2.40	2		PS	S		0
LH1.01	58.0	18.50	JT	107	86	1.30	1		PS	S		0
LH1.01	59.0	18.78	JT	101	87	2.30	2		PS	S		0
LH1.01	60.0	18.98	JT	99	70	2.40	2		PS	S		0
LH1.01	61.0	19.27	JT	100	72	1.70	1		PS	S		0
LH1.01	62.0	19.15	JT	93	85	1.20	1		PS	S	CH	0
LH1.01	63.0	19.73	JT	99	71	2.10	2		PS	S		0
LH1.01	64.0	20.40	JT	103	80	1.70	2		PS	S		0
LH1.01	65.0	20.88	JT	303	82	1.80	2		PS	S		0
LH1.01	66.0	21.35	JT	112	78	1.30	2		PS	S		0

Large Scale Features

SITE	NNUM	SPACE	TYPE	DDIR	DIP	TRC	CEN	MNLz
GPBZ	1.01	0.0	BZ	130	88	8	0	TAR
GPBZ	1.02	3.6	BZ	119	84	5	1	TAR
GPBZ	1.03	10.4	BZ	130	81	8	0	TAR
GPBZ	1.04	15.5	BZ	307	89	25	0	TAR
GPBZ	1.05	19.5	BZ	138	85	8	0	TAR
GPBZ	1.06	35.1	BZ	123	78	3	0	TAR
GPBZ	1.07	37.7	BZ	309	89	17	0	TAR
GPBZ	1.08	40.4	BZ	130	80	5	0	TAR
GPBZ	1.09	41.1	BZ	121	80	9	0	TAR
GPBZ	1.10	44.0	BZ	130	80	14	2	TAR
GPBZ	1.11	77.0	BZ	134	89	14	2	TAR
GPBZ	2.01	5.1	BZ	135	86	9	1	TAR
GPBZ	2.02	12.2	BZ	125	89	12	1	TAR
GPBZ	2.03	22.0	BZ	134	89	5	1	TAR
GPBZ	4.01	87.0	F			8	0	TAR
GPBZ	5.01	0.0	BZ	134	86	12	1	TAR
GPBZ	5.02	9.8	BZ	138	80	8	1	TAR
GPBZ	5.03	16.0	BZ	138	80	5	0	TAR
GPBZ	5.05	90.0	BZ	139	87	5	1	TAR
NV497	101.01B	0.0	BD	38	7			
NV497	101.05B	18.4	BD	47	8			
NV497	103.01B	11.9	BD	21	9			
NV497	104.02A		AT	330	71			
NV497	104.06B	35.0	BD	353	30			
NV497	105.02B	10.7	BD	6	33			
NV497	105.06B		BD	2	27			
NV497	106.02A		AT	168	80			
NV497	101.002	9.0	HL	68	11			
NV497	101.003		HL	332	66			
NV497	101.004		HL	339	5			
NV497	101.006	18.4	F	284	71	3	2	
NV497	102.001	46.0	F	296	81	31		TAR
NV497	102.002		F	74	45	5		
NV497	103.002	15.3	F	74	67	4	1	
NV497	103.003	17.0	F	70	53	8	2	
NV497	103.004	18.2	HL	356	8			
NV497	104.001	19.0	HL	64	5			
NV497	104.003	21.3	F	74	59		2	
NV497	104.004	25.3	F	70	80	8	2	TAR
NV497	104.005	29.7	F	290	85	11		TAR
NV497	105.001	10.7	F	75	85	15	1	TAR
NV497	105.003	12.6	F	332	84	8	1	TAR
NV497	105.004	17.8	F	71	64	16	0	TAR
NV497	105.005	24.8	F	129	62	9	2	
NV497	106.001	12.8	HL	272	4			
NV497	106.003		F	263	76	34		
NV497	106.004		F	250	70	10	2	
NV497	106.005		F	238	56	13	2	
NV497	106.006		F	243	85	11	2	
NV497	106.007		F	252	44	4	2	
NV497	106.008		F	220	60			
NV501	133.01B	1.0	BD	154	25			
NV501	133.02B	2.0	BD	73	15			
NV501	133.03B	3.0	BD	73	16			
NV501	133.04B	4.0	BD	27	49			
NV501	134.001	0.8	BZ	132	75	100	2	TAR
NV501	134.002	21.0	BZ	316	66	100	2	TAR
NV501	134.003	23.2	BZ	284	85	5	0	TAR
NV501	134.004	25.7	BZ	314	75	100	2	TAR
NV501	134.005	32.5	BZ	116	72	100	2	TAR

SITE	NNUM	SPACE	TYPE	DDIR	DIP	TRC	CEN	MNLz
NV501	134.006	44.0	BZ	140	88	10	2	TAR
NV501	134.007	46.2	BZ	335	56	80	2	TAR
NV501	134.008	48.2	BZ	328	52	80	2	TAR
NV501	134.009	52.4	BZ	325	89	90	2	TAR
NV501	134.010	58.0	BZ	313	52	13	2	TAR
NV501	134.011	60.0	BZ	134	84	13	2	TAR
NV501	134.012	63.4	BZ	310	75	20	2	TAR
NV501	134.013	71.7	BZ	293	76	40	2	TAR
NV501	134.014	120.0	HL	109	7			
NV501	134.015	169.9	BZ	310	53	70	2	
NV501	134.01B	3.5	BD	32	16			
NV501	134.02B	42.7	BD	16	27			
NV501	134.03B	90.0	BD	106	9			
NV501	134.04B	135.9	BD	39	11			
NV501	134.05B	167.0	BD	32	27			
NV501	134.06B	206.0	BD	41	10			
NV501	135.01B	27.0	BD	70	14			
NV501	135.02B	43.6	BD	56	21			
NV501	136.001	14.0	BZ	128	75	45	2	
NV501	136.002	26.0	HL	90	18			
NV501	136.01B	26.0	BD	122	14			
NV501	137.001	8.0	HL	100	15			
NV501	137.002	50.6	BZ	305	42	100	2	CARB
NV501	137.01B	50.0	BD	122	19			
NV501	138.001	2.2	BZ	98	80	100	2	CARB
NV501	139.001	87.2	BZ	107	74	70	2	CARB
NV501	139.002	90.0	HL	60	30			
NV501	139.004	122.5	BZ	84	65	35	2	
NV501	139.01B	59.0	BD	154	20			
NV501	139.02B	70.0	BD	139	14			
NV501	139.03A	90.0	AT	60	90			
NV501	139.03B	104.5	BD	327	20			
NV501	140.001	14.0	F	72	46	8	2	
NV501	140.002	41.0	F	110	74	7	2	CLAY
NV501	140.003	45.5	BZ	82	54	7	2	
NV501	140.004	48.0	F	88	85	5	2	CLAY
NV501	140.005	64.7	BZ	91	80	6	2	CLAY
NV501	140.006	71.5	F	316	53			
NV501	140.007	81.0	F	252	36			
NV501	140.008	87.0	HL	78	6			
NV501	140.009	97.0	F	306	41			
NV501	140.010	105.2	HL	40	18			
NV501	140.011	140.0	HL	210	24			
NV501	140.012	159.0	F	135	89			CLAY
NV501	140.013	161.0	F	314	63			CLAY
NV501	140.01B	46.5	BD	348	10			
NV501	140.02B	65.0	BD	172	5			
NV501	140.03B	81.0	BD	155	22			
NV501	140.04B	115.0	BD	294	10			
NV501	144.01B	110.0	BD	14	9			
NV501	145.01B	138.0	BD	28	19			
SV474	401.001	24.0	F	206	88	4	2	CLY
SV474	401.003	60.0	BZ	243	56	8	2	CLY
SV474	401.004	72.0	F	231	46	10	2	CLY
SV474	401.005	72.0	HL	210	11			
SV474	401.01B	30.0	BD	224	55			
SV474	401.05A	72.0	AT	236	62			
SV474	401.05P	72.0	AP	297	76			
SV474	405A.002	4.5	HL	336	12			
SV474	405A.006	9.0	F	290	84	4	2	TAR
SV474	405A.01B	0.0	BD	216	28			

SITE	NUM	SPACE	TYPE	DDIR	DIP	TRC	CEN	MNLz
SV474	405A.02A	4.5	AT	48	20			
SV474	405A.02A	4.5	AT	238	72			
SV474	405A.02B	8.8	BD	204	29			
SV474	405A.02P	4.5	AP	250	72			
SV474	407.007	6.0	F	78	86	3	1	
SV474	407.008	10.0	HL	314	2			
SV474	407.01B	8.0	BD	201	27			
SV474	407.02B		BD	226	75			
SV474	407.08A	10.0	AT	46	30			
SV474	408A.001	3.5	BZ	94	80	6	1	TAR
SV474	408A.002	9.1	BZ	271	84	9	1	TAR
SV474	408A.003	15.0	BZ	343	78	7	0	
SV474	408A.004	18.6	F	323	80			
SV474	408A.005	21.8	F	343	73	21	2	TAR
SV474	408A.006		HL	138	6			
SV474	408A.01B	0.0	BD	207	20			
SV474	408A.02B	25.0	BD	196	56			
SV474	408A.03B	30.0	BD	221	16			
SV474	408B.001	1.4	F	40	15	5	0	
SV474	408B.01B		BD	212	27			
SV474	408C.001	3.3	F	347	69			TAR
SV474	408C.01B	6.0	BD	206	30			
SV474	409.001	27.0	HL	144	18			
SV474	410A.001	4.3	F	1	85	8	2	TAR
SV474	410A.002	13.5	F	314	76	5	2	TAR
SV474	410A.003		HL	168	18			
SV474	410A.01B	0.0	BD	211	26			
SV474	410A.02B	6.0	BD	86	14			
SV474	410A.03B	12.1	BD	94	27			
SV474	410A.04B		BD	161	17			
SV474	410B.001	4.0	HL	153	20	5		
SV474	410B.002	7.0	HL	145	20	4		
SV474	411A.001	30.0	F	47	21	9	1	
SV474	411B.001	7.5	F	125	75	5	1	
SV474	411B.002	11.8	BZ	134	86	6	2	TAR
SV474	411B.003	28.5	BZ	326	82	5	2	TAR
SV474	411B.01B	2.0	BD	164	15			
SV474	411C.001	2.6	BZ	112	84	4	2	TAR
SV474	411E.001	0.0	HL	147	18			
SV474	411F.004	1.8	HL	144	19			
SV474	411E.007	8.8	F	113	16			
SV474	411E.008	9.0	HL	110	2			
SV474	411E.009	16.2	HL	318	11			
SV474	411E.01A	0.0	AT	237	14			
SV474	411E.01B	3.0	BD	222	16			
SV474	411E.02B	3.0	BD	75	67			
SV474	411E.03B	8.0	BD	54	63			
SV474	411E.04B	9.2	BD	144	10			
SV474	411E.05B	16.9	BD	197	11			
SV474	411E.06B	25.9	BD	221	24			
SV474	411E.08A	9.0	AT	189	18			
SV474	411E.09A	16.2	AT	240	20			
SV474	411F.012	9.5	F	211	85	3		
SV474	411F.013	11.3	F	26	67	3		
SV474	411F.014	11.7	F	195	16	9		
SV474	411F.015	25.0	F	282	69	4		TAR
SV474	411F.016	29.4	HL	344	12			
SV474	411F.16A	29.4	AT	240	56			
SV474	411G.018	34.4	HL	326	11			
SV474	411G.018	38.5	F	194	12	16		
SV474	411G.019	57.6	HL	334	28			

SITE	NNUM	SPACE	TYPE	DDIR	DIP	TRC	CEN	MNLz
SV474	411G.020	57.6	F	207	24	9		
SV474	411G.18A	34.4	AT	216	64			
SV474	411G.19A	57.6	AT	214	58			
SV474	412A.001	0.0	HL	312	8			
SV474	412A.002	0.0	F	212	19		2	
SV474	412A.003	9.0	F	211	21			
SV474	412A.004	21.0	F	212	22			
SV474	412A.005	35.0	F	214	25			
SV474	412A.01A	0.0	AT	214	58			
SV474	413.001		F	310	78	8		CLY, SIL
SV475	514A.001	0.0	F	284	86			TAR, CARB
SV475	514A.002	1.0	F	312	82	25	2	TAR, CARB
SV475	514A.003	3.3	F	312	70	25	2	TAR, CARB
SV475	514A.004	7.0	F	124	88	25	2	TAR, CARB
SV475	514A.005	9.2	F	296	70	25	2	TAR, CARB
SV475	514A.006	11.5	F	303	88	25	2	TAR, CARB
SV475	514A.007	12.7	F	303	82	25	2	TAR, CARB
SV475	514A.008	14.5	F	292	75	25	2	TAR, CARB
SV475	514A.009	17.0	F	310	80	25	2	TAR, CARB
SV475	514A.010	21.5	F	306	78	10	2	TAR, CARB
SV475	514A.011	22.5	F	304	85	10	2	TAR, CARB
SV475	514A.012	25.5	F	198	84	20	2	TAR, CARB
SV475	514A.013	27.3	F	313	88	20	2	TAR, CARB
SV475	514B.001	3.5	BZ	336	75	10	2	TAR, CARB
SV475	514B.002	3.5	HL	132				
SV475	514B.01B	3.5	BD	191	19			
SV475	514C.001	22.0	BZ	322	82	9	2	CARB
SV475	514D.001	15.0	HL	118	7			
SV475	514D.01A	15.0	AT	109	16			
SV475	515.001	42.0	BZ	316	83	25	2	TAR, CARB
SV475	516.001	63.0	BZ	300	78	25	2	
SV475	516.002	63.0	HL	135	6			
SV475	517.001	91.0	BZ	112	84	25	2	CARB
SV475	518.001	28.0	BZ	156	84	5	2	CARB
SV475	519.001	43.0	F	107	85			
SV475	519.002	43.0	HL	220	18			
SV475	520.001	4.8	F	187	76		2	CLY, TAR
SV475	520.002	7.6	F	168	80	20	2	CLY, TAR
SV475	520.003	9.2	F	352	80		2	CARB, CLY
SV475	520.004	10.2	BZ	132	85	30	2	
SV475	520.005	14.3	BZ	177	74	30	2	
SV475	520.01B	9.5	BD	204	12			
SV475	521.001	18.0	BZ	330	84	7	2	CLY, TAR
SV475	521.002	45.0	HL	142	8			
SV475	522.001	45.0	BZ	332	85	30	2	
SV475	522.01B	45.0	BD	162	20			CARB
SV475	523.001	75.0	F	337	76	40	2	
SV475	524.001	105.0	HL	324	27			
SV475	524.01A		AT	59	7			
SV475	525.001	145.5	BZ	160	72	8	2	
SV475	525.01B	145.5	BD	253	14			
SV475	526.001	165.0	BZ	348	66	10	2	
SV475	527.001	78.0	BZ	172	85			CL, T
SV475	528.001	87.0	BZ	171	86			CL, T
SV475	529.001	135.0	BD	262	35			
SV475	530.001	7.5	BZ	166	88	25	2	
SV475	531.001	54.0	BZ	143	64	20	2	CARB
SV475	532.001	81.0	BZ	354	65	30	2	
SV475	533.001	150.0	HL	108	16			
SV475	533.01B	138.0	BD	223	26			
SV475	534.001	15.0	F	147	75	6	2	

SITE	NNUM	SPACE	TYPE	DDIR	DIP	TRC	CEN	MNLz
SV475	534.01B	15.0	BD	216	26			
SV475	535.001	33.0	F	137	84	10	2	
SV475	536.001	42.0	ED	126	21			
SV475	536.002	43.0	HL	140	12			
SV475	536.02A	43.0	AT	215	84			
SV475	537.01B	60.0	BD	232	63			
SV475	539.001	9.0	F	334	50	30	2	CARB
SV475	540.001	18.0	F	101	63	20	2	CARB,SIL
SV475	540.001	8.0	F	287	86	20	2	CARB,SIL
SV475	540.002	13.0	F	110	84	20	2	CARB,SIL
SV475	540.01B	0.0	BD	211	56			
SV475	540.02B	9.0	BD	269	75			
SV475	541.001	6.0	F	315	60	25	2	CAR,S,T
SV475	541.002	6.0	HL	145	8			
SV475	541.01B	6.0	BD	209	47			
SV475	542.001	15.0	F	332	56	25	2	
SV475	543.001	24.0	BZ	309	56	30	2	CAR,S,T
SV475	544.001	29.0	F	302	86	25	2	CAR,S,T
SV475	544.01B	30.0	BD	213	52			
SV475	545.001	36.0	BZ	321	76	25	2	CARB,TAR
SV475	546.001	45.0	F	104	46	20	2	
SV475	546.01B	45.0	BD	209	46			
SV475	547.001	66.0	F	309	44	15	2	
SV475	547.002		F	314	86			
SV475	548.001	72.0	HL	146	31			
SV475	548.01B	72.0	BD	189	50			
SV475	549.001	90.0	F	290	89	20	2	CLY,SIL
SV477	750.01	0.0	BZ	348	86	60	2	TAR
SV477	750.01b	9.0	BD	44	36			
SV477	750.02	2.0	BZ	286	86	60	2	TAR
SV477	750.02b	27.7	BD	80	17			
SV477	750.03	11.8	F	86	61	60	2	TAR
SV477	750.03b	33.0	BD	204	29			
SV477	750.04	16.5	F	100	75	60	2	
SV477	750.04b	40.0	BD	174	25			
SV477	750.05	30.5	HL	158	11			
SV477	750.05a	30.5	AT	240	88			
SV477	750.05b	78.3	BD	208	56			
SV477	750.06	32.0	F	78	76	45	2	TAR
SV477	750.06b	89.0	BD	220	58			
SV477	750.07	37.3	BZ	245	88	60	2	CL,TR
SV477	750.07b	92.0	BD	220	50			
SV477	750.08	36.9	BZ	255	89	60	2	CL,TR
SV477	750.09	37.0	HL	139	10			
SV477	750.09a	37.0	AT	48	88			
SV477	750.10	40.8	HL	180	22			
SV477	750.11	52.8	BZ	250	86	35	2	CL,T,SUL
SV477	750.12	60.0	BZ	99	80	60	2	CLY,TAR
SV477	750.13	55.4	BZ	188	70	90	2	TAR
SV477	750.14	73.0	F	212	56	90	2	TAR
SV477	750.15	59.5	F	214	78	90	2	
SV477	750.16	70.0	BZ	337	80	4	2	
SV477	750.17	86.5	F	72	78	90	2	CL,TR
SV477	751.01	122.0	HL	148	24			
SV477	752.01b	142.0	BD	236	50			
SV477	753.01b	24.0	BD	221	15			
SV477	755.001	17.5	F	185	87	8	2	CLY
SV477	755.002	32.8	F	110	71	8	2	CLY
SV477	755.003	43.0	HL	0	12			
SV477	755.004	63.0	F	150	71	10	2	
SV477	755.005	75.0	F	180	88	12	2	

SITE	NNUM	SPACE	TYPE	DDIR	DIP	TRC	CEN	MNLz
SV477	755.006	74.5	F	184	79	10	2	
SV477	755.01B	7.0	BD	35	20			
SV477	755.02B	16.0	BD	15	30			
SV477	755.03B	36.5	BD	30	20			
SV477	755.04B		BD	52	10			
SV477	755.05B	80.0	BD	100	42			
SV477	755.06B	92.0	BD	55	25			
SV477	755.07B	94.0	BD	44	18			
SV477	755B.007	106.5	F	153	79	10	2	
SV477	755B.008	109.0	F	142	82	2	2	
SV477	755B.009	129.0	F	127	72	10	2	
SV477	755B.010	119.5	F	316	81	5	2	
SV477	755B.011	142.5	F	315	80	7	2	
SV477	755B.012	159.0	BZ	10	85	40	2	TAR
SV477	755B.013	137.1	F	296	86	4	1	
SV477	755B.014	140.5	HL	168	4			
SV477	755B.015	158.0	HL	170	10			
SV477	755B.016	189.0	BZ	168	60	6	2	TAR
SV477	755B.017	195.0	BZ	355	88	6	2	TAR
SV477	755B.01B		BD	33	14			
SV477	755B.02B		BD	110	20			
SV477	755C.018	209.0	F	174	81	4	2	TAR
SV477	755C.019	220.0	F	177	86	6	2	
SV477	755C.01B		BD	115	10			
SV477	755C.020	229.0	F	350	55	7	2	TAR
SV477	755C.021	244.0	BZ	342	70	20	2	CLY
SV477	755C.022	246.5	BZ	0	85	20	2	
SV477	755C.023	254.8	BZ	14	81	20	2	
SV477	755C.024	292.0	BZ	340	82	20	1	TAR
SV477	755D.01B	352.0	BD	175	10			
SV477	755D.025	337.0	BZ	265	78	15	1	TAR
SV477	755D.026	375.0	BZ	270	50	2	2	
SV477	755D.027	360.0	HL	4	2			
SV477	755D.028	381.0	BZ	285	83	15	2	TAR
SV477	755E.01B		BD	130	10			
SV477	755E.029	400.0	F	337	84	15	2	TAR
SV477	755E.02B		BD	160	10			
SV477	755E.030	418.0	BZ	335	80	9	2	
SV477	755E.031	436.0	BZ	152	80	25	2	CLY
SV477	755E.032	462.0	BZ	306	18	4	2	CLY
SV477	755E.033	470.0	BZ	320	24	4	2	CLY
SV478	854.001	12.0	BZ	245	80			TAR
SV478	854.002	23.9	F	162	80	8	2	TAR
SV478	854.003	24.7	HL	314	22			
SV478	854.004	25.5	HL	222	42			
SV478	854.005	91.5	BZ	334	62	8	2	CL, TR
SV478	854.006	96.0	BZ	325	74	8	2	TAR
SV478	854.007	96.0	BZ	142	85	8	2	
SV478	854.008	126.0	F	5	85	12	2	
SV478	854.009	145.0	BZ	255	50	25	2	
SV478	854.010	181.0	F	134	85	6	2	TAR
SV478	854.011	186.0	F	170	84	5	2	TAR
SV478	854.012	200.0	F	276	88	5	2	
SV478	854.013	205.0	F	165	68	15	2	
SV478	854.014	211.5	F	326	83	10	2	TAR
SV478	854.015	222.5	F	325	65	12	2	SAND
SV478	854.016	237.3	F	310	82	15	2	SAND
SV478	854.017	245.5	BZ	308	85			
SV478	854.018	261.8	BZ	316	85			TAR
SV478	854.019	277.5	F	192	50	10	2	
SV478	854.01B	12.0	BD	245	50			

SITE	NNUM	SFACE	TYPE	DDIR	DIP	TRC	CEN	MNLz
SV478	854.020	282.0	BZ	350	83	25	2	TAR
SV478	854.021	292.0	BZ	317	54	12	2	
SV478	854.022	302.0	BZ	185	64	15	2	TAR
SV478	854.023	318.0	F	302	62	20	2	CLY
SV478	854.024	365.6	BZ	168	82	2	2	CLY
SV478	854.025	378.0	BZ	324	86		2	
SV478	854.026	381.5	BZ	344	85	3	2	TAR
SV478	854.027	429.5	F	153	65	12	2	
SV478	854.028	450.0	F	338	87	12	2	
SV478	854.029	472.0	F			15	2	
SV478	854.02B	23.5	BD	237	40			
SV478	854.030	482.0	BZ			8	2	
SV478	854.031	498.0	BZ	293	80	30	2	TAR
SV478	854.032	480.0	BZ	4	75			CL, TR
SV478	854.033	500.0	F	11	81	20	1	
SV478	854.034	523.0	F	353	56	30	2	
SV478	854.035	542.0	F	36	55			TAR
SV478	854.03B	23.5	BD	42	88			
SV478	854.04B	39.0	BD	250	25			
SV478	854.05B	90.0	BD	241	22			
SV478	854.06B	140.0	BD	233	21			
SV478	854.07B		BD	230	17			
SV478	854.08B		BD	354	15			
SV478	854.09B		BD	190	16			
SV478	854.10B		BD	56	25			

APPENDIX B. Examples of Scanline Maps for Both Surveys

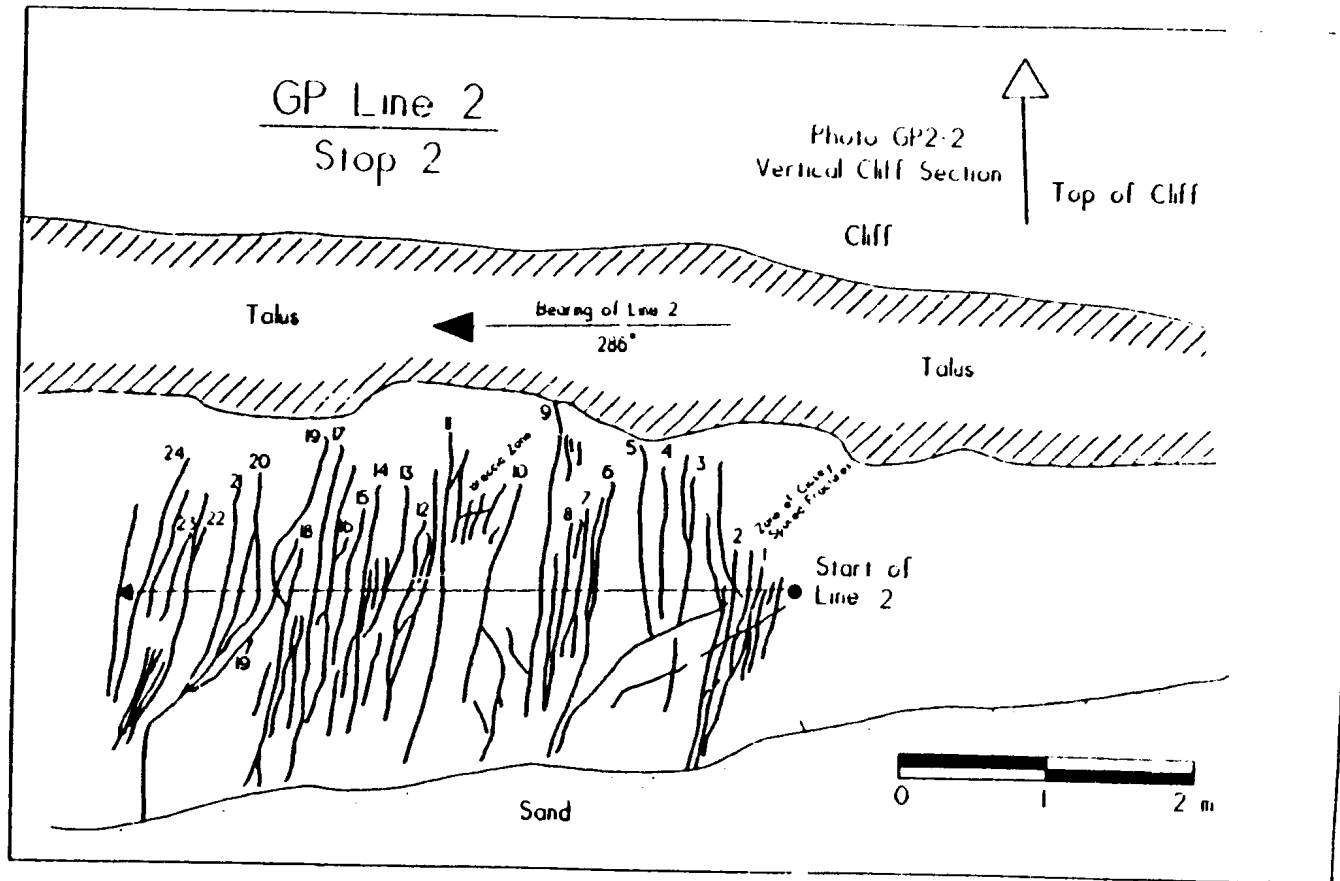


Figure B.1. Examples of small-scale fracture survey scanline maps. Portion of mapped cliff section at Government Point site 2, first part of scanline 2. ● - indicates start of scanline, ▲ - indicates end of scanline.

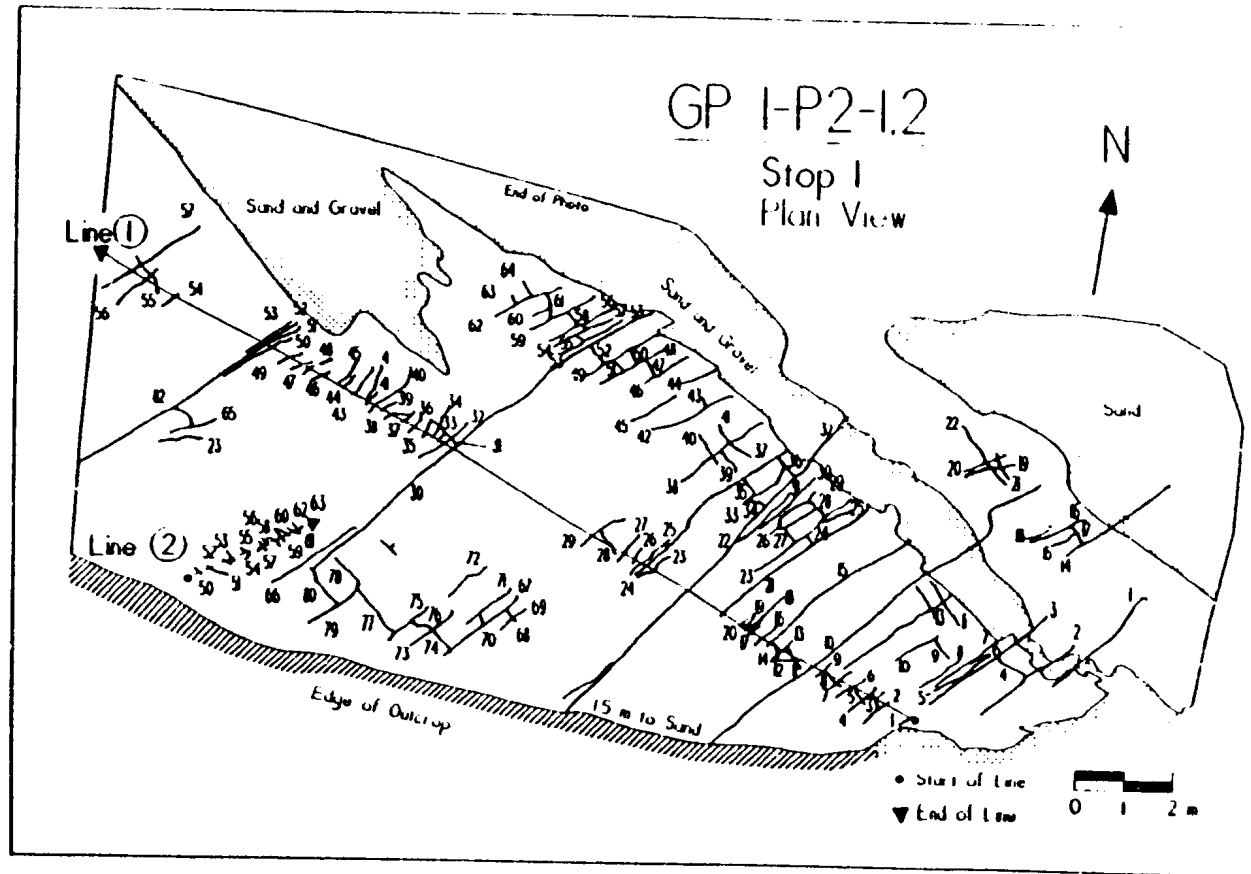


Figure B.1 (con't). Examples of small-scale fracture survey scanline maps. Mapped horizontal exposure at Government Point site 1, station P2, scanlines 1 and 2.

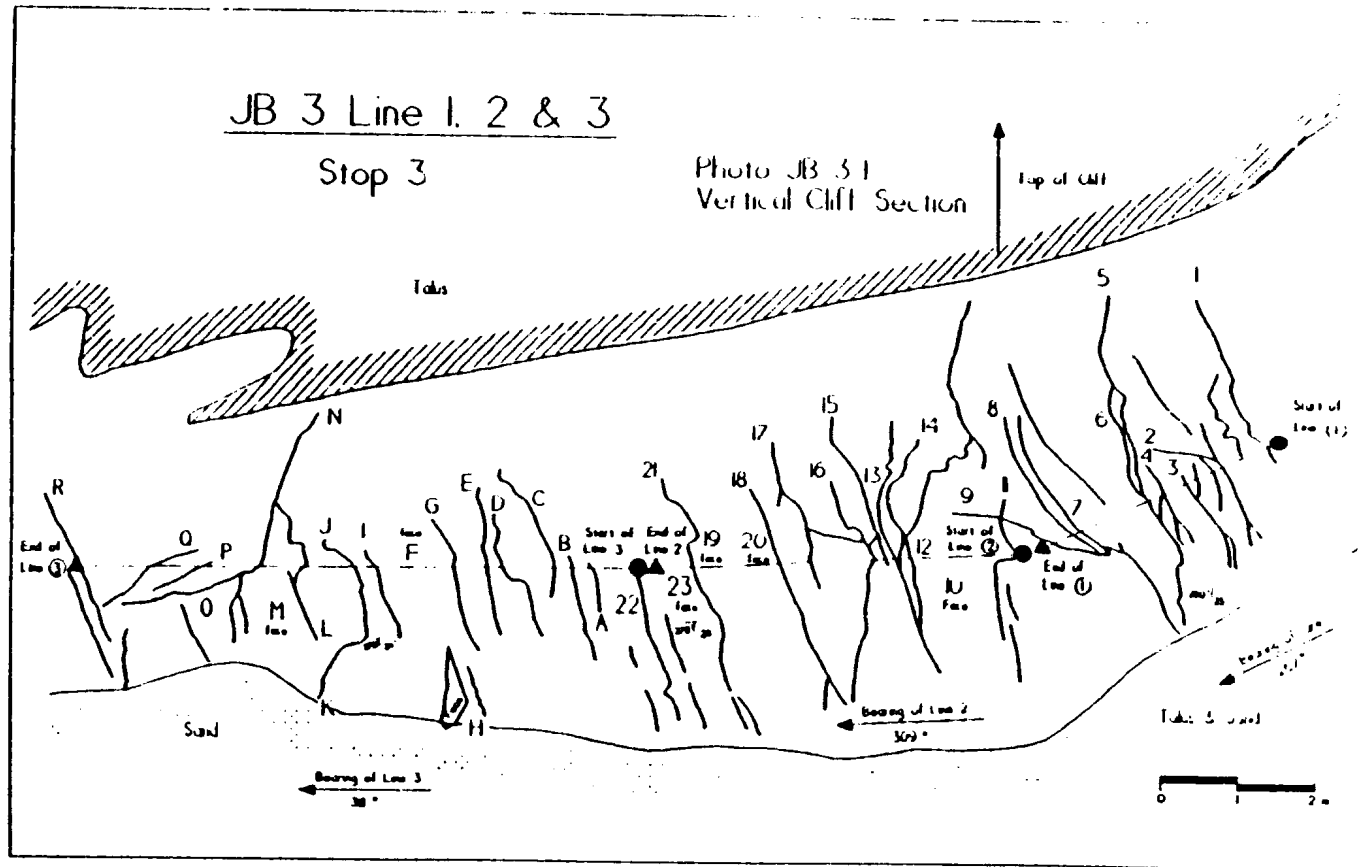


Figure B.1 (con't). Examples of small-scale fracture survey scanline maps. Mapped vertical cliff exposure at Jalama Beach site 3, scanlines 1, 2 and 3.

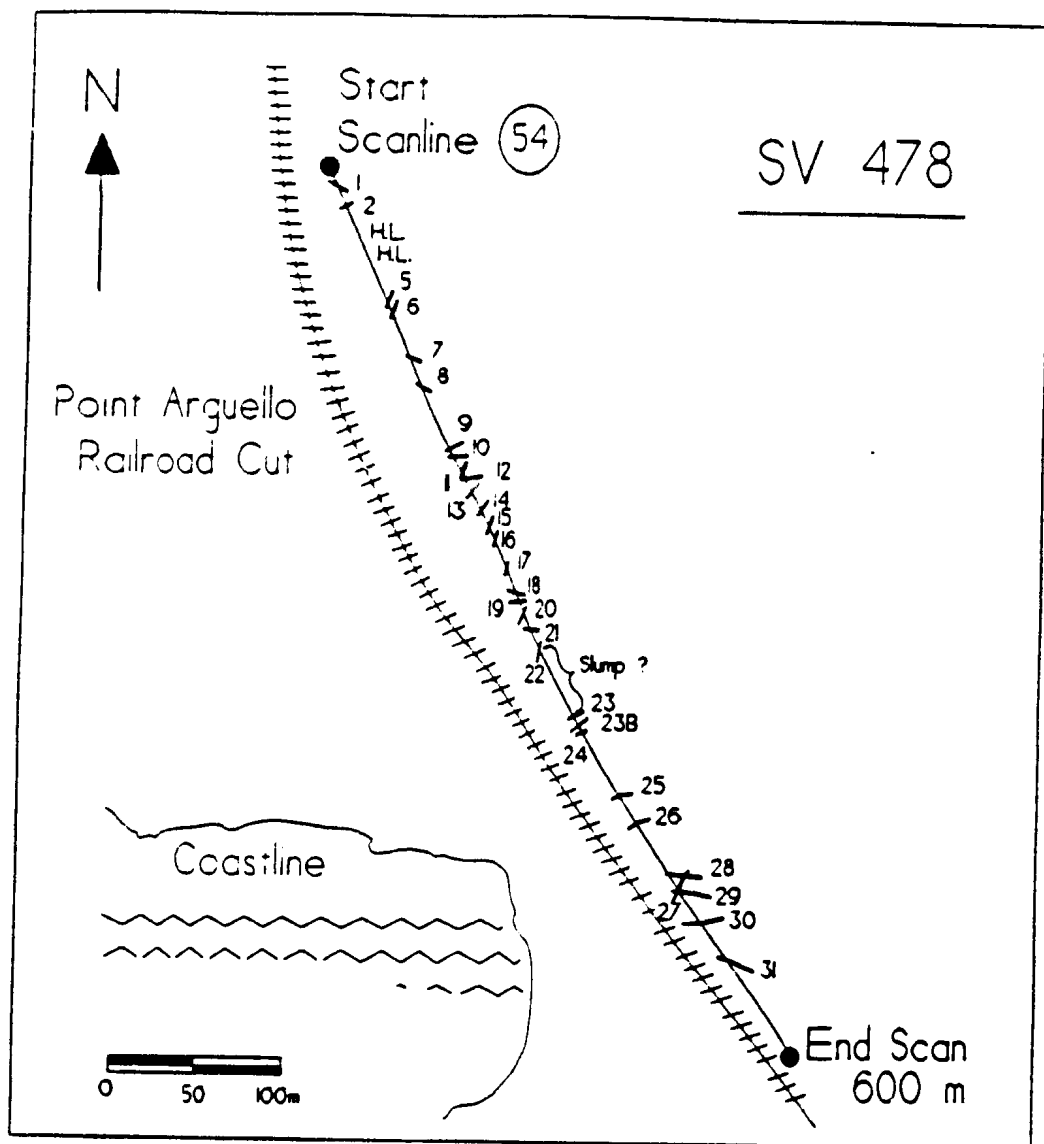


Figure B.2. Examples of large-scale fracture survey scanline maps. South Vandenberg railroad cut on photo 478.

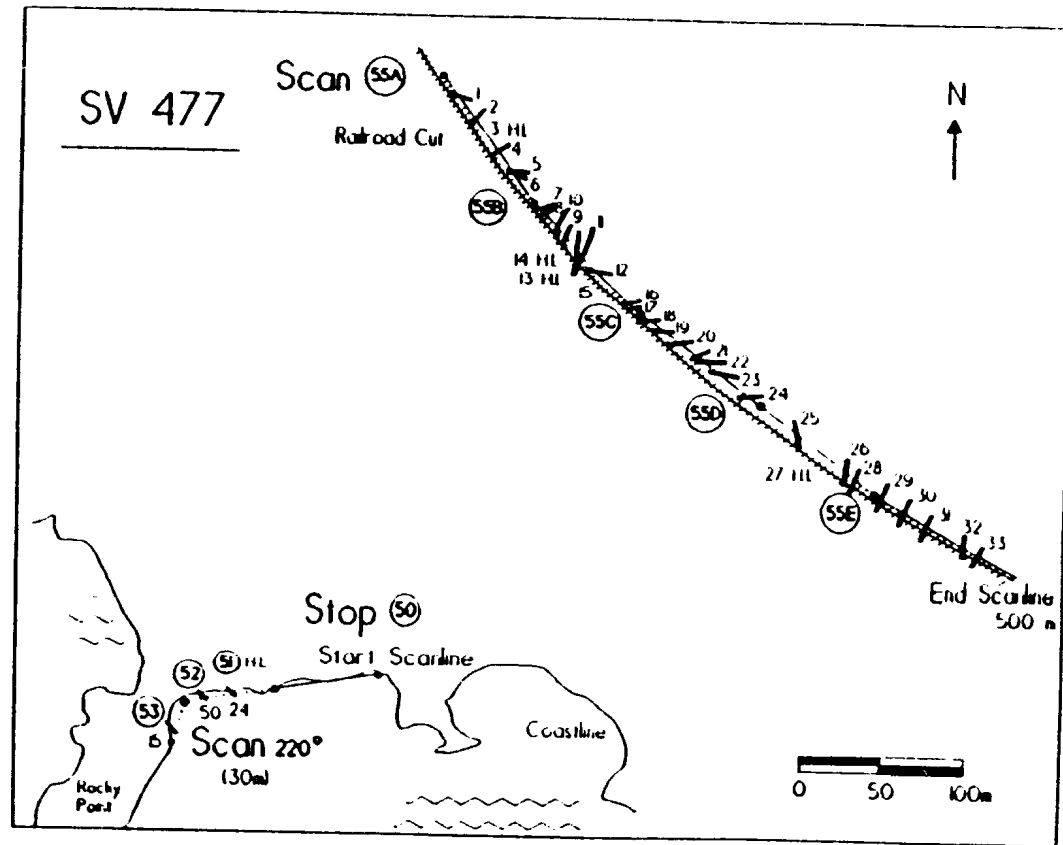


Figure B.2(con't). Examples of large scale fracture survey scanline maps. South Vandenberg, railroad cut and coast exposures on photo 477.

APPENDIX C. Determining Fracture Sets and Orientation Bias

As a standard procedure for analyzing fracture orientation data, the poles to fracture planes were plotted on lower hemisphere equal area diagrams. To determine if there are any similarities between sites, each station or site was plotted separately. A correspondence of general groupings or clusters of points between sites and/or stations are seen in the equal area plots shown in Figures C.1 through C.3 (all figures and tables presented at end of appendix), for the small-scale data. Often equal area plots are contoured to define concentration of poles. Even though the general pattern of concentration of points in most of these plots is evident, and with the understanding that contouring is sensitive to the method and area over which data points are counted, contour plots are presented for each site in Figures C.4 through C.6, for completeness of presentation. The contouring of the plots were done by the program Quickplot (van Everdingen et al., 1992) using a one percent area counting circle. Further explanation of the contouring method can be found in the above reference.

In all plots it is observed that the points are concentrated near the perimeter of the circle and grouped in two or three sets of bipolar clusters. Even though this visual assessment of groupings is fairly obvious in this suite of stereoplots, it is still subjective, so a more objective method, CLUSTRAN (Gillett, 1987), was employed to help determine the joint sets.

The computer program called CLUSTRAN uses a clustering algorithm posed by Wishart (1968) and advanced by Shanley and Mahtab (1976). Clusters are chosen based on minimizing an "objective function" that is based on an angular cluster radius supplied by the

user, usually several angles need and should be tried before a minimum is obtained. The angular cluster radius determines how close, in euclidian distance, the poles should be, to be included in the same cluster. For a full explanation of how clusters are determined see Gillett (1987). After CLUSTRAN determines the sets, the individual sets can be extracted out and the cluster of points can be compared to spherical distributions such as, the Fisher, Bingham, and the Dimroth-Watson types. If the cluster contains more than 40 points, goodness-of-fit tests can be run. Since the clusters, as determined by CLUSTRAN, were slightly modified, none of the statistical results from the program are presented. Even though most of the capabilities of CLUSTRAN were not fully used, the program was useful in making a "first pass" analysis of the data set and in extracting and separating the orientation data related to the joints in each set.

With this data set the clusters determined by CLUSTRAN were "fine tuned" by examining the field scanline maps and the field notes (Appendices A and B) to ascertain cross-cutting relationships between joints and the relationship of joints to bedding. From this process it was determined that there are two sets at all the Government Point sites, at Jalama Beach sites 1 through 4 and at Lompoc Landing, with three sets at Jalama Beach sites 5 and 6. In a general sense set 1 are the poles clustered in the NE and SW quadrants and clusters in the NW and SE quadrants are called set 2, at each site. The third set of clustered poles shown on the stereoplots for Jalama Beach sites 5 and 6 are grouped just west of the north direction. The Lompoc Landing data show 2 "conjugate" sets, separated by about 55°, with one set of poles clustered primarily in the NW quadrant and the other set in the SW quadrant. Lions Head had one dipole cluster of points with mean orientation WNW.

Once the sets were established, the sampling or orientation bias was investigated following the technique proposed by Priest (1985). This technique was carried out on the Government Point, Jalama Beach, and Lompoc Landing data. The orientation bias was not checked at the other site, Lions Head, located in the Onshore Santa Maria domain because of the small amount of data. It is recognized that since only one scanline along a small vertical cliff was used at the Lions Head site, orientation bias could be high. But, since the poles on the stereoplot for the Lions Head data are tightly clustered and define only one set, it was determined that no advantage would be gained by correcting for the orientation bias for this one set at this site.

With Priest's method each discontinuity is weighted according to the angle(δ) between the sampling line and the normal to the discontinuity plane. The weight factor(W) equals $1/\cosine \delta$, where $\cos \delta$ can be written as $\cos(\alpha_n - \alpha_s)\cos(\beta_n - \beta_s) + \sin\beta_n\sin\beta_s$, with $\alpha_n, \beta_n, \alpha_s, \beta_s$, as the trend and plunge for the discontinuity normal and the sampling line, respectively. Thus all weight factors will be greater than 1 and a discontinuity that is at a small angle to the sampling line will have a large weight factor. After W is calculated for each discontinuity the weight factors are summed(N_w) for each set, then each weight factor is normalized(w) by multiplying by the set sample size(N) and dividing by the total weighted sample size(N_w), so $w = W*N/N_w$. This is done so the normalized weighted sample size will be equal to the original sample size without changing the relative weighting of each discontinuity, and as pointed out by Priest(1985) the sample size is important in estimating the precision of the data. To determine if there is any sampling bias, weighted and non-weighted direction cosines are calculated for the discontinuities in each set, the weighted and non-weighted

resultants are found and from which the mean trend and plunge can be calculated. The weighted mean direction and the non-weighted mean direction can be compared to determine the relative sampling bias. Priest also used Fisher's constant(K)(Mardia, 1972, p.228; Priest, 1985 p.46), where $K = N-1/N-R$ (R is the magnitude of the mean resultant), as a measure of the degree of clustering of poles in each set. In doing this, it is assumed that the data can be represented by the Fisher distribution, that the mean orientation is represented by the resultant of the direction cosines, and that normalized weighted data can be used in Fisher's method of analysis. If it is found that the data fits the Fisher distribution, then confidence circles can be made around the mean orientation and the mean orientations can be compared between sites.

A simple program in QuickBasic was written using the algorithms from Priest (1985) with the results for Government Point, Jalama Beach and Lompoc Landing areas presented in Table C.1. As mentioned earlier, in this data set the poles plot near the perimeter of the diagram, and thus discontinuities in the same set can have poles 180° apart (bipolar), and since the Priest's algorithms were meant to be used on vector data, the algorithms were modified to treat the data from the same set as axes, thus it is possible for a normal to have a negative dip (plot on the upper hemisphere).

As seen in Table C.1, for these data there was no appreciable sampling bias, since for each set the weighted and non-weighted mean directions, are within each others 95% zone of confidence. The mean direction was calculated from the resultant vector of the mean direction cosines, and the number given as the zone of confidence is the cone angle, centered on the mean vector, with which there is a 95% confidence that the true mean orientation lies

within the described locus. This probability is usually best where the sample size is greater than 30. Fisher's constant (K) is a measure of the degree of clustering in a given set, a large value indicates the data are clustered around the mean, with a smaller value the data would be more dispersed. It was estimated using the unbiased estimator ($K = N-2/N-R$) given by Mardia (1972), where N is the sample size and R is the magnitude of the resultant vector. If the data are concentrated on the mean vector, R has a large value, and has a small value if the data are more uniformly distributed. The spherical variance (Var in the table) was calculated from $N-R/N$, from Mardia (1972). As the table shows, for almost all of the sets from the different sites, R and K are relatively large and the spherical variance is low, indicating the poles for each set are tightly clustered around the mean direction. The values for the zone of confidence indicate, for sites with a large sample size, there is a 95% probability the true mean orientation will lie within a cone angle of less than 8 degrees of the given mean direction. With this zone of confidence angle, mean directions for each set can be compared between different sites. But first, it should be demonstrated that the distribution of the observed orientation data are represented reasonably well by the Fisher distribution. Also, the structural position of the sites being compared should be similar.

To visually evaluate how well the data match the Fisher distribution, graphs (Figure C.7) of the observed data versus the theoretical values were plotted following Priest's (1985) method, and lower hemisphere stereoplots were made of the poles centered around the mean orientation direction, which was rotated to the center of the diagram (Figure C.7). The graphs plot the proportion [$P(\theta < \theta)$] of fracture normals that are less than the solid angle θ away from the mean on the ordinate against the angle [θ] on the abscissa, for the

observed and theoretical values. These graphs were mainly used to compare how closely the observed data match the theoretical curve of the Fisher distribution. As can be seen in Figure C.7, the observed values follow the theoretical curve reasonably well. This observation holds for the example graphs as well as for all sets at all sites where the sample size was greater than 25. But to compare if the normals are circularly distributed around the mean direction as the Fisher distribution is, stereoplots like the examples in the lower portion of Figure C.7 were used. Set 1 at station P1 is reasonably uniformly dispersed around the mean (the center of the net) but normals of set 2 are more elongate in distribution. These types of graphs and plots give a good general "feel" for the distribution of the orientation data, but for a more statistical evaluation, Chi-squared tests were also performed following Mardia's (1972) method on a few of the sites. It quickly became apparent that the data only marginally pass the Chi-square test and would be highly sensitive to the degree interval at which observed and theoretical values were compared. A few possible reasons for not matching the Fisher distribution are that the Chi-square test is based on estimated parameters and is not very robust. Also the Fisher distribution has vectors randomly dispersed about the mean, these data have a wide range of azimuths but a fairly tight range of dips (as can be seen in Figures C.1 to C.6, and C.7), thus would not be evenly distributed about the mean. These data may be better represented by another statistical distribution such as the Bingham distribution. The Bingham distribution applies to moment-of-inertia analysis and is flexible in describing a data set according to the relationship of its two parameters, one for shape, the other for concentration, but it is mathematically cumbersome to use and further analysis was not attempted.

In the strict sense, to compare the mean orientations from site to site it should be proven that the samples at each site come from populations that have a similar distribution. Even though the only attempt was the statistically inconclusive comparison to the Fisher distribution, it will still be assumed that since the data were collected from similar lithologies and roughly the same tectonic history, the overall population distribution is the same from site to site. But to compare the mean orientations of each set between the different sites the structural differences need to be corrected. For the small-scale data this is discussed in Chapter 3.

It should be noted that it is hard to say that these data represents an adequate sample of the sites. It is obvious that, if present, the horizontal discontinuities would have been under-sampled. No direct proof can be offered, but from field observations and what is presented in the literature, there is no small-scale horizontal joint set in the Monterey Formation at these study sites. At most sites, however, numerous bedding planes were observed to be open to fluid flow, and could be considered a discontinuity set.

Lower hemisphere equal area stereoplots for the large-scale data are presented in Figures C.8 and C.9, with the contour plots in Figures C.10 and C.11. As seen on the diagrams there is some small clustering of points, but variability in the amount of dip is much greater than that shown for the small-scale fractures and also there is a wide range of azimuths. Since these large-scale fractures are related to the folding and could not conveniently be grouped by outcrops which were in similar structural position, the data needed to be normalized. To normalize or standardize the orientations of the large-scale fractures the bedding in which the feature was located was rotated to a common strike then to a horizontal position. This

rotation was done using the stereogram where the poles to the fracture planes are rotated about the vertical axis until the bedding strike coincides with the N-S direction and then rotated "up" to the horizontal by the amount of bedding dip. During the mapping phase, several bedding dip azimuths and dips were recorded for the bedding near each feature. Great care was taken that in the rotation process the bedding attitude used was not an artifact of the large-scale feature, but are representative of the general bedding trend of the nearby surrounding area. Once all the data were rotated, they were combined into two data files, one for the two sites in the northern section of this study area and one for the 4 sites in the southern region. Figure C.12 shows the bedding-rotated, large-scale data, for the sites in the Santa Barbara structural domain (the southern region) and Figure C.13 is for the sites in the Onshore Santa Maria domain (the northern region). As with the small-scale data, CLUSTRAN was used as a first pass analysis of the orientation data. Even after rotating the data there is a fairly wide variability to the azimuthal directions, but in CLUSTRAN the data are checked for overall randomness and the distribution of poles was found to differ at the 5% level from the Poisson distribution. Statistically the data were found to be clustered in six groups with strong overlaps in azimuth for the southern region and two widely dispersed, overlapping groups in the northern region. After a visual assessment was done using these stereoplots, combined with the observed field relationships, three sets were determined for the southern sites and possibly three sets for the northern data. For the southern region one set is dispersed about the bedding strike direction, another set scattered about the bedding dip direction, and the third is horizontal. Due to the large variability in orientations for the fractures in the northern region and the relatively small sample size, it is difficult to confidently define the discontinuity sets. However, from observed field relationships, three

sets were chosen. One set represented by 29 fractures, strikes parallel with the bedding dip direction, another set ($N=10$) strikes approximately 55° to the right of the first set's strike, and two fractures form the third set that strikes parallel with bedding strike. Further analysis of the large-scale orientation data is discussed in Chapter 3.

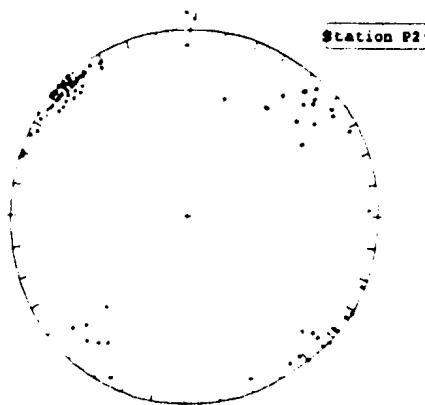
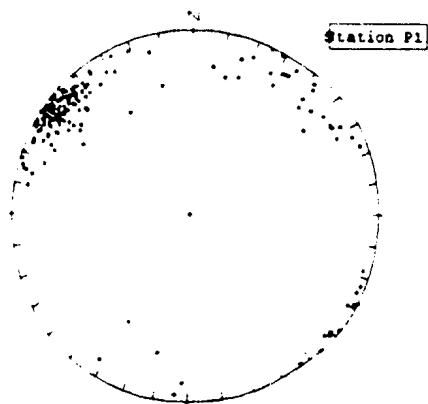
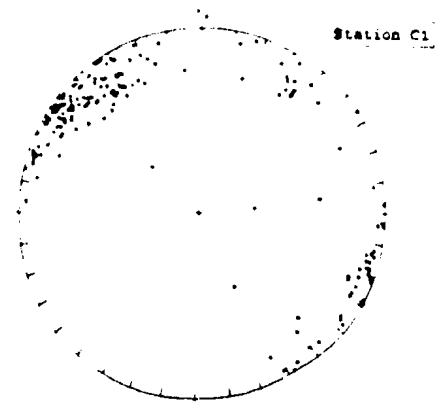


Figure C.1. Lower hemisphere equal area plots of poles to fracture planes at Government Point, stations C1, P1, and P2.

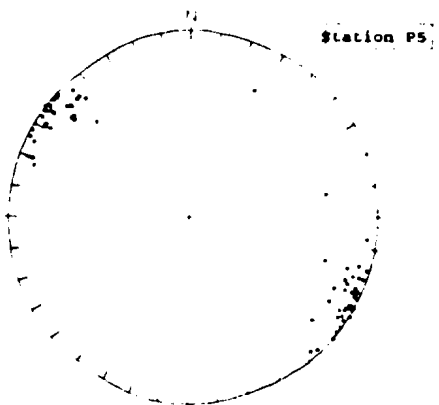
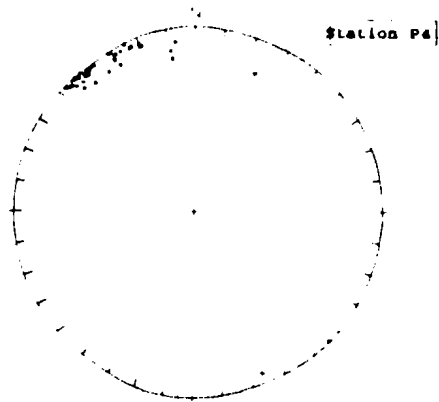
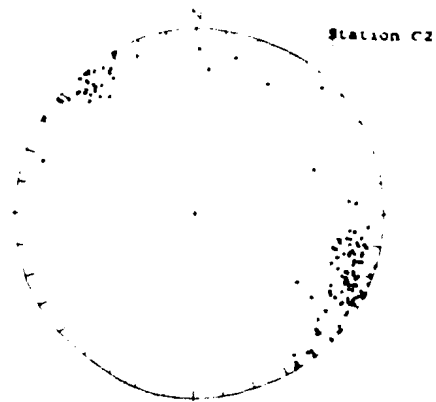


Figure C.1 (con't). Lower hemisphere equal area plots of poles to fracture planes at Government Point, stations C2, P4, and P5.

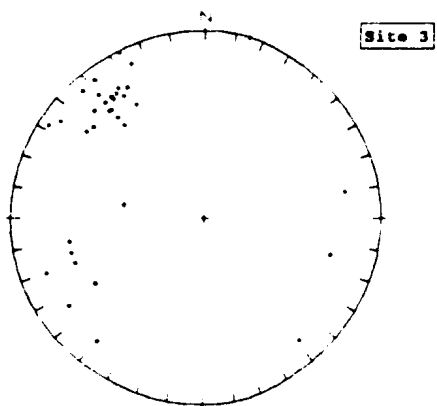
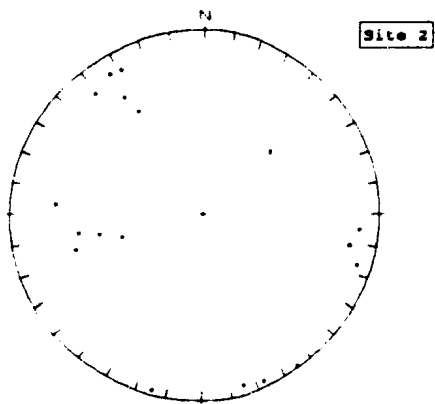
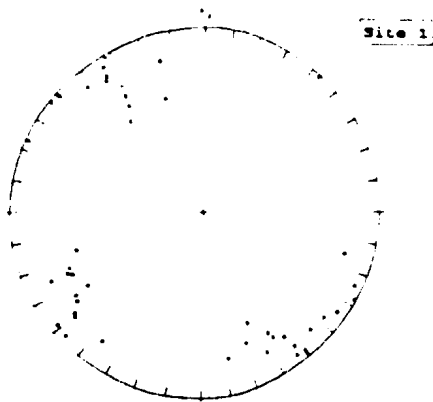


Figure C.2. Lower hemisphere equal area plots of poles to fracture planes at Jalama Beach, sites 1, 2, and 3.

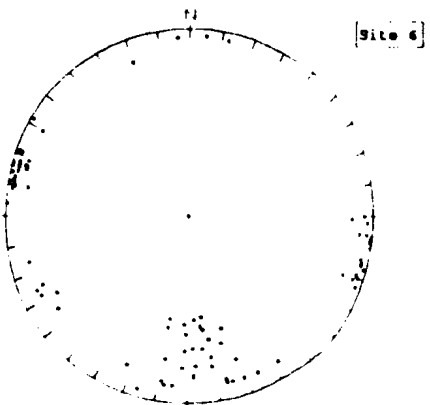
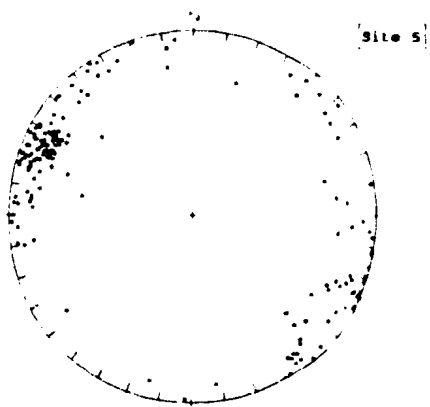
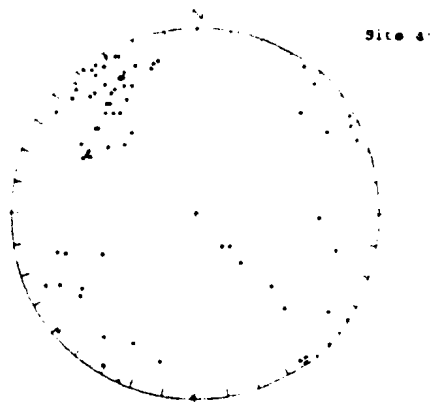


Figure C.2 (con't). Lower hemisphere equal area plots of poles to fracture planes at Jalama Beach, sites 4, 5, and 6.

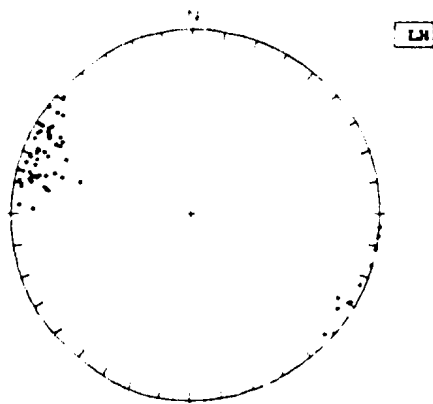
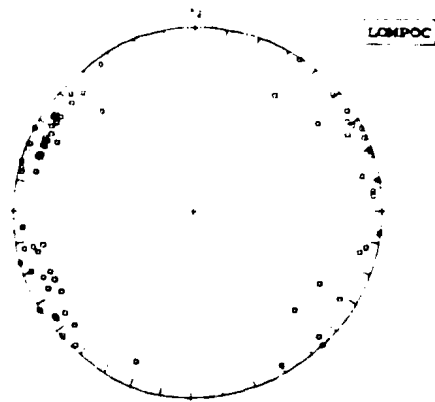


Figure C.3. Lower hemisphere equal area plots of poles to fracture planes at Lompoc Landing and Lions Head.

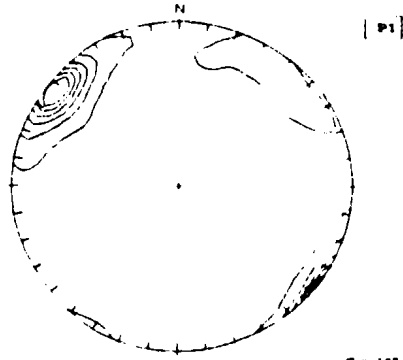
Max. value counted:
18.7 times uniform
at 126/84



Contours:
1 5 10 15

N - 101
Poles to Planes

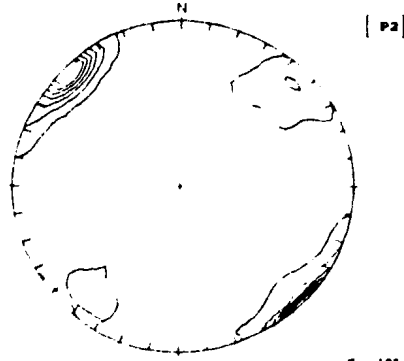
Max. value counted:
33.3 times uniform
at 126/84



Contours:
1 5 10 15 20 25

N - 102
Poles to Planes

Max. value counted:
37.7 times uniform
at 136/84

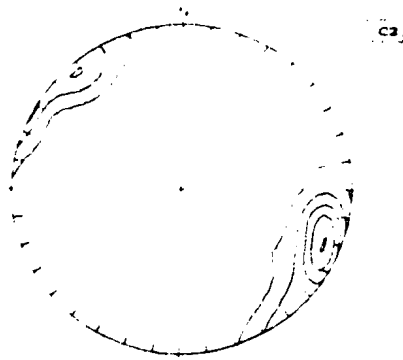


Contours:
1 5 10 15 20 25

N - 104
Poles to Planes

Figure C.4. Contoured lower hemisphere equal area plots of poles to fracture planes at Government Point, stations C1, P1, and P2.

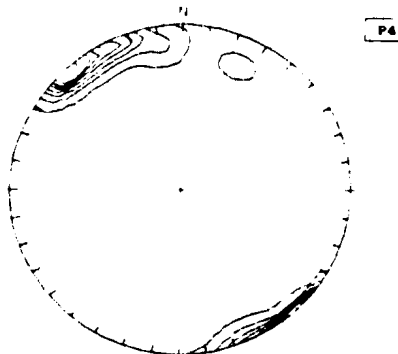
Max. value counted:
20.9 times uniform
at 290/79



Contours:
1 5 10 15 20

N - 328
Pole to Plane

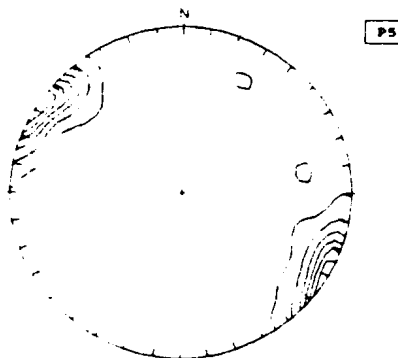
Max. value counted:
45.2 times uniform
at 318/90



Contours:
1 5 10 15 20 25 30

N - 48
Pole to Plane

Max. value counted:
31.2 times uniform
at 303/90

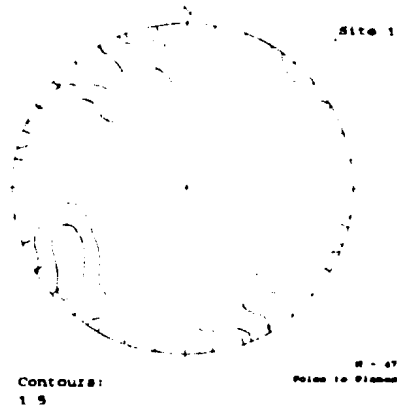


Contours:
1 5 10 15 20 25

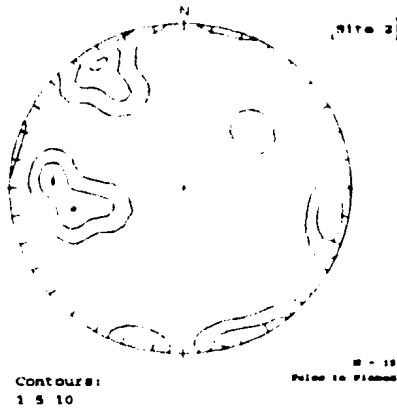
N - 73
Pole to Plane

Figure C.4 (con't). Contoured lower hemisphere equal area plots of poles to fracture planes at Government Point, stations C2, P4, and P5.

Max. value counted:
9.52 times uniform
at 143/79



Max. value counted:
11.4 times uniform
at 147/79



Max. value counted:
25.6 times uniform
at 142/69

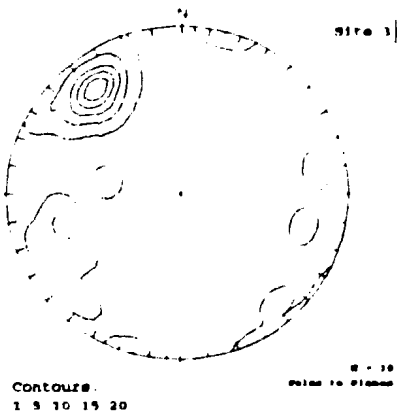
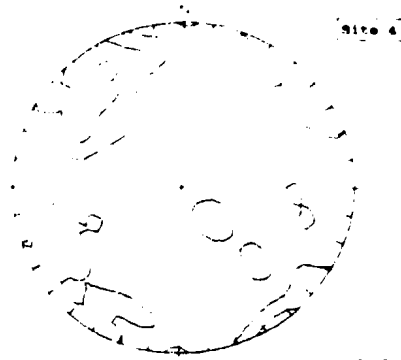


Figure C.5. Contoured lower hemisphere equal area plots of poles to fracture planes at Jalama Beach, sites 1, 2, and 3.

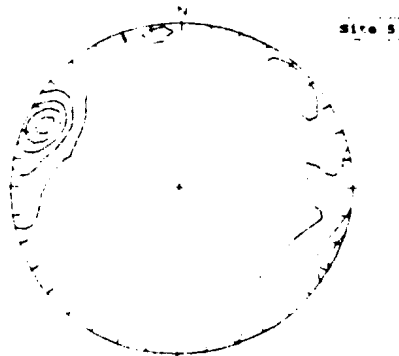
Max. value counted:
11.1 times uniform
at 150/89



Contours:
1 5 10

N - 78
Pole to Plane

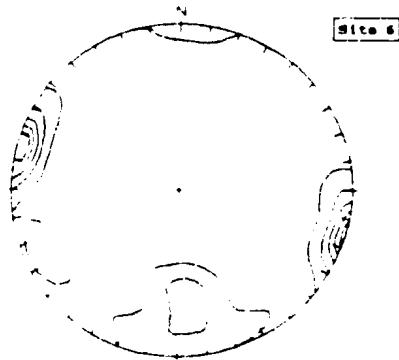
Max. value counted:
22.0 times uniform
at 116/74



Contours:
5 10 15 20

N - 179
Pole to Plane

Max. value counted:
26.1 times uniform
at 285/90

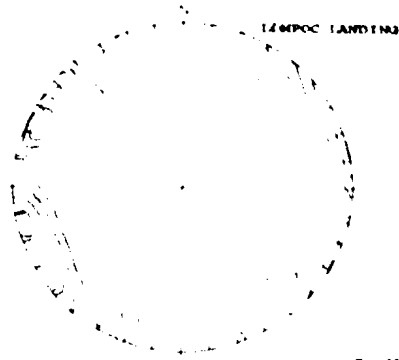


Contours:
1 5 10 15 20

N - 32
Pole to Plane

Figure C.5 (con't). Contoured lower hemisphere equal area plots of poles to fracture planes at Jalama Beach, sites 4, 5, and 6.

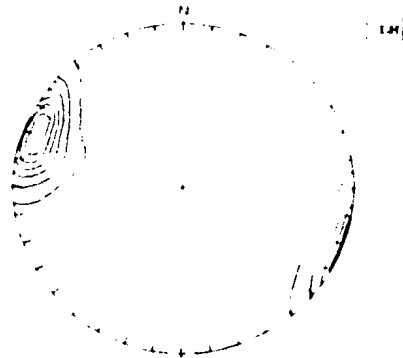
Max. value counted:
15.0 times uniform
at 113/79



Contours:
1 3 6 9 12

W - 22
Poles to Planes

Max. value counted:
39.1 times uniform
at 111/84



Contours:
1 5 10 15 20 25

W - 22
Poles to Planes

Figure C.6. Contoured lower hemisphere equal area plots of poles to fracture planes at Lompoc Landing and Lions Head.

Table C.1. Statistics of orientation data presented as normals on stereonet in Figures C.1 through C.3. Table continued on next page.

Site	Station	SET	N	K	Mean orientation		R	Var	Zone of conf. °
					Trend	Plunge			
GP1	C1	1	20	11.6	40.0	18.2	18.4	0.078	9.6
		1w		13.3	44.2	14.6	16.6	0.068	8.9
		2	161	16.1	309.4	6.8	151.1	0.061	2.8
		2w		13.7	310.3	7.1	149.4	0.072	3.1
GP1	P1	1	31	13.2	35.1	8.5	28.7	0.073	7.4
		1w		10.7	42.1	7.3	28.3	0.088	8.1
		2	154	42.8	307.9	7.7	150.4	0.023	1.8
		2w		40.2	307.7	7.8	150.2	0.025	1.8
GP1	P2	1	23	13.6	42.6	6.6	21.5	0.067	8.2
		1w		16.1	39.1	5.7	21.7	0.057	7.5
		2	83	45.3	313.4	2.8	81.2	0.022	2.3
		2w		44.7	315.4	2.6	81.2	0.022	2.3
GP2	C2	1	5	7.9	30.5	20.4	4.6	0.076	23.3
		1w		8.7	30.3	18.1	4.7	0.069	22.1
		2	131	17.1	120.6	7.3	123.5	0.058	3.1
		2w		16.5	120.9	7.3	123.2	0.060	3.1
GP3	P4,P5	1	2	0.0	26.0	21.5	2.0	0.001	-
		1w		0.0	25.1	20.4	2.0	0.001	-
		2	113	20.7	309.3	1.4	107.6	0.047	3.0
		2w		19.2	125.3	0.8	107.2	0.051	3.1

#w = weighted data.

R = magnitude of the mean resultant of the direction cosines.

K = Fisher's constant, degree of concentration.

Var = spherical variance (N-R/N).

*Zone of confidence: $[\arccos(1 + (\ln(1-0.95))/(K*R))]$, .95 probability true mean orientation lies inside a locus centered on mean.

Table C.1 (con't). Statistics of orientation data presented as normals on stereonets in Figures C.1 through C.3.

Site	Station	Mean orientation			Trend	Zone of Plunge	R	Var	conf.*
		SET	N	K					
JB1	1	1	14	32.1	235.4	18.1	13.6	0.027	6.7
		1w		31.1	235.6	18.5	13.6	0.028	6.7
		2	33	12.0	320.6	0.2	30.4	0.078	7.4
		2w		13.9	142.5	3.0	30.8	0.068	6.9
JB2	1	1	10	5.0	267.0	14.8	8.4	0.160	21.8
		1w		3.7	261.1	13.1	7.8	0.217	26.4
		2	9	12.4	334.9	9.3	8.4	0.063	13.7
		2w		7.7	353.5	4.7	8.1	0.101	17.8
JB3	1	1	9	7.7	254.1	22.1	7.9	0.344	32.6
		1w		7.7	254.6	22.0	7.7	0.358	33.6
		2	29	11.5	326.3	16.9	26.6	0.081	8.0
		2w		5.1	340.6	12.4	23.7	0.184	12.8
JB4	1	1	21	5.3	255.9	14.0	17.4	0.170	14.6
		1w		7.5	247.9	4.5	18.5	0.121	12.0
		2	57	6.0	331.6	7.7	47.8	0.161	8.3
		2w		4.5	337.4	3.9	44.8	0.215	9.9
JB5	1	1	12	12.8	38.8	7.2	11.2	0.065	11.7
		1w		22.6	48.6	6.0	11.6	0.037	8.7
		2	134	22.2	291.5	7.0	128.0	0.044	2.6
		2w		18.3	288.6	6.0	126.8	0.054	2.9
		3	24	24.7	149.1	2.9	23.1	0.037	5.9
		3w		23.2	149.2	3.2	23.1	0.040	6.1
JB6	1	1	6	107.6	243.4	14.4	6.0	0.006	5.5
		1w		112.2	242.5	14.7	6.0	0.006	5.4
		2	47	75.7	285.0	1.3	46.4	0.013	2.4
		2w		73.8	284.7	1.1	46.4	0.013	2.4
		3	39	18.3	175.9	21.9	37.0	0.052	5.4
		3w		17.7	179.9	22.8	36.9	0.054	5.5
LL	1	1	38	23.7	299.5	3.6	36.5	0.040	4.8
		1w		17.0	304.2	1.2	35.9	0.056	5.7
		2	42	21.3	244.1	2.5	40.1	0.045	4.8
		2w		21.4	246.9	2.6	40.1	0.044	4.8

#w = weighted data.

R = magnitude of the mean resultant of the direction cosines.

K = Fisher's constant, degree of concentration.

Var = spherical variance $(N-R/N)$.

*Zone of confidence: $[\arccos(1 + (\ln(1-0.95))/K*R)]$, .95 probability true mean orientation lies inside a locus centered on mean.

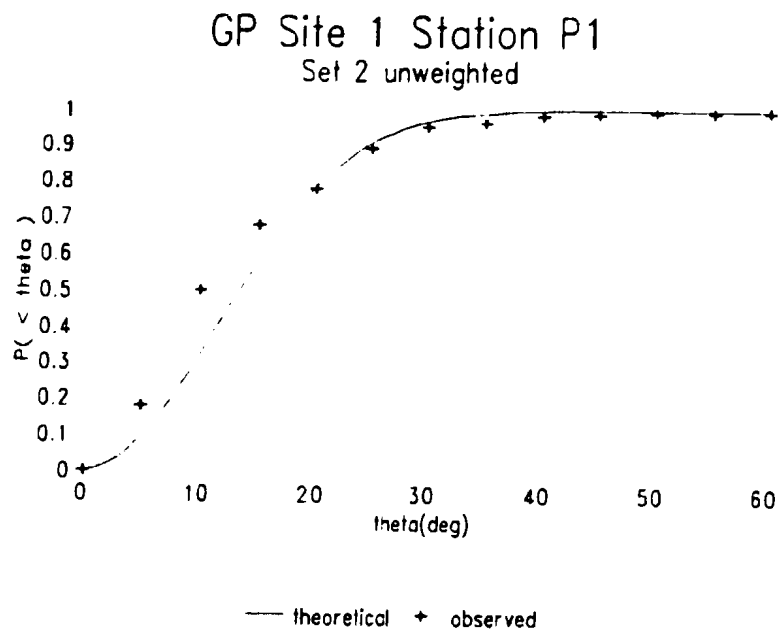
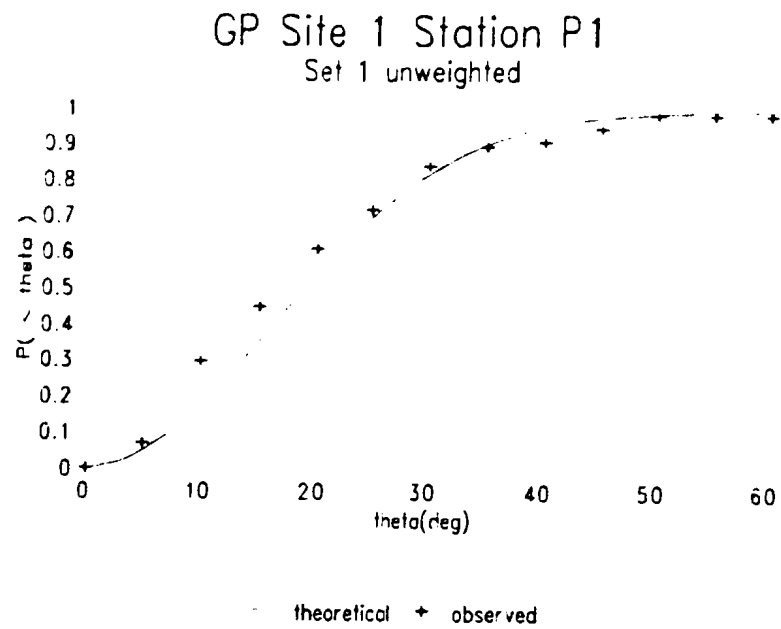


Figure C.7. Examples of graphs and stereoplots used to visually evaluate the fit of the orientation data for each set to the theoretical Fisher probability distribution. See text for further discussion.

P1 Set 1

Eigen values:
.864 .092 0.042
Eigen vectors:
Dip-Dir Dip
121.7 89.96
327.7 1.321
237.1 4.812
Confidence Radius
95% Signif.: 7.37 deg.
K = 13.2

N = 11
Poles to Planes

P1 Set 2

Eigen values:
.955 3.18 0.012
Eigen vectors:
Dip-Dir Dip
358.1 89.96
234.1 2.581
144.1 2.211
Confidence Radius
95% Signif.: 1.75 deg.
K = 42.8

N = 154
Poles to Planes

Figure C.7 (con't). Examples of stereoplots used to visually evaluate the fit of the orientation data for each set to the theoretical Fisher probability distribution. See text for further discussion.

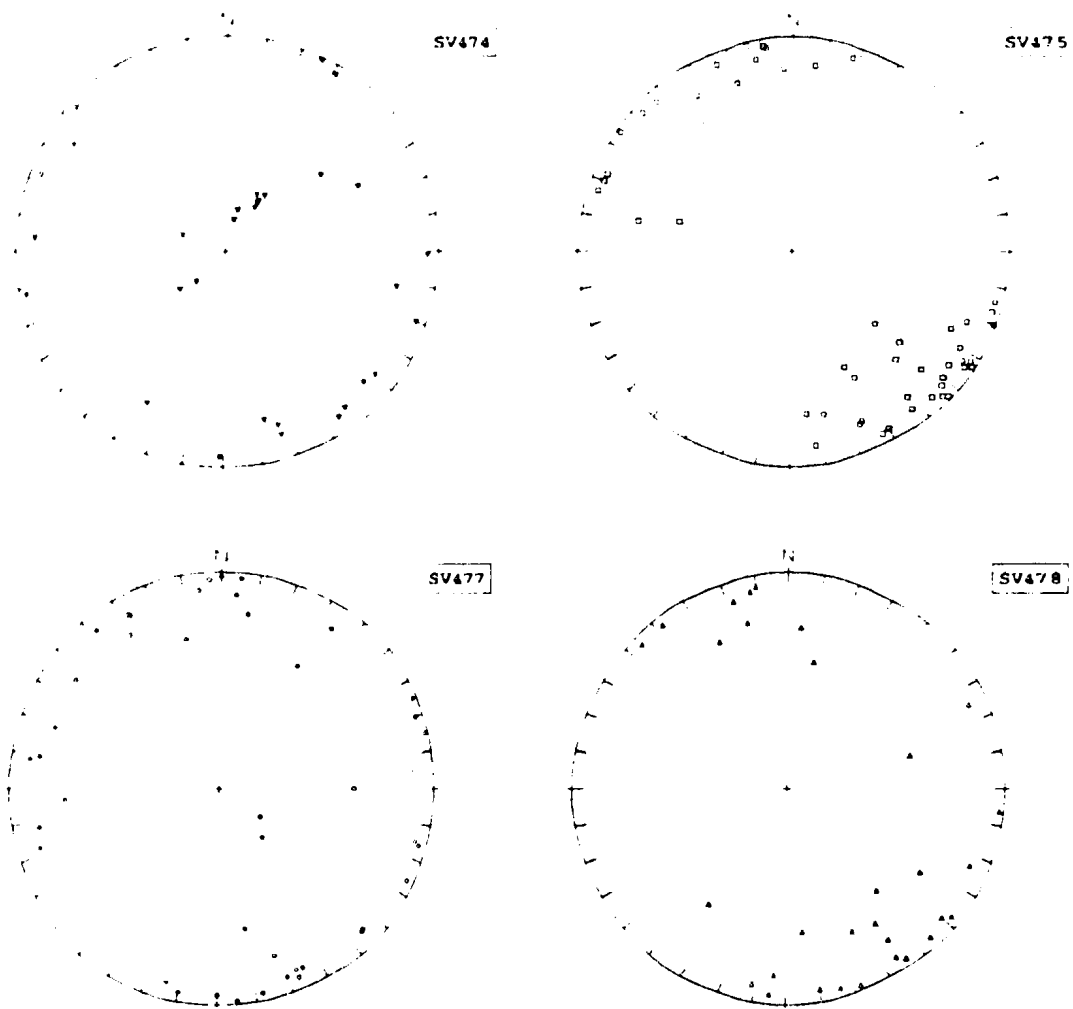


Figure C.8. Lower hemisphere equal area plots of poles to fracture planes for the large-scale fractures mapped along the coast southeast of Rocky Point, SV474 and SV475 are the numbers of the photo map base, and for railroad cuts near Rocky Point (SV477) and Point Arquello (SV478).

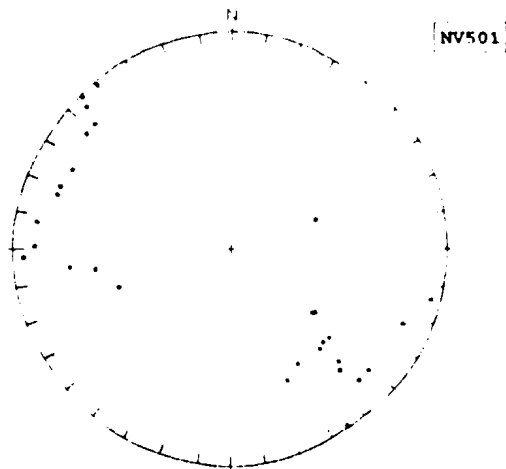
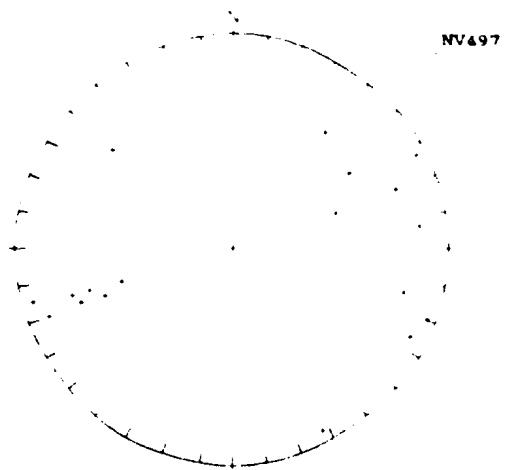
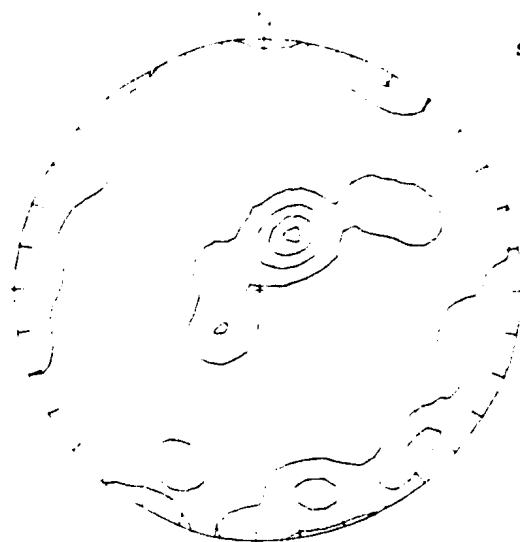


Figure C.9. Lower hemisphere equal area plots of poles to fracture planes for large-scale tructures mapped near Lompoc Landing (NV497) and Purisma Point (NV501).

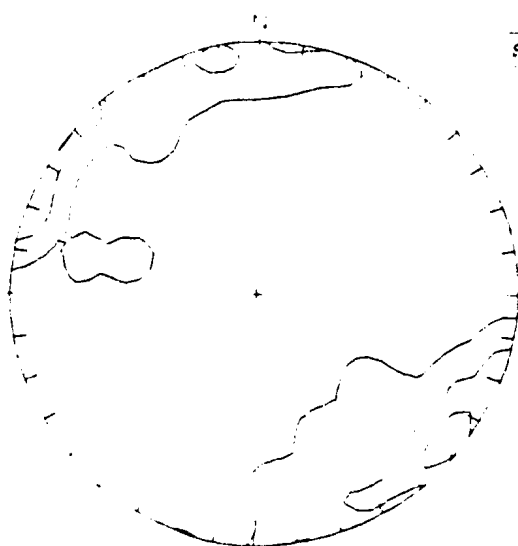
Max. value counted:
16.0 times uniform
at 204/20



Contours:
1 5 10 15

N = 31
Poles to Planes

Max. value counted:
13.3 times uniform
at 306/84



Contours:
1 5 10

N = 50
Poles to Planes

Figure C.10. Contoured lower hemisphere equal area plots of poles to fracture planes for the large-scale fractures mapped along the coast southeast of Rocky Point, SV474 and SV475 are the numbers of the photo map base. Contours are percent of poles in one percent area.

Max. value counted:
9.53 times uniform
at 180/90

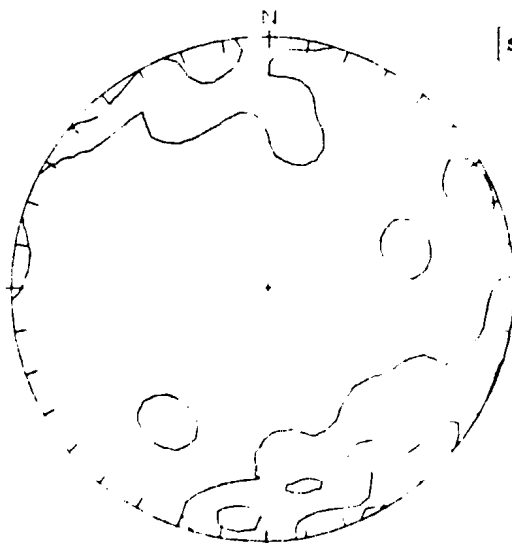


SV477

Contours:
1 5

N = 43
Poles to Planes

Max. value counted:
8.48 times uniform
at 167/84



SV478

Contours:
1 5

N = 31
Poles to Planes

Figure C.10 (con't). Contoured lower hemisphere equal area plots of poles to fracture planes for the large-scale fractures mapped along the railroad cuts near Rocky Point (SV477) and Point Arquello (SV478). Contours are percent of poles in one percent area.

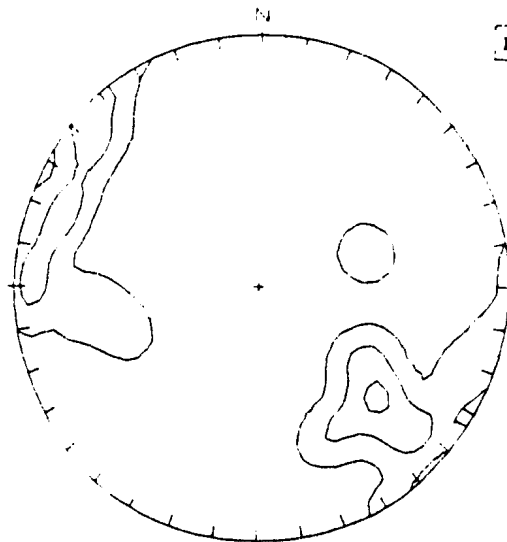
Max. value counted:
14.6 times uniform
at 72/64



Contours:
1 5 10

N = 18
Poles to Planes

Max. value counted:
11.5 times uniform
at 314/55



Contours:
1 5 10

N = 29
Poles to Planes

Figure C.11. Contoured lower hemisphere equal area plots of poles to fracture planes for large-scale fractures mapped near Lompoc Landing (NV497) and Purisma Point (NV501). Contour interval is percent of one percent area.

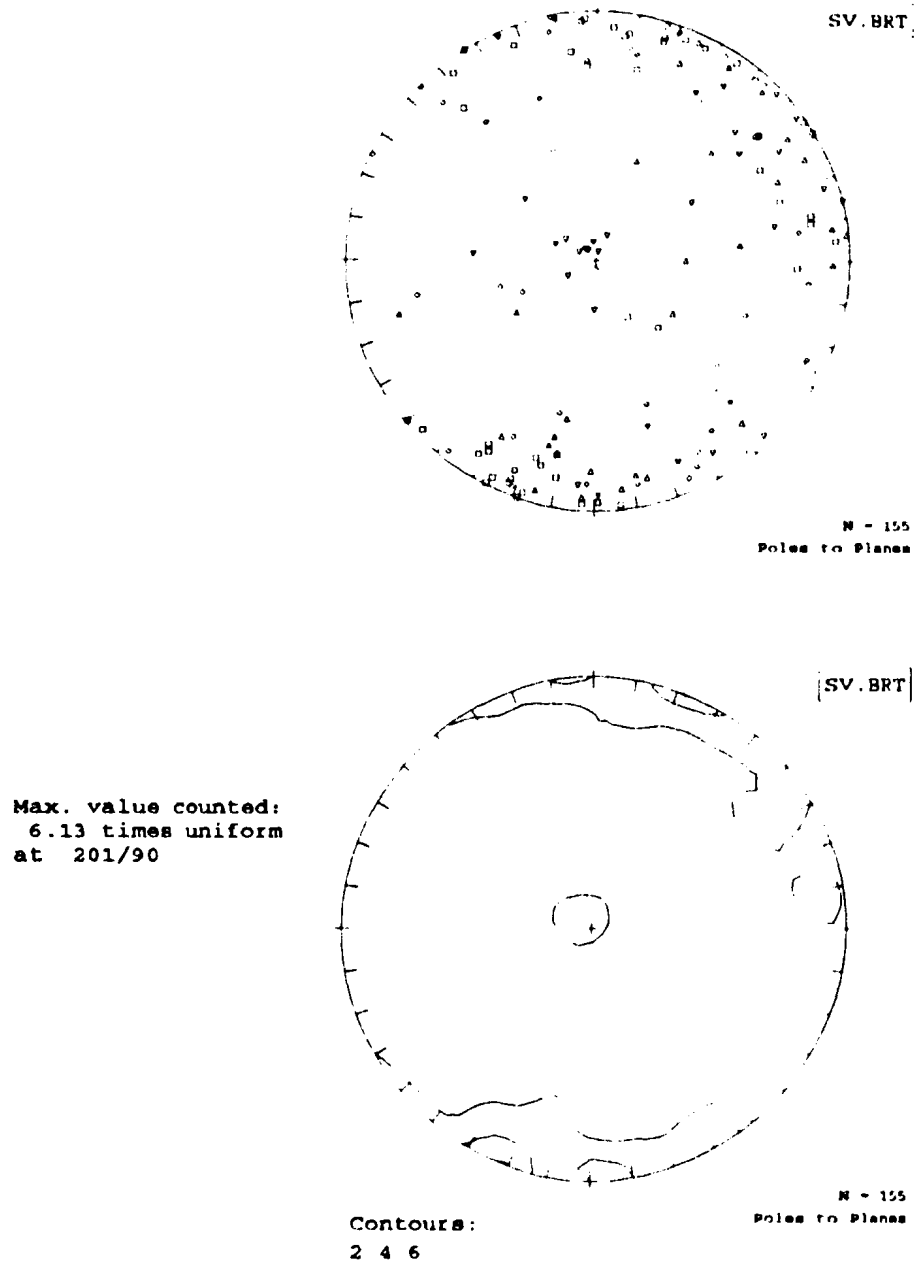
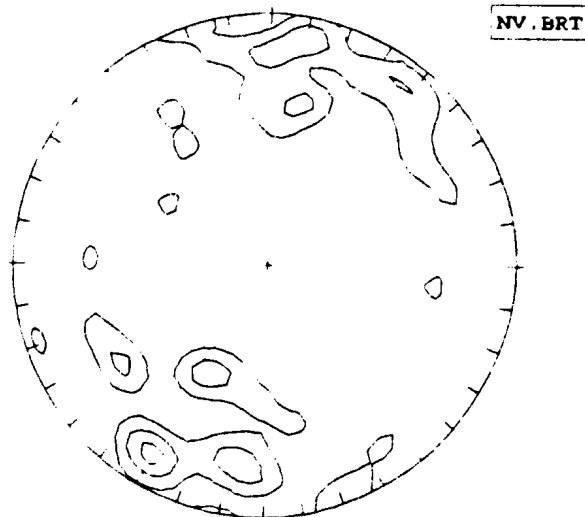
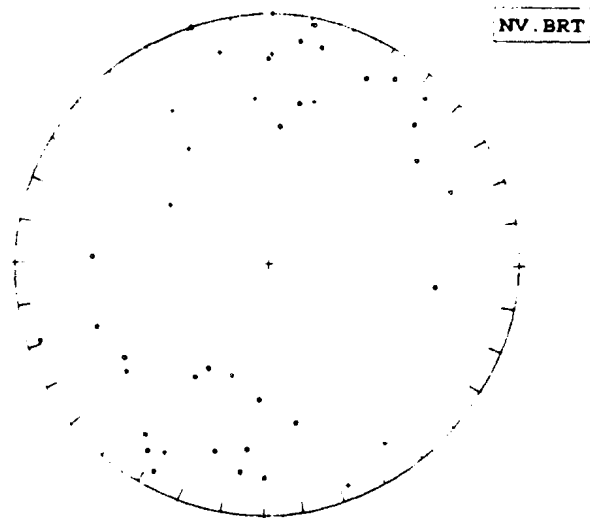


Figure C.12. Lower hemisphere equal area stereoplots of poles to planes for all large scale features mapped in the Santa Barbara Channel structural domain. Poles have been rotated so bedding strikes north-south and is horizontal. Contour interval is percent of poles per one percent area.

Max. value counted:
6.68 times uniform
at 32/74



Contours:
2 4 6

N = 41
Poles to Planes

Figure C.13. Lower hemisphere equal area stereoplots of poles to planes for all large-scale fractures mapped in the Onshore Santa Maria structural domain. Poles have been rotated so bedding strikes north-south and is horizontal. Contour interval is percent of poles per one percent area.

